Deformation Behaviour of Woven Fibre Elastomeric Composites

By

Mohamed Mousa Moraga Milad

Thesis submitted for the degree of Doctor of Philosophy at

Lancaster University

Submitted

April 2020

Acknowledgements

First of all, I must thank my supervisor **Professor Sarah Green** and **Professor Jianqioa Ye** for giving me the opportunity to undertake this project and for helping, advising and supporting me throughout. Without their guidance and extreme patience, I would never have been able to complete this task.

I must thank the Higher Education Commission of **Libya**, for providing financial assistance in the form of a Doctoral Scholarship, and the Physics Department of The University of **Tobruk** for providing research resources.

I am grateful to the academic staff of the Lancaster University Engineering Department. My appreciation also goes to Mark Salisbury, Andy Baker, Nicolas Renninson and Gavriluk, Andrew for providing the technical support in carrying out the experimental work reported in this thesis.

I am truly indebted and thankful to Gerald Steele and Dr Harald Schlegl for their advice and support. Their kindness and understanding made this project a pleasant experience.

Finally, this PhD was the dream of my late father. I will never forget the support and encouragement that came from him. It is for his faith in me that I thank him. I am obliged to other family members who supported me throughout my academic journey. My mother and my wife were great strengths, allowing me to carry on with my studies through difficult times. My sisters and brothers also provided invaluable support. I owe many apologies to my sweet kids Rodina, Mousa, Ahamed, Rawan and Raghad, that I was unable to give them the time they deserved because of the time taken by my study.

List of Publications and Presentations

Milad, M., Green, S. and Ye, J., 2018. Mechanical properties of reinforced composite materials under uniaxial and planar tension loading regimes measured using a non-contact optical method. Composite Structures, 202, pp.1145-1154.

A nonlinear hyperelastic constitutive model for woven fibre reinforced composite "submission to Engineering Structures"

Video Gauging the Behaviour of Sheet Anisotropic Materials during a Hydraulic Bulge Test "submission to Composite Structures"

ABSTRACT

The focus of this thesis is both to improve the characterisation of hyperelastic materials and to develop a simple hyperelastic constitutive model for different composites materials, including woven fabric reinforcements with a hyperelastic matrix. Physical tests are performed on PVC/nitrile elastomer with woven continuous nylon reinforcement composite sheet under loading under uniaxial extension, pure shear, picture frame and bulge tests achieved via wide strip tension testing. Through the novel use of an advanced non-contact optical strain measurement technique, the hyperelastic material behaviour of the composite is investigated, and materials parameters reported for both the warp and the weft directions of reinforcement fibre alignment. To characterise the materials, an appropriate constitutive model is determined by fitting experimental shear and uniaxial tension data. The non-contact technique is used to acquire normal and shear strains at the surface of the composite sheet material when loaded to tensile strains (stretches). Directly measured shear strains are compared to those derived from the normal strain outputs of an optical rectangular strain rosette array, where the two measures are in close agreement. The measured mechanical behaviour under loading is used to determine an approximate strain energy function for the composite via ABAQUS software hyperelastic materials modelling curve fitting, with the Ogden and Yeoh hyperelastic models showing reasonable agreement to experimental data. A simple hyperelastic constitutive model is developed to investigate nonlinear mechanical properties of composites (loaded to large deformations) made of an elastomeric matrix containing biased woven fabric reinforcement. The strain energy function of the developed constitutive model is decomposed into four parts via a series of strain energy contributions. These include the strain energy from the matrix, the tensile energy from fibre elongation in the warp and weft directions and the shearing energy from the interaction between the warp and weft yarns. Furthermore, a new method is proposed to calculate shear strain whereby measurements are taken directly from the surface of the

sample. The three-dimensional digital image correlation (3D-DIC) technique is shown to be a useful tool for obtaining the membrane stress and strain fields during the bulge test. The 3D video gauging, combined with DIC, captures three-dimensional surface geometry and deformed surface displacements.

Table of Contents

Acknowledgements i

List of Publications and Presentations ii

ABSTRACT iii

Table of Contents v

List of Figures ix

List of Tables xiv

Chapter One 1

1.1 Background 1

1.2 Aims 5

1.3 Motivation and Contributions 5

1.4 Objectives 6

1.5 Scope 7

1.5 Thesis Structure 7

Chapter Two 9

2.1 Rubber material 9

2.1.1 Synthetic rubbers 12
2.1.1 The chemical structure of the natural vs synthetic rubber 13
2.1.2 Rubber Elasticity 16
2.1.3 Thermal effects 19
2.1.4 Crystallisation 21
2.1.5 The Glass-Rubber Transition 22
2.1.6 Energy Storing Capability 23

2.2 Composite materials 24

2.2.1 Fibre-reinforced composites 25

2.3 Fabrics Materials 27

2.3.1 Constructions of flexible composites 28
2.3.2 Fabric types 30
2.3.3 Fabric material and coatings comparison 33

2.4 Determination of the mechanical properties of composites with rubber-coated fibre ... 33

2.4.1 Uniaxial testing 35
2.4.2 Stress-Strain Curve of fibre 35
2.4.3 Shear fabric test 36
2.4.4 Planar tension test 37
2.4.5 Picture frame test 37
2.4.6 Biaxial Tensile Testing 38
2.4.7 Constitutive model 41
2.4.8. General formulation of anisotropic hyperelasticity 44
2.4.8 Extension into Principal Directions 46
2.4.10 Anisotropy of Composite Woven Fabric Tensile Properties 47

2.4.11 Ogden model 48
2.4.12 Yeoh model 48

2.5. Summary 50

Chapter Three 51

3.1. Materials 51
3.1.1 Material 1 51
3.1.2 Material 2 52
3.1.3 Material 3 53
3.1.4 Composite Volume Fraction Estimation 54

3.2. Video Gauging 56
3.2.1. The principle of Video Gauging 56
3.2.2. Advantages of Video Gauging 56
3.2.3 Limitations of video gauging 59
3.2.4 Equipment used for video gauging 60
3.2.5 Validation of video gauging measurements 60
3.2.6 Software used for Video Gauging – Digital Image Correlation 61
3.2.7 Targeting Points 62
3.2.8 Target Pattern 62
3.2.9 Measurements and Post-Process 63
3.2.10 Principle of 3D measurements 63
3.2.11 2D Strain Map 64

3.3. Normal Stress and Strain 65

3.4. Combined Test Methods 69

3.5. Poisson's Ratio 70

3.6 Results and Discussions 72

3.7 Full-Field Strain Measurements 88

3.8 Conclusions 92

Chapter Four 94

4.1 Introduction 94

4.2 Shear deformation 95

4.3 Planar tension test 96
4.3.1 Test method description and specimen design 96

4.4 Strain gauge rosette 99
4.4.1 Test setup and specimen preparation 102
4.4.2 Shear strain in Picture Frame tests 105

4.5 Test data and discussion 107
4.5.1 Stress-shear strain curves at different sample locations 107
4.5.2 Shear stress – shear strain for different samples 108

4.6 Strain fields for the planar test 114

4.7 Picture frame test 118
4.7.1 Results and discussion of the Picture Frame Test 118

4.7.2 Strain fields for Picture Frame Test 123

4.8 Conclusions 125

Chapter Five 127

5.1 Isotropic hyperelastic material models 127

5.2 Anisotropic hyperelastic material models 133

5.3 A particular application for fabrics of composites 135

5.4 Characterisation of three fibre reinforced composite materials 138

5.4.1 Identification of the material parameters 138

5.5 Numerical Validation of the Model 148

5.5.1 Mesh 149

5.5.2 Boundary Conditions and Loads 149

5.5.3 Results and Discussion 150

5.6 Conclusion 156

Chapter Six 158

6.1 Introduction ..... Error! Bookmark not defined.

6.2 Bulge Equipment Setup 158

6.2.1. Assembly of the Bulge Chamber 159

6.2.2. Pressurisation System 160

6.2.3. Pressure Sensor and Control System 160

6.3. 3D measurements 161

6.4. Experimental Procedure 162

6.5. Theoretical Investigation 165

6.6. Results and Discussion 167

6.6.1 Strain Fields For Bulge Test 179

6.7. Conclusions 182

Chapter Seven 184

7.1 Conclusions and future work 184

7.1.1. General 184

7.1.2. Conclusions 185

7.1.3. Recommendations for future work 187

References 189

APPENDIX 1 208

APPENDIX 2 209

APPENDIX 3 210

APPENDIX 4 211

APPENDIX 5 212

APPENDIX 6 213

APPENDIX 7 216

List of Figures

Figure 1. 1: Storage Tank Seals, B. fuel and water storage (Trelleborg) 2
Figure 1. 2: Dynamic Earth Centre, Edinburgh, U.K (Centre, 2014) 4
Figure 1. 3: Saga headquarters, Kent, U.K (1999). 4
Figure 2. 1: Typical load-extension curve for vulcanised rubber (Treloar 1975). 12
Figure 2. 2: Structure of molecule of (a) Hevea rubber (b) gutta-percha (Treloar 1975). 13
Figure 2. 3: Internal energy and entropy components of tensile stress as functions of extension (Freakley and Payne, 1978) 18
Figure 2. 4: Typical neoprene rubber stress-strain relationship (%) for various loading modes (Aboshio, 2014). 19
Figure 2. 5: Temperature rise with an adiabatic extension (Treloar 1975). 20
Figure 2. 6: Molecular structure of crystalline rubber (diagrammatic). The parallel bundles represent crystallites. 22
Figure 2. 7: Composite material composition. 25
Figure 2. 8: Classification of composite materials a) based on a matrix and b) based on reinforcement. 26
Figure 2. 9: SEM photographs of (a) natural and (b) human-made fibres (Williams, R.W., 2010). 27
Figure 2. 10: Coated woven fabric components (Zhang, L., 2010). 29
Figure 2. 11: Schematics of common woven fabrics. (a) Plain weave. (b) Twill weave. (c) Satin weave (Gay and Hoa, 2007). 31
Figure 2. 12: Typical plain-woven fabric showing warp and weft fibres (Tan et al., 1997). 31
Figure 2. 13: Schematic of a typical structural braided fabric (Atex, 2015). 32
Figure 2. 14: Schematic diagram of knitted fabrics (a) Weft-knitted fabric, (b) Warp-knitted fabric (Li and Dai 2006). 32
Figure 2. 15: Schematic of a typical load-extension curve. 36
Figure 2. 16: (a) Direct shear force measurement, (b) bias-extension test method, and (c) picture frame test method (Taha et al., 2013). 37
Figure 3. 1: Specimen geometry and cross-sections of the composite material showing the warp and weft arrangements for 5 mm thickness. 52
Figure 3. 2: Specimen geometry and cross-sections of the composite material showing the warp and weft arrangements for 3 mm thickness. 53
Figure 3. 3: Specimen geometry and cross-sections of the composite material showing the warp and weft arrangements for 2 mm thickness. 54
Figure 3. 4: Specimen geometry and cross-sections of the woven fabric basic specifications, the warp (x) and the weft (y) fibre orientations within the PVC rubber matrix. 55
Figure 3. 5: Section of the composite showing microscopic images of the weft and warp fibres bundles. 56
Figure 3. 8: Schematic of samples preparation. 66
Figure 3. 9: Experimental set-up showing the video gauge system and sample position within the tensile testing frame. 67
Figure 3. 10: Strain gauges longitudinally aligned with the uniaxial tension load direction (Sample has been prepared with a speckle surface pattern). 68
Figure 3. 11: (a) Displacement of the composite specimen before the loading; (b) after the loading, showing the strain. 69

Figure 3. 12: (A) Poisson's ratio of a virtual strain gauge in x- and y-direction; (B) Poisson's ratio method shows the location in a typical composite sample in tensile loading. 72
Figure 3. 13: Mode for specimens before and after loaded parallel to the warp and weft fibre direction tested..... 74
Figure 3. 14: Uniaxial testing stress-strain for the composite specimens loaded parallel to warp fibre direction (EXA-1196). 74
Figure 3. 15: Uniaxial testing stress-strain for the composite specimens loaded parallel to warp fibre direction (EXA-1180). 75
Figure 3. 16: Uniaxial testing stress-strain for the composite specimens loaded parallel to warp fibre direction (EXA-1182). 75
Figure 3. 17: Uniaxial testing stress-strain for the composite specimens loaded parallel to weft fibre direction (EXA-1196). 76
Figure 3. 18: Uniaxial testing stress-strain for the composite specimens loaded parallel to weft fibre direction (EXA-1180). 76
Figure 3. 19: Uniaxial testing stress-strain for composite specimens loaded parallel to weft fibre direction (EXA-1182). 77
Figure 3. 20: Uniaxial testing stress-strain for composite specimens of all different materials 78
Figure 3. 21: Uniaxial tensile stress-strain graph for the composite specimens loaded parallel to the warp fibre direction. 82
Figure 3. 22: Uniaxial tensile stress-strain graph for the composite specimens loaded parallel to the weft fibre direction. 82
Figure 3. 23: Poisson's Ratio for the composite specimens loaded parallel to the weft fibre direction (EXA-1196). 84
Figure 3. 24: Poisson's Ratio for the composite specimens loaded parallel to the weft fibre direction (EXA-1180). 85
Figure 3. 25: Poisson's Ratio for the composite specimens loaded parallel to the weft fibre direction (EXA-1182). 85
Figure 3. 26: Poisson's Ratio for the composite specimens loaded parallel to the warp fibre direction (EXA-1196). 86
Figure 3. 27: Poisson's Ratio for the composite specimens loaded parallel to the warp fibre direction (EXA-1180). 87
Figure 3. 28: Poisson's Ratio for the composite specimens loaded parallel to the warp fibre direction (EXA-1182)..... 87
Figure 3. 29: Strain maps for the composite specimens loaded parallel to the warp fibre direction. . 90
Figure 3. 30: Strain maps for the composite specimens loaded parallel to the weft fibre direction. .. 90
Figure 3. 31: Strain maps for the composite specimens loaded parallel to the weft fibre direction, reduced colour mapping interval..... 92
Figure 4. 1: Planar tension schematic representation (Wadham, 2006) 96
Figure 4. 2: Planar tension test 97
Figure 4. 3: Schematic diagram of grips 98
Figure 4. 4: Wide strip (pure shear) specimen geometry showing the six video gauge locations and the equivalent stress state. 100
Figure 4. 5: Strain gauge rosette individual gauge orientations. 100
Figure 4. 6: Shear strain versus shear stress from a rosette strain gauge for the warp direction of fabric loading, experimental results and calculations. 101
Figure 4. 7: Stress-shear strain curves derived from different sample positions of the EXA-1180 sample mounted parallel to the weft direction. 107

Figure 4. 8: Planar shear-oriented stress vs strain behaviour for fibre-filled composite specimens loaded parallel to the warp fibre directions of EXA-1196. 108
Figure 4. 9: Planar shear-oriented stress vs strain behaviour for fibre-filled composite specimens loaded parallel to the weft fibre directions of EXA-1196. 109
Figure 4. 10: Planar shear-oriented stress vs strain behaviour for fibre-filled composite specimens loaded parallel to the warp fibre directions of EXA-1180. 109
Figure 4. 11: Planar shear-oriented stress vs strain behaviour for fibre-filled composite specimens loaded parallel to the weft fibre directions of EXA-1180. 110
Figure 4. 12: Planar shear-oriented stress vs strain behaviour for fibre-filled composite specimens loaded parallel to the warp fibre directions of EXA-1182. 110
Figure 4. 13: Planar shear-oriented stress vs strain behaviour for fibre-filled composite specimens loaded parallel to the weft fibre directions of EXA-1182 111
Figure 4. 14: Shear strain versus shear stress for composite specimens of all different materials 113
Figure 4. 15: Strain contour map results for a sample of EXA-1196 thickness loaded parallel to the weft and warp. 115
Figure 4. 16: Strain contour map results for a sample of EXA-1180 thickness loaded parallel to the weft and warp. 116
Figure 4. 17: Strain contour map results for a sample of EXA-1182 thickness loaded parallel to the weft and warp. 117
Figure 4. 18: Shear-frame test. 103
Figure 4. 19: Experimental setup for the picture frame testing. 104
Figure 4. 20: Specimen shape and size. 105
Figure 4. 21: Picture frame test (a) at the start and (b) at the end of the test. 119
Figure 4. 22: Picture Frame shear stress vs shear strain behaviour for fibre-filled composite specimens of EXA-1196. 120
Figure 4. 23: Picture frame shear stress vs shear strain behaviour for fibre-filled composite specimens of EXA-1180. 121
Figure 4. 24: Picture frame shear stress vs shear strain behaviour for fibre-filled composite specimens of EXA-1182. 121
Figure 4. 25: Shear Strain versus shear stress in a picture frame test for composite specimens of all different materials 122
Figure 4. 26: Strain contour map results for a picture frame of EXA-1196. 124
Figure 4. 27: Strain contour map results for a picture frame of EXA-1180. 124
Figure 4. 28: Strain contour map results for a picture frame of EXA-1182 thickness. 125
Figure 5. 1: Typical simple tension response of (a) rubber and (b) soft tissue (Ogden, 2011). ..... **Error! Bookmark not defined.**
Figure 5. 2: Fitting of uniaxial data for samples loaded parallel to the weft direction using different hyperelastic models (EXA-1196). 131
Figure 5. 3: Fitting of different hyperelastic models with planar data for samples loaded parallel to the weft direction (EXA-1196). 131
Figure 5. 4: Fitting of different hyperelastic models with uniaxial data for samples loaded parallel to the warp direction (EXA-1196). 132
Figure 5. 5: Fitting of different hyperelastic models with planar data for samples loaded parallel to the warp direction (EXA-1196). 132
Figure 5. 6: Schematic approach giving a description of parameters. 139
Figure 5. 7: Strain energy density against invariant in uniaxial tensile stress-strain graph in weft direction for EXA-1196. 140

Figure 5. 8: Strain energy density against invariant in uniaxial tensile stress-strain graph in weft direction for EXA-1180. 141
Figure 5. 9: Strain energy density against invariant in uniaxial tensile stress-strain graph in weft direction for EXA-1196. 141
Figure 5. 10: Strain energy density against the invariant in uniaxial tensile stress-strain graph in the weft direction for EXA-1196. 142
Figure 5. 11: Strain energy density against the invariant in uniaxial tensile stress-strain graph in the weft direction for EXA-1180. 143
Figure 5. 12: Strain energy density against the invariant in uniaxial tensile stress-strain graph in the weft direction for EXA-1182. 143
Figure 5. 13: Strain energy density against the invariant in uniaxial tensile stress-strain graph in the warp direction for EXA-1196. 144
Figure 5. 14: Strain energy density against the invariant in uniaxial tensile stress-strain graph in the warp direction for EXA-1180. 145
Figure 5. 15: Strain energy density against the invariant in uniaxial tensile stress-strain graph in the warp direction for EXA-1182. 145
Figure 5. 16: Strain energy density against the invariant $\boldsymbol{I8}$ in the picture frame test for EXA-1196. 146
Figure 5. 17: Strain energy density against the invariant $\boldsymbol{I8}$ in the picture frame test for EXA-1180. 147
Figure 5. 18: Strain energy density against the invariant $\boldsymbol{I8}$ in the picture frame test for EXA-1196. 147
Figure 5. 19: ABAQUS model of displacement distribution in a composite for warp direction. 151
Figure 5. 20: ABAQUS model of displacement distribution in a composite for weft direction. 152
Figure 5. 21: True load-displacement relation of the experimental and simulated model under uniaxial loading in the warp direction (EXA-1182). 153
Figure 5. 22: True load-displacement relation for the experimental and simulated model under uniaxial loading in the warp direction (EXA-1180). 153
Figure 5. 23: True load-displacement relation for the experimental and simulated model under uniaxial loading in the warp direction (EXA-1196). 154
Figure 5. 24: True load-displacement relation for the experimental and simulated model under uniaxial loading in the weft direction (EXA-1182). 154
Figure 5. 25: True load-displacement relation for the experimental and simulated model under uniaxial loading in the weft direction (EXA-1180). 155
Figure 5. 26: True load-displacement relation for the experimental and simulated model under uniaxial loading in the weft direction (EXA-1196). 155
Figure 6. 1: Schematic of a Bulge Test (Zioupes et al., 1992). ..... **Error! Bookmark not defined.**
Figure 6. 2: A systematic overview of the setup of the bulge. 159
Figure 6. 3: (A) The pressure pump system. (B) Power supply. (C) Arduino. 161
Figure 6. 4 Assembly of a pressure chamber, die and specimen for the bulge test. 162
Figure 6. 5: Schematic of the bulge testing facility, showing the bulge tester, the pressurising unit, and the video gauge system. 163
Figure 6. 6: Hydraulic bulge test with the video gauge system utilising two cameras. 164
Figure 6. 7: Depicted is the cross-section of a spherical pressure. 165
Figure 6. 8: Biaxial stress state of a membrane under the bulge test at the pole (Aboshio et al., 2015) 167
Figure 6. 9: Pressure versus dome height. 168

Figure 6. 10: Dome height versus bulge radius. 169
Figure 6. 11: Thickness variation versus dome height. 170
Figure 6. 12: Stress versus strain theoretical (T) and experiential (E). 171
Figure 6. 13: Stress versus strain (bulge test). 172
Figure 6. 14: Stress versus strain (tensile test). 173
Figure 6. 15: Schematic view of directions (angles) in the strain direction. 174
Figure 6. 16Stress versus strain for all orientation angles θ for materials of EXA-1196. 175
Figure 6. 17: Stress versus strain for all orientation angles θ for materials of EXA-1180. 175
Figure 6. 18: Stress versus strain for all orientation angles θ for materials of EXA-1182 thickness... 176
Figure 6. 19: Schematic shear strain with a position on the surface. 177
Figure 6. 20: Pressure versus shear strain for materials of EXA-1196. 177
Figure 6. 21: Pressure versus shear strain for materials of EXA-1180. 178
Figure 6. 22: Pressure versus shear strain for materials of EXA-1182. 178
Figure 6. 23: The specimen viewed from above during a test 180
Figure 6. 24: Maps of the strain components on the undeformed configuration for $\boldsymbol{\varepsilon}_{xx}$ and $\boldsymbol{\varepsilon}_{yy}$ 180
Figure 6. 25: Maps of the shear strain components on the undeformed configuration 181

List of Tables

Table 2. 1 The Structural formulae of some typical rubbers 15
Table 2. 2: Energy storage capabilities of various materials (Freakley and Payne,1978) 23
Table 3. 1 Material properties EXA-1196. 52
Table 3. 2 Material properties EXA-1180. 53
Table 3. 3 Material properties EXA-1182. 54
Table 3. 4 Volume fraction of matrix and fibre. 55
Table 3. 5 Comparison of Poisson’s ratio (EXA-1196). 72
Table 3. 6 Strain for the materials. 78
Table 3. 7 Young's modulus. 82
Table 3. 8 Poisson’s ratio of different materials. 83

Chapter One

1.1 Background

Since their first general acceptance, the development of new materials has had regard to the mechanical and geometric properties of composites, where it is essential to understand the elastic behaviour of fabric-reinforced rubber elastomeric composites.

Now among the most advanced and versatile of engineering materials, composites have brought advances in regard to the specific strength and stiffness of automotive and aircraft structures, where the woven fibre composites deliver enhanced elastic properties. Elsewhere fibres have proven suitable and cost-effective in covering large spaces, for example, stadium walls and tennis courts (Awais et al.,2020).

Composites, of different types of fibre and elastomer or rubber-like matrix materials, offer a variety of technical uses. The distinguishing characteristic of elastomer-based composites is their useable deformation ranges. These exceed those of composites with stiffer matrices, such as metals, ceramics, or rigid polymers (Huang et al.,2000). In particular, it is the non-linearity property that presents significant problems in developing a constitutive model to characterise the stress/strain response characteristics of elastomer composites. The fabric-reinforced rubber elastomeric composite is such that strands are generated via the process of weaving. Those strands are interwoven in two orthogonal directions (the warp and fill directions), and saturated with a resin substance (Scida et al.,1999). Fibre-reinforced composite materials offer greater out-of-plane stiffness, strength, and toughness capabilities than laminate composites. The complicated geometry of this composite class gives rise to an almost limitless number of designs and elements, where many aspects may be altered, including the microstructure geometry, weave type, hybridization, and the composition of the component elements (e.g. geometrical and mechanical parameters of strands and resin)(Chou, T.W., 1992).

Fabric-reinforced elastomeric composites play an essential part in a large number of engineering applications, including those in the petroleum, marine, aerospace, transport, and gas distribution industries, as shown in Figure 1.1. One appealing property of elastomer is the capacity to bear large temporary deformations with no significant permanent deformation upon load removal (Treloar, 1973). One reason is their low weight. Advantages also arise from their high strength properties, high absorption capacity and, indeed, their unique material properties (for example, resistance to chemical or climate effects) (Aboshio et al., 2015).

Figure 1. 1: Storage Tank Seals, B. fuel and water storage (Trelleborg)

They can be easily manufactured, as composites of polyester fibres and rubber coating materials are comparatively airtight (Reese, 2001). The fabric has practically no compression stiffness or bending, but has good tension and provides stiffness in tensile structures as it maintains its shape, thereby preventing flutter and excessive deflection (Bridgens, 2005; Testa, 1987).

In traditional forms of construction, fabrics have been in use for thousands of years in many applications involving temporary structures. In modern times, many applications have been

developed for fabrics, such as insulation, roofing work and fillers. Figures 1.2 and 1.3 show typical applications of fabrics in modern structures. Modern fabric-composites have a greater capacity to absorb impact than conventional materials (Reddy and Miravete, 1995). This property is enhanced when the fabric is coated with rubber. Other beneficial advances that reduce the extensibility of rubber in, for example, the strengthening crash barriers

Typical carcass materials include neoprenes, silicones and butyl rubbers (Testa and Yu, 1987; Reese et al., 2001). For woven textile reinforcements, the textile yarn orientation is a function of the method of manufacture and textile architecture. If warp yarns are defined, by their direction of orientation in the axial/lengthwise directions of the textile, then the weft yarns are woven across the warp yarns, running in the transverse direction. The load-deflection response of a woven textile is a function of the yarn material properties and also the overall textile architecture (Jacobsen et al., 2004). To protect the yarns from both mechanical abrasion and chemical degradation, textiles are commonly coated or moulded within an elastomeric carcass. Synthetic rubbers such as PVC/nitrile composites enhance thermal stability and deliver excellent ozone and oil resistance, making these types of fibre-filled composites commonplace in the petrochemical industries (Hardiman, 2000).

Figure 1. 2: Dynamic Earth Centre, Edinburgh, U.K (Edinburgh Architecture 2014).

Figure 1. 3: Saga headquarters, Kent, U.K (Saga Group Ltd 1999).

The behaviour of woven textiles is determined by complex structural interactions in yarn and fibre.

Vulcanised rubber components often have spatial heterogeneity (non-homogeneity) in their chemical and mechanical characteristics; examples include crosslink density, hardness, shear modulus, and so on. Material non-homogeneity is caused by non-uniform transit factors such as temperature during manufacture (e.g., compression moulding) or by the detrimental impact of oxidation. Aside from this inadvertent non-homogeneity, several studies have proposed purposeful tailoring of the continuous spatial variation of rubber. This is known in materials engineering as grading or functional grading. Although functional grading is well-established for metal-ceramic composites and other polymeric composites, it appears to be relatively new for rubberlike polymers (elastomers). It is widely known that, by spatially customising the relevant material characteristics, the mechanical, thermal, and optical performance of materials, including polymers, may be considerably enhanced and optimised for particular applications (Bilgili, 2004).

1.2 Aims

The aims of this research on fibre-reinforced composites materials are twofold: first is to understand their mechanical properties, where the particular focus is on rubber matrix mixes with fibres; second to investigate behavioural characteristics when the materials are subjected to deformation.

1.3 Motivation and Contributions

Developments in numerical methods have improved our ability to simulate fabric-reinforced elastomeric composites materials. There is a perpetual need to develop reliable techniques to determine the mechanical parameters of new materials. These include analytical modelling, numerical simulations, and experimental data to build a based understanding of characteristics of materials.

1.4 Objectives

Specific objectives are to:

1. Understand the physical properties of materials whose specification comprises a:
    a. vulcanised, carbon-filled black PVC/nitrile compound and nylon tyre cords fabric with a two-directional warp and weft (Trelleborg reference data sheet EXA-1196).
    b. vulcanised carbon-filled black PVC/nitrile compound and nylon woven fabric (Trelleborg reference data sheet EXA-1180).
    c. vulcanised polychloroprene compound and nylon-coated base fabric, (Trelleborg reference data sheet EXA-1182).
2. Advance a non-contact optical technique to measure composite deformation behaviour.
3. Perform tensile tests on all fibre-reinforced composites to understand more about composite deformation behaviour parallel to the warp and weft fibre directions.
4. Analyse tensile test results critically and establish relationships with fibre architecture.
5. Perform appropriate tests to develop a reliable test technique to determine the shear characteristics of composite materials under large deformations.
6. Develop numerical methods to improve the simulation capability of a constitutive model that closely correlates with the phenomenological response of fibre-reinforced composites under various loads. Also, to draw comparisons between the Finite Element Model and the experimental data.
7. Develop the three-dimensional digital image correlation (3D-DIC) technique, to measure the surface height of a pressurized membrane and strains when loaded in a

bulge test. Unlike simple tensile tests, the new method records effective stress and strain before the material peak, thereby providing comprehensive details of the mechanical properties of the material.

1.5 Scope

The first part of this research focuses on experimentally based uniaxial tension and shear tests of the three fibre-reinforced composite materials used for the carcasses of structures.

The second part is concerned with the development and validation of composite materials constitutive models. To this end, the existing analysis theory is implemented.

The third part focuses on the experimental investigation of the properties/characteristics of the different fibre-reinforced composites materials used in the hydraulic bulge test.

1.6. Thesis Structure

The thesis is comprised of seven chapters. Chapter 1 provides a general introduction and background to the aims and objectives of this research.

Chapter 2 offers an overview of rubber-like materials, woven-fibre composites, and fibre-reinforced composites. This chapter establishes the context of previous work and the current state-of-the-art in all areas pertinent to the research: fibre, yarn, coating and fabric properties, fabric test methods, the representation of uniaxial and planar shear biaxial test data, use of test data in membrane structural analysis, fibre-reinforced composites, applications and modelling and typical tests used to assess their properties.

Chapter 3 describes different types of fibre-reinforced composite materials. It also describes how the various apparatus used, namely Video Gauge and Zwick machines, communicate with each other and the two sets of respective data can be combined. It also describes the benefits

of the video gauge and how it can be used for different testing methods. In addition, the uniaxial tests the mechanical behaviour of the different fibre-reinforced composites, are evaluated under different conditions. The results, which should give the characteristic behaviours of the composites, are analysed and discussed.

Chapter 4 studies new planar shear and picture frame test methods, by using the video gauge to induce large deformations under small loads and subsequently to retain the initial configuration after the load is removed; i.e., with no permanent deformation. With significant results, this allows further comparisons of the different fibre-reinforced composites in terms of their shear test behaviours. Finite element modelling supplements the results from the picture frame test.

Chapter 5 introduces and briefly reviews the literature on constitutive relation formulation for anisotropic materials. It also focuses on: continuum mechanics theory and constitutive relations for hyperelastic materials; the identification of model parameters; and the validation of the material model using the FEA software. Comparative results from the modelling are presented.

Chapter 6 describes the bulge tester, a widely used testing facility for applying a nearly equibiaxial state of stress to a plate. This chapter describes the bulge tester that was designed and fabricated for this study and the results of the various bulge experiments performed.

Chapter 7 presents a summary of the conclusions of each chapter and presents a number of recommendations for further work.

Chapter Two

This chapter offers an overview of rubber-like materials, woven fibre composites, and fibre-reinforced composites. It reviews previous work and the current state-of-the-art in areas that are pertinent to the research, such as fibre, yarn, coating and fabric properties, fabric test methods, representation of uniaxial, planar shear, biaxial, and bulge test data, and the use of test data in membrane structural analysis and modelling. In this chapter, the mechanical properties of rubber, fabric, analytical modelling, numerical simulations, and experimental data reviewed.

2.1 Rubber material

Rubber is a series of long-chain molecular polymers that contains repeating subunits. The term Polymer is derived from the Greek words "poly" (many) and "mer" (parts). Polyisoprene is the chemical term for natural rubber. Isoprene is the “monomer” (one part) from which it is made., Although rubber is made up of repeated isoprene units, isoprene is not the beginning monomer. Rubber is produced by a sequence of biological events that begin in the tree with isopentenyl pyrophosphate. The term ‘elastomer’ is used interchangeably with ‘rubber’. Rubber has a wide variety of applications across many industries, including piped, vibration isolators, medical devices and structural bearings. (Smith, 1993).

Natural rubber is a one-of-a-kind material found only in nature, where coagulation is used to extract sap ("latex") from rubber-producing plants. The commercial market is completely dominated by Hevea Brasiliensis. The majority of NR molecules are cis-1,4-polyisoprene, where there is no indication of trans material in the natural product. Although the natural polymer's molecular weight is extremely high, it varies across lattices from different tree clones. Average molecular weight (M_w) values can range from 3.4 10^6 to 10.2 10^6 g/mol. A

low glass transition temperature (T_g) of roughly 64°C is due to the highly flexible backbone. NR is also capable of crystallisation because of its highly regular structure. Stretching samples, such as in a tensile test, can also cause crystallisation. Microscopic crystal structures are generated by stress-induced crystallisation. Thereby, natural rubber has a higher vulcanizate strength than styrene-butadiene rubber, which does not crystallise. The inclusion of the methyl group in 1,4-polyisoprene increases the activity of the double bond, so making it more reactive - than styrene-butadiene rubber or polybutadiene rubber - to a wide range of chemicals including vulcanization solutions. However, the high unsaturation low saturisation of the carbon backbone brings several disadvantages, such as abrasion sensitivity, low oil and heat resistance, and assault by oxygen and ozone, as well as UV light (Hernández et al.,2018; Bai, and Yin,2015).

Natural rubber manufacturers from the Far East (Malaysia, Indonesia, Thailand, and Sri Lanka) comprise almost 80% of the market. In the year 2000, around 7 million metric tonnes of natural rubber were produced. By 2017, this had increased to over 13.2 million metric tonnes (compated with worldwide consumption, up cd by 1.4 percent in 2017, to 12.9 million tonnes (Osgooei, and Konstantinidis, 2014; Board, 2016; Fong, and Lim, 2018;)

Because of its greater building tack, improved processing, hot tear resistance, high resilience, and outstanding dynamic and fatigue qualities, natural rubber is favoured over other synthetic rubbers. This, it is an excellent choice for tires and tire goods, particularly carcasses and sidewalls. Other products include footwear, carpet and rug backing, surgical items, adhesives, and textile thread (Hernández et al.,2018).

Natural rubber belongs to the polymer group and have long-chain molecules made up of repeated units. The requirements for a material to be an elastomer are as follows:

- The molecules must be extended (chain-particles) with a capacity to rotate freely about the bonds at the ends of molecules joining neighbouring molecule units.
- Either by chemical bonds or by mechanical entrapment, referred to as cross-links, the molecules must be joined at various points to form a three-dimensional system.
- Aside from the cross links, the molecules must have the capacity to move quickly past one another; ultimately, the intermolecular attraction between them must be relatively small (Bever, 1992).

In addition to elastic recovery, elastomers have unique physical properties (flexibility, extensibility and durability). Excellent weather resistance, chemical attachment and a host of valuable mechanical properties are generally realised in processes such as vulcanisation (Morton, M. 2013). As identified by Faraday (1826), natural rubber, is primarily a hydrocarbon with the formula C5H8. This hyperelastic non-linear stress-strain behaviour of rubber is characterised by the absence of a single, well-defined modulus of elasticity. As noted by Morton, by their inherently highly irregular chain structure, when tension is used elastomers including natural rubbers butyl and neoprene become crystallised. However,strain-crystallizing properties are not generally available to all elastomers (Bever, 1992) and may not be appropriate in the preparation of the materials for certain technical applications.

The most important physical characteristics of natural rubber are (1) the high level of deformability under relatively little stress and (2) the recovery of the initial configuration after the load is removed. Given the highly non-linear stress-strain characteristics, a simple elasticity test is insufficient. Hence, the importance of ascertaining the elastic behaviour of extensible nonlinear materials. (Shahzad, et al., 2015).

A force-stretch curve for rubber is illustrated in Figure 2.1. The extensibility is typically in the region of 500 – 1000% as compared to unloaded rubber (Treloar 1975). Spinal polymer chains

usually align when strain is applied, so causing the whole structure to display a crystallisation behaviour.

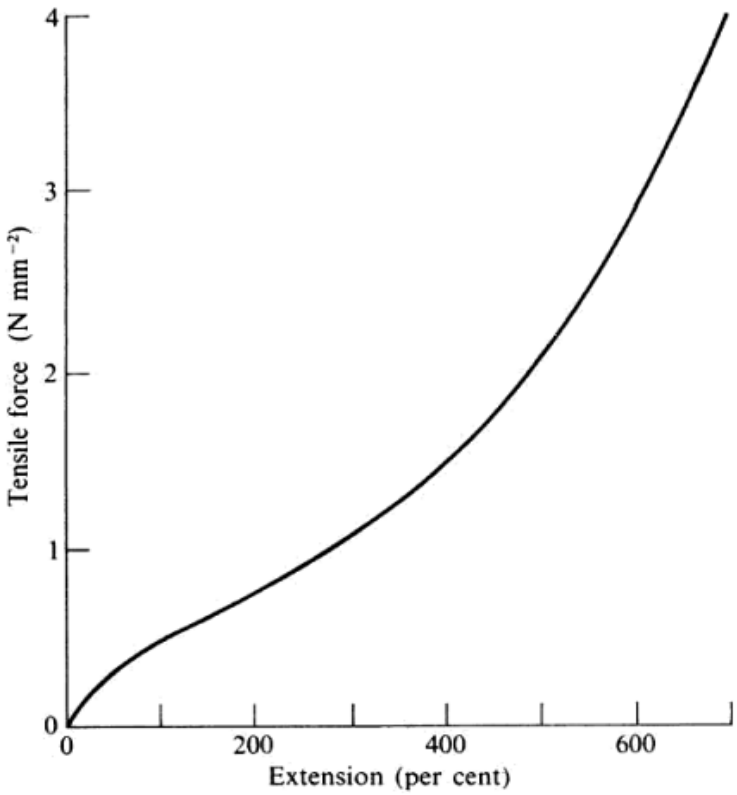

Figure 2. 1: Typical load-extension curve for vulcanised rubber (Treloar 1975).

2.1.1 Synthetic rubbers

A butadiene-styrene copolymer (SBR) is the most frequently used synthetic general-purpose rubber. It was produced on a massive scale in the United States during World War II to compensate for the loss of the world's primary rubber-growing regions (Malaya and the Dutch East Indies). Butyl rubber, which is made from polyisobutylene and has a low gas permeability, is widely used in inner tubes and other applications. When compared to natural rubber, polychloroprene (Neoprene) has a higher resilience to deterioration, as well as reduced oil absorption and flammability, These features make it suitable for engineering applications, especially when oil or petrol contamination is possible (Nurazzi et al.,2021) (Treloar 1975).

2.1.1 The chemical structure of the natural vs synthetic rubber

Natural rubber is fundamentally a hydrocarbon, and Faraday (1826) determined its composition to be consistent with the formula (C_5H_8). When suspended in either a watery liquid or a serum to a concentration of approximately 35%, the rubber particles include small latex globules of 0.1-1.0 /µm diameter. Unless protein is absorbed on the surface, those particles coalesce to form a protective layer or sheath of non-rubber components. Rubber may then be strengthened, either by drying the water or by using acid precipitation. As most non-rubber components remain in the serum, acid precipitation gives purer rubber (Treloar 1975).

The rubber hydrocarbon is a polymer having a high number of isoprene (C_5H_8) units connected in the form of a continuous chain (as shown in Figure 2.2). The progression of isoprene units in the chain is perfectly regular, with each fourth carbon atom in the chain carrying a methyl (CH_3) side-group. The stereochemical structure of the chain around its double bonds is critical because these bonds largely decide the susceptibility of the elastic structure to oxidation or other degradative responses, which then lead to the degradation of its physical properties (Treloar 1975).

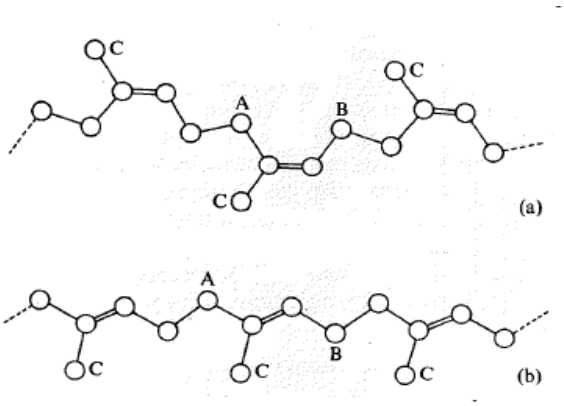

Figure 2. 2: Structure of molecule of (a) Hevea rubber (b) gutta-percha (Treloar 1975).

The structure of Gutta-percha, the other natural polymer of isoprene, varies slightly but noticeably from rubber. The single change, as shown in Figure 2. 2, is the placement of the single C—C bonds in relation to the double bonds in the chain backbone. The single bonds in rubber are on the same side of the double bond, making the cis-configuration, but they are on different sides of the double bond in Gutta-percha, forming the trans-configuration. Gutta-percha crystallises more easily than rubber as a result of this difference; it is crystalline at ambient temperature and only becomes rubber-like when heated over the crystal melting point, which is 65 °C (Treloar 1975).

Although the two single bonds nearest to the double bond are permanently set in a single plane (whether in the cis- or Jrans-configuration), the other single bonds are not. They may rotate out of the plane created by nearby bonds. Some common rubbers and related materials structural formulas are shown in Table 1.

Table 2. 1 The Structural formulae of some typical rubbers

$-CH_2-C(CH_3)=CH-CH_2-$	Polyisoprene (natural rubber, gutta-percha)
$-CH_2-CH=CH-CH_2-$	Polybutadiene
$-CH_2-C(Cl)=CH-CH_2-$	Polychloroprene (Neoprene)
$-CH_2-CH(Cl)-$	Polyvinyl chloride
$-CH_2-CH(C_6H_5)-$	Polystyrene
$-CH_2-C(CH_3)_2-$	Polyisobutylene (basis of 'butyl' rubber)
$-CH_2-CH=CH-CH_2-CH_2-CH(C_6H_5)-$	†Butadiene-styrene (BSR) rubber
$-CH_2-CH=CH-CH_2-CH_2-CH(CN)-$	†Butadiene-acrylonitrile ('nitrile') rubber
$-O-Si(CH_3)_2-$	Polydimethyl siloxane (silicone rubber)
$-CH_2-$	Polyethylene (polythene)
$-CH_2-CH(CH_3)-$	Polypropylene
$-CH_2-C(CH_3)(COOCH_3)-$	Polymethyl methacrylate (Perspex)

† In these copolymers the respective monomer units occur in a random sequence along the chain.

2.1.2 Rubber Elasticity

The property of rubber elasticity may be measured by noting movements due to thermal vibrations, which cause its particles to take on an irregular winding shape with an end-to-end distance that is shorter than the fully extended length. A length of unstretched rubber is a tangled mass of long, randomly arranged molecules. As the rubber is extended, the molecules become more aligned in the direction, in which it is being stretched (Treloar, 1973; Freakley and Payne, 1978),).

Variations in this outcome are mainly determined by the composition of the particular rubber, the manufacturing process and the design and shape of the product. Vulcanization results in substantial changes in properties in terms of hardness, elasticity or strength depending on the amount and type of chemicals and additives being used (Hanhi, and Tirila, 2007). The Gough-Joule effect immediately follows from the initial assumptions of kinetic theory. Given changes in internal energy, it is thus possible to mathematically express them as

$$dU = dQ + dW \tag{2.1}$$

Internal energy is assumed independent of the extension; that is, dE = 0 for the rubber, as for the single chain (at constant temperature).

Where

- dU is the change in internal energy
- dQ is the change in heat input
- dW is changed in work input

With the use of:

$$dQ = T\,d\,S \tag{2.2}$$

And

$$dW = Fdl \tag{2.3}$$

$$dE = TdS + Fdl$$

It follows that:

$$F = \frac{dE}{dl} - T\,\frac{dS}{dl} \tag{2.4}$$

Where F is the force, T is temperature and *dl* the change in length, dS is changed in entropy.

$\frac{dE}{dl}$ Represents the rate of changes in internal energy during deformation.

$T\,\frac{dS}{dl}$ represents the rate of change of entropy.

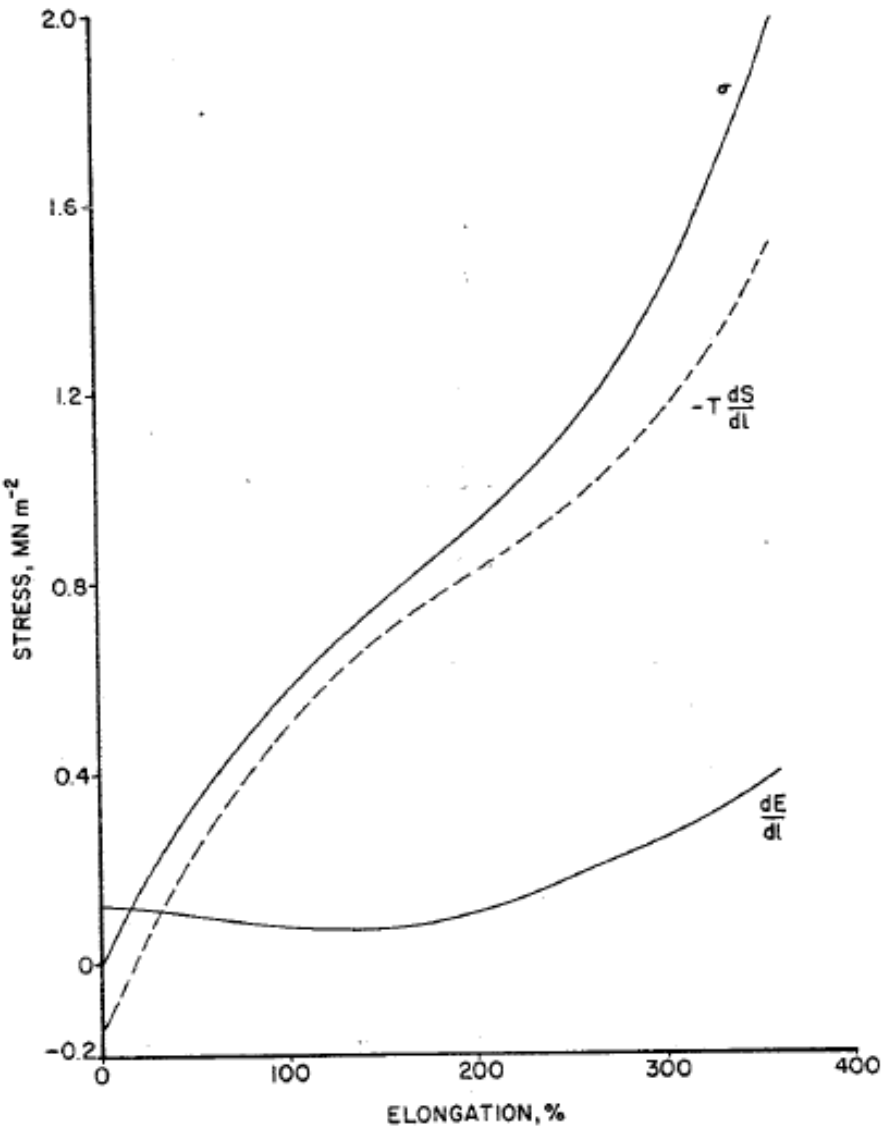

Figure 2. 3: Internal energy and entropy components of tensile stress as functions of extension (Freakley and Payne, 1978)

Within a unit cross-sectional area, the force F in equation (2.4) becomes stress (σ). The stress-strain curves of a strain-crystallising rubber are shown in Figure 2.3. Figure 2.4 shows the stress-strain relation of neoprene rubber, under both uniaxial and biaxial shear load conditions (Aboshio, 2014). As indicated by both figures, this relationship is clearly non-linear across all stretch regimes (Hooke's law does not apply). Although an approximately linear relationship between stress-strain is sometimes used in rubber, it is valid only in areas of low strain, i.e., not exceeding 5 %.

The high entropy shift due to the introduction of order in the system as the rubber is extended is another key element as seen in Figure 2.1. The same parameters are not observed for other materials especially metals, where entropy change is very low so that the rate of internal energy change (dl/dE) predominates. From this, it follows that the interatomic distances of the metal molecules, rather than the structure of molecules, change to bend metal. In short, the area of elasticity of metal relative to rubber is very weak (Freakley and Payne, 1978).

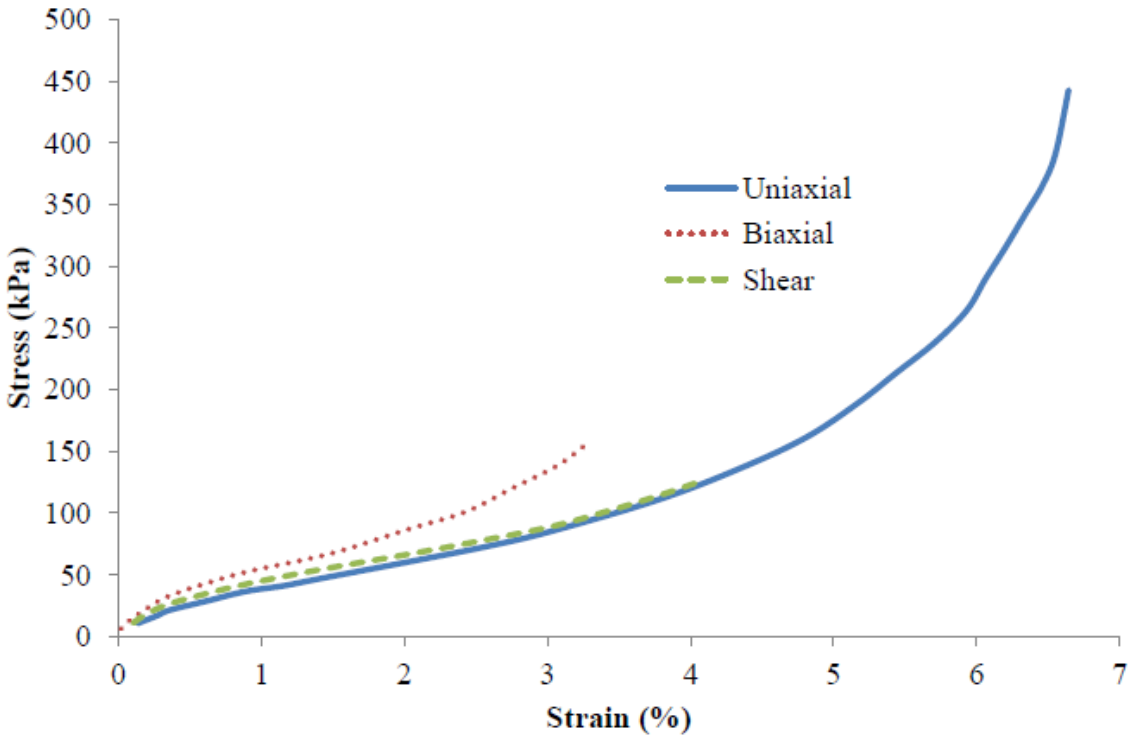

Figure 2. 4: Typical neoprene rubber stress-strain relationship (%) for various loading modes (Aboshio, 2014).

2.1.3 Thermal effects

In addition to its mechanical properties, rubber has some remarkable thermodynamic, or thermoelastic, properties. In 1805, Gough showed that stretched rubber contracts on heating and extends on cooling. He also showed that heat within the material is developed on extension and absorbed on retraction.

The explanation of this effect is very simple and follows directly from the basic concept of the kinetic theory, namely, that the deformation of a rubber (at constant temperature) is associated with a reduction of entropy, with no change in internal energy. Putting dE = 0 in Equation (1) obtain:

$$dE = dW \text{ (constant T)} \tag{2.5}$$

The work done by this stretching force is inherently positive. The heat consumed by dQ; therefore, is negative, i.e., heat is evolved on an extension. The heat shift is the same as the work done on the rubber by the applied force (Treloar 1975).

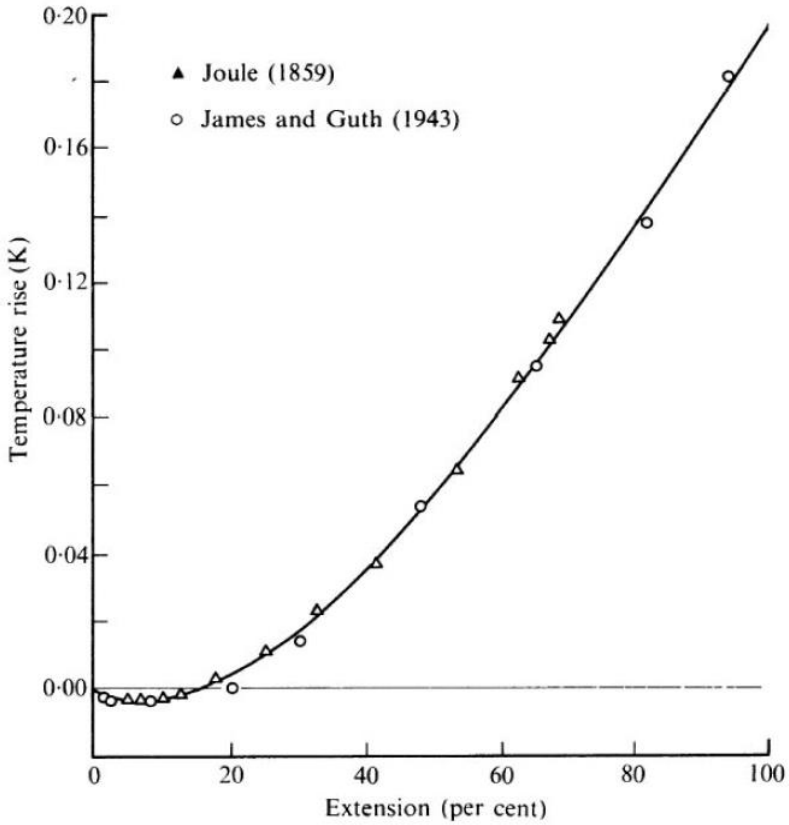

Figure 2. 5: Temperature rise with an adiabatic extension (Treloar 1975).

The illustration presented in Figure 2.5 shows Joule's original data and later results provided by James and Guth (1943) on the adiabatic increase of temperature upon extension of rubber material.

The two effects in question are often referred to as the Gough-Joule effects. Taken from Joule's writings, the second of these depicts the increase in temperature as it stretches to an 100 percent extension.

Experiments that have investigated the relation between temperature change and expansion/ contraction complement each other; i.e., the temperature changes because of expansion/contraction, and expansion/contraction causes a change in temperature. This thermal effect does not vary from natural rubber, but is indicative of rubber-like conditions and occurs in a wide range of synthetic rubber polymers.

2.1.4 Crystallisation

Treloar (1942) was aware that unvulcanized rubber becomes hard and inextensible if kept at 0°C or lower. Subsequent to being stretched fully, under suitable conditions raw rubber remains stretched, only retracting to its original length if subsequently heated to a particular temperature. As indicated by X-ray spectroscopy, these effects are caused by crystallisation. Therefore, the picture emerges from a compilation of crystallites produced by the tridimensional arrangement of chain segments interspersed within an ongoing matrix of non-crystalline, disorganised material Figure 2.6 (a). Figure 2.6 (b) the single crystals from polymers such as dilute-platelets or lamellae formed by the normal foldings in the back and forth of single polymer chains, with the chains axis almost perpendicular to the plane of the lamella, is obtained by crystallization the diluted solution.

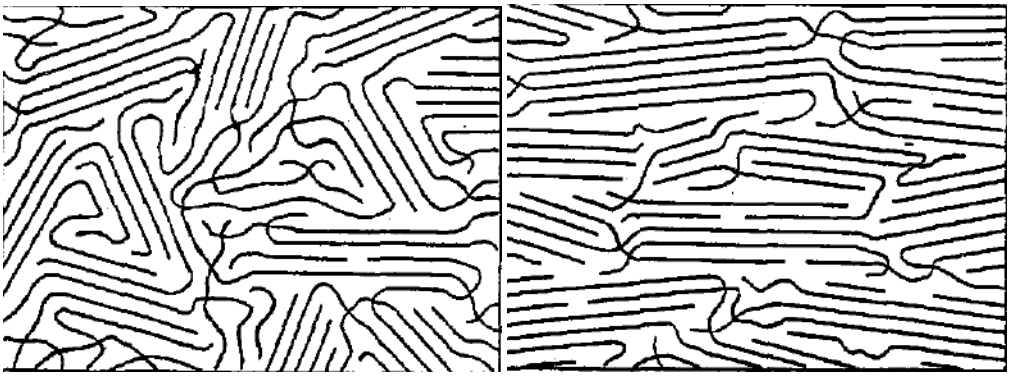

(a) Unstretched (b) Stretched

Figure 2. 6: **Molecular structure of crystalline rubber (diagrammatic). The parallel bundles represent crystallites (Treloar 1942).**

At 90°C, vulcanised elastic crystallises only beyond a 500% extension. Thus, although associated by implication with the phenomenon of elasticity, crystallisation is viewed as a secondary effect. Representing the structure of partially crystalline cellulose fibres (with which rubber has numerous common essential elements), Figure 2. 6 shows the molecular structure of (a) unstretched and (b) stretched rubber. (Treloar 1942).

2.1.5 The Glass-Rubber Transition

The rubber-like state depends on the spontaneous thermal motion of chain elements produced by the rotation of single bonds in the chain backbone. As the temperature falls, significant rotation ceases. The material then loses its rubber-like properties and becomes hard and rigid. This is referred to as the 'glass transition' between the elastic and the glass-like properties of rubber materials. One of the most important advantages of the crystallisation transition for elastomer rheology and treatment is stress-induced crystallisation. The various elastomers, including natural rubber, can show crystallisation when extended in a tensile testing unit. At the point of transition, the modulus and viscosity of rubber increase by multiple orders of magnitude over only a small temperature range. Yet, there are no associated discontinuous changes in volume, entropy or enthalpy (Bower; 2010, Bever; 1992).

Trealoar (1971, 1976) and Bever (1992) have shown how the elastic state of rubber materials relates to rotation about single bonds in the backbone chain. That rotation depends on the thermal motion of chain elements. As the temperature falls, significant rotation ceases. The material then loses its rubber-like properties and becomes hard and rigid.

2.1.6 Energy Storing Capability

The intrinsically high-energy conservation capacity is also an important mechanical feature of rubber. This makes it highly suitable for use in structures that are susceptible to crash or impact loads, such as in-car air sacks or fender structures and bridge dampers and high-rise buildings and masts. Due to its weak strain / elastic properties compared to other engineering materials, the high-energy potential of rubber materials is established. (Aboshio, 2014).

As shown in Figures 2.1 and 2.2, the unique nonlinear stress-restrictive characteristic of rubber results from the capacity to store huge amounts of energy, most of which is released when retraction takes place (Bever 1992). In terms of storing energy, Freakley and Payne (1978) found the stress-strain properties of rubber to be some 150 times greater than an equal weight of hardened steel.

Table 2. 2: Energy storage capabilities of various materials (Freakley and Payne,1978)

Material	Energy [J / kg]
Grey cast iron	1.11
Extra soft steel	9.18
Phosphor bronze	12.2
Rolled aluminium	22.6
Hardened Steel	284
Hickory wood	365
Vulcanised rubber	44800

2.2 Composite materials

Composite materials are created by combining two or more materials with distinct qualities that do not disintegrate or blend. With natural composites, long cellulose fibres are bound together in a piece of wood. by a chemical called lignin. Various materials within the composite work together to deliver distinctive features.

Over thousands of years, composite materials have been used in a variety of applications. Around 1500 BC, early Egyptians and Mesopotamian settlers utilised a mixture of mud and straw to build robust and enduring structures. The combination of mud and straw provides a brick with excellent resistance to squeezing, ripping, and bending. Among other ancient composite items, ceramics and boats were reinforced with straw.

By 1945, about 7 million pounds of glass fibres had been employed in a variety of goods, the majority of which were for military purposes. After World War II, composite materials exploded in popularity. Composite pioneers were breaking into new markets like aircraft, building, and transportation. The public sector quickly learned about the advantages of fibre-reinforced polymeric composites, particularly their corrosion resistance (Ngo, T.D., 2020).

There is an ongoing quest for stronger, more robust, durable, lightweight and adapted structures and components. Figure 2.7 illustrates compositions of fibres and a matrix of composite materials. On a macroscopic scale, a combination of two or more materials is referred to as a composite material. In comparison with naturally existing materials, composites are usually lightweight and strong, delivering material characteristics that enhance performance and endurance. Although their fibres and resin matrix achieve their strength, composites are often viewed as a combination of high strength but brittle fibres in a weak but ductile matrix.

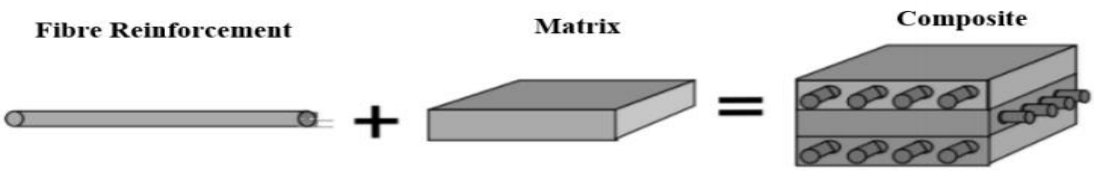

Figure 2. 7: **Composite material composition (Ullah, H., 2013).**

While maintaining the geometric fibre arrangement, as the matrix transmits the load to those fibres, it strengthens and stiffens the mechanical properties of the compound (Gay, D. and Hoa, S.V., 2007, Ullah, H., 2013). The resulting composite material is capable of intermediate mechanical performance, higher than that of the matrix but lower than that of the fibrous reinforcement.

2.2.1 Fibre-reinforced composites

Non-orthogonal reticulated fibre fabric and pure rubber matrix make up the reticulated fibre fabric reinforced composite, which may be broken down into two primary fibre families. For the manufacturing of composites, fibres in various forms (chopped or continuous) are combined with the matrix to give flexibility in regard to cost, strength, and process requirements. The position of the fibres within a coordinated system is referred to as the architecture (Xu et al., 2021, Awais et al.,2020).

It is now common to manufacture a variety of materials such as metal-matrix composites (MMCs), ceramic-matrix composites (CMCs), and polymer-matrix composites (PMCs). Based on the type of reinforcement, such composites are further classified into three categories (*viz.*, particulate composites, fibre-reinforced composites and structural composites) as shown in Figure 2.8 (see Jones, R.M., 2014; Mallick, 2007; Yang et al., 2012). The highly elastic mechanical behaviour of elastomers varies from thermosets and thermoplastics (Erden, 2017). Thermosets have cross-linked polymer chains, which contribute to a permanently rigid product.

By contrast and more generally, further heat treatment converts thermoplastics into various products. As heating does not affect structural rigidity, the advantage of thermosets is that they can be used at high temperatures.

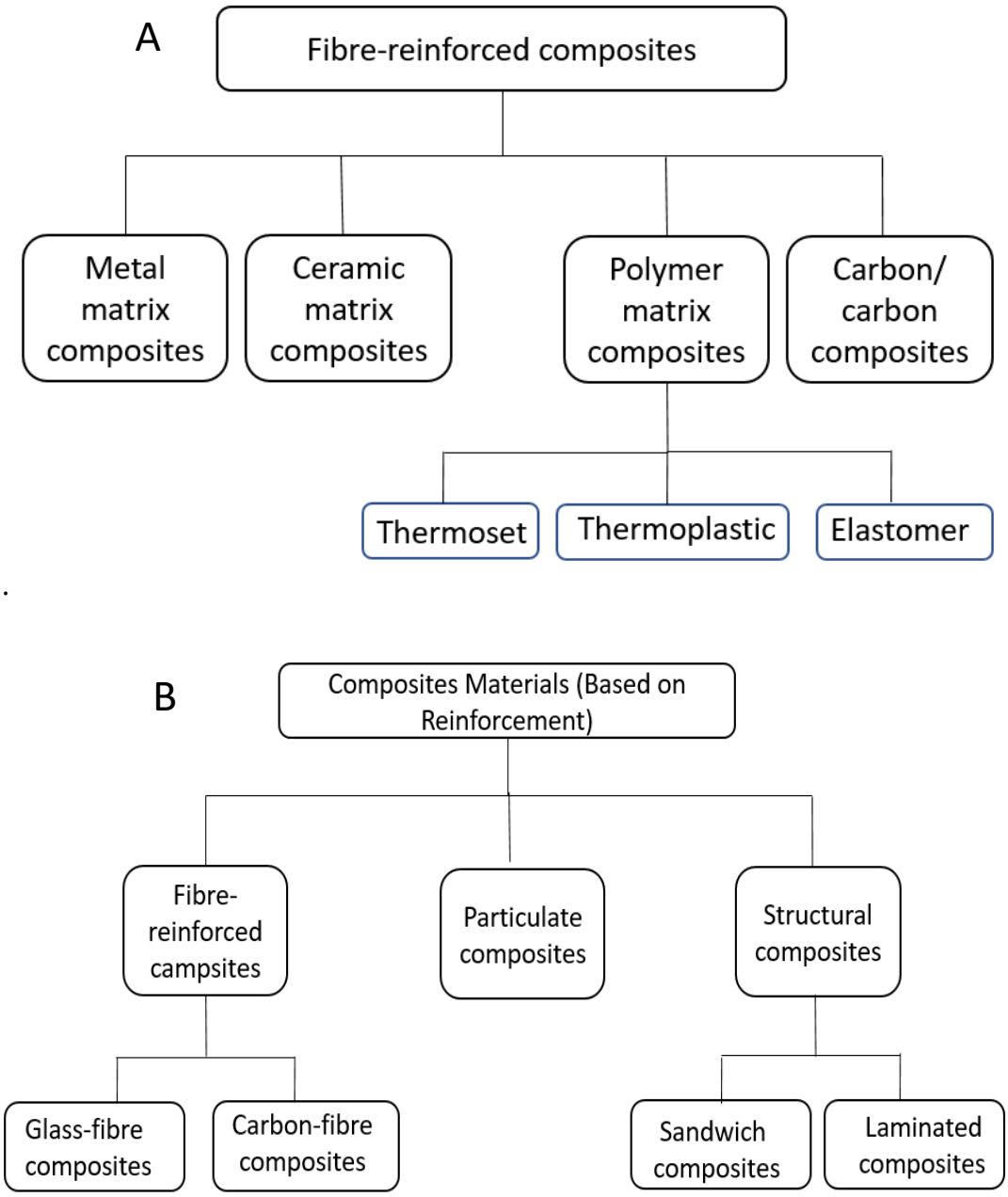

Figure 2. 8: **Classification of composite materials a) based on a matrix and b) based on reinforcement.**

A composite matrix consists of the matrix of polymer in combination with fibrous, distributed strengthening. The composites of the polymer matrix consist of several short or permanent

fibres linked to an organic polymer matrix. The strengthening of a polymer composite matrix provides high strength and rigidity. Polymer matrix composites are constructed in such a way that the reinforcement meets the mechanical loads to which the structure is subjected in operation. The matrix's function is to link the fibres and transmit loads between them (Tong et al., 2016). For fibre-reinforced polymer composites, this matrix system consists of polymer resin and a curing agent. The structural properties of the fibre-matrix interface play a crucial role in the physical and mechanical properties of composite materials (Gowda et al., 1999).

2.3 Fabrics Materials

Industrial uses of rubber elastomer carcass woven fabric reinforced composites are extensive, and because of the wide variety of their applications, there is considerable interest in the use of experimental techniques to determine in-service mechanical performance (Yang et al., 2016). As the use of woven fibre composites increases, it is essential to understand their elastic behaviour. Composites are among the most advanced and versatile engineering materials. Reinforcement fabrics, which can be woven or nonwoven, include natural filaments or man-made materials such as glass fibres, polyesters or nylons (see figure 2.9).

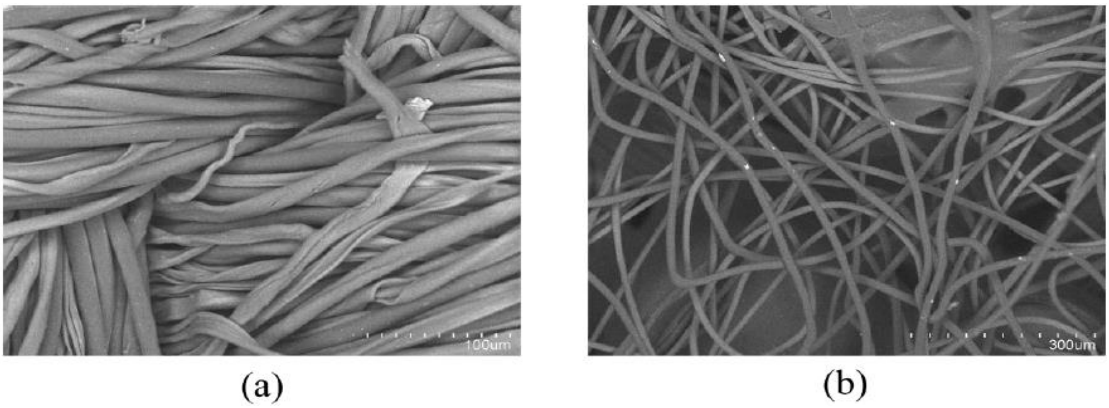

Figure 2. 9: **SEM photographs of (a) natural and (b) human-made fibres (Williams, R.W., 2010).**

Figure 2.9 shows two images from a scanning electron microscope (SEM) (Williams, R.W., 2010). The image on the left is a close-up of cotton fibres forming the exterior of cotton polyester fusion yarns. On the right is an image of human-made fibres that form a non-woven material.

Although woven fabric can be bent insome degree without shear deformation, if it is bent to far it becomes sheared. In most fabrics, this shearing is attributable to the change of angle between intersecting threads; but it may also be the result of the bending and twisting of yarns between intersecting threads. In many practical applications, the shearing properties of fabrics are important. With the specialised use of bias binding, the change of angle between the yams is used to produce extensibility (Cusick, G.E., 1961).

Shear deformation is often the most significant material characterisation process (Khan, 2009). The forming processes of a woven fabric may induce significant in-plane shear angles that allow the reinforcement to conform to complicated contours and complex forms. As the correct characterisation of this material property can be important, that property of woven reinforcements is undertken using two de facto standard tests of a planar tension and picture frame. The specifics of those tests are described below.

2.3.1 Constructions of flexible composites

Composites require a careful selection of materials and structures to form basic fabrics and materials for coating / laminating. In the manufacturing process of woven composites, as illustrated in Figure 2.10:

FIBRE > YARN > FABRIC > COMPOSITE

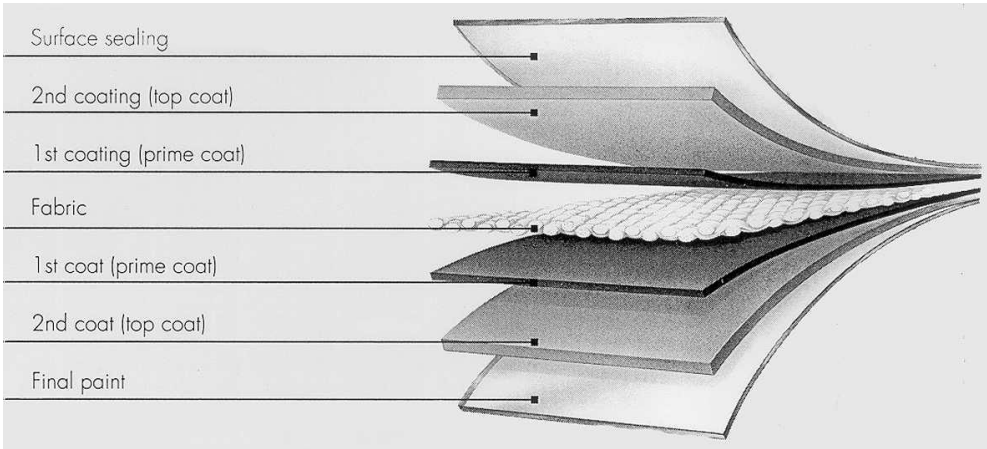

Figure 2. 10: **Coated woven fabric components (Zhang, L., 2010).**

In the production of composites, fibres are grouped according to a specific design, then impregnated with yarn-forming resin. The yarns are then linked in specific patterns to form fabrics (Ullah, H., 2013, Barbero, E.J., 2010). For woven textile reinforcements, the textile yarn orientation is a function of the method of manufacture and the textile architecture (Cox and Flanagan, 1997).

Interlacing between two sets of yarns - the warp (0^0) and weft (90^0) - delivers a regular woven/weaving structure. The mechanical interlocking of yarns maintains the integrity of the fabric. A balanced fabric is one in which the number and weight of fibres are identical in yarns along the warp and weft. The load response of a woven textile is a function of the yarn material properties and also the overall textile architecture (Jacobsen et al., 2004).

To afford protection to the yarns from the effects of both mechanical abrasion and chemical degradation, textiles are commonly coated or moulded within an elastomeric carcass.

Whether woven or non-woven, such fabrics can be made with normal filaments such as fleece, cotton, hemp, or silk, or man-made strands such as fiberglass, polyester, nylon, or Kevlar; the coatings are typically vinyl, neoprene, silicone, or Teflon (Testa and Yu 1987).

When a fabric is subjected to uniaxial stress, the crimp (‘waviness’) in the direction of loading is progressively reduced, as the crimp in the transverse threads is increased. Where the crimp reduction in warp yarns is equal to the increased crimp in weft yarns (so that the total yarn crimp remains constant) is termed the ‘interchange of crimps’. In general, the properties of woven fabric are governed by the weave design, fabric density (number of warp and weft yarns per unit distance), and fibre content. Those characteristics are governed by (i) weave architecture, yarn sizes, yarn spacing and yam crimp; (ii) laminate parameters such as stack orientation and fractional volume of total fibre; and (iii) yam and resin stiffness parameters (Naik, R.A., 1996). Yarns can be pre-stretched before coating to induce isotropic behaviour (Fang, R., 2009, Forster, B., 1985) (Divya and Suresha 2021).

2.3.2 Fabric types

(i). Woven fabrics are the most generally utilised type of textile composites in structural applications. Woven fabrics utilised in textile composites are straightforward and essential weaves, i.e., plain, twill and satin weaves, which are distinguished by the repeated examples of interlaced regions in the warp and weft directions

Figure 2.11 (a) shows a plain weave structure (the most commonly used), where one warp yarn is repeatedly woven under and over weft yarns. A twill weave passes the weft thread over one or more warp threads, then under two or more warp threads, and so on, with a "step" or offset between the rows to create a distinctive diagonal pattern (Figure 2.11 (b)). With this structure, twills generally drape well. A satin weave is woven, as shown in Figure 2.11 (c). It has a smooth surface with good drapability and reduced thickness.

Figure 2.12 shows an in-plane view of the plain-woven fabric, illustrating warp and weft fibre directions.

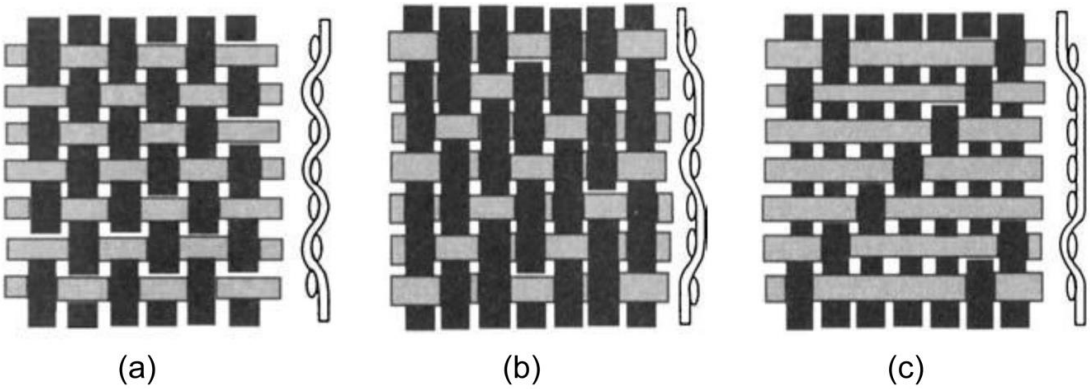

Figure 2. 11: **Schematics of common woven fabrics. (a) Plain weave. (b) Twill weave. (c) Satin weave (Gay and Hoa, 2007).**

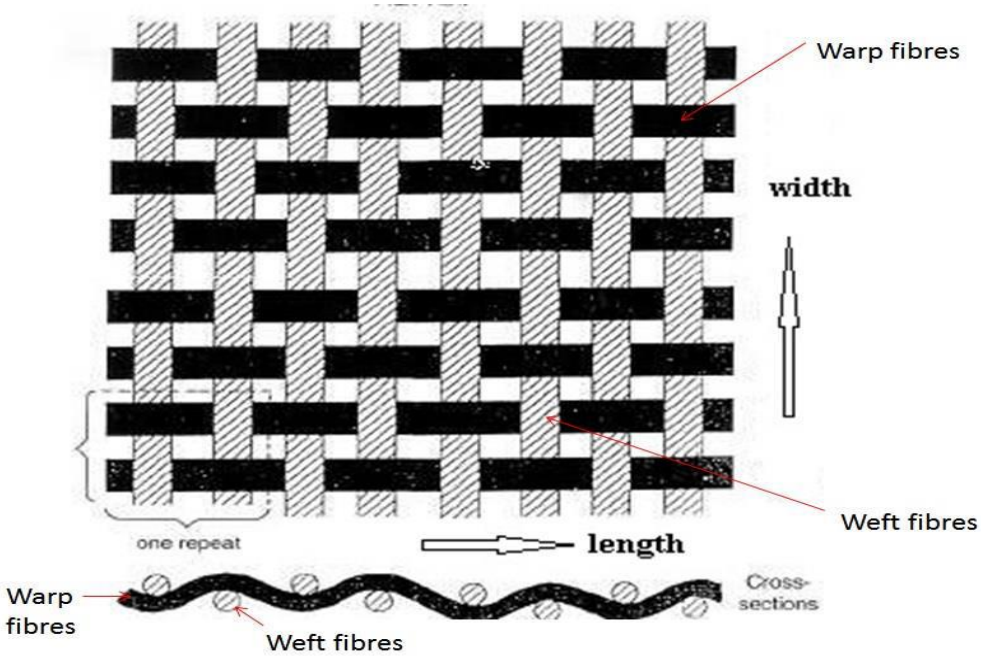

Figure 2. 12: **Typical plain-woven fabric showing warp and weft fibres (Tan et al., 1997).**

(ii). Braided fabrics are developed by intertwining or orthogonally intertwining two (or more) sets of yarns to form an integral structure, as shown in Figure 2.13. Tan et al. (1997), in contrast with twisted or knitted fabrics, records streamlined systems of braided fabrics to have improved impact resistance characteristics. However, under axial compression, they have poor stability in the direction of the yarn system.

Figure 2. 13: **Schematic of a typical structural braided fabric (Atex, 2015)**

(iii). Knitted fabrics are of two types, as shown in Figure 2.14: weft-knitted and warp-knitted. Knitted fabrics interlock loops of yarns. As illustrated in Figure 2.14 (a), in weft-knitted fabric, the yarns run width-wise, and a single weft yarn forms loops. The row of loops in the longitudinal direction is called the warp and that in the transverse direction is called the weft. In warp-knitted fabrics, overlaps in alternate warps and wefts are generated, as shown in Figure 2.14 (b) (Tan et al., 1997).

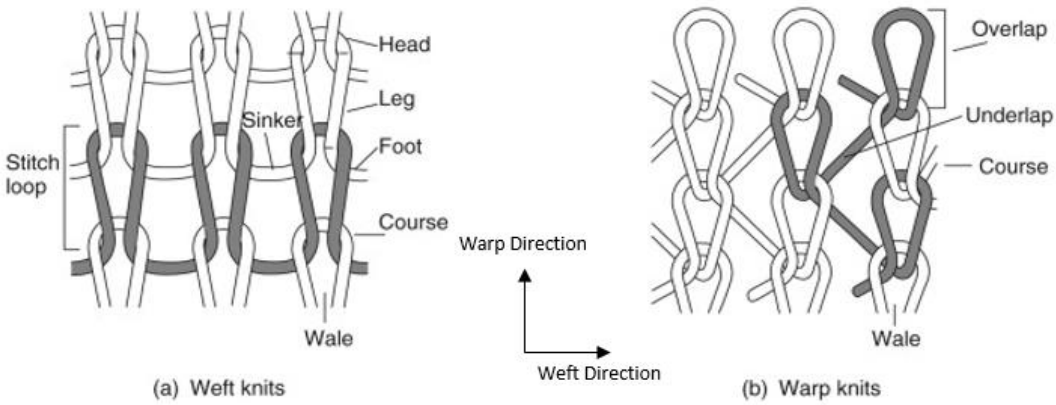

Figure 2. 14: **Schematic diagram of knitted fabrics (a) Weft-knitted fabric, (b) Warp-knitted fabric (Li and Dai 2006).**

2.3.3 Fabric material and coatings comparison

Polyester fabric has a low tensile strength but, but a higher modulus of elasticity and stiffness than nylon. By its greater rigidity, this lower polyester strength is 'traded' for reduced deformations. Although polyester fibres are more susceptible than nylon fibres to ultraviolet degradation, they are easier to protect and more durable overall. Polyester provides better dimensional stability, shrinking strength, and light /UV resistance, while nylon is characterised by good resilience and elasticity, high abrasion resistance and thermal absorption (Fang, R., 2009). As the materials used in conventional buildings must have consistent strength qualities, safety factors are tight. Yet, material qualities such as weathering, deterioration, and repetitive loading may cause fabric materials to display unpredictable behaviour, and their properties may alter dramatically over time. (Fang 2009).

The prerequisite of these properties is that practical clothing is subject to a wide range of final applications, such that an internal and an external element (sunlight, wind, rains and cold weather conditions, fibre, yarn fine, warp/whistle, fabric width, thickness, fabric numbers and external conditions) affects a garment. Such factors influence practical apparel efficiency and behaviour (Venkatraman, 2015).

2.4 Determination of the mechanical properties of composites with rubber-coated fibre

The mechanical properties of coated reinforced rubber composites are rigorously tested, by such as the uniaxial test, pure shear test, biaxial test, balloon or bulge test and shear test. Composites are not isotropic since the characteristics of such materials depend on the direction in which they are being tested. When the material properties differ in three mutually perpendicular directions, they are referred to as orthotropic. The inherent anisotropy of

composite materials results in mechanical features that differ considerably from conventional isotropic materials (Jones, 2014). The mechanical parameters of anisotropic laminates include strength, rigidity and other physical properties, objectives that are achieved via experimental composite characterisation. The basic mechanical properties of materials are elastic and strengths. In order to describe their mechanical behaviour, the quality of independent material consistency such as stiffness and the Poisson ratio depends on the plane of the material under consideration.

The uniaxial tensile test is the most commonly performed test for the determination of mechanical component behaviour. The uniaxial tensile test characteristics can be applied to material specifications as well as to the assessment of their carriage capacities. Almost all strength criteria include tensile strength (Bridgens, 2005; Lei, 2010; Bassett et al., 1999).

The use of biaxial planar and bulk tests to evaluate the mechanical properties of rubber-coated materials and most other rubber-reinforced composites, is becoming increasingly important. Unfortunately, due to limited testing equipment, these tests are rarely performed. Most planar biaxial test rigs are limited to testing materials of low strength, which effectively excludes composites reinforced by fibre (Bridgens, 2005). Similarly, a test set, designed and developed by Bhatnagar et al. (2007), is only effective for testing low-strength (biological) materials Brieuet al., 2007).

The selection of a test method should, therefore, depend on its benefits, limitations, and availability, and the level of precision required for the intended purpose of the to-be-designed composite structure. The uniaxial test technique can be considered sufficient for assessing the mechanical behaviour of materials that only undergo small extensions in composite materials, excluding specials or unusual conditions.

2.4.1 Uniaxial testing

The standard uniaxial tensile testing procedures for coated woven cloth are (1) the ASTM D-5035-06 (ASTM-D5035-06), 'Standard test process for Break Force and Elongation of Textile Fabric (Strip method)' and (2) the EN ISO 1421:1998 (Blether-EN-ISO-1421-Standard, 1998) Rubber or Plastic Coated Textile – Determination of Tensile Strength and Elongation at Break'. The main difference between these two methods is in the rate of stretching, which in ASTM D-5035-06 standard it is 305 mm (12 inches) per minute and in EN ISO 1421:1998 is 100 mm per minute (Aboshio, 2014). The uniaxial tensile test is the most commonly used method to classify composite mechanical behaviour. Most important in regard to textile performance are the tensile properties. Difficulties arise due to the high degree of bulkiness in the structure of the fabric and the variation of strain during deformation. As each piece of fabric consists of many fibres and yarns, any slight deformation of the fabric leads to a chain of complex movements between constituent fibres and yarns. The situation becomes more complicated when both fibres and yarns behave in a non-Hookean manner during deformation and exhibit hysteresis over time (Konopasek, 1970).

2.4.2 Stress-Strain Curve of fibre

Figure 2.15 shows a typical load-extension curve for a tensile test of a woven fabric, where there are three separate regions:

- The first region, the initial part of the curve, is dominated by (usually minimal) interfiber friction; i.e., the frictional resistance due to yarns (thread) was bending.
- The second region, the lower module, is the deciphering area that arises from the thread straightening in the direction of the operation of the load; a corresponding increase of the crimp is in a direction perpendicular to the direction of the thread.

- The third region, the final part of the load-extension curve, is the extension of the yarn; i.e., the tensile loading of threads in the direction of stress. As the crimp decreases, the magnitude of the loading force rises very rapidly. As a result, the fibres themselves begin to expand (Murman and Suresh, 2011; Schwartz, 2019).

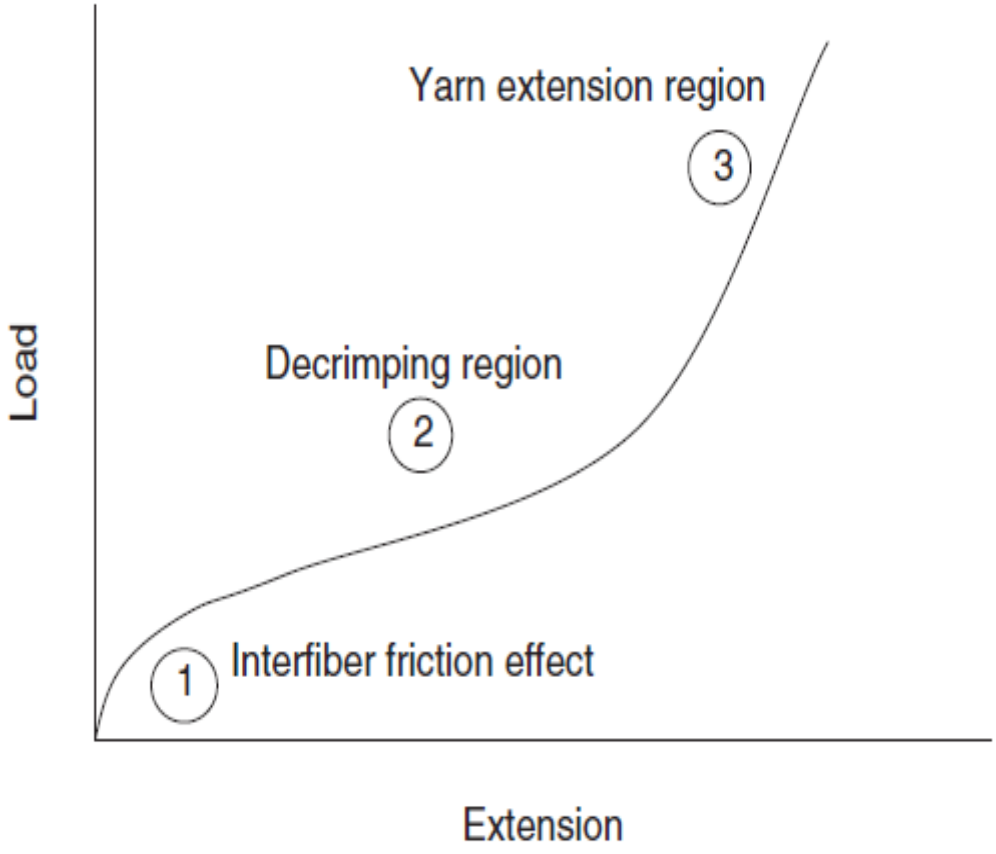

Figure 2. 15: **Schematic of a typical load-extension curve (Murman and Suresh, 2011).**

2.4.3 Shear fabric test

The shear modulus for composites or covered fabrics can be obtained using either the planar biaxial test or the uniaxial testing technique (Lei, 2010). However, other methods have been developed, such as the trellising or picture frame test. There are three primary techniques used to quantify fabric shear consistency and locking angle: the Direct Shear Force Measurement (DSFM) test method; the Bias-Extension (BE) test method; and the Picture Frame (PF) test

method, as schematically presented in the figure 2.16 (Taha et al., 2013). The shear properties of fabrics use two methods, namely the picture frame test and the bias extension test

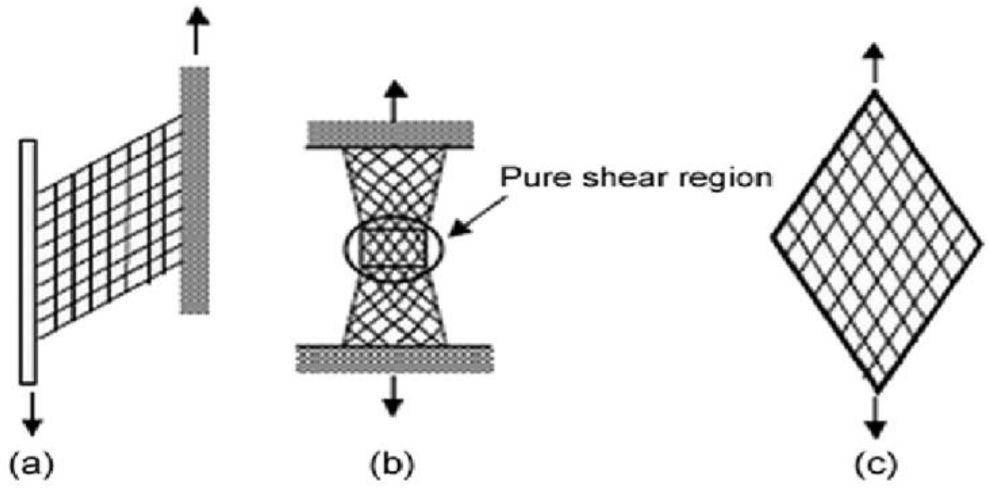

Figure 2. 16: **(a) Direct shear force measurement, (b) bias-extension test method, and (c) picture frame test method (Taha et al., 2013).**

2.4.4 Planar tension test

Unlike conventional uniaxial tensile tests, the key feature of the planar test is that there are no lateral strains. This is achieved by using specimens with a particularly high aspect ratio of specimens (large width to length) specimen is used for planar tension tests (Duncan et al., 1999). The planar tension test imposes plane strain conditions on the test specimen by preventing its edges from contracting. “Pure shear consists of a trellising action, whereby the tows in the fabric rotate about the cross-over points” (Sharma 2003). However, there is no standard test strategy by which to decide the in-plane shear behaviour of a textile (Treloar, 1944; Miller and Kurt, 2000).

2.4.5 Picture frame test

More recently, the test has been widely used for in-plane testing of all forms of sandwich plates, including honeycomb and foam core constructions with laminated plastic or metal face sheets

(Iosipescu, 1967, Walrath and Adams, 1983, Adams, 1990, Adams and Lewis, 1995). As there has been no standardisation for these tests and test procedures, a wide variety of fixture configurations have been established over the years. McGuinness and O'Bradaigh developed the picture-frame experiment to create a homogeneous time-dependent deformation in uni- or bi-directionally reinforced sheets, as a way of testing the rheological activity of composite materials in intra-ply shearing. With the picture-frame experiment, a flat pre-consolidated composite specimen is subjected to a consistent shearing deformation using a specially designed four-bar linkage connected to its sides.

A picture frame is a square hinged frame whose sides are equal in size. A tensile tension is applied diagonally across opposite corners of the the picture frame rig, so causing the frame to distort into a lozenge. A clean and uniform in-plane shear strain is theoretically applied to the specimen within the image frame (Gong et al.,2020). The axial load is applied to two diagonal corners to cause shear loading. Typically, tension loading is used to prevent the frame buckling. The fibres which reinforce the specimen are parallel to the sides. The deformation is created by stretching along a diagonal of the sample (Spencer, 2000; McGuinness and O'Brádaigh, 1997, Standard, 1993, Arumugam et al., 2016).

2.4.6 Biaxial Tensile Testing

Many different tests of the biaxial-tensile type have been undertaken (see Hutchings et al. (2009) and Reinhardt (1976)), where biaxial testing of coated fabrics is a more challenging operation than uniaxial textile testing (see Bridgens, 2005). Although tests are regularly undertaken using methodologies found in the literature (including Hutchings et al., 2009; Bridgens, 2005; Reinhardt, 1976)), neither British nor international standards for biaxial fabric testing currently exist. Uniaxial testing remains the primary test to gauge fabric strength (Lei, 2010). That hydraulic bulge test has been used for many years as a laboratory tool to determine

fundamental material behaviours. Mostly it has been used to evaluate the mechanical properties of materials under biaxial tension, as obtained for sheet materials such as rubber, steel plate and thin films (Tsakalakos, 1981). Thereby, the stress-strain curves measured by the hydraulic bulge test correspond to equi-biaxial stretching (see Mersch, J.P., 2013; Ranta-Eskola, A.J., 1979). The test involves rigidly clamping the specimen at its periphery onto a circular, rectangular or elliptical diaphragm. It is then inflated with liquid from one side of the sample by pumping hydraulic fluid or pressurised gas into it at a uniform rate. The resultant balloon shape of the specimen and its axial symmetry then requires tthe strain and the stress at the top of the bulge to be perfectly biaxial. The more the balloon is deformed, the more uniform becomes the stress and strain distributions across a wide region of the specimen (Aboshio et al., 2015; Sasso et al. 2008). This technique carries a risk of fracture, because the clamping system creates a very high and non-equi-biaxial stress state (Sasso and Amodio., 2006).

The idea behind the bulge test has been in existence since the Treloar (Treloar, 1944) first used this method to characterise rubber materials by their material constants. The specimen is locked between two plates, before inflating it using air, water, or oil to create a blister/bulge, (see Figure 2.17). For a spherical membrane, the average membrane stress, σ, is then defined by the Rule of Laplace as

$$\sigma = \frac{1}{2} P\rho \tag{2.6}$$

where P is the applied pressure and ρ the corresponding radius of the sphere.

This concept can be used to examine any membrane experimentally. Depending on the particular form of anisotropy, the inflated form of an initially flat ring disc of an anisotropic material is axisymmetric. Inflating an initially flat circular disc of an orthotropic material produces a surface with oval contours. The major and minor axes of the oval shape are defined by the two directions of the elastic symmetry axes of the material (Zioupes et al., 1992).

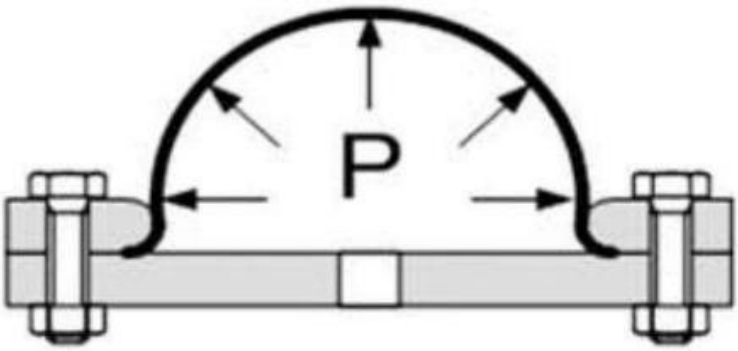

Figure 2. 17 Schematic of a Bulge Test (Zioupes et al., 1992).

By its accuracy, the "bulge test" has a wide range of applications in various thin-film mechanical tests. It has been used mostly to evaluate the mechanical properties of materials under biaxial tension, which are obtained for sheet materials such as rubber, steel plates and thin films of other materials. The "bulge test" addresses most of the problems related to tensile testing, such as poor mounting, rough handling, tearing of the film at the edges, and grip slipping (Tsakalakos, 1981). An additional advantage of the bulging technique is that it allows the reproduction of more than one type of stress-strain in a cost-effective manner, most notably as compared to the uniaxial stress test (Ramezani et al., 2010).

The stress-strain curves measured by the hydraulic bulge test correspond to equi-biaxial stretching (Mersch, J.P., 2013; Ranta-Eskola, A.J., 1979). Stresses are calculated based on the pressure applied, where strains are measured from the height of the bulge. As the phenomenon of "necking" from biaxial deformation is absent, the bulge test can be applied up to the failure of the entire plastic deformation zone. The circular bulge test has been used to estimate material stress under biaxial loads (Jaia, 2015; Siegert et al., 2003; Hecht et al., 2005; Gutscher et al., 2000; Altan et al., 2006). For incompressible materials, the equal biaxial tension of a specimen induces a state of deformation equivalent to that under compression (Day and Miller 2000). Therefore, it is generally preferred despite its slightly more complicated test procedure.

Hydraulic bulge tests on composites were conducted by rigidly clamping the material onto a circular diaphragm. The material was then inflated from one side of the sample by pumping either hydraulic fluid or pressurised gas at a uniform rate, until the specimen shows a "balloon-like" shape. That shape of the specimen and its axial symmetry requires the strain and stress at the top of the bulge to be perfectly biaxial. The more the balloon is deformed, the more uniform the stress and strain distributions across a wide region of the specimen (Aboshio et al., 2015; Sasso et al. 2008.). Again, there is a risk of fracture because the clamping system creates a very high and non-equi-biaxial stress state (Sasso and Amodio., 2006). In the field of experimental solid mechanics, video gauging combined with a DIC method is widely accepted as a representative non-interfering optical technique. It is commonly used as a powerful and flexible tool for measuring surface deformation. A comparison between the surface images of the un-deformed (or referenced) specimen and the deformed specimen, directly show full-field displacements and strains (Pan et al., 2009).

2.4.7 Constitutive model

Strain-energy density functions are a prime characteristic of hyperelastic material models. Over more than one hundred years, scholars have studied hyperelastic and rubber materials (Borst et al., 2012}. More recent work was inspired by Mooney (1940) and Rivlin (1948). Mooney proposed (and Rivlin further developed) a two-term phenomenological model for large elastic deformations. Subsequently, Valais and Landel (1967) further developed this work. For reversible, high strain efficiency, biologic tissue and elastomers are widely used. Elastomers are a crucial component to allow broad strain action in synthetic nastic material studies.

Constitutive equations explain the behaviour of material under the impact of external stimuli. Constitutive equations for hyperelastic materials, as well as other types of materials, are often derived from experimental evidence. Choosing the correct constitutive relation for a specific

hyperelastic material is essential in modelling. Although there are no physical standards to determine these mathematical relations, there are guidelines, or basics, for the development of scientific models leading to appropriate constitutive behaviour. These models and the mathematical relations must be validated by comparing them to reaction properties observed in physical experiments. In general, the constitutive relations can be mathematical, differential, or integral relations, as contingent with the behaviour of the material. These constants are measured utilising straightforward tests like the uniaxial tension test or the pure shear test. Due to their direct and clear physical results, engineering constants are utilised in determining stress-strain relations (Reddy, 2010). The behaviour of nonlinear materials is extremely complicated, but there are three methods for modelling a nonlinear material: the first, the empirical function-fitting method, is only usually successful in straightforward cases; the second, rational analysis, which is based on a particular theoretical method, is generally overly complicated; the third method, a combination of the first and second for developing constitutive models for hyperelastic materials, is the most commonly used (Bever, 1992).

The stress-strain relationship for hyper-flexible solids is usually characterised by indicating its strain energy density as an element of its deformation inclination tensor or as a function of its strain invariants or the extent to which the material stretches.

For elastic materials, the numerous constitutive models hypothesised in the literature, relate to isotropic hyper-flexible materials. Such models have evolved primarity in commercially available component codes. The determination of model constants to describe hyperelastic materials has been achieved by experimental information fitting, including Mooney-Rivlin, Yeoh, neo-Hookean, Arruda-Boyce, Polynomial, Ogden constitutive equations, and many others (Hoss and Marczak, 2010) (Külcü, 2020).

Most of these models perform well over relatively confined ranges of deformation, and under particular deformation modes. However, few are accurate, up to a strain magnitude of 600-700% The Hoss and Marczak (2010) model is used for larger deformation ranges (e), for uniaxial tensile tests with $0 \leq e \leq 700\%$ and also for small deformations of $0 \leq e \leq 100$ %. There are more than 37 different models for rubber deformation. And for greater deformations ranging from $0 \leq e \leq 700$ % for uniaxial tensile, $0 \leq e \leq 400$ % for pure shear, and $0 \leq e \leq 350$ % for biaxial testing, the constitutive models having power-law terms of the first strain invariant match well. In comparing the hyperelastic models of Arruda-Boyce, Mooney-Rivlin, neo-Hookean, Yeoh and Ogden against experimental data (see Brown et al., 2009), models delivered a more accurate fit at the higher strain rate of $0.1s^{-1}$ (than at $0.025s^{-1}$). However, polynomial models were generally unable to capture the stress-stretch ratio characteristics, beyond a strain rate of $0.025s^{-1}$. Brown et al., also suggested using Mooney-Rivlin or Yeoh hyperelastic models. As defined as the force divided by the undeformed area, the first Piola-Kirchoff stress tensor is not symmetrical. The implication, the product does not correspond to the pressure energy density with Cauchy stress, and the small strain tensor, when combined with the Green24 Lagrangian strain tensor, is multiplied.

This makes it unsuitable for numerical analysis for the first Piola- Kirchoff stress. The second Piola-Kirchoff stress tensor s the total force in the undeformed configuration divided by the undeformed field. This tensioner is ideal for energy density since the second stress and the Green-Lagrangian strain of strain energy is the stress density of the Cauchy stress and small strain tensor. In many cases, the stretch is both a deformation measure and strain for hyperelastic materials. The length / original length ratio is deformed. Therefore, the stretch is unity and strain zero when there is no deformation.

Mechanical characteristics of rubber and fabrics, as well as those of coated composites from these materials, have been reviewed in this chapter. Rubber Stress-strain relationships are generally non-linear and have a very high elastic range. Vulcanised rubbers have good weathering resistance, resistance towards chemical attack and excellent capacity to absorb energy. Compared to many engineering materials, however, they are of a low modulus. Composites of the fabric-reinforced polymer are found a wide range of applications. When covered, their mechanical properties generally improve significantly as compared with their uncoated properties. It is essential to characterise the material behaviour through experimental tests in order to understand the complex process of deformation of woven composites linked to their architecture.

2.4.8 General formulation of anisotropic hyperelasticity

A great deal of attention has been devoted to the constitutive modelling of elastoplastic fabrics for materials in the finite deformation range. Powerful computers and effective finite-element methods have made it possible to solve large-scale finite deformation problems, thereby increasing the demand for precise designs (Eterovic and Bathe 1990).

To investigate the mechanical behaviour of biological soft tissue - where there are parallels with the hyperelastic matrix composite materials explored in this thesis - strain energy functions have been determined for traverse isotropic materials. Most recently, the mechanical behaviour of smooth biological tissues has attracted interest, especially in regard to arterial wall tissue (Holzapfel and Ogden 2010).

Figures 5.1a and 5.1b present typical stress-stretch relationships, respectively between isotropic plastic fabric and anisotropic (soft tissue) fabric. These are comparable with the distinctive stress-stretch relationship for most rubber-fibre composites. In comparison with

isotropic rubber material, in the initial stress state, the stress-stretch profile for anisotropic material is found to be flatter and then tougher under high stress. The implication is that the rubber surface is more robust in the initial stress state than the reinforced fibre material (soft tissue). The relatively massive extension (stretch) at low stress can be observed in Figure 2.18 (Ogden, 2011).

This behaviour of fibre-reinforced material is related to its distribution in the matrix. The general conclusion is that the flexible response of the soft tissue in *the initial stress state* arises from the loose nature of the fibres; but at *a higher stress rate*, the fibres exceed their stretch limit and thus become steeper as the undelaying matrix response is overridden (Reese et al., 2001, Ogden, 2011).

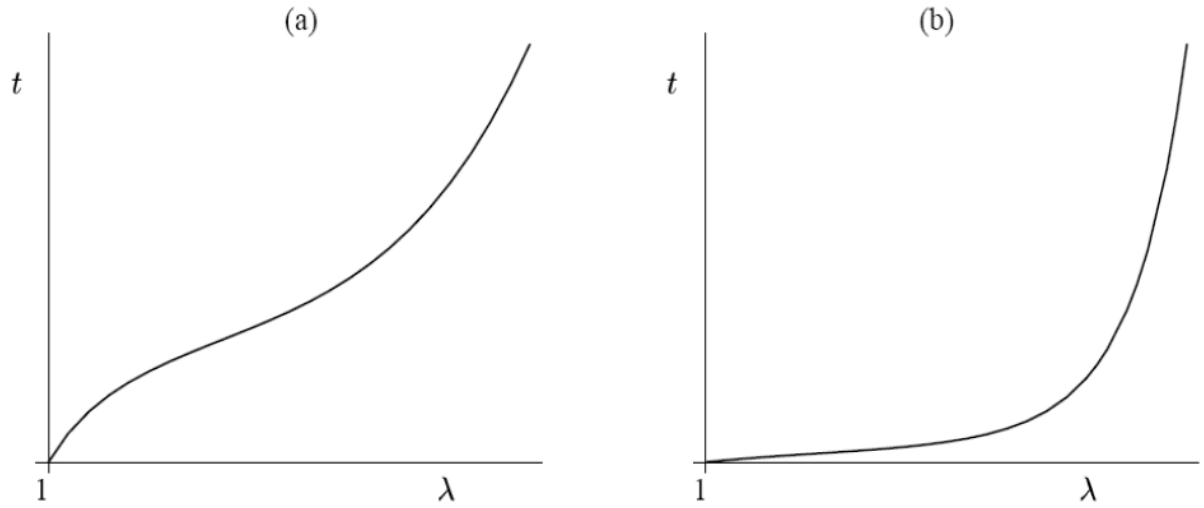

Figure 2. 18 Typical simple tension response of (a) rubber and (b) soft tissue (Ogden, 2011).

In applying the continuum theory of anisotropic material, the strain energy function can be expressed precisely in terms of tensor and fibre orientation invariants. (Spencer, 1984). An illustration would be that of a composite material composed of an anisotropic hyper-elastic

matrix combined with a variety of fibre families. Fibres are defined by a set of unit vectors, where the stress-energy depends, not only on the deformation but also on the orientation of the fibre (Aboshio et al., 2014).

2.4.9 Extension into Principal Directions

Typically, the straightening of crimped yarns also occurs when a plain-woven fabric is extended in either of the principal directions. A decrease in the amplitude of the yarn and the angle of weave can be observed in the direction of warp and weft. Those yarns appear to be less flattened during tensioning due to their consolidation into a tighter cross-section (Hearle et al., 1969; Hu, 2004).

With regard to the uniaxial tensile properties of plain-woven fabrics, De Jong and Postle (1977a, b) indicate that six separate dimensionless parameters must be considered in the case of a balanced woven fabric (produced from identical warp and weft yarns). Those parameters are: (a) the ratio of warp to weft yarn length per weft yarn; (b) the ratio of yarn diameter to modular yarn length; (c) the ratio of yarn compression rigidity to bending rigidity; (d) the yarn compression index; (e) the ratio of yarn extension rigidity to bending rigidity; and (f) the degree of a set. Jong and Postle also argue tha, as the ratio of yarn compression rigidity to bending rigidity may be determined by the length of the yarn, a significant part of the extension of the fabric can be explained by the extension of the yarn when the ratio is lower. In the selected range, where the inter-yarn distance may be increased in order to make yarns transform into a rounder or more circular transformation during tensioning, average Poisson's ratios can be determined. (Hu, 2004) (Khajehsaeid, and Naghdabadi, 2013).

2.4.10 Anisotropy of Composite Woven Fabric Tensile Properties

Anisotropy is a feature of most fabrics, particularly woven, where the effect of the direction of loading has been widely investigated (Dai & Zhang, 2003; Kilby, 1963; Kovar & Dolatabadi, 2009; Kovar, 2003; Pan & Yoon, 1996; Postle et al., 1988). Although many publications deal with tissue tensile properties, most are focused upon the warp and weft directions. One difficulty in studying the tensile behaviour of composite woven fabrics is that any extension, occurring at an angle to either the warp or weft direction (Hearle et al., 1969). The modulus is almost entirely determined by the shear behaviour of the fabric in the 45° direction towards either the warp or weft, shearing behaviour cannot play a role if it is extended in the warp or weft directions. Consequently, the tensile strength of the fabric has a tendncy to produce a multi-directional effect.

Woven fabric is highly anisotropic. As most fabric structures are asymmetrical, the strength necessary to stretch fabrics in various directions varies greatly. For instance, if a textile is being tightened, there is shear deformation, and so shear property becomes relevant. The tensile behaviour of fabric varies in accordace with the extension in two main directions (Hearle and Amirbayat, 1986).

Fibre has a higher degree of elongation than the matrix and has a stronger strength and stiffness. When these two constituents are combined, a fibre-reinforced composite is created with tensile qualities that are halfway between the two constituents (Rahman and Putra 2019).

Tensile strength tests create frictional forces in both the warp and the weft directions. With relatively more threads per inch, woven fabric has greater strength in the warp direction than in the weft direction. In measuring yarn-to-yarn frictional forces, the weave interlacing coefficient depends on weave geometry, thread crimp and the fabric shear properties of the composite. The higher weave interlacing coefficient of the plain weave fabric (higher average

yarn interlacing density) is indicative of tensile strength (Özdemir and Mert 2013). The specific tensile strains of structures were found to be proportional to their directional tensile strains in both warp and weft. This is explained by the fact that, owing to its higher interlacing coefficient, there is more crimping of yarns in plain weave. Thus, if yarns extend around the yarn axis during tensile strength testing, both crimp and length are increased. Warp and weft thread fabrics are most commonly pulled or biased when drawn diagonally. These results indicate that stitching yarn type, stitching directions, and stitching density generally influence the warp and weft directional tensile properties of PVC woven fibre reinforced composite. Such findings show that stitching yarn size, stitching directions and stitching density generally affect the directional tensile properties of the warp and weft.

2.4.11 Ogden model

The Ogden model (Ogden 1972) is a phenomenological model based on principal stretches rather than invariants. It is able to accurately capture upturn (stiffening) of the stress-strain curve and model rubber over large ranges of deformation. There is an excellent observational agreement between the Ogden model and Treloar's experimental data for unfilled rubber for extensions of up to 700% (Ogden, 1972; Treloar,1975). The model is defined as follows:

$$W = \sum_{i=1}^{N} \frac{2\,\mu_i}{\alpha_i^2} \left(l_1^{\alpha_i} + l_2^{\alpha_i} + l_3^{\alpha_i} - 3\right) \tag{2.7}$$

Where μi, α_i are temperature-dependent material properties

2.4.12 Yeoh model

Yeoh proposed a phenomenological model in the form of a third-order polynomial based only on the first invariant, I1 (Yeoh 1993). In the same manner as the Ogden and polynomial

models, this model is based on a series expansion (Selvadurai, 2006). The Yeoh model is also called the reduced polynomial model, and for compressible rubber is given by:

$$W = \sum_{i=1}^{3} C_{i0} \, (I_1 - 3)^i \tag{2.8}$$

With a good fit over a large strain range, the Yeoh model can simulate various modes of deformation with only limited data, so leading to reduced requirements for material testing.

Based on the theory of incompressible hyperelastic solids, the constitutive models introduced above are described by the coordinate system X in an undeformed state. The Yeoh and Ogden models are used in terms of strain invariants for the isotropic part, with two terms of an exponential model in terms of a pseudo-invariant used to model the anisotropic response for each set of fibre.

A variety of engineering polymers, such as carbon and glass fibre fabrics, large thermoplastic sheets, reinforced composites and elastomer composites, are subjected to complex loads that result in different biaxial stress/strain conditions. The characterisation of biaxial deformation of engineering polymers is made difficult by the extent of deformation. The out-of-plane biaxial test (stretching balloons in bulge tests) is commonly used to determine the parameters of large deformations of elastomers for different hyperelastic materials (Jones and Treloar, 1975; Leonhartsberger et al., 2012; Murphy et al.,2005). The wide variety of potential applications explains the considerable interest in the experimental characterisation of their behaviour (Sasso et al., 2008).

2.5. Summary

The mechanical characteristics of rubber and textiles, as well as coated composites made from those materials, and some of the terminology used in the textile field, have been discussed in this chapter. The following summarises the findings.

Stress-strain for rubbers is usually non-linear: for example, they can be extended to approximately 700% of their original length. However, fabrics with low compression and bending stiffness have high tensile strength. In general, their mechanical properties will be different from their uncoated characteristics.

Fabric composites are suitable in many industrial applications, depending on the coating material and the volume fraction used in the composites.

Vulcanised rubbers offer great weathering and chemical resistance, as well as excellent energy absorption ability. They have a low modulus of elasticity when compared to many engineering materials. Among the many applications are hydraulic hoses, seals, vehicle tyres, vibration and shock absorbers, and their use as cladding, roofs, pneumatic hoses, inflatable boats, pneumatic seats, beams and slabs.

Complex structural interactions at both the yarn and fibre scales link the behaviour of woven textiles to the material qualities of the fibres. Loading in tension and shear leads to complicated behaviour that is anisotropic, nonlinear and exhibits irreversible deformation, or hysteresis. In Chapter 5, the results of these tests are utilised to validate the findings of the FE simulations.

Chapter Three

This chapter describes the study of methods and materials used in the experimental work, to understand the mechanical behaviour of the fibre-reinforced composite under different uniaxial loading conditions. Results from the uniaxial tests showing the characteristic behaviour of the different composite conditions are presented and discussed. In addition, there is an analysis of the performance of three different fabrics with composite reinforcements.

3.1. Materials

3.1.1 Material 1

Dunlop GRG Holdings Ltd (Manchester, UK) supplied the composite material used. It is a flexible composite, supplied in sheet-rolls of different thicknesses. The material is a woven rubber fibre matrix composite. Each component of the material and its manufacturing processes influence the mechanical properties of the composite material. Three different composite materials with different thickness, as indicated below, were studied.

The first material's 5 mm thickness specification comprised base fabric with high tenacity and continuous filament nylon tyre cords laid in on opposite diagonals coated with black PVC/ nitrile blend compounds and vulcanised. The continuous filament nylon is a woven fabric with a two-directional warp and weft (Trelleborg reference data sheet EXA-1196) material properties data – from manufacturers materials data specifications as shown in Table 3.1.

Figure 3.1 shows the anisotropic nature of this material when the experimental strips are cut in different directions.

Table 3. 1 Material properties EXA-1196.

Test Property	Units	Specification	Typical Result	Test Method
Mass	g/m^2	2372 max 1840 min	2110	BS EN ISO 2286-3 Method A
Breaking Load Warp Weft	 N/50mm N/50mm	 5400 min 5400 min	 6400 6750	BS EN ISO 1421 Method 1
Puncture Resistance x warp/ x weft	N	670 min	850	Spec No.279 Issue 9-2.1.2.7
Coating Adhesion Outer Cover Un-aged After 3 days @40°C in Fuel B Inner Lining Un-aged After 3 days@40° in Fuel B	 N/50mm N/50mm N/50mm N/50mm	 113.9 min 65.7 min 113.9 min 65.7 min	 177 142 239 159	BS EN ISO 2411
Permeability to Fuel B Original	$Cm^3/m^2/day$	50 max	TBA	Spec No 279 Issue 9-2.1.2.4

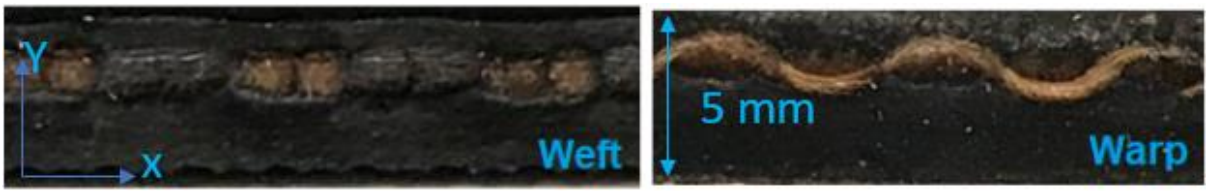

Figure 3. 1: Specimen geometry and cross-sections of the composite material showing the warp and weft arrangements for 5 mm thickness.

3.1.2 Material 2

The second material of 3 mm thickness, is a base fabric with high tenacity, continuous filament nylon tyre cords laid-in on opposite diagonals, coated with black PVC/nitrile compounds and vulcanised. (Trelleborg reference data sheet EXA-1180) material properties data – from manufacturers materials data specifications as shown in Table 2. The anisotropic nature of the

material presents a different appearance when an experimental number of strips are cut in various directions, as shown in figure3.2.

Table 3. 2 Material properties EXA-1180.

Test Property	Units	Specification	Test Method
Mass	g/m^2	2950	BS EN ISO 2286-2 Method A
Gauge	mm	2.54	BS EN ISO 2286-3
Breaking Strength in cords directions	N/50mm (KgF/50mm)	4400 (448.6)	BS EN ISO 2421 Method 1
Coating Adhesion - **Original** - **"Wet"**	N/50mm (KgF/50mm) % retention	158 (16.1)	BS EN ISO 2411

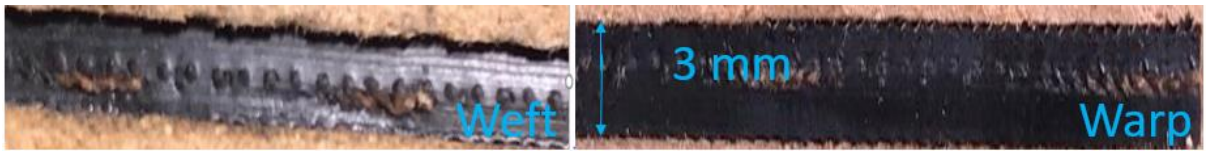

Figure 3. 2: Specimen geometry and cross-sections of the composite material showing the warp and weft arrangements for 3 mm thickness.

3.1.3 Material 3

The third material was manufactured to 2 mm nominal thickness. The woven material is high tenacity, continuous filament nylon base fabric that is coated with polychloroprene compounds on the outer cover and inner lining sides and vulcanised material properties data – from manufacturers materials data specifications as shown in Table 3. Figure 3.3 shows that the series of strips cut in warp and weft directions present alternative appearances (Trelleborg reference data sheet EXA-1182).

Table 3. 3 Material properties EXA-1182.

Test Property	Units	Specification	Test Method
Mass	g/m^2	4,750	BS EN ISO 2286-2 Method A
Breaking Strength Warp Weft	 N/50mm N/50mm	 8,750 11,000	BS EN ISO 1421
Puncture Resistance x warp/ x weft	N	890	ASTM D751
Coating Adhesion Outer Cover and inner Lining	N/50mm	100 min	BS EN ISO 2411
Abrasion Resistance	cycles	25,000 to exposure of fabric, outer only	FED-STD-191, Method 5306, H22 wheel, 1000g load
Tear Strength, warp and weft	N	100	BS EN ISO 2411

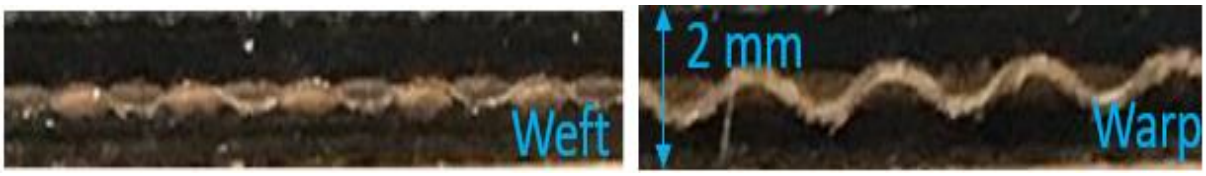

Figure 3. 3: Specimen geometry and cross-sections of the composite material showing the warp and weft arrangements for 2 mm thickness.

3.1.4 Composite Volume Fraction Estimation

The Zeiss Stemi, Zeiss GmbH Optical Microscope fitted with an axiom digital acquisition system, used to scale images of a section of the composite. Figure 3.4 illustrates the nature of the fabric crimp in both warp and weft directions. The weft fibres (also described as fill fibres) are linear in their un-stretched state; and they occupy the space relative to the undulating/sinusoidal warp fibres, having the same structure in the three materials.

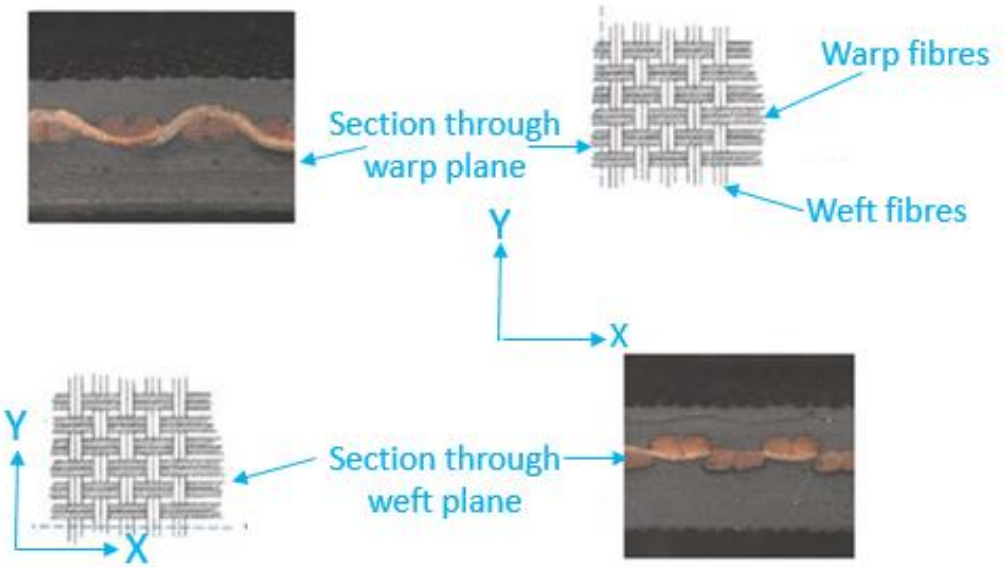

Figure 3. 4: **Specimen geometry and cross-sections of the woven fabric basic specifications, the warp (x) and the weft (y) fibre orientations within the PVC rubber matrix.**

Volume fractions of constituents of the composite were computed from mass values provided by Trelleborg raw materials as supplied by Dunlop Holdings Figure 3.5. The estimated volume fraction of PVC/nitrile and nylon tyre cords in the fibre-reinforced composite were approximately computed, as shown in Table 3.4.

Table 3. 4 Volume fraction of matrix and fibre.

Materials	PVC	Fibre
EXA-1196	89.5 %	10.5 %
EXA-1180	88.5%	11.5%
EXA-1182	81.9%	18.1%

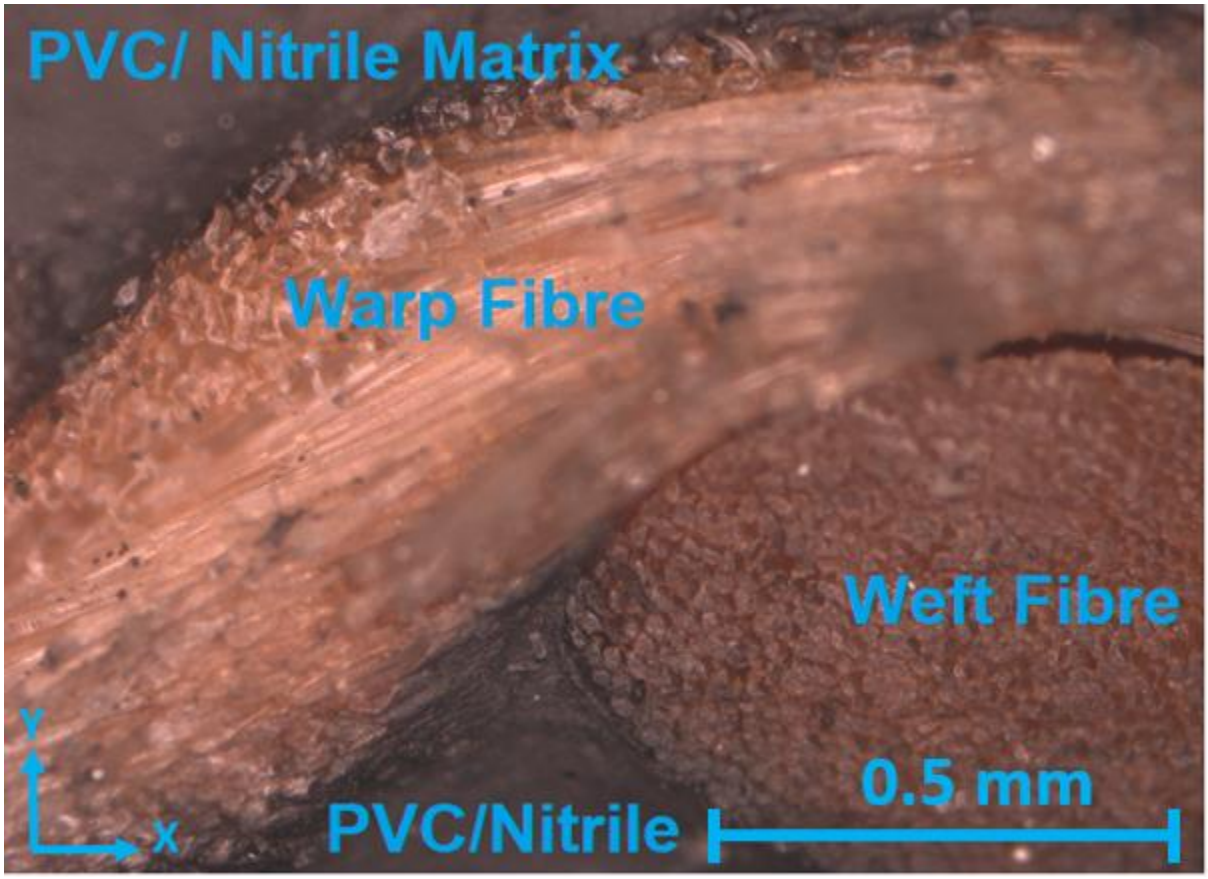

Figure 3. 5: Section of the composite showing microscopic images of the weft and warp fibres bundles.

3.2. Video Gauging

3.2.1 The principle of Video Gauging

The accurate measurement of strain was obtained by video gauging, which gauges the distance between two points and the position and movements of points on a sample. One video camera measures the distance and position within a xy plane perpendicular to the optical axis of the camera and two cameras mounted on a camera bar obtain 3D measurements including the z coordinate of points along the optical axis.

3.2.2 Advantages of Video Gauging

The use of contactless video gauging (as with the Imetrum system) provides advantages in terms of accuracy and additional information, over a conventional stress-strain curve

measurement. The optical system and related computer software can capture movements and position change in the range of 1μm and below. The optical video system catches the pure real-time strain of the specimen, without underlying expansions in the whole system from a mechanical stress-strain test. Inaccuracies in strain measurements by mechanical systems derive from the expansion of the grips and other parts of the testing machine as well as imperfect sample restraint (slipping of the specimen inside the clamps).

A mechanical stress-strain test only examines the strain experienced in the direction of the stress over the complete length of the sample. Video gauging captures such additional features as multi-directional strains, even those perpendicular to the stress direction. The use of a second camera also identifies such three-dimensional features as a change of sample thickness. Any two points on the sample surface that are visible to the cameras can be a start point or endpoint for strain measurement. This is particularly important for revealing inhomogeneous or anisotropic strain, where a 2D strain map can capture and visualise the strain conditions over every surface point of the specimen. (See figures 3.6 and 3.7).

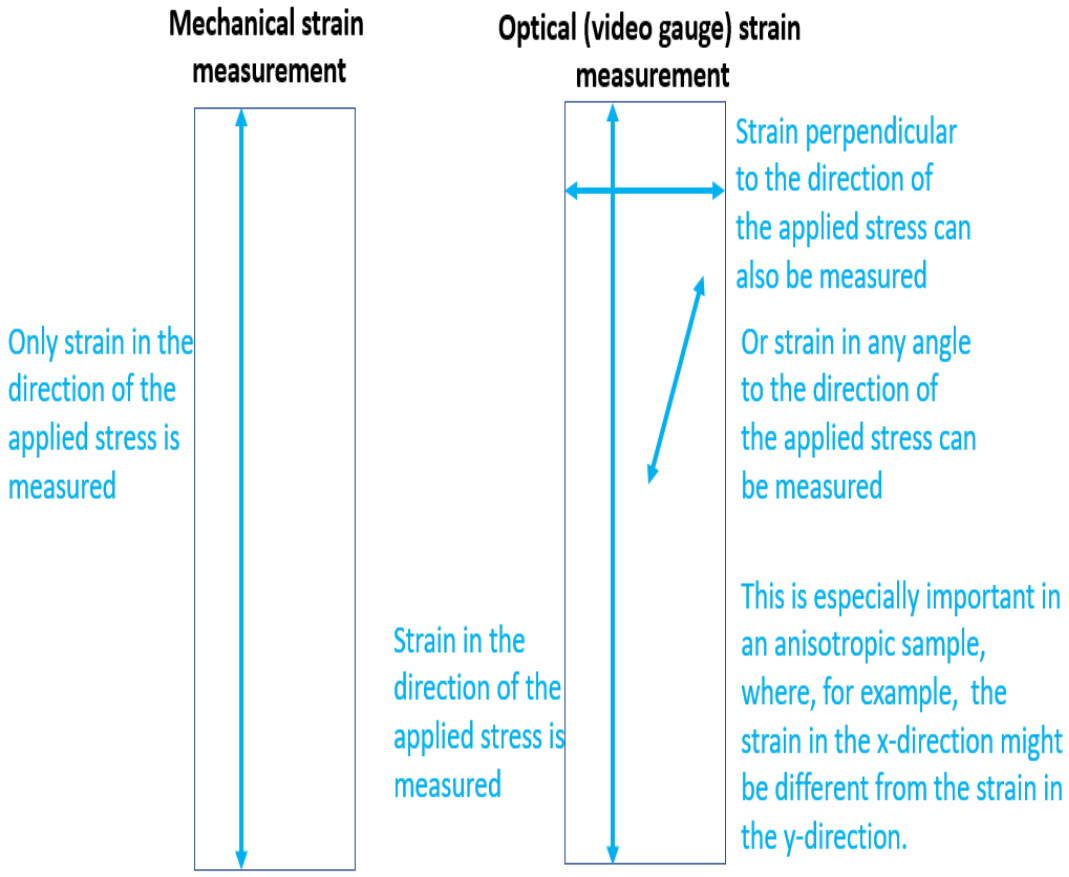

Figure 3. 6: Capability of video gauging capturing strains in different directions

The contactless strain measurements used in video gauging eliminate any influence measurement might have on the material behaviour. Video gauge is particularly suitable for testing hyperelastic materials because of the large deformations possible with such material. Overall, a host of practical reasons speak for the use of video gauging, where many different measurements can be performed at different parts of the sample, together with additional "post-processing" measurements that are possible after the experiment has ended.

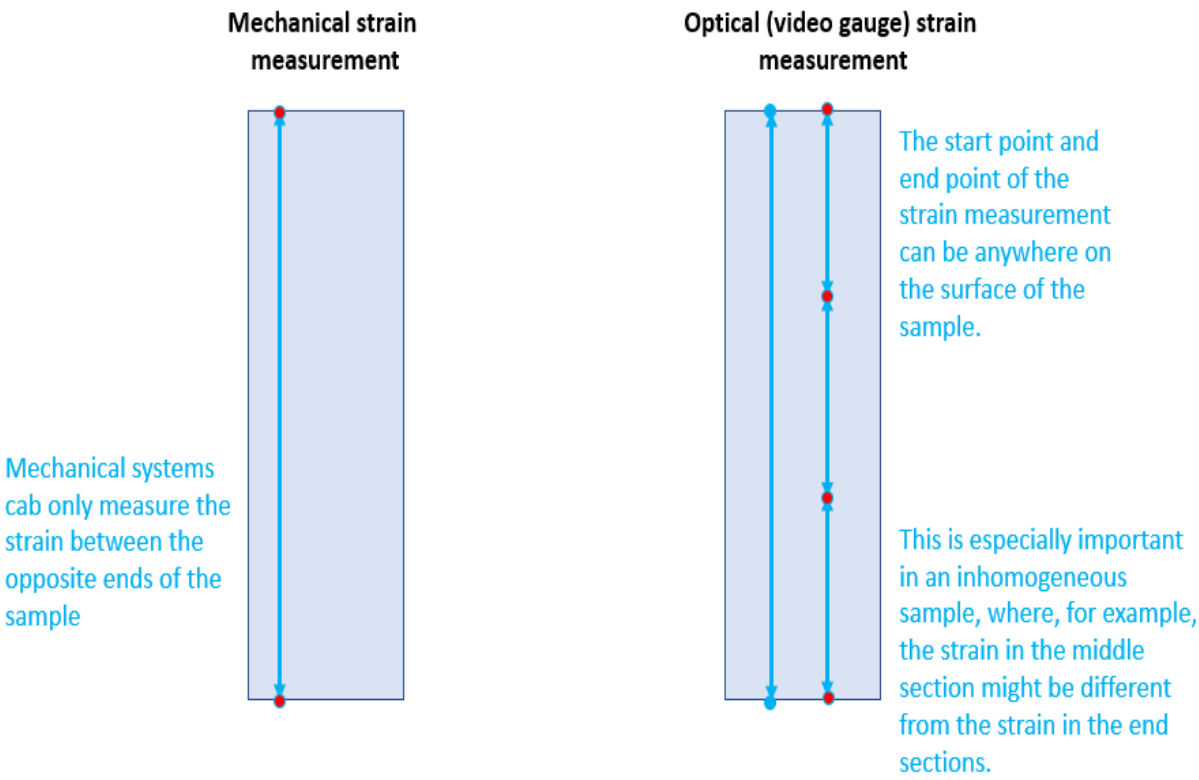

Figure 3. 7: Capability of video gauging to identify strain values between any two sample points

3.2.3 Limitations of video gauging

There are several limitations of the video gauging methodology. It is essetial to ditect small scale motion, ideally of length smaller than a pixel. That requirement can be overcome by the use of DIC software as described in 3.2.6. That the camera must be rigidly fixed in one place, makes necessary the use of a sturdy tripod. Even then, a noisy environment will corrupt the results. Another limitation is that motion signals are only detectable in areas with good contrast, motion of areas without a texture is impossible to trace unless these areas are pre-treated with a painted pattern. The volume of data from by digital 2D or 3D measurements is potentially enormous, especially if techniques like 2D strain maps (see 3.2.11) are used. These vast data makes a powerful computer necessary where processing may take hours. Real-time observation via 2D strain maps was not possible in our case.

3.2.4 Equipment used for video gauging

As mentioned in section 3.2.1 video gauging equipment consists of two cameras including a stable tripod stand and 2 sets of LED panel lights with tripod stands, a camera bar with a fixed camera position if more than one camera is used, a computer to control and record the video and process the received data and cables to connect the cameras to the computer and each of the components with electrical power. The video gauging equipment used in this research was purchased from the company Imetrum, Bristol, UK. The two cameras are industrial Gigabit ethernet cameras which are powered over the ethernet (GigE PoE cameras). They are capable of a maximal frame rate of 15 Hz and provide a resolution of 2452 x 2056 monochromatic pixels with a pixel size on the sensor of 3.45μm x 3.45 μm. The cameras are fitted with low distortion lenses with a focal length of 50 mm, with an optimal focus achieved at a working distance of 660mm. For a working distance of 660 mm, the maximum field of view can be calculated as 111mm in width and 93mm in height, which is also confirmed experimentally. The actual pixel size depends on the size of the field of view and the working distance. With the working distance of 660 mm used in the optical experiments in this work, the actual pixel size projected onto the target object is 45.2μm x 45.2μm.

3.2.5 Validation of video gauging measurements

Using an electrical stage custom-built at the Lancaster University Engineering Department, validation was achievd by moving the stage by 0.5mm (nominal) for each of three steps forward and then for three steps backwards. The movement of the stage was measure and then captured in a video of the Imetrum system.

The average measured movement was 0.507mm forward and 0.509mm backward (an average relative error of around 1.6%). The standard deviation of the forward and backwards steps was

0.015mm (3% of the average displacement). The movements of the electro stage were in close accordance with measurements recorded from the Imetrum system.

3.2.6 Software used for Video Gauging – Digital Image Correlation

Digital Image Correlation (DIC) is a software method used to achieve the sensitivity of motion detection at a level smaller than one pixel. DIC software tracks optical information across a set of images (a movie) that serve to calculate translation, rotation and deformation of a visually marked area on the surface of a filmed object. The accuracy of DIC can be very high using a technique called "sub-pixel grey level interpolation". As a black spot of diameter 1 pixel moves across a uniform white background, neighbouring pixels react to the displacement of the original point by adopting a grey level value proportional to the surface of the black dot overlapping the white area of the neighbouring pixel.

Digital Image Correlation (DIC) software enhances the displacement resolution of the cameras and lenses. Sub-pixel interpolation makes it possible to measure displacement amplitudes smaller than 0.1 pixel and, under favourable experimental conditions, even below 0.005 pixels Digital Image Correlation used in the Imetrum system is theoretically capable of detecting shifts of magnitude 1/200 of the size of one pixel (with focal length and working distance used in this research work, by 0.225 μm). Although the actual displacement resolution is dependent on other factors, experiments done with the Imetrum video gauging system at the Engineering department of Lancaster University show that a displacement of 1μm is detectable.

The idea of using cross-correlation to quantify changes in data sets has been recognised for a long time and has been extended to digital images since at least the early 1970s (Anuta, 1970, Keating et al., 1975). For DIC to work effectively, pixel blocks need to be random and unique, with a range of contrast and intensity levels (Abdul-Aziz and Wroblewski 2016). The

techniques were developed to obtain subpixel resolutions and to enable the algorithms to be performed efficiently. This allows high-resolution measurements to be made so that surface deformation can be measured with commercially available digital photography down to one part per million of the field of view (McCormick and Lord 2010, Potter and Setchell 2014)

3.2.7 Targeting Points

Video Gauge is used to define several target regions of interest. The targets describe the location and the area around the location to monitor during the test. At the start of the test, Video Gauge 'learns' a region of interest, where it identifies a point of interest or target point by the appearance of its surrounding area. It then monitors how the target point shifts in the form of displacement over time. From the displacement of the target points quantities such as point-to-point strains, extensions, or rotations can be derived (Solutions, 2009; Kock, 2015; Guide, 2009).

Since a mechanical test can deform the surface of a sample, the targeting system must tolerate abnormalities while permitting accurate identification at specific points of interest. In experiments, the Imetrum system proved itself capable of this kind of flexibility. Even so, if the appearance of the neighbourhood of a target point changed either too rapidly or by too much, the location of the point was "lost" and the measurement aborted.

3.2.8 Target Pattern

To identify the exact position of a target point (section 3.2.5), the surrounding area should have a pattern distinguishing it from all other points. Thus, for a plain sample surface, it is necessary to apply a pattern. The Video Gauge does not require a specific shape or appearance of target patterns. There are several types of target patterns, such as Speckles, Blobs, Concentric Rings,

and Dashes. In the experiments performed in this thesis, the sample surface was plain, with black, white speckles painted on top of the sample surface.

3.2.9 Measurements and Post-Process

Measurements define and identify target points and measure their position or displacement, from the primary results of two or more target points other variables such as distance, strain, Poisson's Ratio, and shear strain can be calculated. In a simple procedure, the video window is used to display the exact location of the measurement on the sample surface. The Imetrum Video Gauging system can track more than 100 points in real-time, opening the possibility of multiple simultaneous measurements while only performing one physical experiment. Video Gauge can perform measurements in real-time using a video camera, but it can also save the footage from the camera to an AVI file for later re-processing. This AVI file can be viewed in Windows Media Player, on any PC or other video player. It also serves to set an additional position, distance, strain or Poisson’s ratio measurements long after the physical experiment has ended. This process of gaining additional data using a pre-recorded material is called “post-processing”.

3.2.10 Principle of 3D measurements

For measurements in three spatial dimensions, the Imetrum system has a 3D coordinate frame, where at least two cameras are required. Position points along the optical axis of the camera are calculated from differences between the two images from the cameras. The method is also used to measure the deformation of both curved and planar surfaces; i.e., the 3D coordinate frame measures the positions (x, y, and z) for each measuring point. For this thesis, it was particularly useful in measuring the z coordinates of points on the surface undergoing a bulge test.

3.2.11 2D Strain Map

As previously mentioned (3.2.1 and 3.2.2) video gauge achieves contactless measurement of strain between two or more points. During mechanical tests, images from an optical camera allows measurement of axial and transversal strain (εxx and εyy) as well as shear strains (εxy). Figure 3.29 indicates one advantage of video gauge over conventional strain measurement methods; i.e., the capacity to simultaneously measure strain at different locations on the surface of a sample.

With the "Strain Map" function of the Imetrum system, comparing strains at different locations is taken one step further. From three strain measurements (figure 3.29), knowledge is gained of the strain at the top, middle and bottom of a sample. Here, the strain map overlays a rectangular area of the sample surface. The dimensions of this area and the number of strain measurement nodes are identified from the grid spacing. Depending on the size of each area relative to the grid spacing, targets may overlap each other. Strain and displacements are used to measure the Lagrangian strain tensor at each grid node.

The resultant strain map gives a clear idea of the strain distribution. In particular, it shows if the strain is evenly distributed or if there are local concentrations. The distribution of the strain is depicted using a colour mapping. A maximum and minimum strain value for the colour mapping is defined either by the user or is set to the absolute maximum and minimum of strain in all of the nodes. The interval between the maximum and minimum strain value is coloured coded red, orange, yellow, green, blue and violet across decreasing values. The high strain values at the centre of the sample are red.

The individual strain maps of axial and transversal strain (ε_{xx} and ε_{yy}) and shear strains (ε_{xy}) are identified as the results of different stress experiments: a tensile test, planar test, picture frame test and bulge test. Respectively, these feature in sections 3.6, 4.6, 4.7.4 and 5.15.

The maps of all composite samples are useful in validating theories relating to strain distribution. Both strain and shear strain measures obtained with single or multiple video gauges gave values close to the values obtained from 2D strain maps. In respect of a practical application, strain maps are ideal for identifying crack growth

3.3. Normal Stress and Strain

Standard uniaxial stretching tests according to BS EN ISO 1421 (2015) were performed at room temperature on six samples of the composite. The samples were 200 mm (length) x 50 mm (width) x 5 mm, 3mm, and 2 mm (thicknesses). Since the stress-strain behaviour of the textile is usually directed in the orthogonal warp and weft directions, two sets of test samples were prepared. As shown in figure 3.8, one set had a warp running parallel to the load application axis, while the second set had a weft running parallel to the load application axis. For each of the three composites, tests undertaken at room temperature were performed on ten specimens of the composite: five were loaded in parallel to the weft fibre direction, and five were loaded in parallel to the warp fibre direction. As can be seen in the figure. 3.9, uniaxial tension was applied to the maximum load the sample was capable to withstand before destruction by a Zwick Z020 (Zwick GmbH) universal testing machine. Each specimen of the composite was uniaxially stretched at a cross-head extension rate of 100 mm/min. Load and extension data were recorded at a frequency of 10 data per second. Nominal stress and strain data were then calculated based on the sample original cross-sectional area and gauge length.

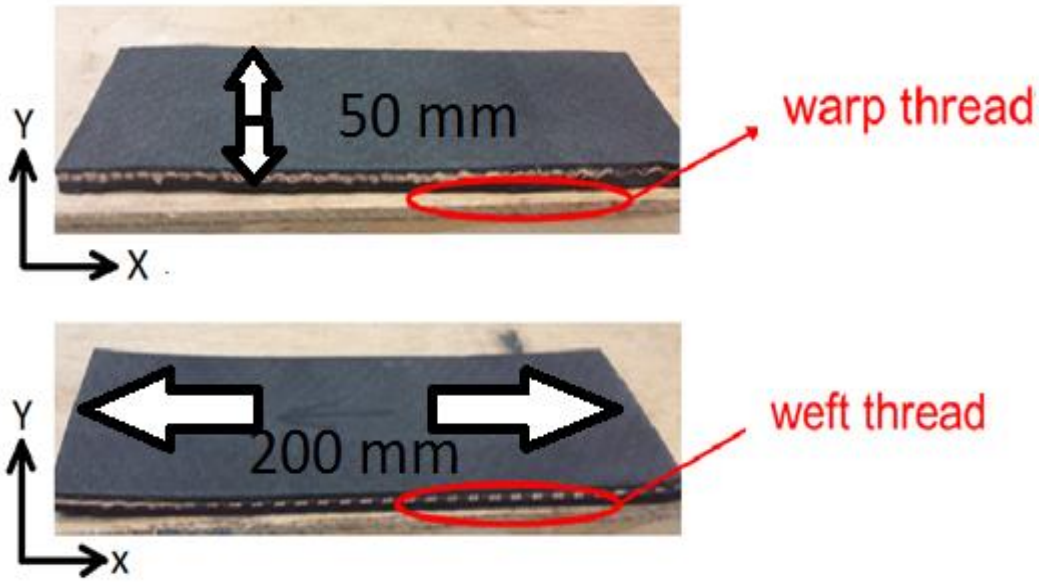

Figure 3. 8: **Schematic of samples preparation.**

The load was measured by a 20 kN load cell. An internal displacement transducer within the test machine Zwick Z020 (Zwick GmbH) measured the displacement, which is proportional to the nominal strain. The true strain through the gauge part of the specimen was measured by a high-resolution Video Gauge, as described in section 3.2. The results reported were limited to two-dimensional (in-plane) measures of surface displacement. These were acquired using a single camera focused on the sample surface during testing (see Fig. 3.11). The strain data-sets arising from the video images were processed using a commercial software package.

As shown in figure 3.9, the camera was located behind the equipment and pointing towards a Perspex screen, in order to avoid reflection. Lighting was to one side and at the same height as the camera.

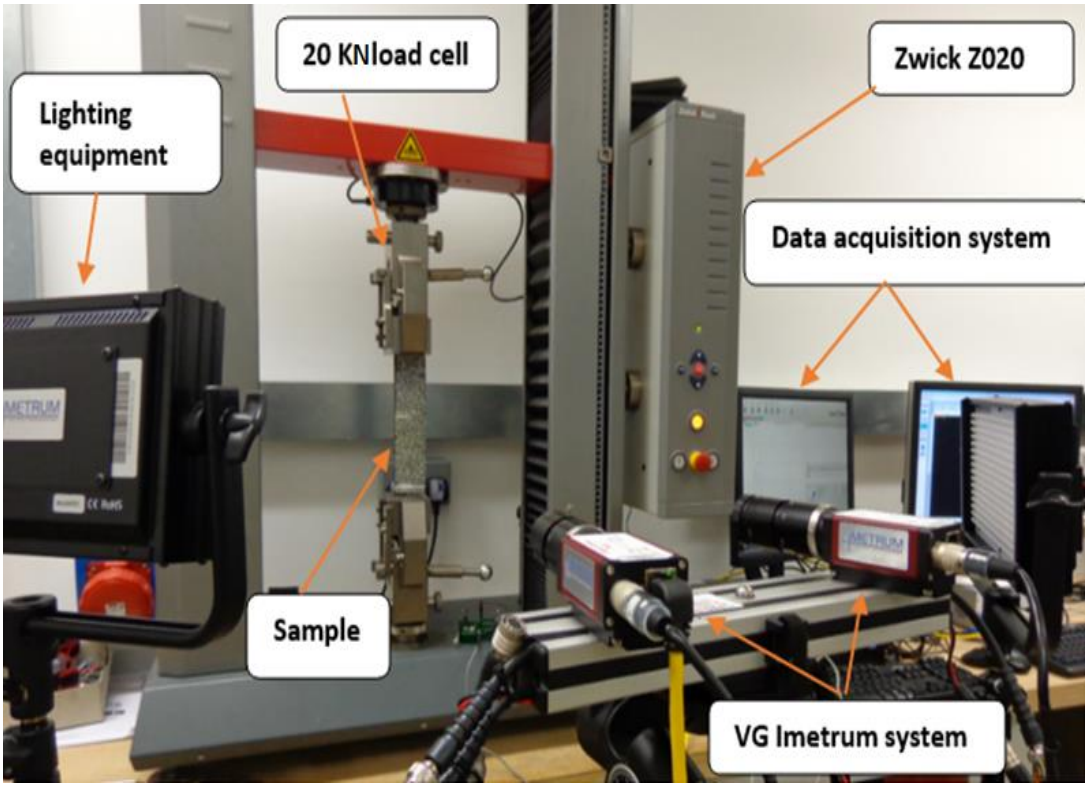

Figure 3. 9: **Experimental set-up showing the video gauge system and sample position within the tensile testing frame.**

To enhance contrast, samples were prepared with a speckle target pattern, multiple white dots were painted onto the black colour of the material. This allowed the video gauge to identify certain locations and track their movement and to provide an accurate measure of the dynamic displacement of the sample. The principle of creating a pattern on the surface of a sample for location identification is described in detail in section 3.2.6.

To control the homogeneity of strain within the observed area, five optical video gauge lengths were defined longitudinally within the areas tested for different gauge lengths (i.e., 30,40,50,60 and 70), from which measures of true strain during testing were obtained (figure 3.10).

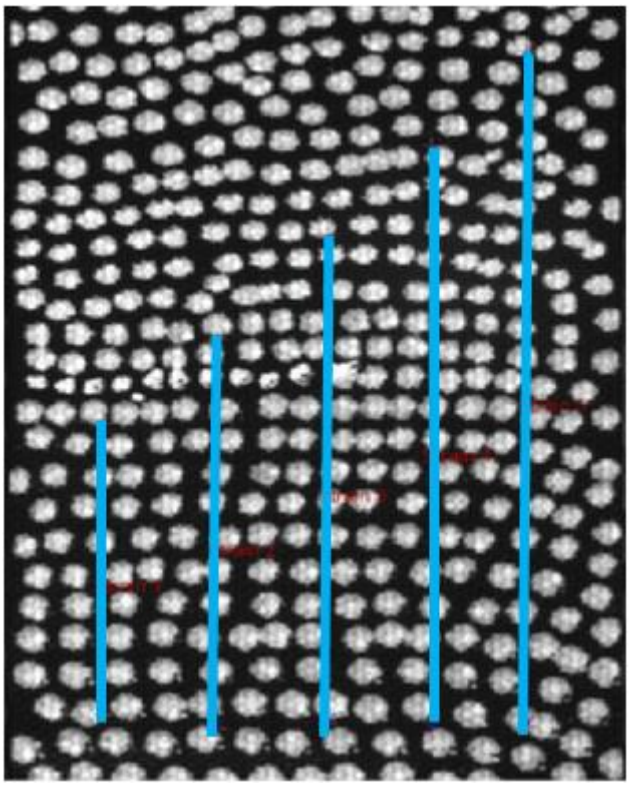

Figure 3. 10: **Strain gauges longitudinally aligned with the uniaxial tension load direction (Sample has been prepared with a speckle surface pattern).**

On deformation, each surface point of the specimen moves in coordination with its neighbours. The surface position of white speckles, both before and after the deformation, are captured on camera. The distance between the two (as depicted by blue lines) define the measuring points (Figure 3.11 (a) and (b)). As the surface points move under stress, the change of the blue line gives the strain value and a rough idea of its direction. As the distance between each of the white pattern speckles increases, their shape changes from circular to elliptic.

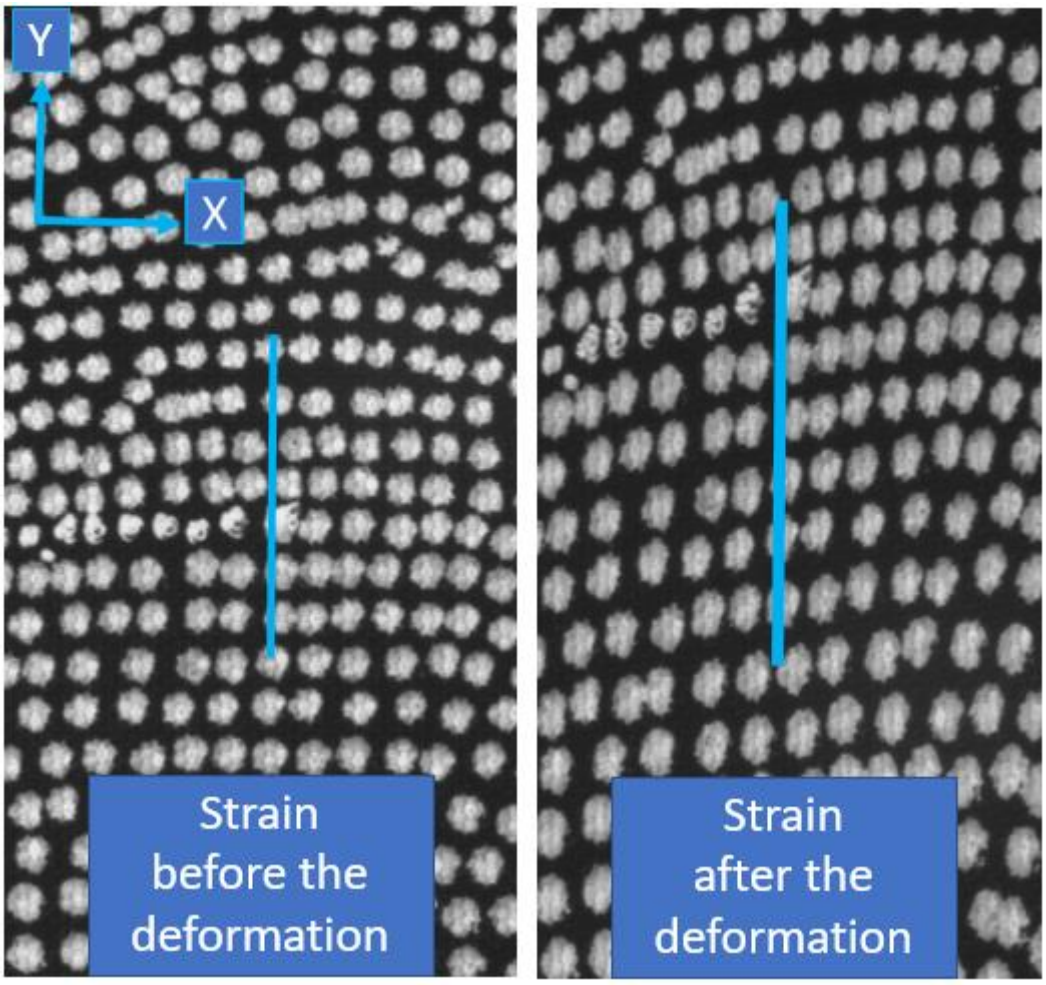

(a) (b)

Figure 3. 11: (a) Displacement of the composite specimen before the loading; (b) after the loading, showing the strain.

3.4. Combined Test Methods

The combination of data obtained by a mechanical stress-strain test and a video gauge strain measurement improves accuracy and gives additional insights into specimen material properties. From the uniaxial testing of samples, as loaded either parallel to the weft direction or parallel to the warp direction in a Zwick extension-testing machine, the video gauge provides further useful information for the load cell curves. While the Zwick measures the strain of the whole system (sample, machine, and metal grips holding the sample in the machine), the video gauge measures the strain of the sample explicitly, taking two points of measurement to provide

the real length of the sample in real-time. Finally, it is necessary to combine the two sets of data created by these two methods.

The time-alignment of the two data sets is a challenge since neither strain values nor the starting time of the experiment is the same. The time of the highest applied force was used as a reference point and aligned with the time of the largest strain values in both the mechanical experiment and the video gauging. To compare the data sets at different times and under different loads, the time of the complete experiment was subtracted from the reference point of the highest load to give a common starting point for the experiment and the duration of the experiment divided into 20 sections of the same time length.

3.5. Poisson's Ratio

As tensile force is applied to the fabric in one direction, the fabric contracts in a perpendicular direction to that load. This is represented by Poisson's ratio (Penava et al., 2014), which is a structural parameter, which results from the geometry of the armour, the mechanical features of the yarn and the interactions yarn-yard. Poisson ratios for textile fabrics are different from standard engineering materials (Boubaker et al., 2010; De Jong and Postle, 1977; Sun et al., 2005). The study of the effect of physical fabric parameters on the value of Poisson's ratio is helpful because of its anisotropic nature. It provides a better understanding of the behaviour of this material. Due to the inherent nature of the fabric, it is difficult to measure this ratio accurately and reliably. (Shahabi et al., 2013). Poisson's ratio of the fabric is defined as the ratio of the longitudinal strain to the transverse strain:

$$v_{wa} = -\frac{\varepsilon_{we}}{\varepsilon_{wa}}$$

$$v_{we} = -\frac{\varepsilon_{wa}}{\varepsilon_{we}} \tag{3.2}$$

Where v_{wa} and v_{we} are Poisson's ratio in the warp and weft directions, respectively, v_{wa} is the axial strain in the warp (0°) orientation, ε_{we} is the transverse strain showed by the material in the weft (90°) direction onto uniaxial loading in the warp (0°) direction (Ben Boubaker et al., 2010; Clyne et al., 1995).

To obtain a measure of the Poisson's ratio, a uniaxial tension test was performed on samples of size 200 × 50 × 5 mm. Tests at room temperature were undertaken on six specimens of each composite: three were loaded in parallel to the weft fibre and three in parallel to the warp fibre. Uniaxial tension was applied using a Zwick Z020 (Zwick GmbH) universal testing machine, to maximum loads. Each specimen of the composite was uniaxially stretched at a cross-head extension rate of 100 mm/min. Load and extension data were recorded at a frequency of 10 data per second

Two methods were used. The first applies a manually defined optical strain gauge (longitudinal and transverse aligned uniaxial gauges) to calculations from equations (3.2). The results are then compared with those from the video gauge for the (EXA-1196) shown in Table 3.5. The second method uses a software-generated (image processing) measurement of υ, as shown in Figure 3.12. With both methods, Poisson's ratios for samples loaded parallel to the warp direction were higher than for those loaded parallel to the weft direction.

Table 3. 5 Comparison of Poisson's ratio (EXA-1196).

Elastic Properties	Weft direction of loading	Warp direction of loading
Poisson's ratio manually defined optical strain gage	0.17	0.37
Poisson's ratio machine defined	0.18	0.36

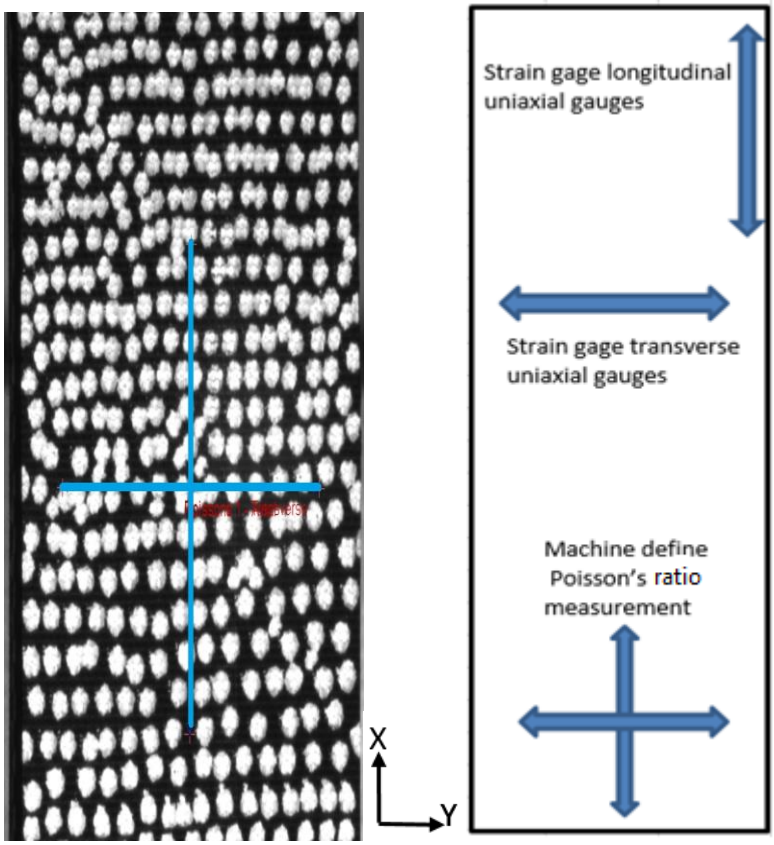

(A) (B)

Figure 3. 12: (A) Poisson's ratio of a virtual strain gauge in x- and y-direction; (B) Poisson's ratio method shows the location in a typical composite sample in tensile loading.

3.6 Results and Discussions

For various materials, Figure 3.13 depicts findings from three tests, both when the load was zero and again when the maximum load was reached (6000 N). Specimens loaded parallel to

the weft fibre failed first due to nylon fibre overload. This was followed by a secondary constriction of the composite inside the gauge region, although there were no obvious cracks on the neoprene rubber. Composite delamination saw the rubber material ripping off those specimens loaded parallel to the warp fibre direction. As the work was focused on early deformation, uniaxial testing test was undertaken using a Zwick Z020 universal testing machine to a maximum load of 6000 N. The test results of uniaxial testing stress-strain behaviour measured by video gauge for different composite material are shown in Figs. 3.14 to 3.16. These are the internal cross-head displacement for the samples loaded parallel to the warp fibre directions for the three samples.

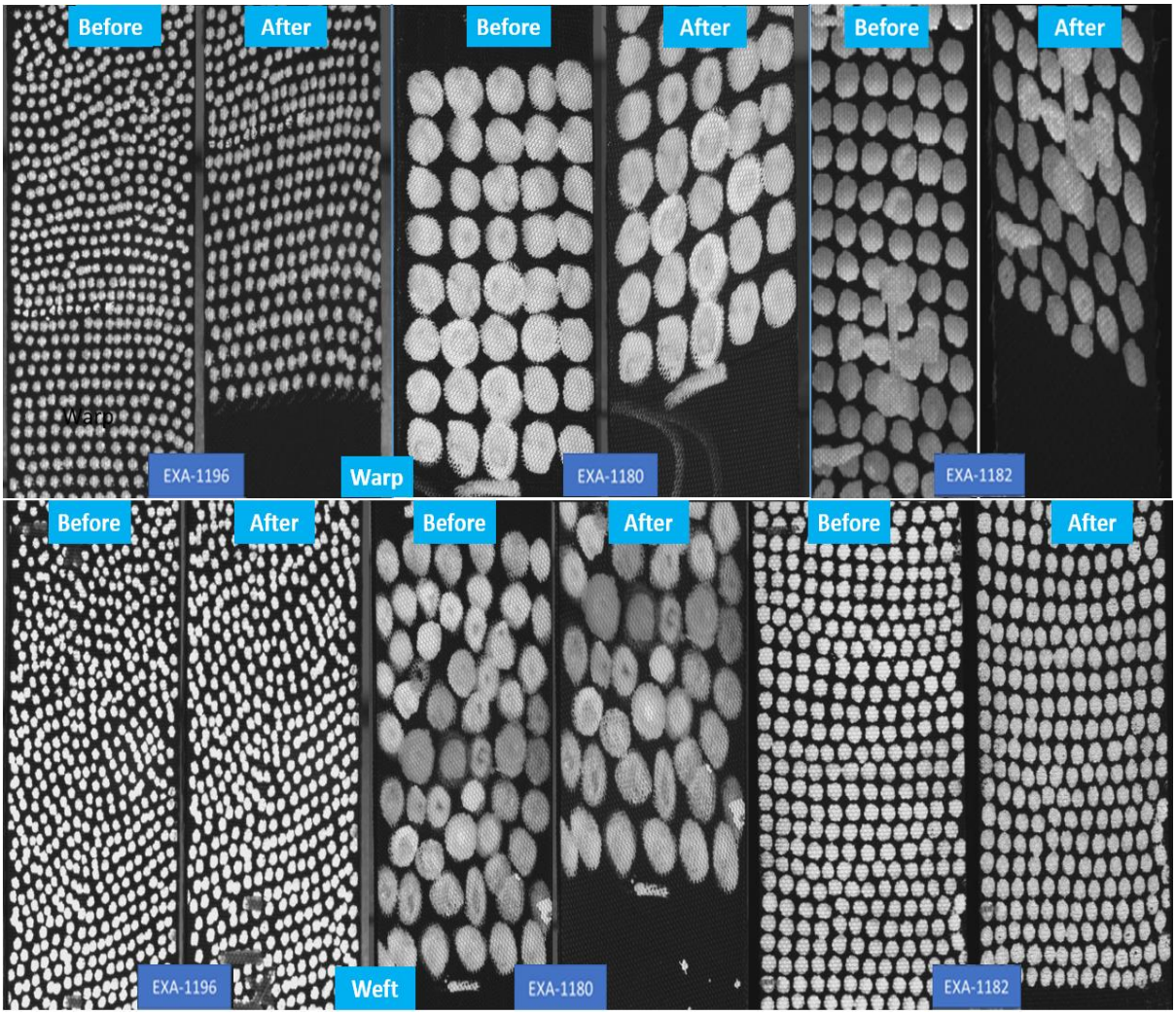

Figure 3. 13: Mode for specimens before and after loaded parallel to the warp and weft fibre direction tested.

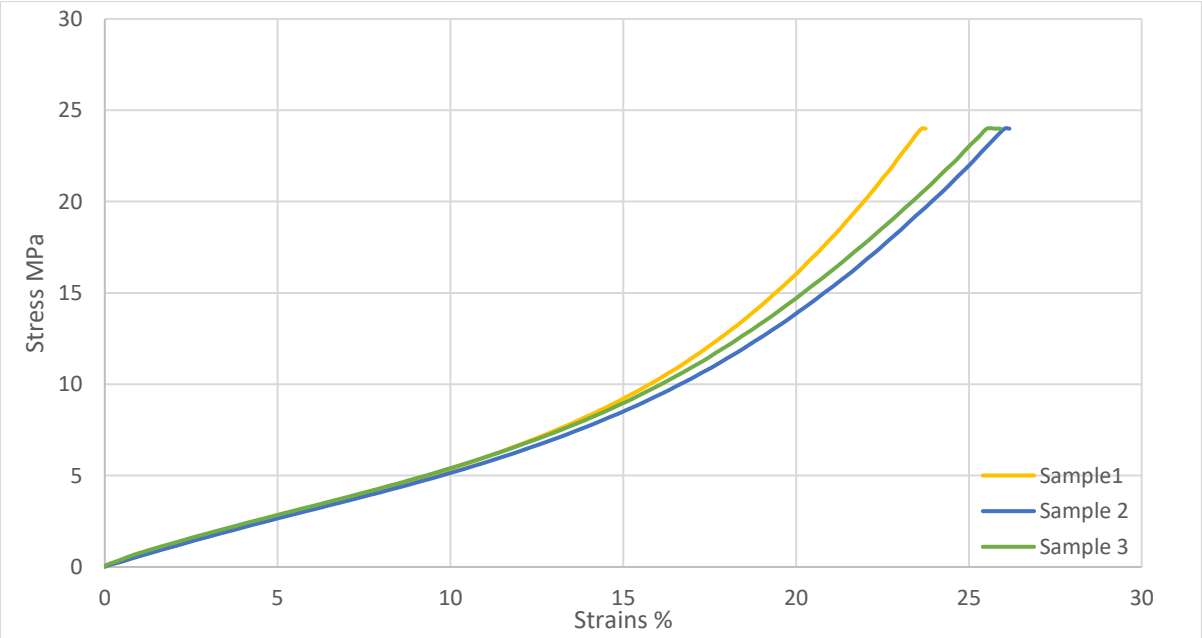

Figure 3. 14: Uniaxial testing stress-strain for the composite specimens loaded parallel to warp fibre direction (EXA-1196).

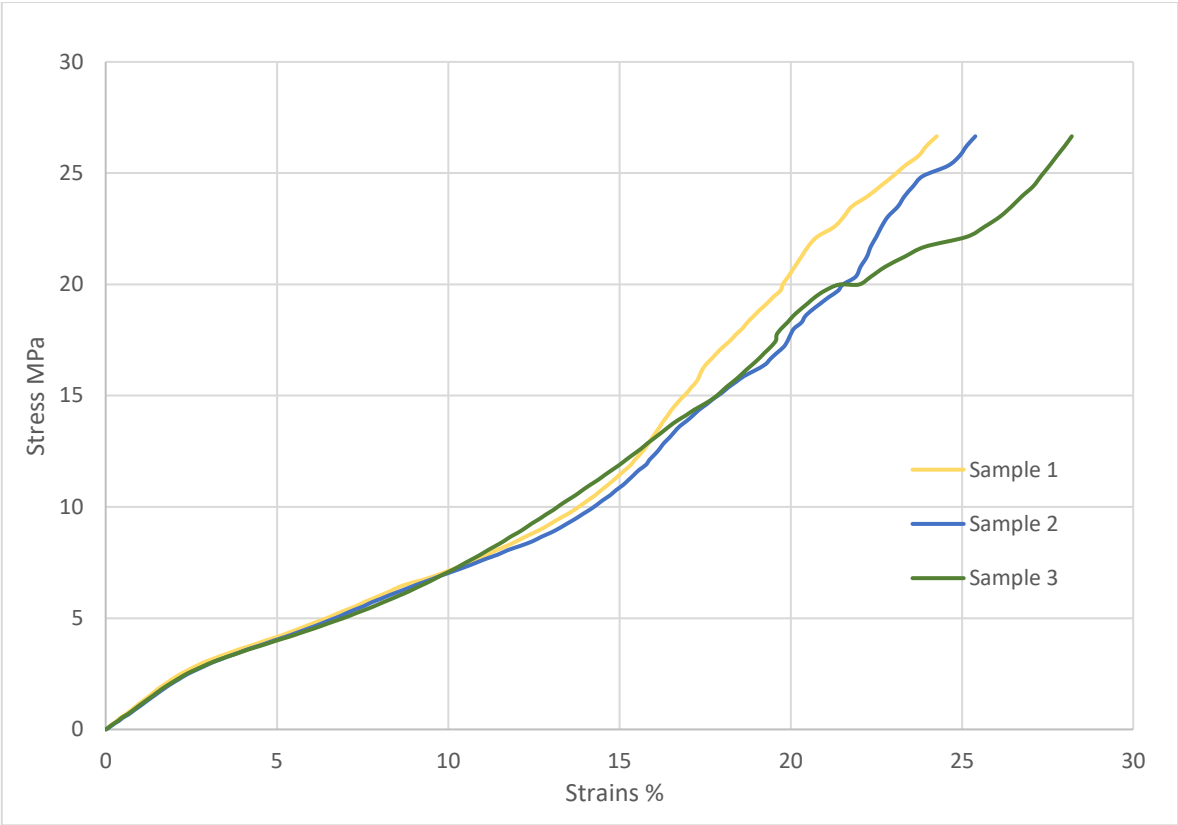

Figure 3. 15: Uniaxial testing stress-strain for the composite specimens loaded parallel to warp fibre direction (EXA-1180).

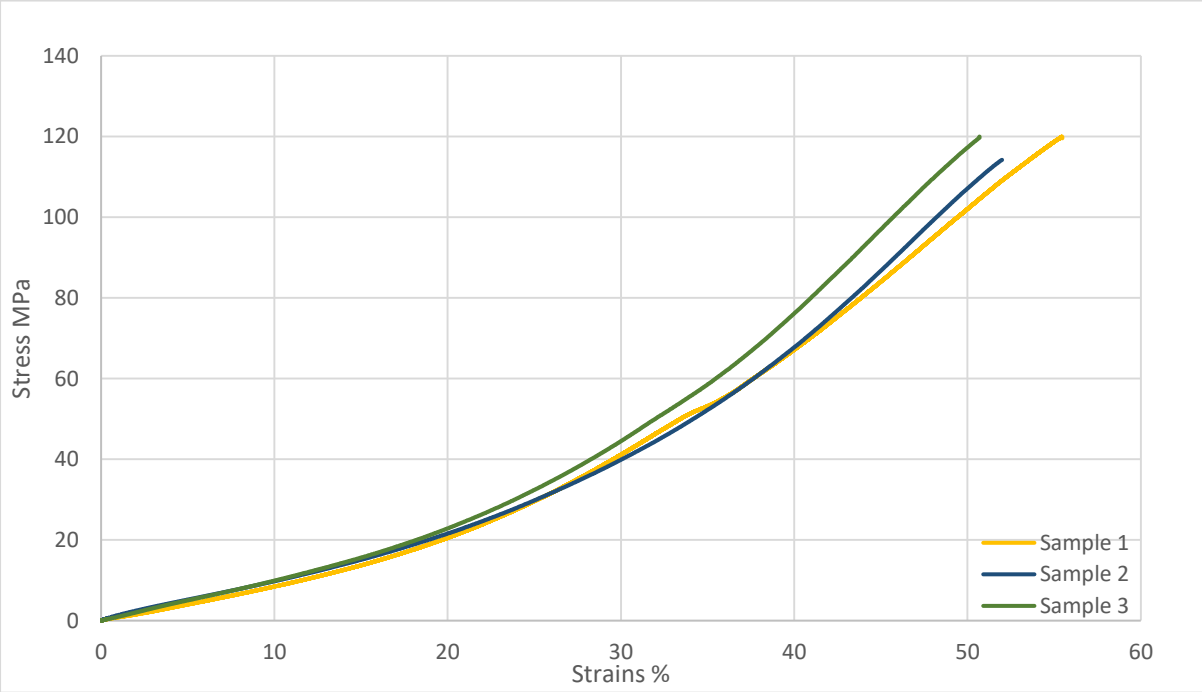

Figure 3. 16: Uniaxial testing stress-strain for the composite specimens loaded parallel to warp fibre direction (EXA-1182).

Figs. 3.17 to 3.19 show the uniaxial tensile stress-strain testing results of the composite specimens loaded parallel to the weft direction.

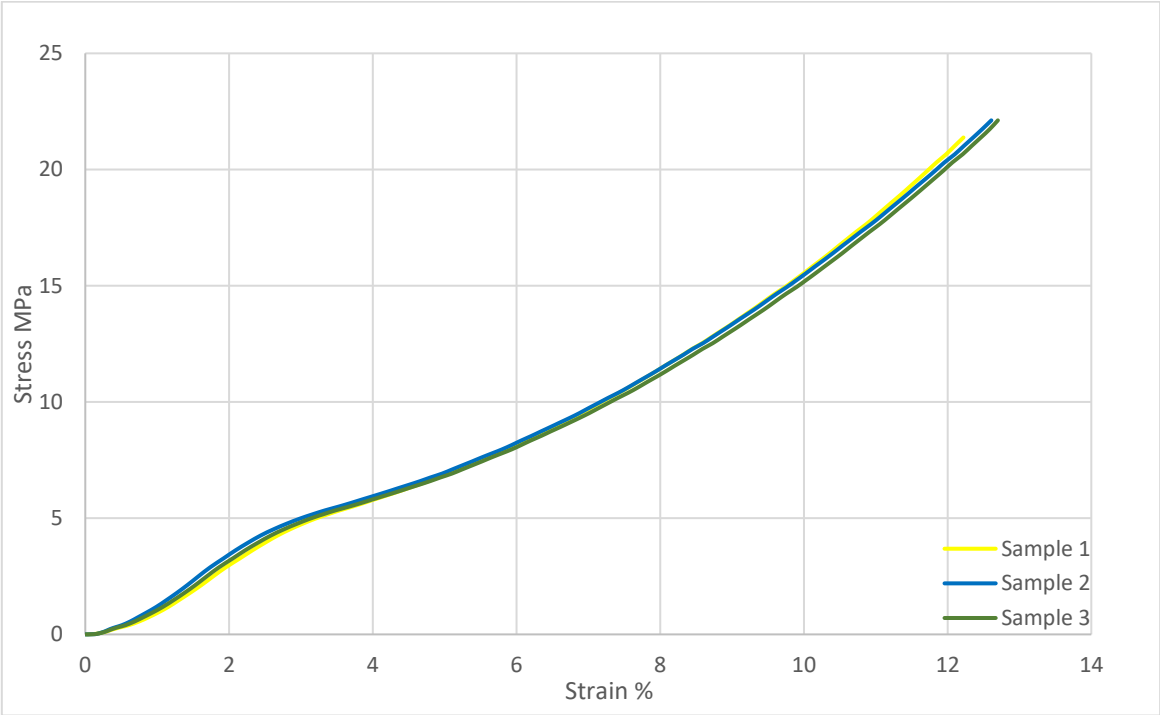

Figure 3. 17: **Uniaxial testing stress-strain for the composite specimens loaded parallel to weft fibre direction (EXA-1196).**

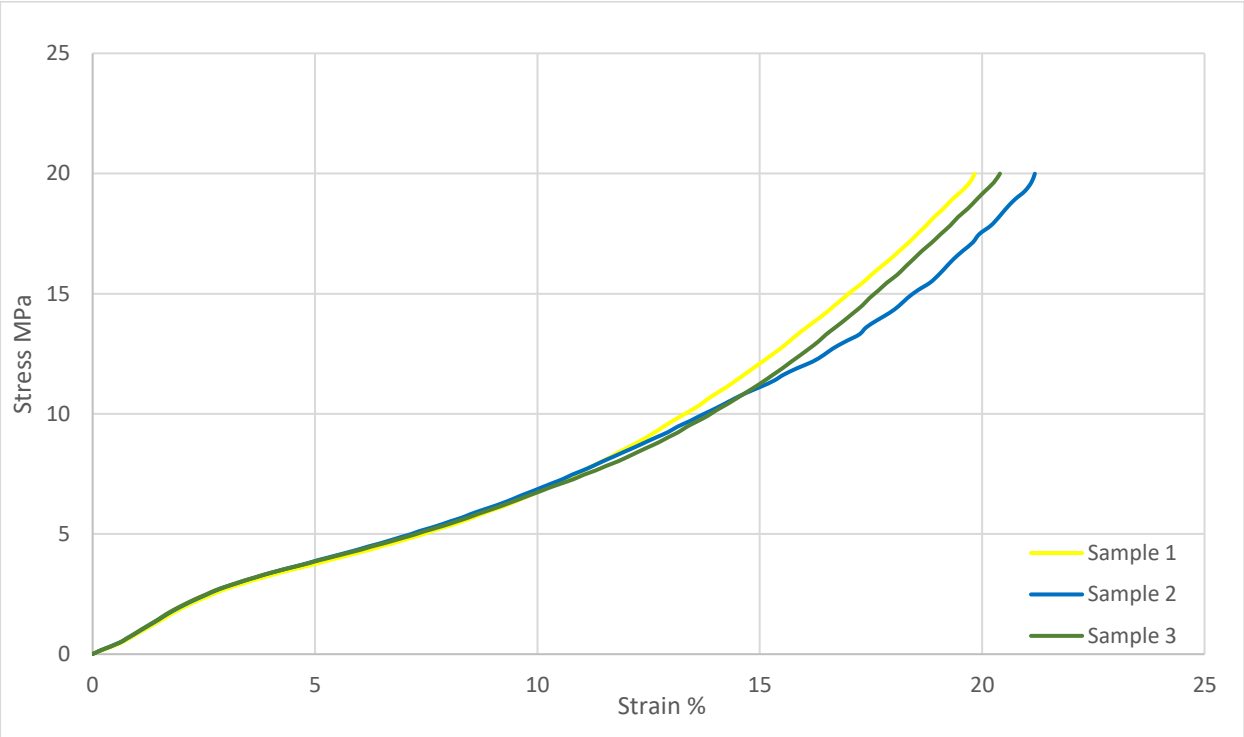

Figure 3. 18: **Uniaxial testing stress-strain for the composite specimens loaded parallel to weft fibre direction (EXA-1180).**

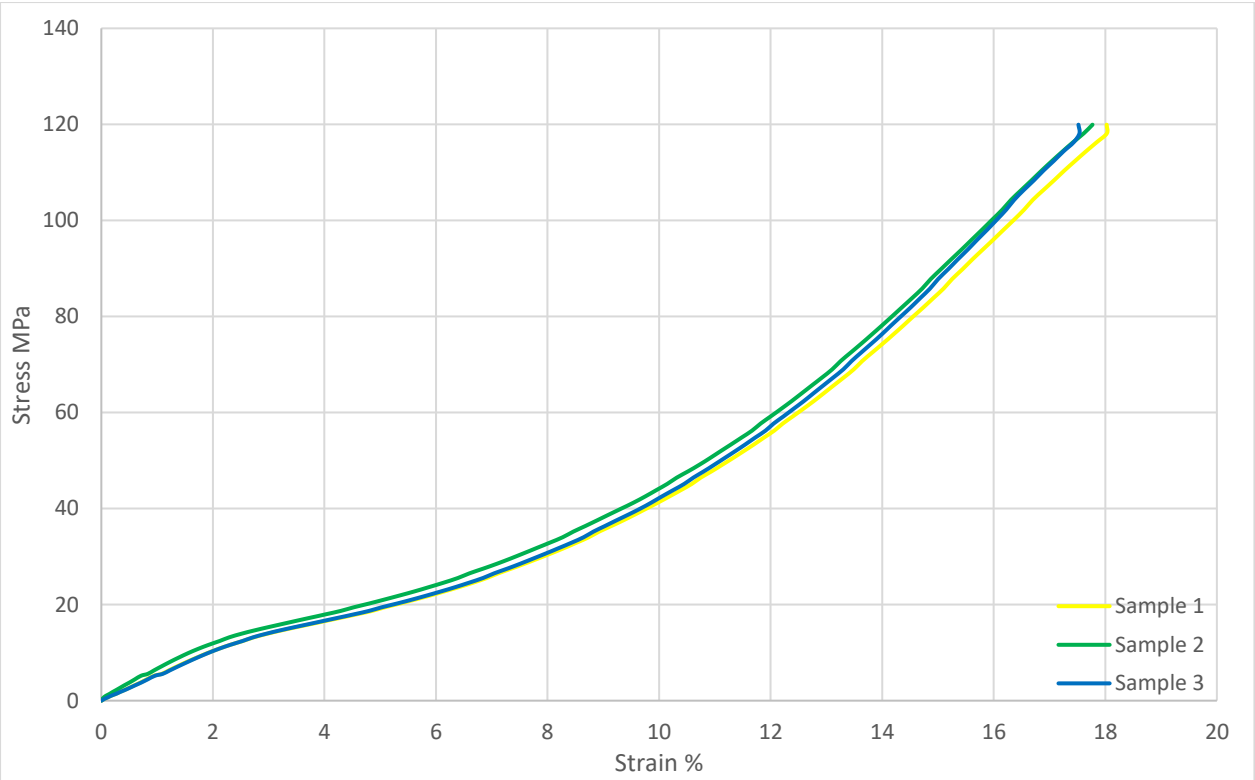

Figure 3. 19: **Uniaxial testing stress-strain for composite specimens loaded parallel to weft fibre direction (EXA-1182).**

Figure 3.20 shows the stress-strain curves of all different samples loaded in different directions. For comparison reasons data is only displayed up to a maximal applied load of 3000 N for all samples.

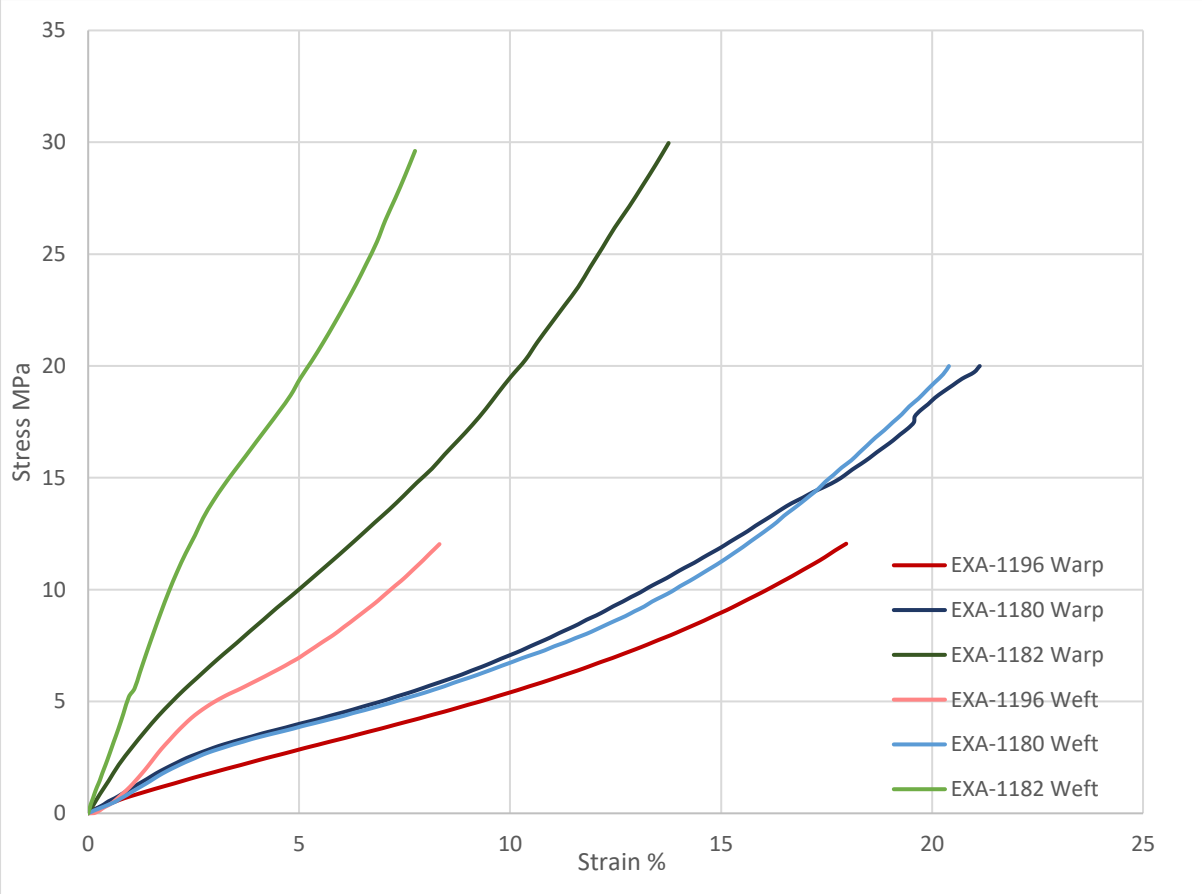

Figure 3. 20: Uniaxial testing stress-strain for composite specimens of all different materials

The average values for a strain in the weft and warp directions for EXA-1196, EXA-1180, and EXA-1180, are respectively shown in Table 3.6 for maximum load. Both sample orientations demonstrate nonlinear (hyperelastic) behaviour for the three different materials.

Table 3. 6 Strain for the materials.

Materials	Warp	Weft
EXA-1196	26%	12%
EXA-1180	23%	21%
EXA-1182	51%	18%

Figures 3.14 to 3.19 show stress-strain curves obtained from each three specimens of the different samples mounted parallel to warp fibre direction and weft fibre direction. The three

samples within each of these figures were cut from the same composite, mounted in the same direction, and thus ideally should show the same or very similar experimental results. Variations within the experimental results of these samples stem from random errors; the size of these variations is a good indicator for the homogeneity, reliability and repeatability of the experiments. Experimental aximal results lay between 23.8% and 25.9% for the EXA-1196 samples, between 24.2% and 28.2% for the EXA-1180 samples and between 50.6% and 55.5% for the EXA-1182 samples. These were mounted in parallel to the warp fibre directions, showing a statistic range of 2.1%, 4.0% and 4.9% respectively **.**Experimental aximal results lay between 12.2% and 12.7% for the EXA-1196 samples, between 19.8% and 21.2% for the EXA-1180 samples and between 17.5% and 17.8% for the EXA-1182 samples. These were mounted parallel to the weft fibre directions, showing a statistic range of 0.5%, 1.4% and 0.3% respectively. Notably, the homogeneity of the strain results is generally better for samples measured in the weft fibre direction than for samples loaded parallel to the warp fibre direction.

Figure 3.20 shows significant differences between the strain values obtained from measurements conducted parallel to the weft fibres and measurements conducted parallel to the warp fibres in the materials EXA-1196 and EXA-1182. The strain values corresponding to certain stress are lower in the weft fibre direction, the material expands less, the curves are steeper in the gradient, Young's modulus is higher, so as a conclusion, samples mounted parallel to the weft fibre direction show a much stiffer behaviour than the same samples mounted parallel to the warp fibre direction. As demonstrated in Table 3.5, the strain in the warp direction was more than twice that in the weft direction when tested under maximum load.

Interestingly, sample EXA-1180 is different and does not follow this trend. The stress-strain curves of this sample mounted parallel to the warp fibre direction and parallel to the weft fibre

direction look almost identical in shape and gradient. As reported in chapter 3 and particularly demonstrated in Figures 3.1, 3.2 and 3.3, material EXA-1180 is different from the other two samples in the optical appearance of the cut planes parallel to the weft and warp fibre directions. The distinctive wave-shaped pattern of the warp threads, clearly visible in the other two samples is hardly visible in sample EXA-1180. Furthermore, after removal of the elastomer matrix with a knife, it becomes apparent that the warp and weft fibres in this sample are strongly interlaced; the whole fibre structure seems denser. All of this makes the warp and weft direction more similar in their optical appearance and might explain why the mechanical differences between weft direction and warp direction are less pronounced in this sample.

In addition, as expected, the elasticity of the composite is a function of the thickness of the sample and the fibre content of the composite. Sample EXA-1196, the thickest sample (5mm) with the lowest fibre content (10.5%) shows a greater elasticity, a higher strain value at the same stress compared to the thinner sample EXA-1182 (2mm) with the highest fibre content (18.1%).

Young's modulus (E) gives the relation between stress and strain in elastic materials and is a useful property for modelling. The elastic modulus for the uniaxial tensile test is defined as the ratio between stress and strain during elastic loading. The four types of elastic modulus in the tensile test are tangent, initial tangent, chord and secant. The behaviour of materials that exhibit nonlinear elastic stress-strain behaviour depends on the stress or strain application regime used (ASM, 2004; Mamlouk and Zaniewski 2011). The quantity (E) are described as primary and secondary chord modules as given by equation (3.1).

Figures 3. 21 and 3.22 show the uniaxial tensile stress-strain for specimens loaded parallel to the weft and warp fibre directions. Using a Zwick Z020 universal testing machine, a maximum

load of 6000 N was applied to samples for each composite. Table 3.6 summarises Young's modulus for the fibre-filled composite materials examined:

$$E = \frac{P_u - P_l}{A \times (\varepsilon_u - \varepsilon_l)} \tag{3.1}$$

E is the primary and secondary chord modulus as defined in figures below.

A is the cross-sectional area.

P_u is the tensile load at upper strain limit.

P_l is the tensile load at lower strain limit.

ε_u is the upper strain limit.

ε_l is the lower strain limit.

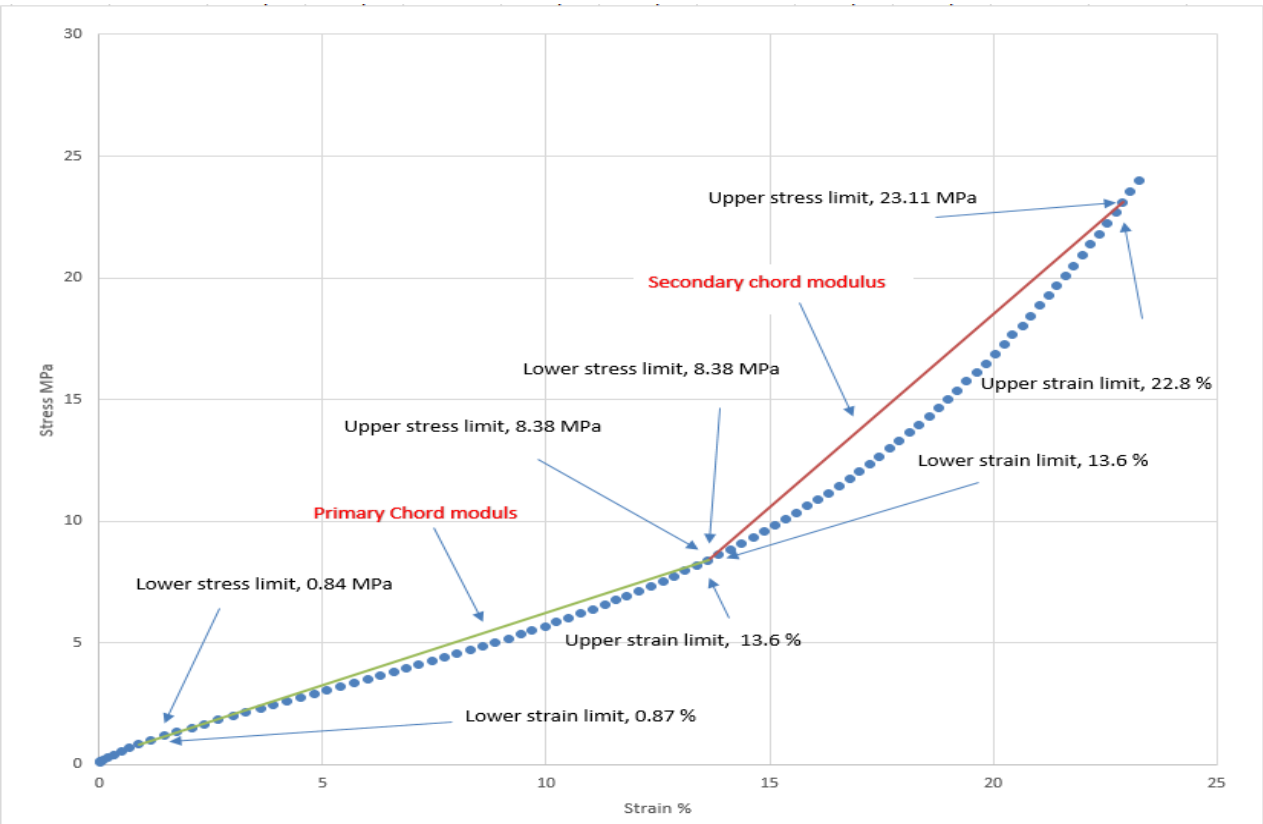

Figure 3. 21: Uniaxial tensile stress-strain graph for composite specimens loaded parallel to the warp fibre direction.

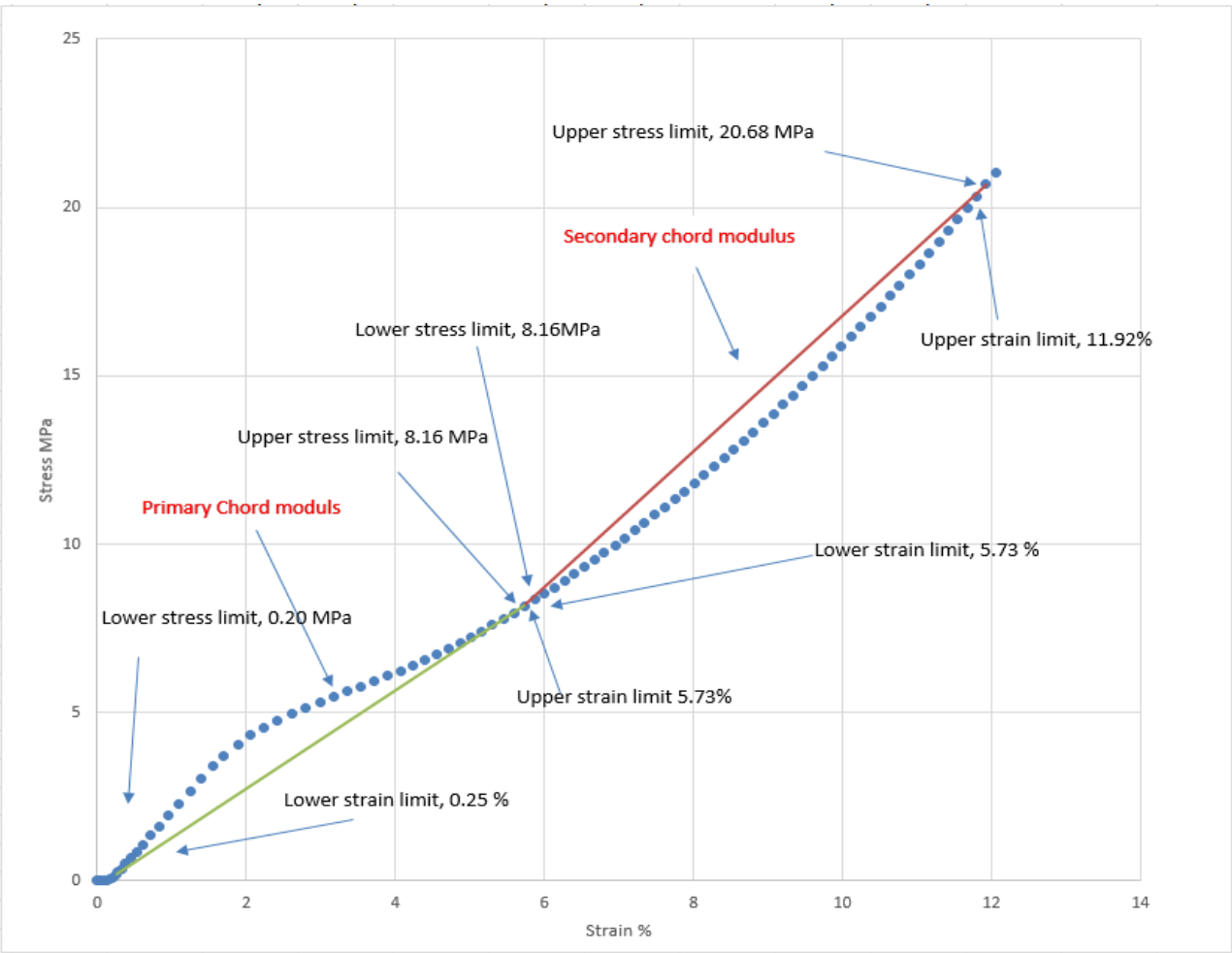

Figure 3. 22: Uniaxial tensile stress-strain graph for the composite specimens loaded parallel to the weft fibre direction.

Table 3. 7 Young's modulus.

Young's Modulus	The thickness of the materials	Weft direction of loading	Warp direction of loading
Primary chord modulus	EXA-1196	1.6 N/m^2	0.59 N/m^2
Secondary chord modulus		2 N/m^2	1.6 N/m^2
Primary chord modulus	EXA-1180	0.67 N/m^2	0.58 N/m^2
Secondary chord modulus		1.17 N/m^2	1.15 N/m^2
Primary chord modulus	EXA-1182	2.4 N/m^2	2.50 N/m^2
Secondary chord modulus		6.2 N/m^2	6.25 N/m^2

Table 3.2 shows that the composites exhibit a higher modulus when loaded parallel to the weft fibre direction rather than to the warp fibre direction.

Figures. 3.23 to 3.25 show samples loaded parallel to the weft for different thicknesses of EXA-1196, EXA-1180, and EXA-1182, respectively. Figures 3.26 to 3.28 show the samples loaded parallel to the warp fibre directions using the virtual strain gauge for the calculations of Poisson's ratio. However, those values converge when the force is increased. The highest Poisson's ratio for the samples loaded parallel to the warp, and weft direction for the different composite materials as calculated by the video gauge are shown in Table 3.3. As previously mentioned, the video gauge processes many measurements at the same time. In addition, Poisson's ratio is theoretically calculated from equations (3.2) and compared with the result obtained from the video gauge for the (EXA-1196) shown in table 3.7

Table 3. 8 Poisson's ratio of different materials.

Materials	Weft direction of loading	Warp direction of loading
EXA-1196	0.18	0.36
EXA-1180	0.16	0.33
EXA-1182	0.16	0.34

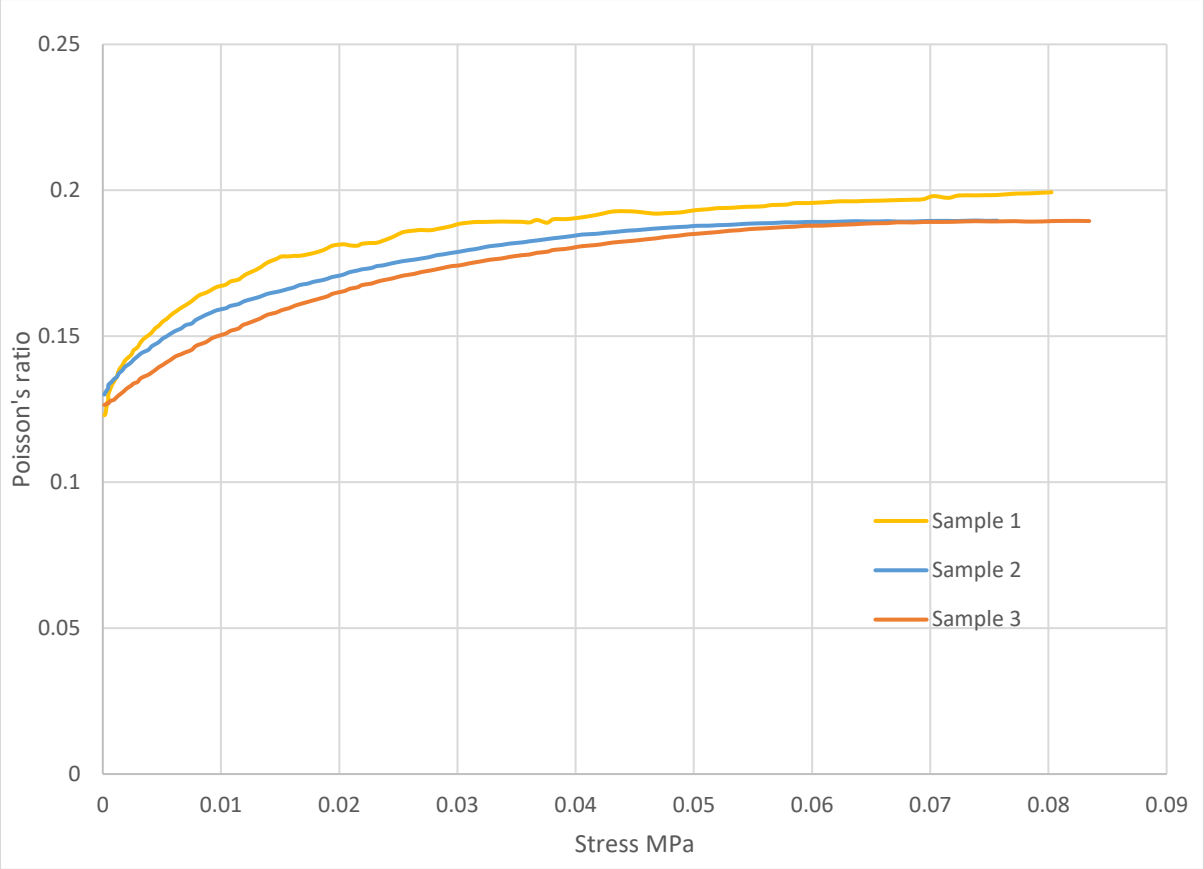

Figure 3. 23: Poisson's Ratio for the composite specimens loaded parallel to the weft fibre direction (EXA-1196).

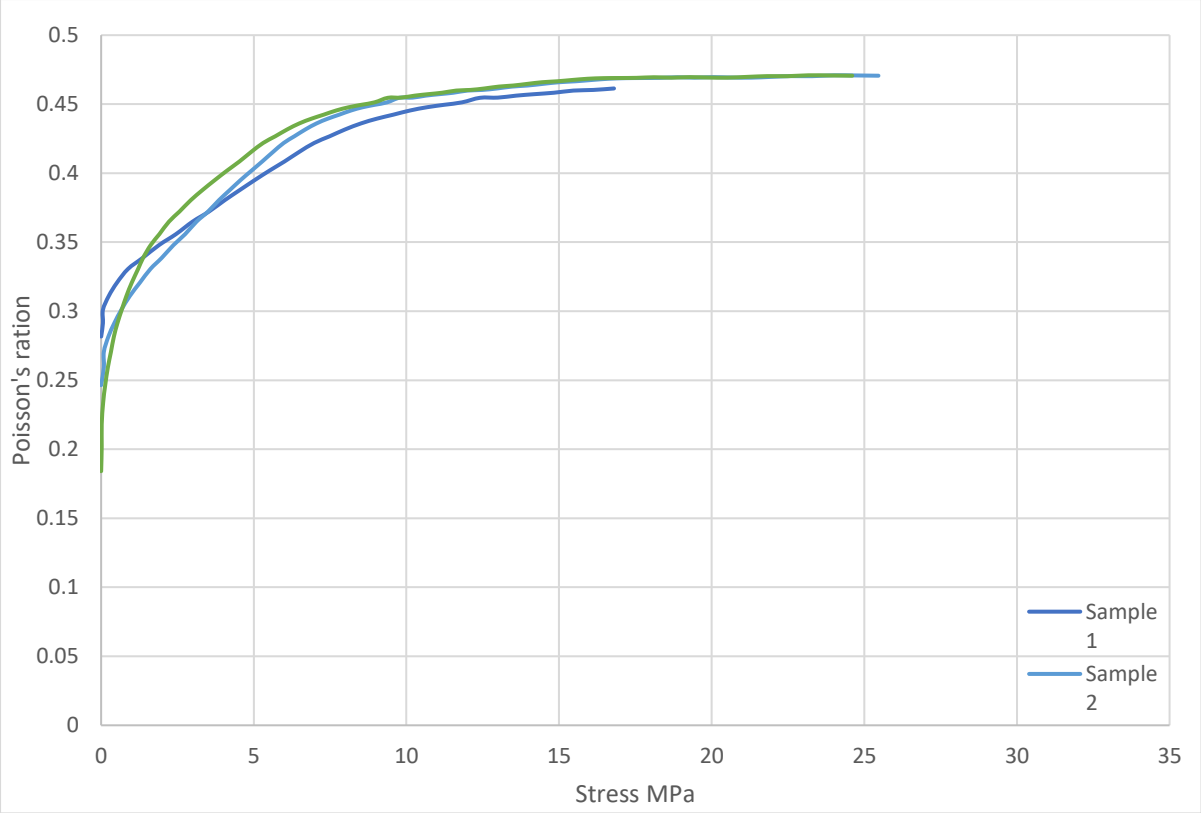

Figure 3. 24: **Poisson's Ratio for the composite specimens loaded parallel to the weft fibre direction (EXA-1180).**

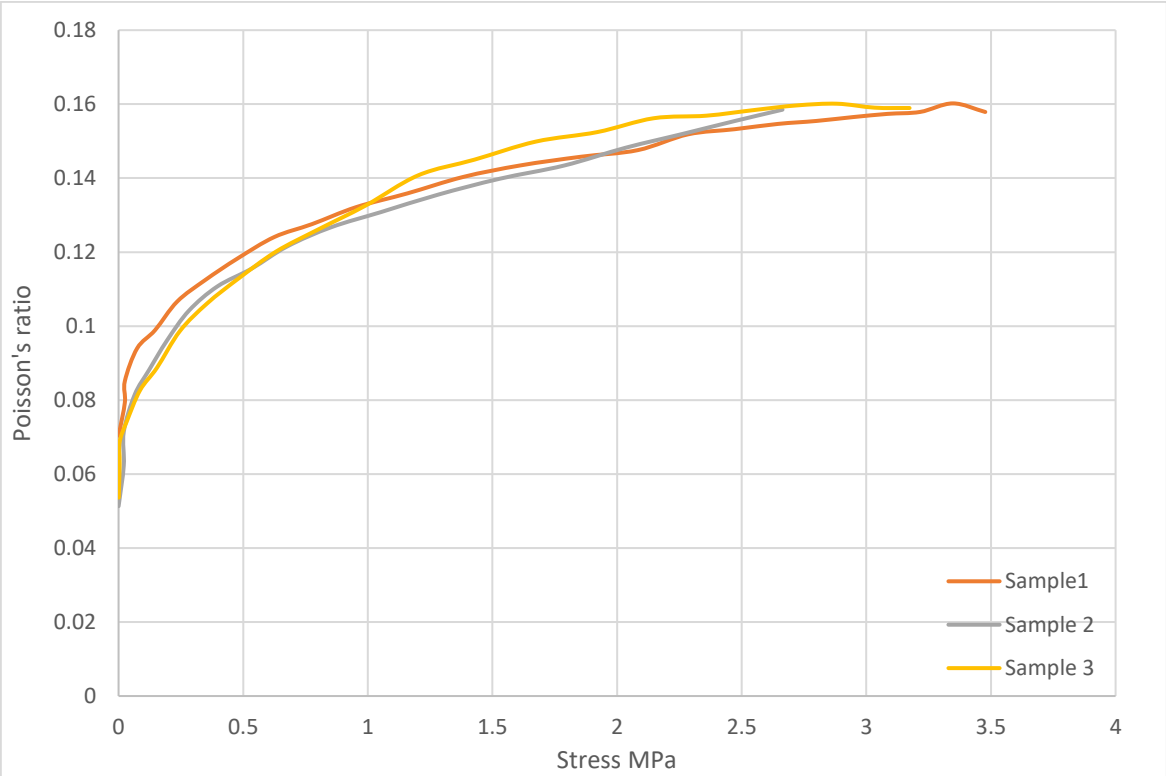

Figure 3. 25: Poisson's Ratio for the composite specimens loaded parallel to the weft fibre direction (EXA-1182).

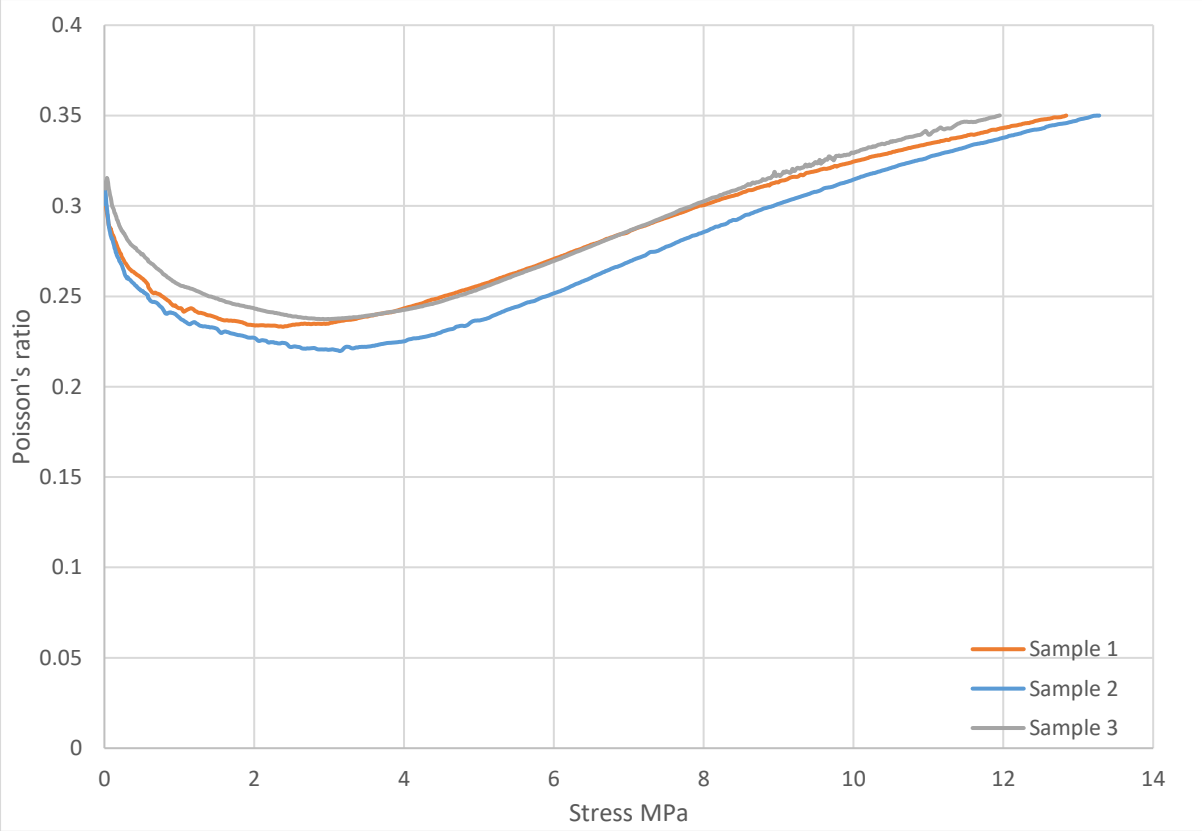

Figure 3. 26: Poisson's Ratio for the composite specimens loaded parallel to the warp fibre direction (EXA-1196).

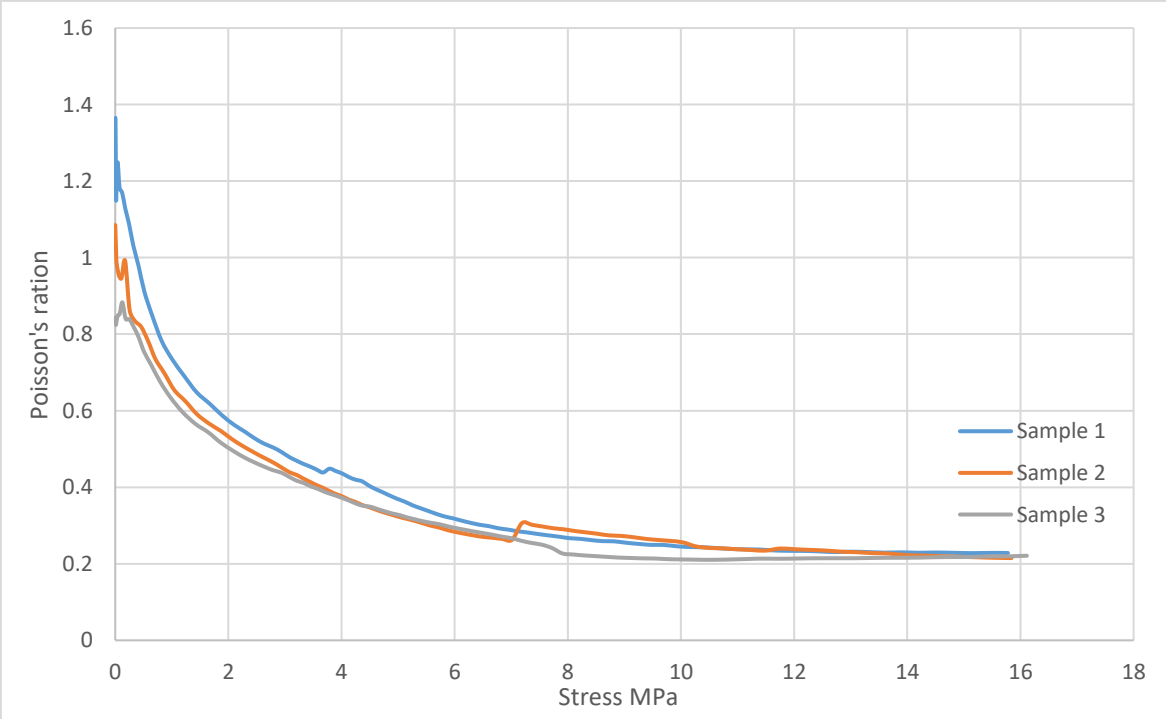

Figure 3. 27: Poisson's Ratio for the composite specimens loaded parallel to the warp fibre direction (EXA-1180).

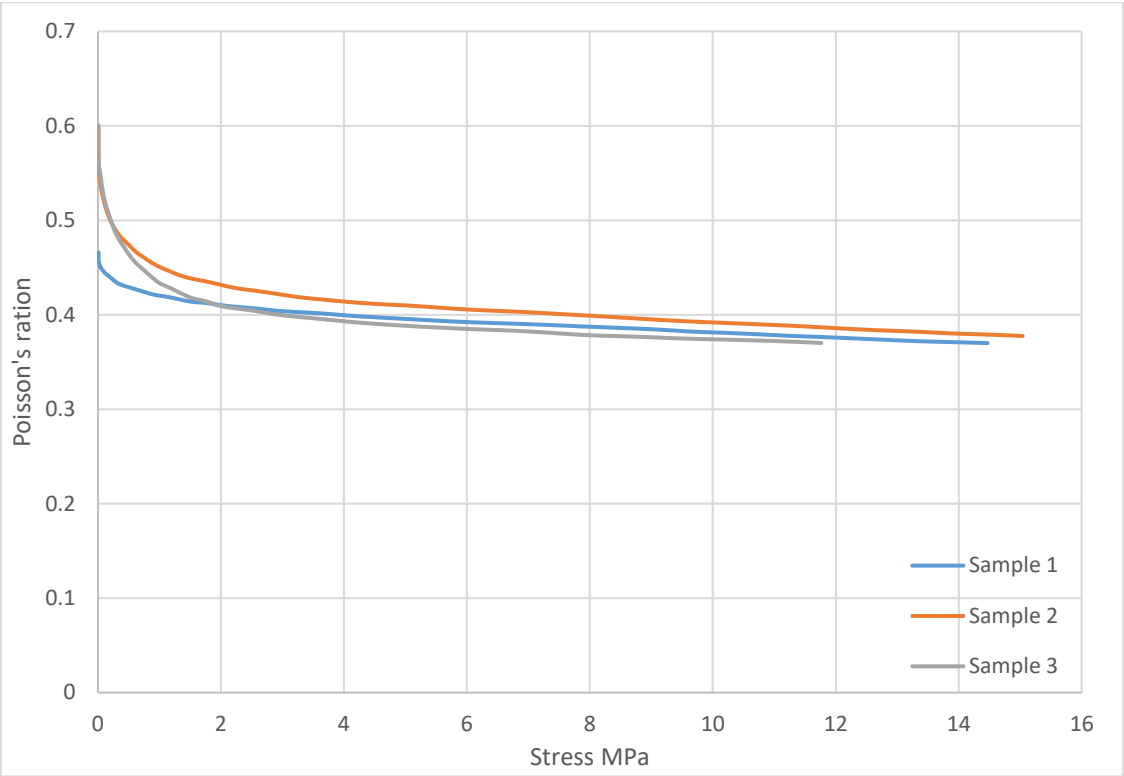

Figure 3. 28: Poisson's Ratio for the composite specimens loaded parallel to the warp fibre direction (EXA-1182).

Literature values for Poisson's ratio lying in the range of 0.2 to 0.5 for similar materials to those contained within the composite bracket the measured values obtained in this study (Hursa et al., 2009; Kraft et al., 2014).

From the improvement in the potential for the fabric's transverse motion, increasing the amplitude of the warp crimp inevitably leads to an increase in Poisson's ratio (Figures 3.18, 3.19 and 3.20).

A woven fabric's lateral contraction can cease for either of two reasons: (1) termination of the flattening of yarn crimp in the stretching direction; (2) when no space remains between adjacent threads. However, if the transverse deformation lies outside Poisson's ratio (between the material's transverse and longitudinal deformation), the ratio has no functional significance.

The impact of the fabric's structure arises from the interaction between the warp and weft yarns, where the mechanical parameters are recorded as the Poisson's ratio.

A Poisson's ratio is not constant and changes with each extension because of the anisotropic nature of the fabric. The fabric's behaviour primarily influences the pattern and shape of the Poisson's ratio curve when there is an extension in the lateral direction. During fabric extension, there is a strong exponential relationship between warp and weft crimp. Textiles with greater yarn density have a higher Poisson's ratio.

3.7 Full-Field Strain Measurements

Full-field optical strain measurements have recently begun to be used in textile deformity research. Video gauge offers qualitative and quantitative information on the homogeneous deformation of an object surface, especially for tensile tests. This can generate two-dimensional (2D) surface strain maps of areas of interest and provide comprehensive data enabling accurate statistical analysis between data sets.

During the tensile test, surface deformations caused by external loads were digitized as phase maps (corresponding to the changes on the grating). Strain measurements have greater uniformity and approximately the same values in the strain map (corresponding to the sample images at maxim deformation).

2D strain maps of similar sizes were created for tensile tests of different samples, where height ranged from 1195 to 1283 pixels and width ranged from 708 pixels to 796 pixels. At a working distance of 660 mm, these translate into dimensions projected onto samples surfaces: height 54mm to 58mm and width 32mm to 36mm. The chosen grid spacing in the tensile testing experiments was 20 pixels, which gave 38 horizontal and 62 vertical nodes within the strain

map. Given the size of the virtual map, nodes providing strain measurements were located at 0.9 mm from each other on the sample surface.

During the tensile test, surface deformations caused by external loads were digitized as phase maps (corresponding to the changes on the grating). Also, this test approved the tensile test above and to get more information about the surface for the three composite specimens. Strain measurements have greater uniformity and approximately the same values in the strain map (corresponding to the sample images at maxim deformation).

Typical examples of the 2D strain maps obtained are shown in Figs. 3.29 and 3.30 for specimens loaded parallel to the warp and weft fibre direction, respectively, of the three different composites. It maps the parallel strain (ε_{yy}) on materials at a tensile load of 6kN. To compare the strain distribution between materials, when mounted parallel to the warp and weft directions, the colour coding of strain in all 6 maps was between a minimum of 0 % (violet) and a maximum of 32 % (red). Figures 3.30 and 3.31 confirm the trends visible in graph 3.31. Firstly, at a load of 6 kN, the strain values of materials EXA-1196 and EXA-1182 are significantly higher when loaded in parallel to the warp fibre direction than to the weft fibre direction. Secondly, the thinner EXA-1182 material shows a higher strain at the same load than the thicker EXA-1196 material. Thirdly, material EXA-1180 shows noticeably different behaviour at the same load: at a thickness of 3 mm, it lies midway between the other two samples but has lower strain values than the other two samples when mounted parallel to the warp fibre direction, and higher strain values than the other two samples when mounted parallel to the weft fibre direction.

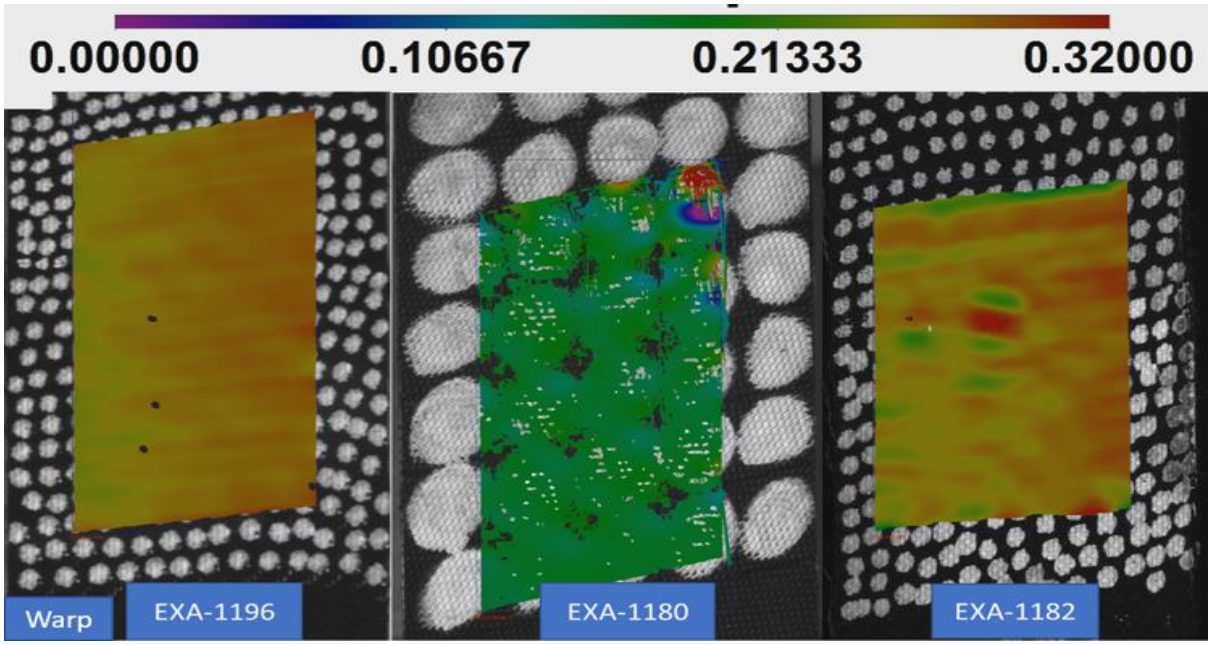

Figure 3. 29: **Strain maps for the composite specimens loaded parallel to the warp fibre direction.**

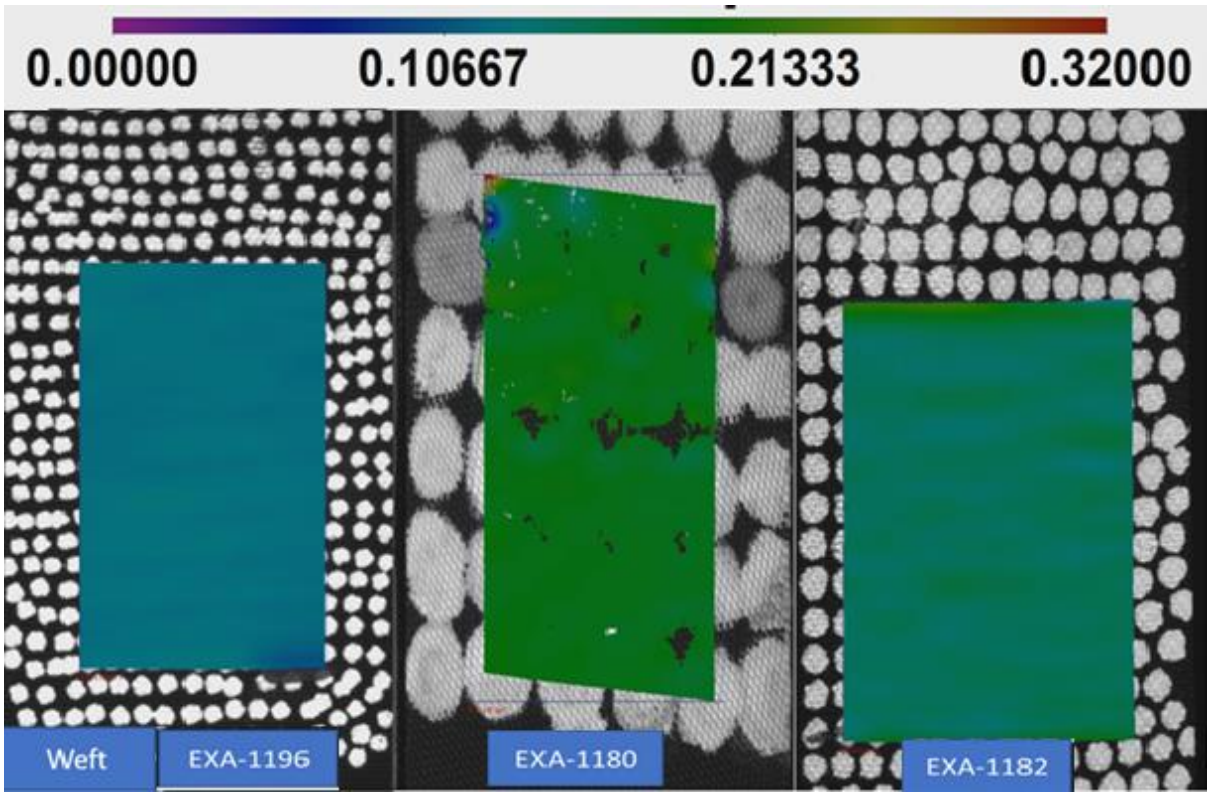

Figure 3. 30: **Strain maps for the composite specimens loaded parallel to the weft fibre direction.**

As mentioned in section 3.2.2, one of the advantages of video gauging over mechanical strain measurement techniques is that it is possible to not only measure the strain over the whole

sample but to explore the strain behaviour in different sections of the sample. This advantage is exploited to the full extent using 2D strain maps, where the sample surface is divided into lots of small areas. In this way, strain maps reveal strain distribution in the fabric deformation zone. Generally, the fabric strain distribution in the 3 mm and 2 mm thick samples EXA-1180 and EXA-1182 was more irregular compared to strain distribution in the thicker EXA-1196 fabric (5 mm), especially in the warp direction. The strain distribution was more even overall fabric locations of the 5 mm sample.

A reduction of the maximal strain used for the colour coding of the 2D strain map from 32% to 23% reveals that the strain distribution in the EXA-1182 sample mounted parallel to the weft fibre direction is not as homogeneous as expected, shown in Figure 3.31. A general area of 16-17 % strain contains insular spots of 3-5 mm diameter, in which the strain is 22-23 %.

This shows a general weakness of the colour mapping in the 2D strain map. A large minimum to maximum interval is well suited to show the differences between different samples, but the smaller strain inhomogeneities inside one particular sample are lost to observation. On the other hand, a smaller minimum to a maximum interval of the colour coding reveals the inhomogeneities in one sample but is not suitable to compare different samples with largely different strain values.

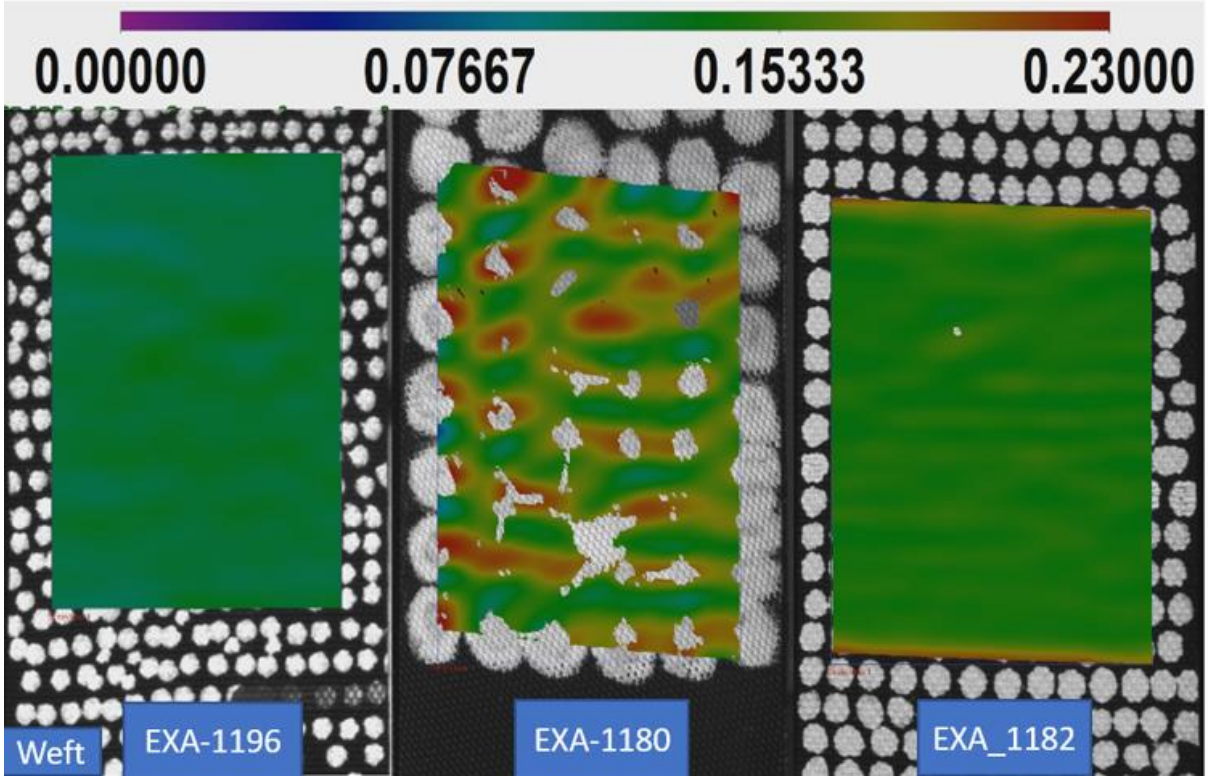

Figure 3. 31: **Strain maps for the composite specimens loaded parallel to the weft fibre direction, reduced colour mapping interval.**

The full-field strain offers an excellent method of studying strain distribution in composite materials during the deformation process. It provides strain measurements over the entire area under examination and offers more detail than strain gauges. Full-field strain measurements show the homogeneity of the sample during deformation, as shown above.

3.8 Conclusions

In this chapter, the mechanical properties of three different woven composite materials have been characterised by their performance in tensile tests upon on-axis specimens in the warp and weft directions. These tests were carried out at room temperature to assess the suitability of the material for structural applications. Where the application of other strain measurement techniques would have been difficult or unfeasible, with a video gauge non-contacting optical system, it was possible to take measurements at multiple points within the loaded gauge section and to gather data in real-time.

In these tests, video gauge proved to be a very useful non-contact technique for acquiring full-field strain maps, where the non-uniform strain was distributed throughout the samples. Values were obtained for strain, shear strain, and the Poisson's ratio. In that context, tested composites demonstrate the anisotropic material behaviour, whereby loading in the weft direction invokes higher stiffness than loading in the warp direction. That result is typical of fibre-filled elastomeric materials, where the fibre architecture dominates the load-deformation response.

For three different composites, observations were made of the nonlinear stress-strain response under uniaxial loading test conditions. As yarns in the loading direction remain relatively straight, crimp rises in transverse yarns due to crimp interchange. This has a major impact on the mechanical properties of the fibre-reinforced composite. Owing to a thickness effect, significant differences exist between the tensile properties of the materials. With matrix cracking and fibre trellising, the tests demonstrate nonlinear behaviour for the three composites loaded parallel to the warp and weft fibre directions.

Chapter Four

Several approaches are used by industry and academia to characterise the stress-strain shear behaviour of fibre-reinforced composite materials. This chapter describes how the shear response of fibre-reinforced composite materials with different thicknesses was investigated to assess the effect of in-plane forces on shear behaviour during two material characterisation tests: the picture frame test and planar tension test.

4.1 Introduction

It is understood that most rubber materials can be deformed to a significant extent even under low stress, where the subsequent mechanical behaviours are nonlinear. Most rubber materials can be deformed by a large strain even under low stress, where again the subsequent mechanical behaviours are nonlinear. This nonlinear mechanical behaviour varies between different deformation states. For example, the stress-strain curves for uniaxial tension, equi-biaxial tension and planar tension for the same type of rubber are distinctly different (Xia et al., 2005).

However, uniaxial data do not meet the requirement for accurate material characterisation in biaxial loading applications such as tubes or membranes. For such applications, a number of methods have been developed. The most commonly used are radial tension of a circular plate, biaxial tension of a thin square sheet, punching tests and bulge tests (Sasso et al., 2008).

Treloar suggested an experiment to allow for the determination of pure shear on a thin rubber-like sheet (Treloar, 1944). In extending experimental and theoretical analysis, Rivlin and Saunders established pure and straightforward shear states of incompressible isotropic material under considerable deformations (Rivlin, 1948. Rivlin and Saunders, 1951). Sasso et al. also carried out the analysis of hyper-elastic rubber-like materials by planar testing (Sasso et al.,

2008). The key obstacles in designing a test method for the calculation of shear properties are (1) the availability of pure and consistent shear stress in the specimen, and (2) a simple methodology for the determination of shear stress and strain (Wang et al., 2020; Hodgkinson 2000; Lee and Munro 1986).

It is not straightforward to determine the intralaminar shear strength of unidirectional polymer matrix composites. Difficulties arise in subjecting the unidirectional composite material to pure and consistent shear stress while avoiding complications, high costs, and the effect of other stresses. Several test methods to characterise the shear strengths of composite materials have been created, each with its own limitations (Odegard and Kumosa 2000). Hodgkinson (2000) addressed many widely used techniques for determining fibre-reinforced fibre in-plane shear properties. He also addressed the problem of increasing anisotropy and inhomogeneity of the substance that cause increases in pure shear. There is a recognised need for an easy, inexpensive test method to calculate the shear properties of these materials, due to the orthotropic nature of most composite materials. Among the methods used are the picture-frame and planar tension shear tests. The popularity of these tests rests with the relative ease of the production and testing of the specimens, the low cost, and the precision of the shear strength values so determined.

4.2 Shear deformation

Shear behaviour is one of the most significant mechanical characteristics that contribute to woven fabric performance and appearance. Due to anisotropy, shear properties of woven fabric are checked in various directions (Penava et al., 2015). The bias-extension test and picture-frame check are the most common approaches for the shear test as applied to woven fabrics. Spivak and Treloar (1968) represent one of the first experiments to study in-plane shear properties of woven fabrics using the bias extension method. Boisse et al. (2017) present a

detailed explanation of the bias-extension process for evaluating the in-plane shear modulus for synthetic composite reinforcements.

4.3 Planar tension test

The planar tension test is intended to test the sample in a state of deformation of the strain on the plane. The sample is thin with a width considerably larger than the height. The test imposes planar strain conditions on the test specimen by preventing its edges from contracting. All thinning appears in one direction (Wadham 2006) (through-thickness), as shown in figure 4.1 (Figure 4.2 shows the planar tensioning test setup.) However, there is no special standard for the planar tension test. An ideal planar tension test, with high aspect ratios, is very much shorter in the direction of the load than the width (Treloar, 1944; Miller and Kurt, 2000).

4.3.1 Test method description and specimen design

The planar tension test was carried out using a Zwick Z020 universal testing machine to a maximum load of 6000 N. The specimen was designed with a width of 200 mm and a length of 40 mm between the clamps. A 100 mm/min predetermined cross-head extension rate was used during the experimental procedure (BS 903-5:2004).

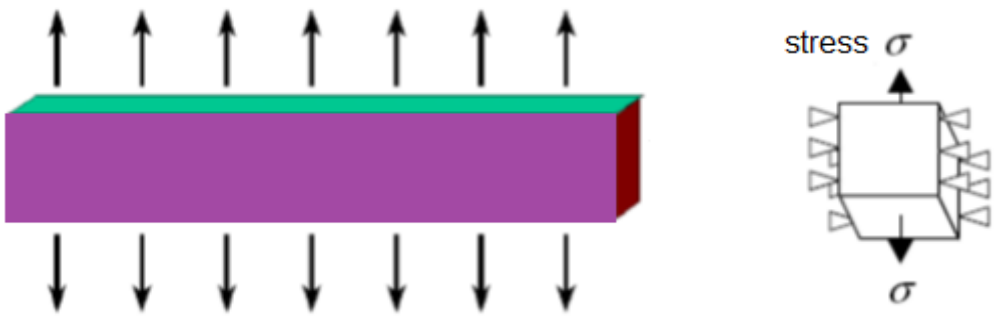

Figure 4. 1: **Planar tension schematic representation (Wadham, 2006)**

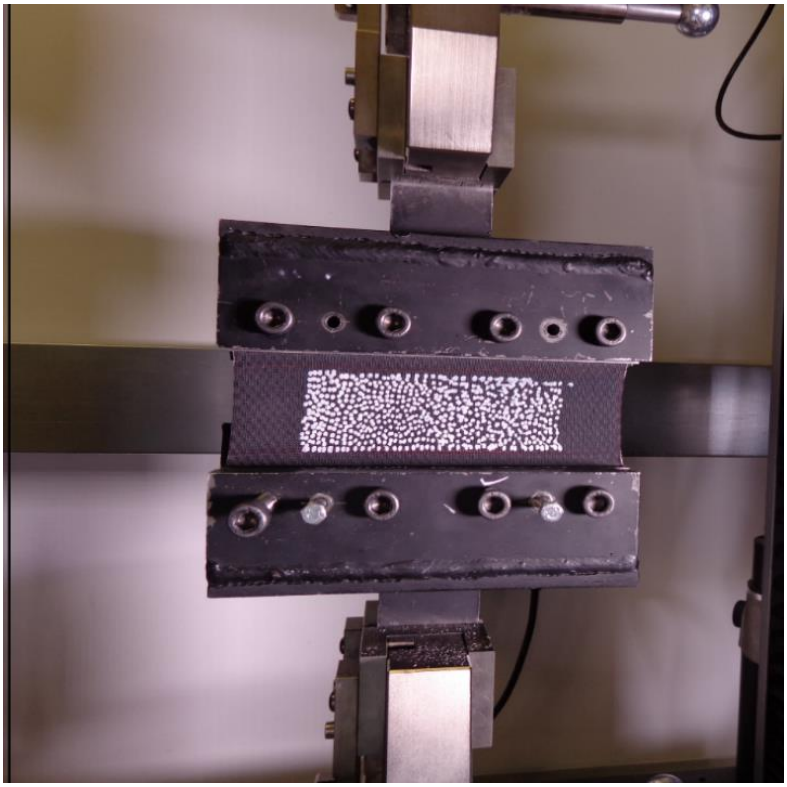

Figure 4. 2: **Planar tension test**

The specimens were securely installed and centrally located in the test machine clamp, with the long dimension perpendicular to the direction in which the force is to be applied. The tension of the specimen is uniform across the clamped width.

As shown in Figure 4.3, for high-strength fabrics which cannot be held in clamps, each specimen was placed around the pins and between the jaws to avoid slippage. As necessary, jaw padding was used. The clamps were tightened to distribute the holding pressure along the top (front) jaw clamping surface. Clamping too tightly could lead to sample damage at the front of the jaws; clamping too loosely could cause slipping or sample damage at the area of the back of the jaws and steel pins (ASTM, 2015).

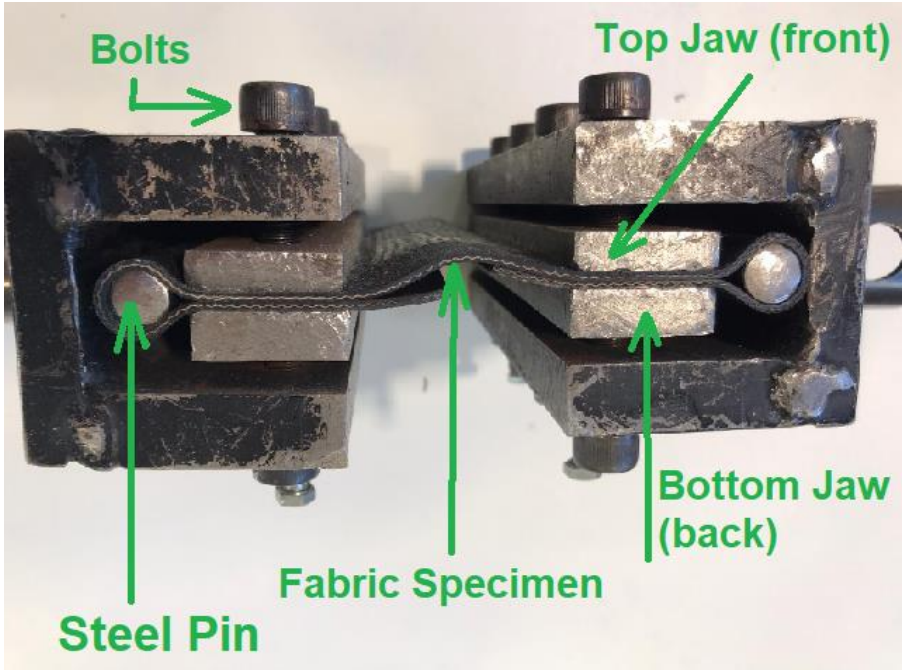

Figure 4. 3: **Schematic diagram of grips**

The shear strain was measured video gauging supported by digital image correlation (DIC). This method was also used to check for possible deboning or sliding at the sample metal interfaces. Video gauge has been described in detail in the previous chapter. The Video gauge system was developed to measure shear strain directly from the surface of a sample. Optical methods for shear strain measurement are ideally suited for these applications because the measurement is performed remotely without interfering with the versatile geometry of the specimen and with no need for any additional load operation. A similar technique has been used to test strains in hyperelastic materials similar to rubber (Potluri and Thammandra, 2007, Chevalier et al., 2001, Sasso et al., 2008, Palmieri et al., 2009). The software for the video gauging system had an internal option for the measurement and recording of shear stress, using the in-plane distortions of square-shaped strain gauge targets orientated at +45 and −45° to the axis of uniaxial tension.

For each material, six samples of the composite were tested, three in parallel to the weft, and three in parallel to the warp. (For materials details, see chapter three). Three were loaded in parallel to the weft fibre direction, and three in parallel to the warp fibre direction. In the wide strip sample, uniaxial tension acting in the Y direction (with respect to the rotated video gauge element in Figure.4.4) generates a stress state equivalent to that of equal and opposite principal normal stresses acting on the element. Measured nominal stresses applied during testing can, therefore, be converted to their equivalent shear stresses by application of a factor of 0.5. The shear strain (γ) measurements were generated from video gauge locations within the constrained central region of the sample, from an area of dimensions 100 mm × 40 mm. In terms of shear strain, it is taken in the middle of the specimen for EXA-1196, EXA-1180 and EXA-1182.

4.4 Strain gauge rosette

A strain gauge rosette is an assembly of two or more similarly spaced gauge grids, arranged to record standard strains in various directions on the underlying surface of the test part (Micro-Measurements, 2008). For a typical rosette, three gauges would set at A = 0°, B = 45°, C = 90°. The three equations would then be solved. A typical strain gauge rosette is a mechanical device attached to the sample surface; in the case of video gauging used for strain measurement, three virtual gauges are performing the measurements.

$$\varepsilon_a = \frac{\varepsilon_x+\varepsilon_y}{2} + \frac{\varepsilon_x-\varepsilon_y}{2} \tag{4.1}$$

$$\varepsilon_b = \frac{\varepsilon_x+\varepsilon_y}{2} + \frac{\Upsilon_{xy}}{2} \tag{4.2}$$

$$\varepsilon_c = \frac{\varepsilon_x+\varepsilon_y}{2} + \frac{\varepsilon_x-\varepsilon_y}{2} \tag{4.3}$$

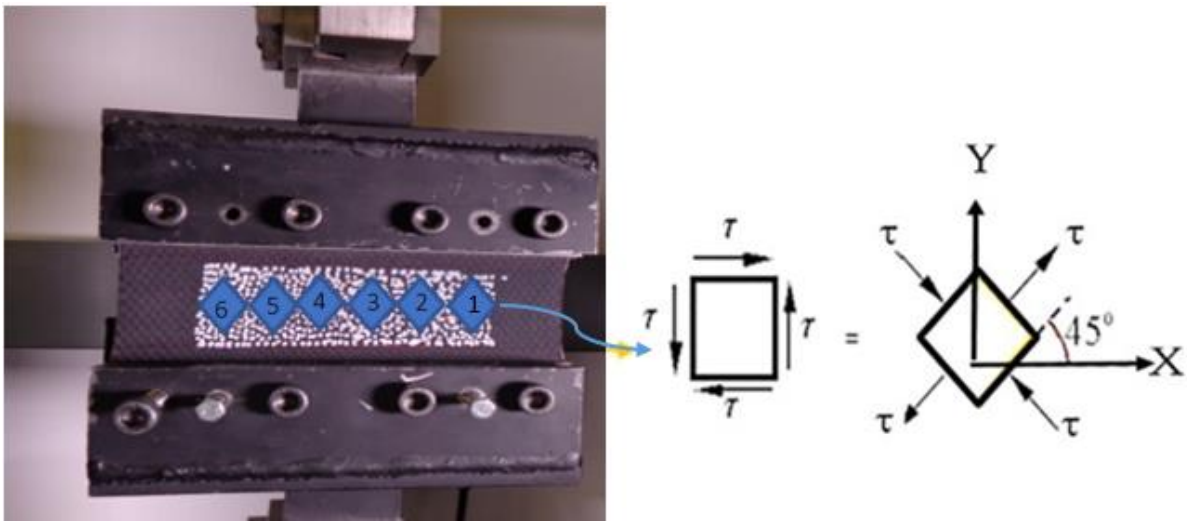

Figure 4. 4: **Wide strip (pure shear) specimen geometry showing the six video gauge locations and the equivalent stress state.**

Where ε_{45} is the normal strain at 45° to the x-axis, ε_x is the normal strain at x° to the x-axis and ε_y is the normal strain at y° to the Y-axis, as shown in the figure 4. 5.

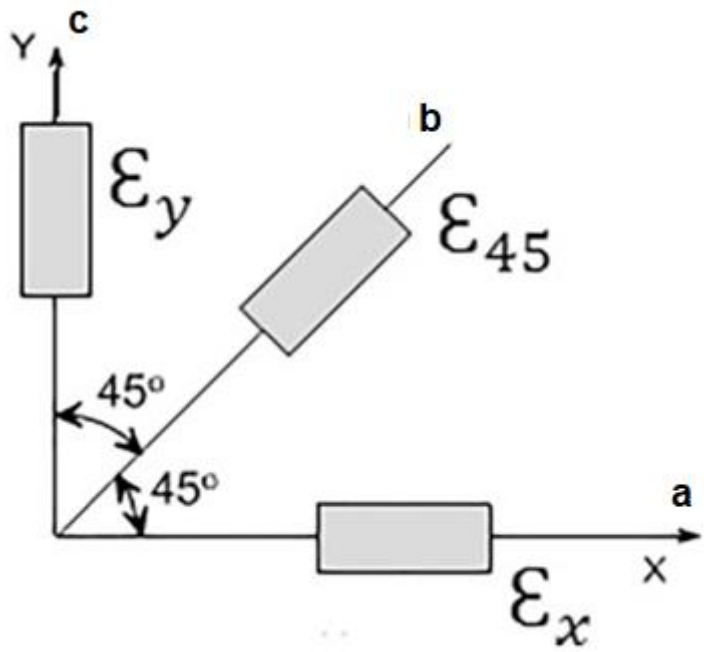

Figure 4. 5: **Strain gauge rosette individual gauge orientations.**

Solving equations (4.1), (4.2) and (4.3) of the strain gauge rosette is an alternative method to calculate the shear strain, which can be compared to the shear strain calculated in the conventional way, only using a 45° rotated target using equation (4).

$$\varepsilon_x = \varepsilon_a \qquad \varepsilon_y = \varepsilon_c$$

$$\gamma_{xy} = 2\,\varepsilon_{45} - \varepsilon_x - \varepsilon_y \tag{4.4}$$

One method for performing a pure shear test is identical to the planar test described above. Since the material is almost incompressible, a state of pure shear exists at a 45 °angle to the stretching direction (K. Miller., 2002). In that state, the specimen exhibits pure shear at an angle of 45°to the stretching direction (Nassiri, F., 2011).

Figure 4.6 compares stress-strain curves from four different positions of the EXA-1182 sample mounted parallel to the warp fibre direction. The shear strain at these four positions is calculated both directly and using a strain gauge rosette.

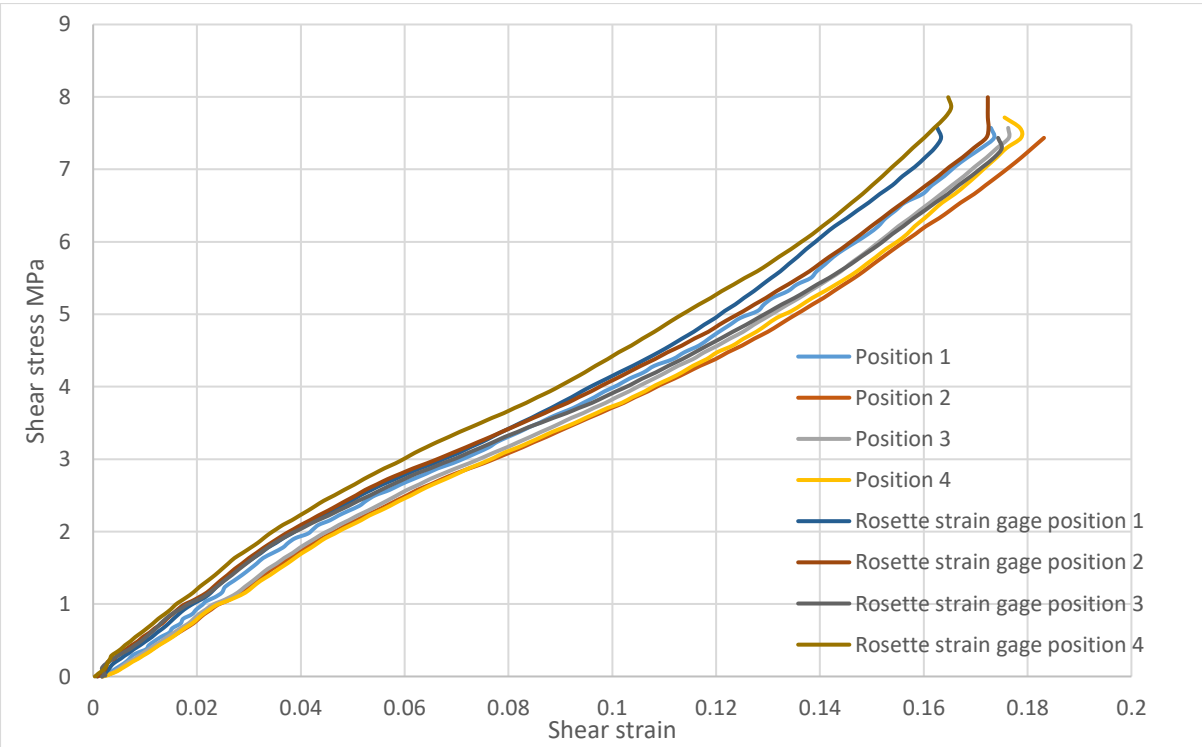

Figure 4. 6: **Shear strain versus shear stress from a rosette strain gauge for the warp direction of fabric loading, experimental results and calculations.**

The strain values calculated with the strain gauge rosette formulas were around 1% lower than the directly calculated strain values, but generally in good accordance.

4.4.1 Test setup and specimen preparation

One of the tests used to characterise the shear resistance of woven composite fabrics is the picture frame test, which can measure the shear behaviour of fabric across a wide range of shear angles, between 50°- 75°. In the picture-frame apparatus, two specimen orientations are possible. The direction of the warp fibre can be either + 45 ° or -45 ° to the axis of rising. If, for example, a -45 ° test is used to shear a specimen in a positive way, then a + 45 ° test would be a negative shear deformation. A schematic examination of the picture frame is provided in Figure 4.7. A tensile force is applied diagonally across opposite corners of the picture frame. This causes the picture frame to shift from an initial square configuration to a rhomboid. The clamped sample, therefore, experiences pure shear.

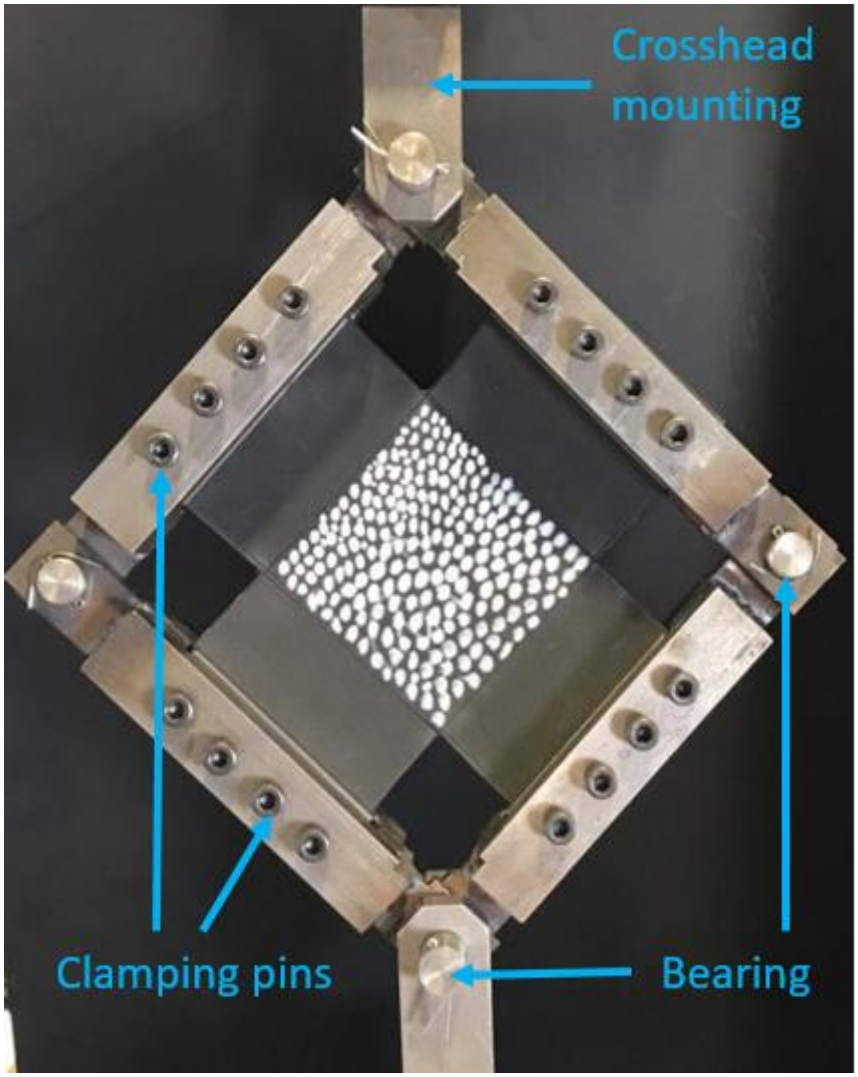

Figure 4. 7: Shear-frame test.

The loading rig, as mounted on a Zwick (Zwick GmbH) universal testing machine to a maximum of 2500 N, is shown in Figure 4.8. The specimen was cut into a cross shape, as depicted in Figure 4.9, and clamped to a square frame of 150 mm x 150 mm^2 at an initial direction to the frame arms of 0/90°. A steel test fixture was built with four arms linked together by four corner hinges with the upper and lower hinges attached to the load heads of the testing machine. The specimen was tested at a cross-head extension rate of 100 mm min-1, so making the two heads distinct from each other, thereby pushing the hinges and reducing the angle between the right and left sides as shown in Figure 4.6. McGuinness and O'Brádaigh (1997) proposed two ways of mounting the material by either clamping (for fabrics) or pinning

(for fibre-reinforced composites). In this study, the samples were securely clamped in the frame and against the gaskets under pressure from a set of bolts (Peng et al., 2004; Zhu et al., 2013).

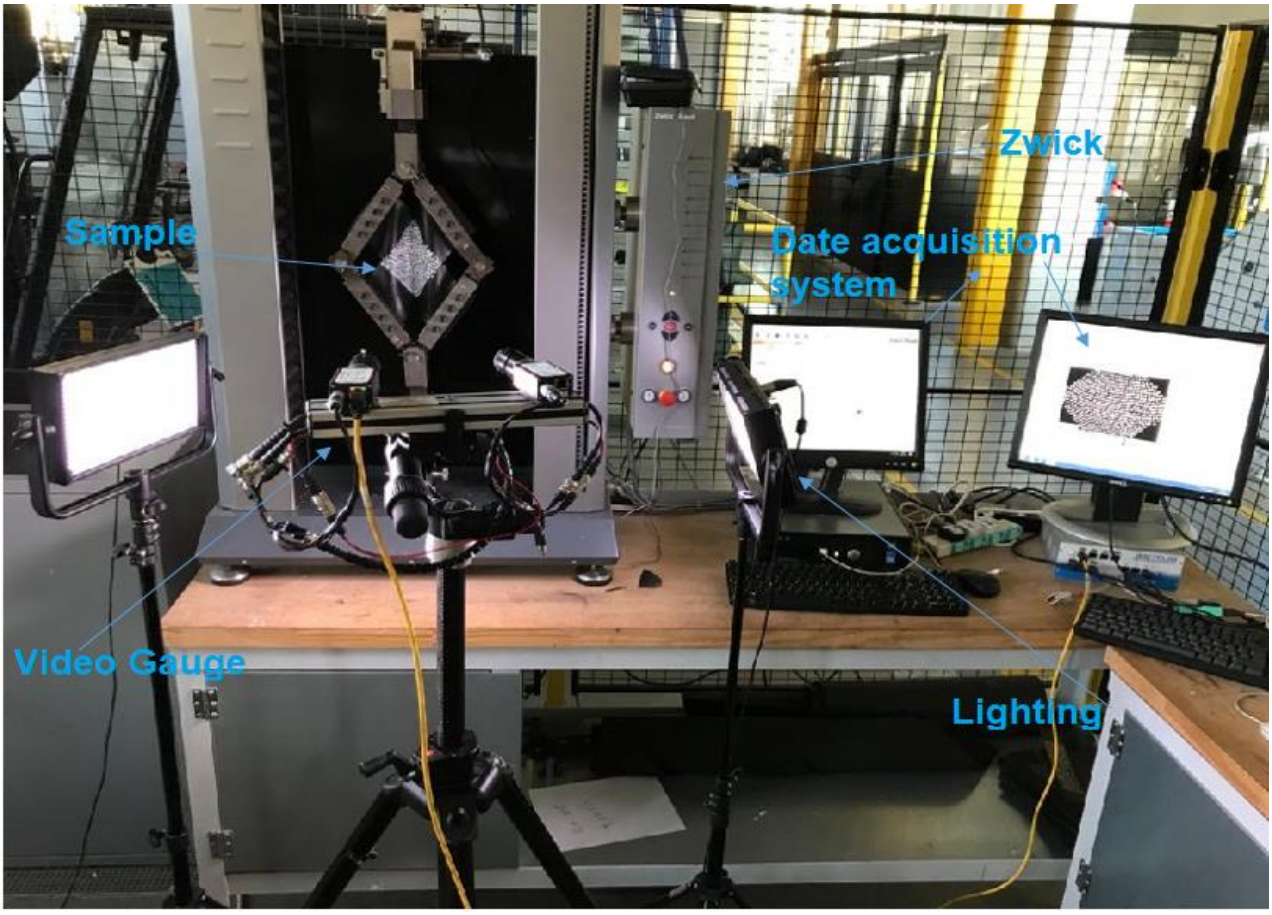

Figure 4. 8: **Experimental setup for the picture frame testing.**

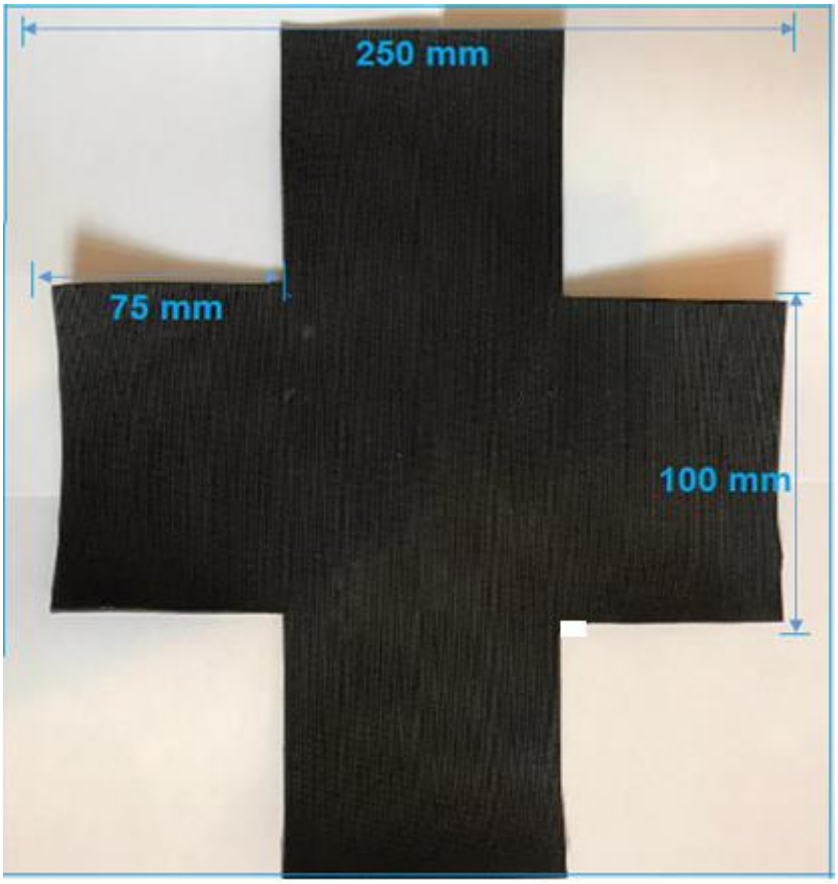

Figure 4. 9: Specimen shape and size.

The sample was clamped to the frame with the help of clamping plates to ensure that no slippage occurred on the metal gaskets between the sample and the frame. As the pins attached to the clamping plate could damage the fibre in the specimen, so affecting the result, additional metal sheets were added under a clamping plate (Boisse et al., 2017; Cao et al., 2008; DIN 2014; Lebrun et al., 2003).

4.4.2 Shear strain in Picture Frame tests

For woven fabric, the shear angle measures the change of the right angle between the warp and weft threading. The shear angle is a significant predictor of the draping quality of reinforced woven materials after deformation (Taha et al., 2013). Figure 4.21 shows the material at the beginning and the end of the shearing test. In the initial state, the yarns are orthogonal to each

other. Upon initiation of interplay shear deformation, the yarns begin to rotate and possibly slip, as two interlaced yarns slide over each other. Launay et al. (2008).

The shear response of woven fabric is different from that of metals and other homogeneous material sheets. The in-plane shear response, in particular, is dominated by the relative rotation of the two yarns. This action is responsible for many distinct features of woven fabrics as found during shear deformation. The shear response was investigated by testing the deformation of a dot pattern applied to the surface of the specimen using a video gauge. The yarns are orthogonal towards each other in the initial stage. During testing, all specimens experience relatively uniform shear deformation in their central areas (Zhu et al., 2013). During the rotation of the yarn, it is assumed that the load primarily reflects the frictional interaction between the adjacent yarns at their crossover points. Compression of fibrous assemblies is well known to be a nonlinear mechanism of increasing rigidity, which describes the dramatic rise in the shear stiffness of the deformation. Further deformation continues until fabric compaction begins (Fetfatsidis et al., 2012).

Härtel and Harrison (2014), and Cao et al. (2008) are among those who call shear angle determination and shear force "normalisation". The main task of normalisation is to transform the reported uniaxial load and displacement into a comparable parameter that represents the shear properties i.e., the shear angle and shear force per unit length. The shear strain in the sample is determined by the difference in angle between the warp and weft orientations (Boisse et al. 2017), which can be observed by geometrical inspection or optical measurement (camera monitoring process) (Cao et al. 2008; DIN 2014; Gatouillat et al. 2013; Harrison et al. 2004; Peng et al. 2004)

4.5 Test data and discussion

4.5.1 Stress-shear strain curves at different sample locations

During loading, the video gauge system was used to measure strain at six positions on the surface of each sample. Six discrete virtual/optical strain gauge regions (VGs 1-6) were defined on the sample surface, from which measurements of the shear strain response to tensile loading was obtained. Shear strain gauges 1 and 6 were placed at an equal distance from the edge of the sample. The same was done for gauges 2 and 5, which were closer to the centre, and for gauges 3 and 4, which were closest to the centre of the sample. For the majority of tests, the closer gauges were to the centre, the higher the shear strain for the same values of stress, as one might expect. Near centre positions 3 and 4 show the highest strain, outside positions 1 and 6 show the lowest strain, over the whole range of applied stress, as an example the stress-shear strain curves of EXA-1180 mounted parallel to the weft direction are displayed in Figure 4.10.

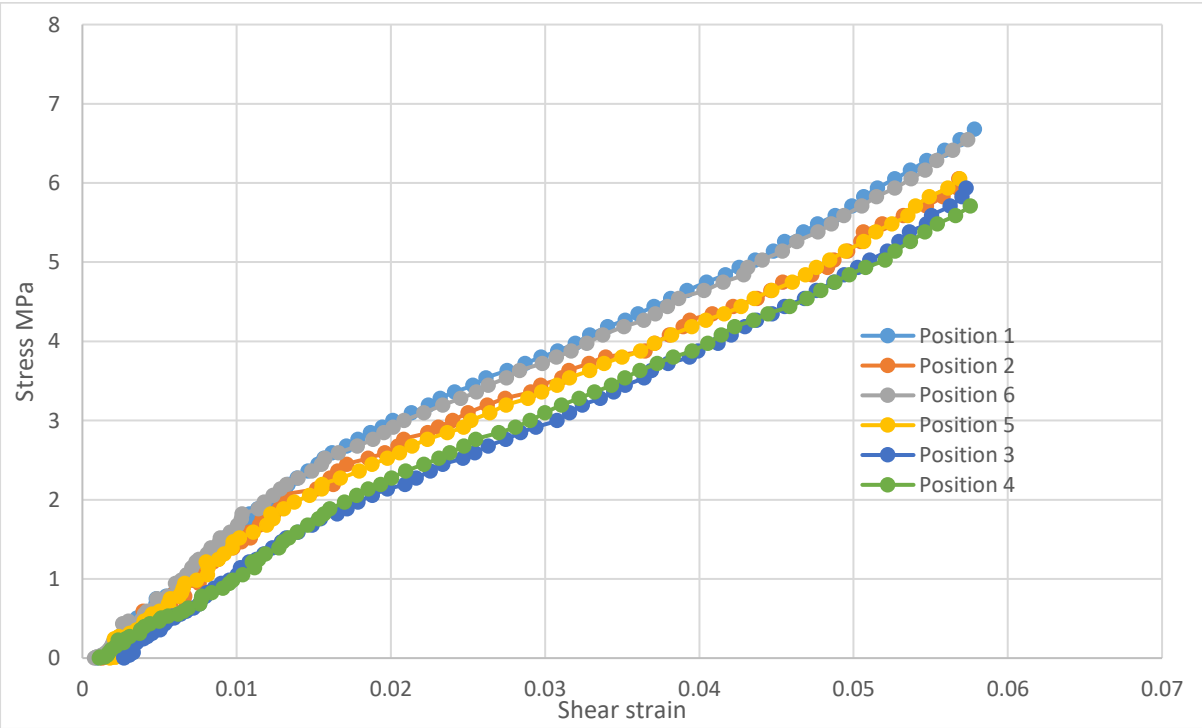

Figure 4. 10: Stress-shear strain curves derived from different sample positions of the EXA-1180 sample mounted parallel to the weft direction.

4.5.2 Shear stress – shear strain for different samples

Shear stress-shear strain results for different composite materials mounted parallel to warp fibre direction and weft fibre direction are shown in Figs. 4.11 to 4.16. These results are derived from a wide strip planar tension test with the shear strain measured by video gauging at a square-shaped target rotated by 45° and located at the centre of the sample.

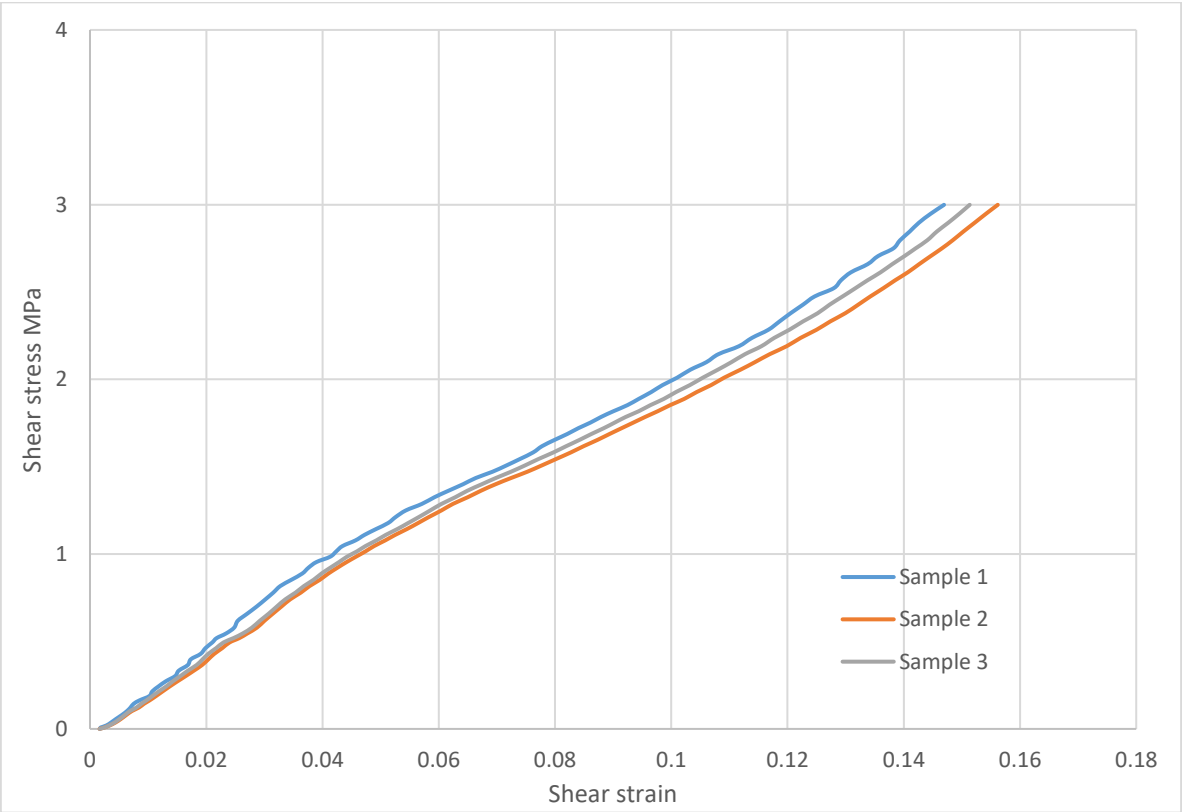

Figure 4. 11: Planar shear-oriented stress vs strain behaviour for fibre-filled composite specimens loaded parallel to the warp fibre directions of EXA-1196.

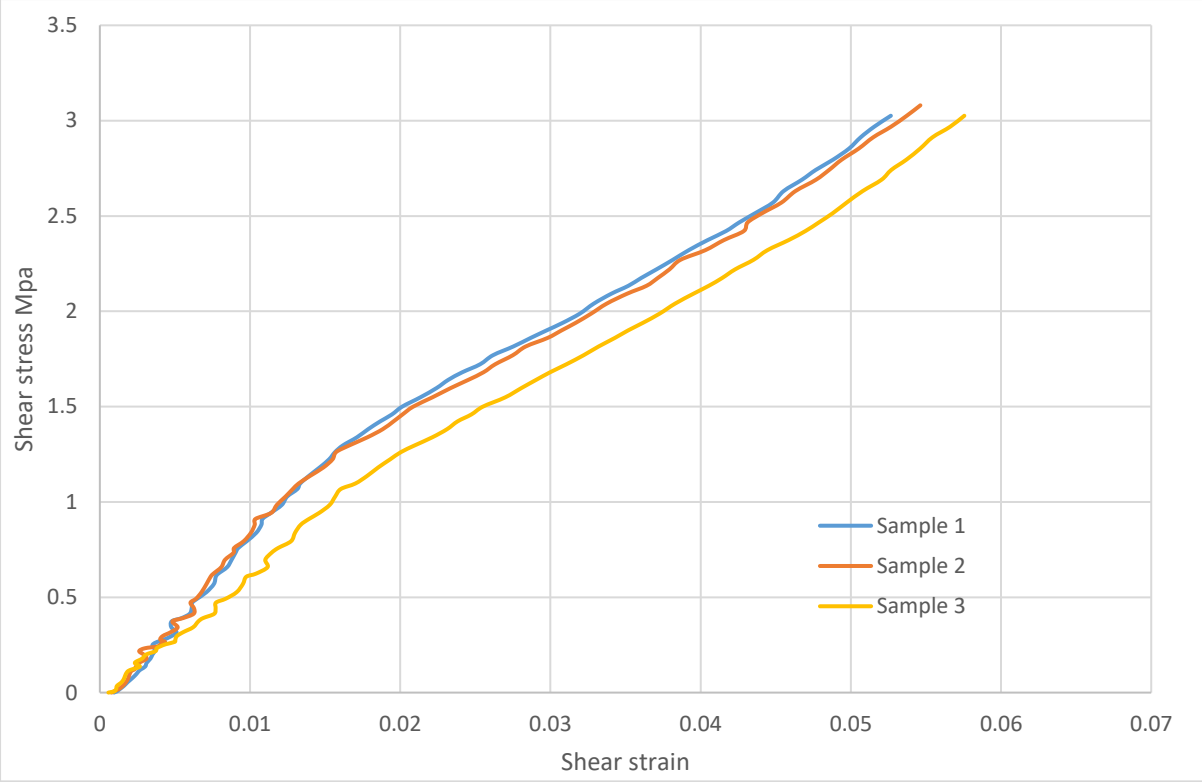

Figure 4. 12: Planar shear-oriented stress vs strain behaviour for fibre-filled composite specimens loaded parallel to the weft fibre directions of EXA-1196.

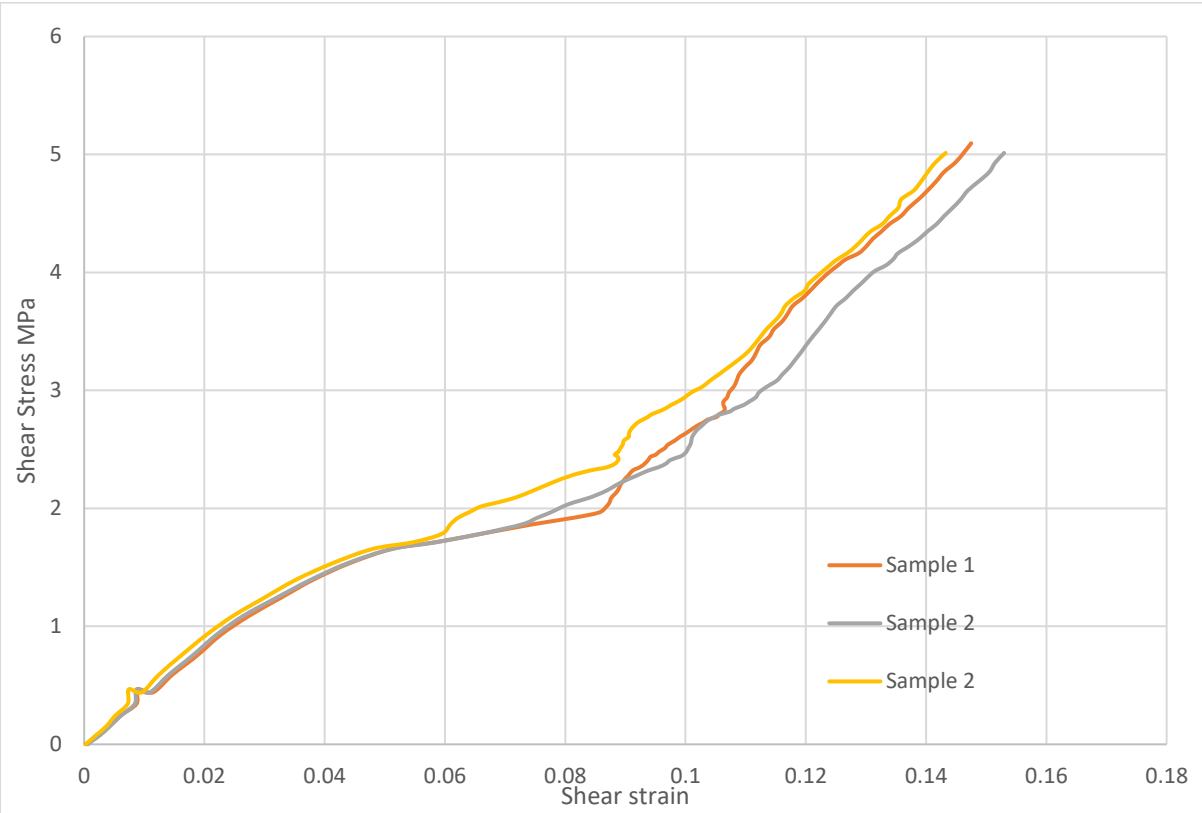

Figure 4. 7: Planar shear-oriented stress vs strain behaviour for fibre-filled composite specimens loaded parallel to the warp fibre directions of EXA-1180.

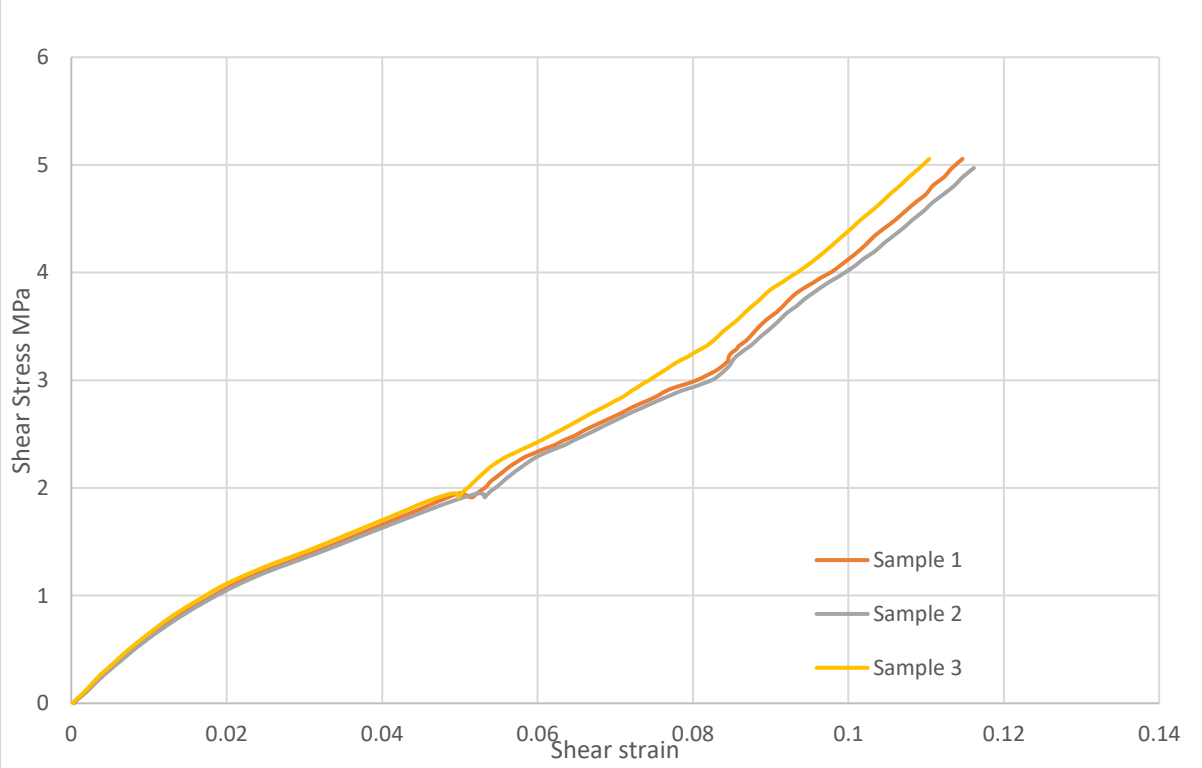

Figure 4. 8: Planar shear-oriented stress vs strain behaviour for fibre-filled composite specimens loaded parallel to the weft fibre directions of EXA-1180.

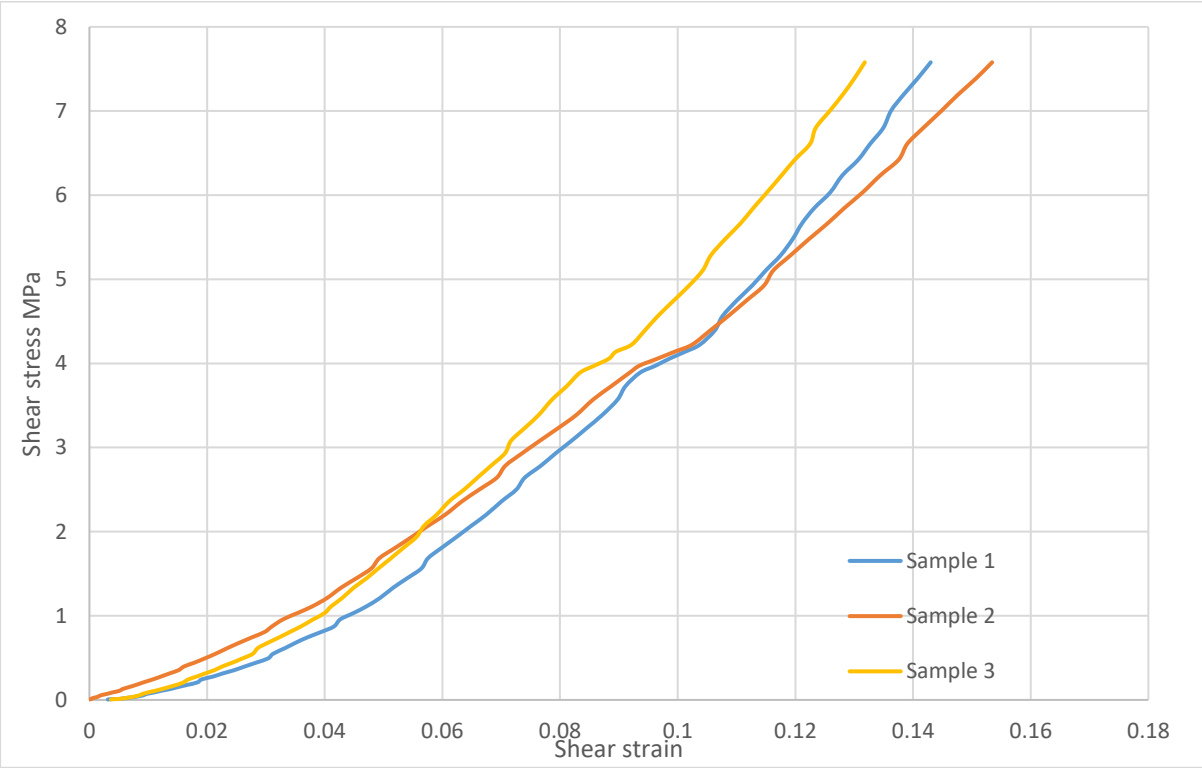

Figure 4. 9: Planar shear-oriented stress vs strain behaviour for fibre-filled composite specimens loaded parallel to the warp fibre directions of EXA-1182.

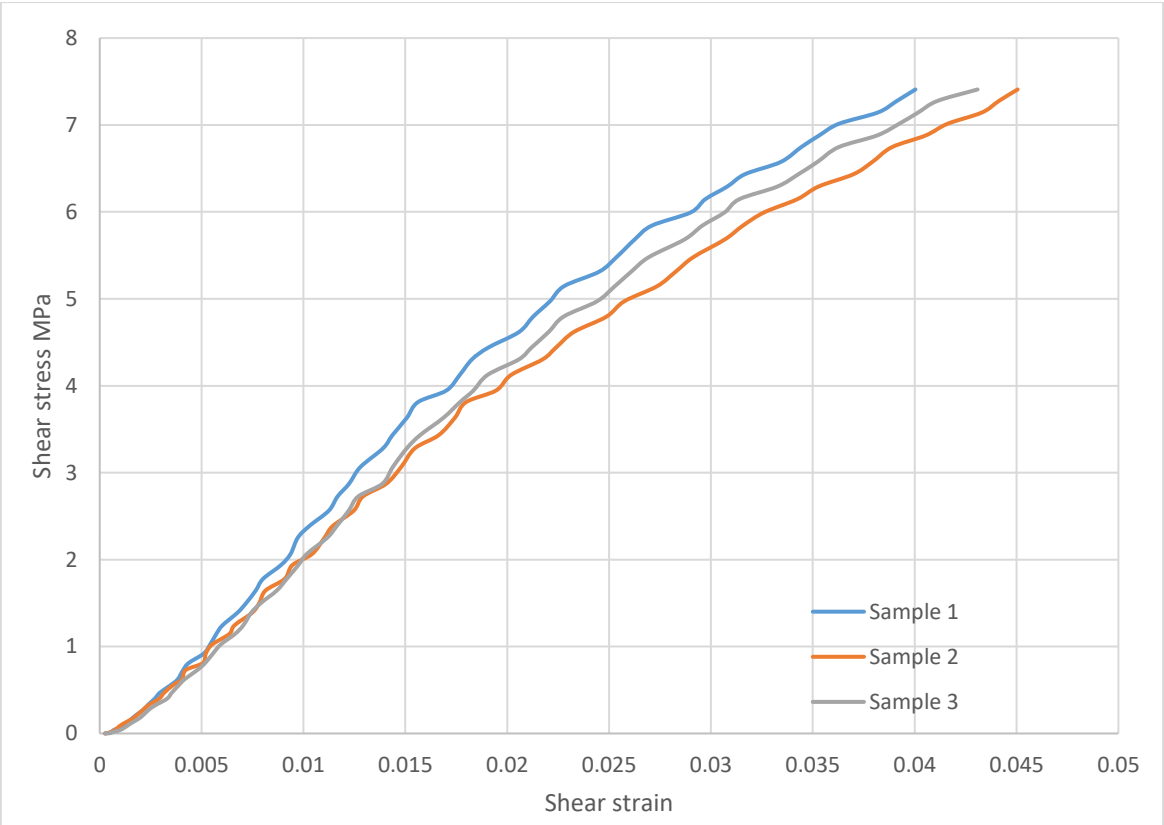

Figure 4. 10: Planar shear-oriented stress vs strain behaviour for fibre-filled composite specimens loaded parallel to the weft fibre directions of EXA-1182

Figures 4.11 to 4.16 show shear strain curves obtained from each of three samples mounted in parallel to warp fibre direction and weft fibre direction. The three samples within each of the figures were cut from the same composite and mounted in the same direction. The variations within the experimental results (attributable only to random errors) are indicative of the homogeneity, reliability and repeatability of the experiments.

With EXA-1196, samples were mounted parallel to the warp direction, and the maximal experimental shear strain lay between 14.7% and 15.6%, with (respectively for low stress and strain, and maximum stress and strain) standard deviations of 0.01% and 0.39%. With EXA-1180, samples were mounted parallel to the warp direction, and the maximal experimental shear strain lay between 14.3% and 15.3% with (respectively for low stress and strain, and maximum stress and strain) standard deviations of 0.01% and 0.41%. With EXA-1182, samples

were mounted parallel to the warp direction, and the maximal experimental shear strain lay between 13.2% and 15.3%, with (respectively for low stress and strain, and the maximum stress and strain) standard deviations of 0.01% and 0.86%.

With EXA-1196, maximal experimental shear strain stress lay between 5.3% and 5.8%. With EXA-1180, maximal experimental shear strain stress lay between 11.0% and 11.6%. With EXA-1182, maximal experimental shear strain stress lay between 4.0% and 4.5%. Respective standard deviations for maximum stress and strain were 0.17% (EXA-1196) and 0.29% (EXA-1180). For both cases, tests were mounted parallel to the weft fibre direction,

Notably, the homogeneity of the shear strain results is generally better for samples measured in the weft fibre direction than for samples loaded parallel to the warp fibre direction similar to the homogeneity of the tensile strain results discussed in section 3.6.

The results from Figures 4.11 to 4.16 also show that the shear strain measured in both orientations of fabric increase non-linearly with respect to the extent of the applied load. This behaviour can be attributed to the effect of reinforcement fibre crimping. As the fabric is woven, “waves” are created in the fabric. As fibres in the warp direction have a higher crimp value, the material experiences a higher strain for the same magnitude of stress as compared to the weft direction. This behaviour can be seen in both the uniaxial tension and pure shear stress tests. The crimp value reduces in the loading direction and increases in the transverse direction and continues until the yarns in the loading direction become straight or the yarns in the transverse direction reached a jammed state.

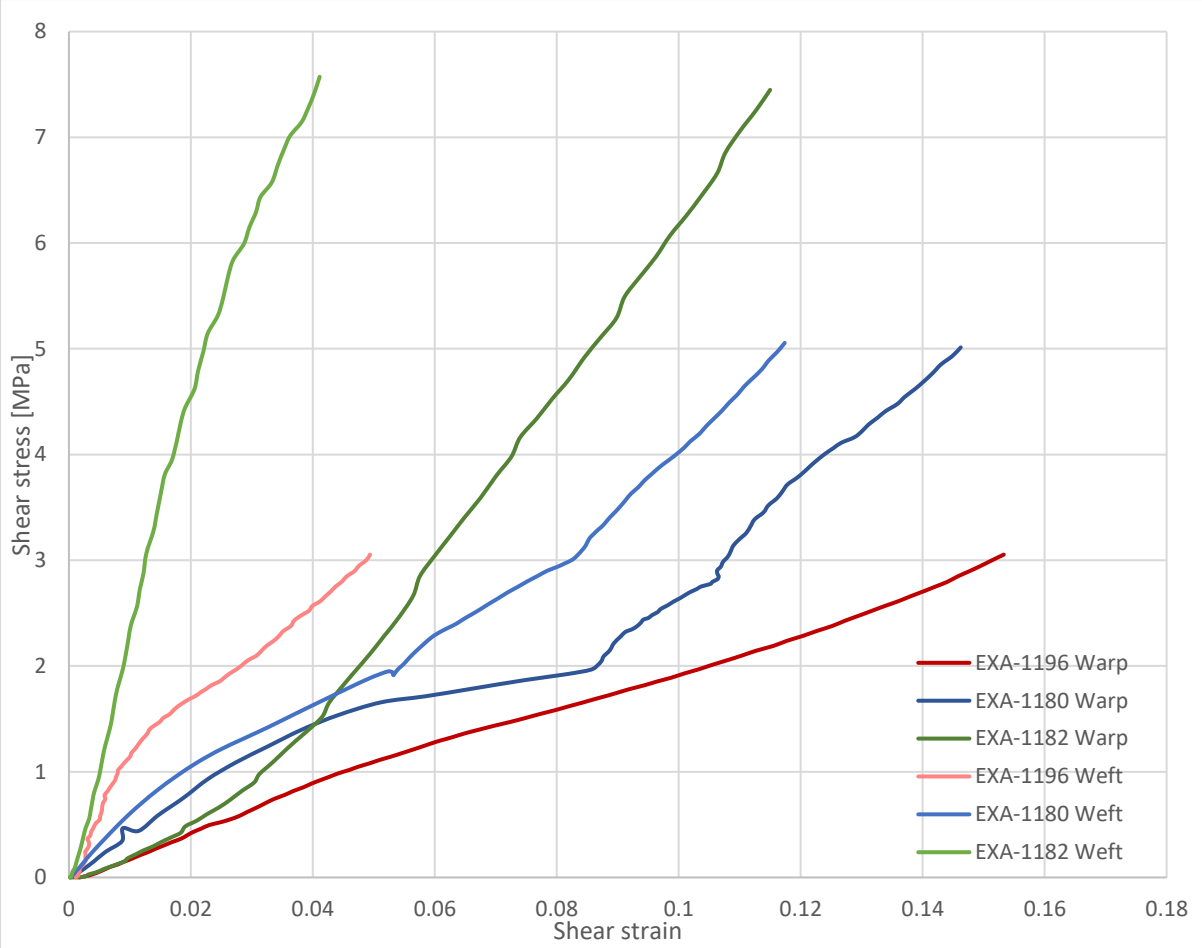

Figure 4. 11: Shear strain versus shear stress for composite specimens of all different materials

Figure 4.17 shows the shear stress-shear strain curves of all three different materials mounted in both directions up to a load of 6000 N for comparison.

Similar to the uniaxial tensile stress-strain tests discussed in section 3.6, there are significant differences between the strain values obtained from measurements conducted parallel to the weft fibres and measurements conducted parallel to the warp fibres. The shear strain values corresponding to certain shear stress are lower in the weft fibre direction, the Shear Modulus is higher, the material is stiffer towards shear stress if it is mounted parallel to the weft fibre direction. In the case of shear strain, this is true for all samples. Sample EXA-1180, which showed no difference in stiffness between warp direction and weft direction in the uniaxial tensile strain test, does show a stiffer behaviour towards shear if mounted in the weft direction,

even if this difference between warp and weft is less pronounced than in the samples EXA-1196 and EXA-1182.

Both tensile tests and shear tests indicate correlation between the thickness and fibre content of the sample and elasticity. For samples with high fibre content, the planar test indicates greater stiffness towards shear. For the same shear stress, a thicker sample with lower fibre content (EXA-1196) shows higher shear strain values than a thinner sample with a higher fibre content (EXA-1182).

4.6 Strain fields for the planar test

Full-field shear strain map (ε_{xy}) measurement of deformation was performed using video gauging. At the centre of the test area, 2D strain maps were created of the approximate height of 400 pixels and width of 1680 pixels. At a working distance of 660 mm, these translated into an area of approximate height 18mm and width 76mm, as projected onto the surface of the samples as patterned with white dots. The chosen grid spacing in the tensile testing experiments was 20 pixels, which resulted in 84 horizontal and 20 vertical nodes within the strain map.

A differential ε_{xy} from the shear strain map was determined. For the contour map, the smallest maximum and the most significant minimum of shear strain values were taken into consideration for calculating the shear strain contrast. Areas of lowest shear strain are colour coded violet and areas of highest shear strain are colour coded red.

For a specimen of materials - EXA-1196 (thickness 5mm), EXA-1180 (thickness 3mm) and EXA-1182 (thickness 2mm) - contour plots for ε_{xy} at a maximum load of 6000N are respectively shown in Figures 4.18, 4.19 and 4.20,

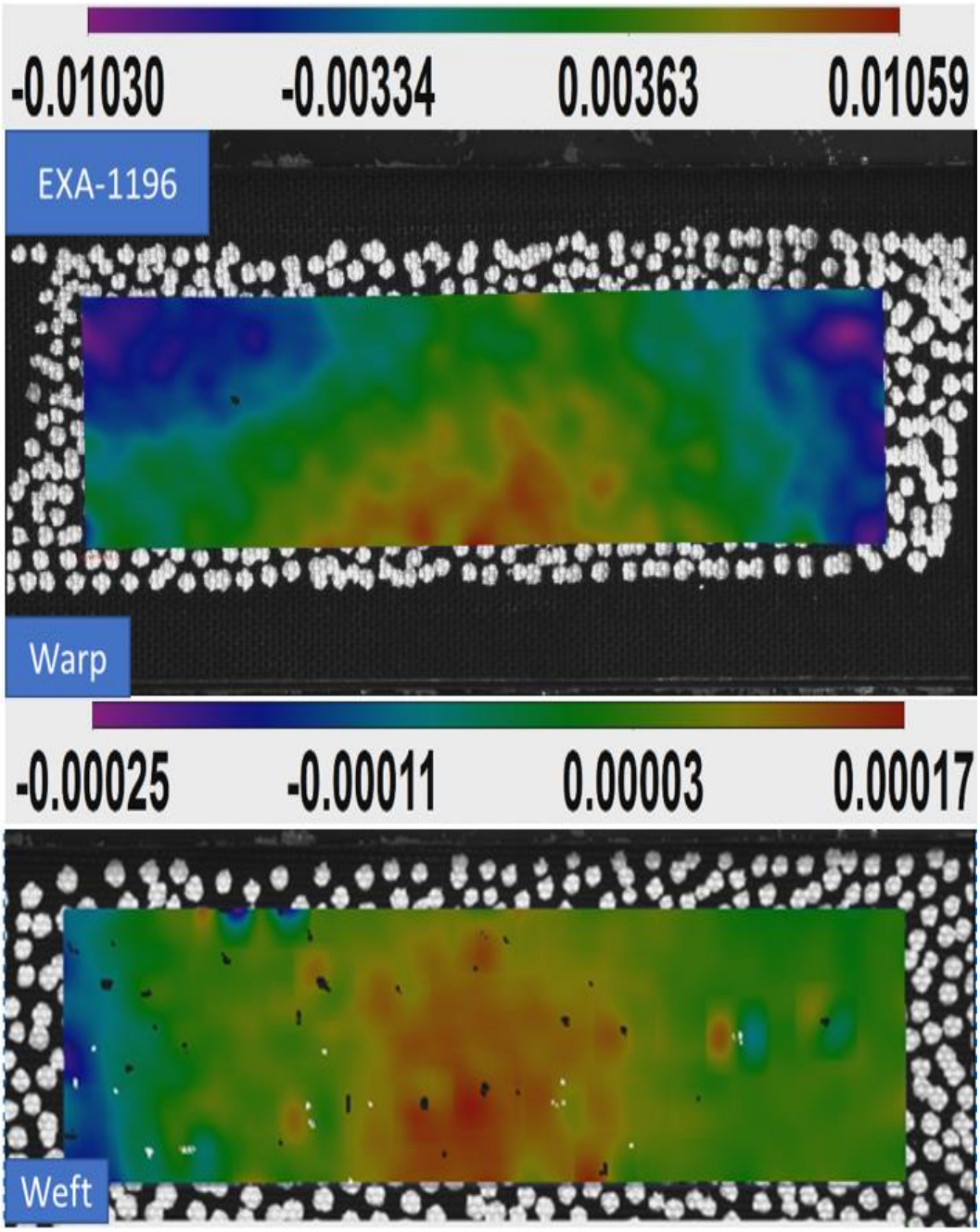

Figure 4. 12: Strain contour map results for a sample of EXA-1196 thickness loaded parallel to the weft and warp.

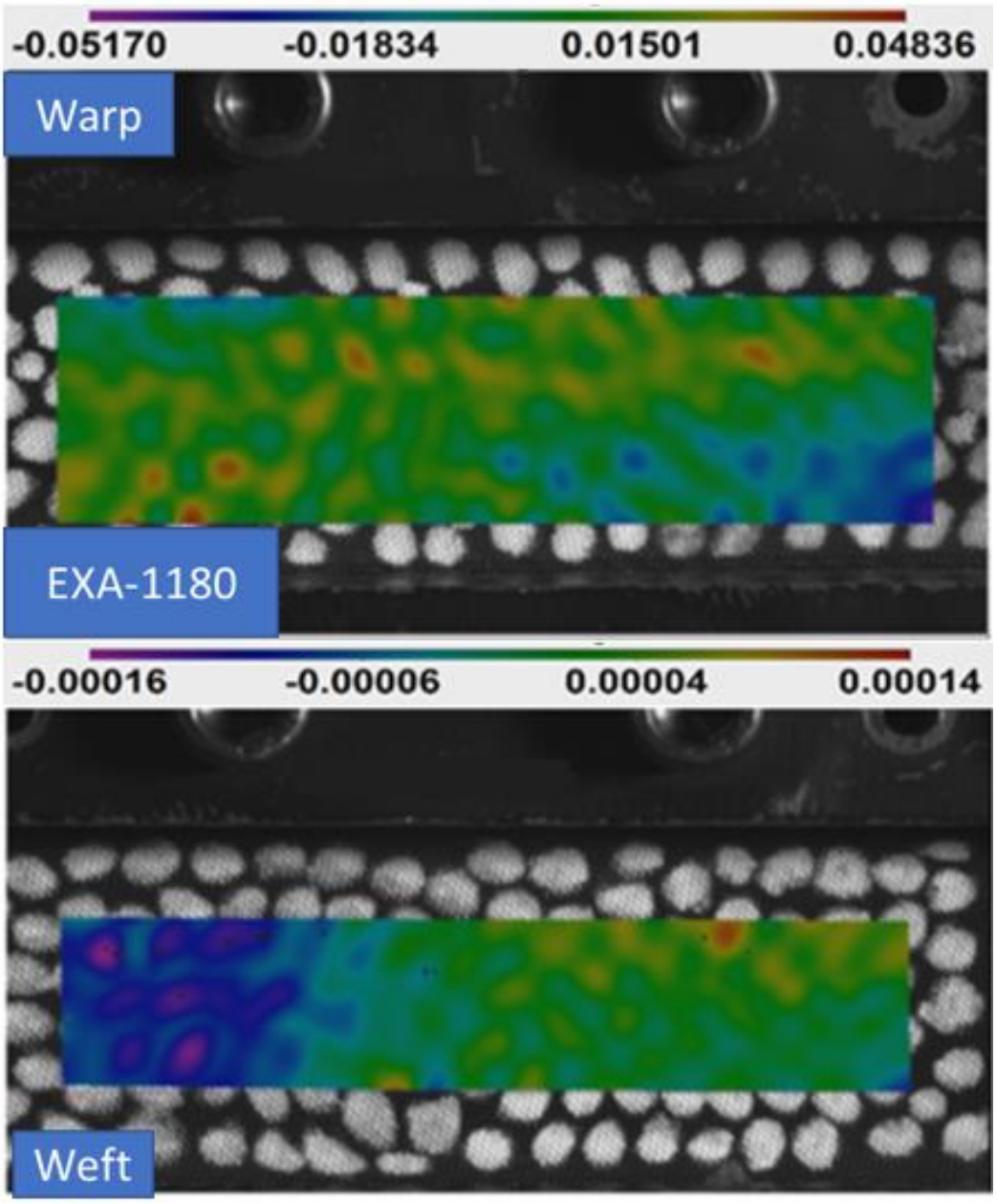

Figure 4. 13: Strain contour map results for a sample of EXA-1180 thickness loaded parallel to the weft and warp.

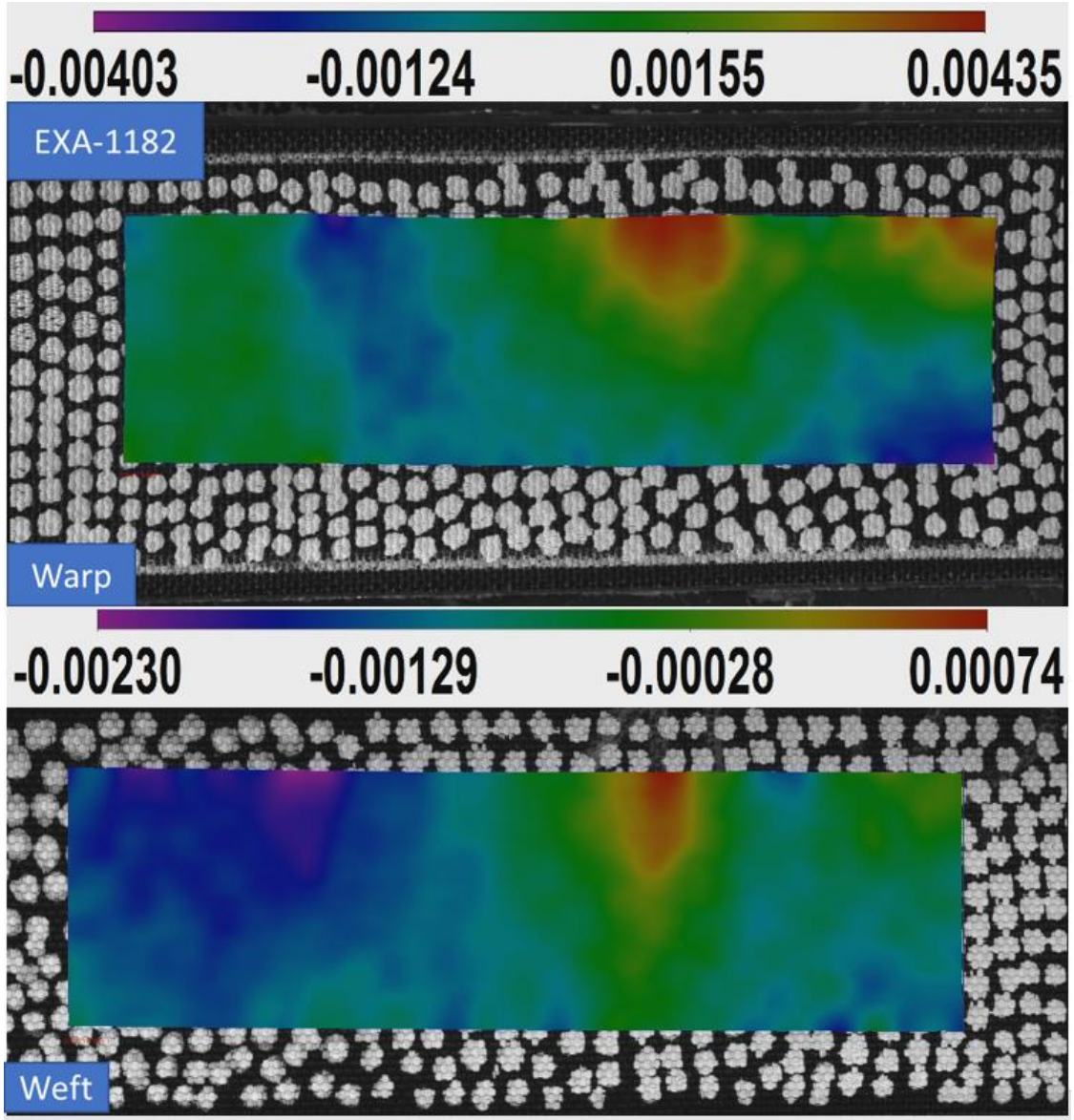

Figure 4. 20: **Strain contour map results for a sample of EXA-1182 thickness loaded parallel to the weft and warp.**

The 2D shear strain maps confirm the results obtained by the shear stress-shear strain curves presented in section 3.5, adding more detail about the strain distribution over the different locations of the sample. The conclusion from Figure 4.6, that positions at the centre of the sample experience higher strain values than the positions outside the centre of the sample is beautifully visualised in the 2D strain maps. Comparison of the minimum and maximum values displayed on the colour coding scales confirm that the woven fabric samples which were

mounted in the warp direction display a higher shear strain than the samples mounted in the weft direction.

4.7 Picture frame test

Over many years, various types of picture frame shear test have been used. Initially, the test was designed as an in-plane shear test tool for such strong laminated materials as plywood and composite laminates.

The Deutsches Institut für Normung (DIN 2014) has suggested a standard test for determining the in-plane shear of fibre-reinforced plastic composites for the picture-frame method. Previously, several other researchers had undertaken substantial work in this field (Cao et al. 2008; Lebrun et al. 2003; Peng et al. 2004; Taha et al. 2013; Zhu et al. 2013).

4.7.1 Results and discussion of the Picture Frame Test

In the previous section, the design of the frame, the preparation of the specimen and the significance and measurement of shear strain in picture frame tests were addressed. In this section, the results obtained for the different materials EXA-1196, EXA-1180 and EXA-1182 are discussed. Shear strain was directly measured at six horizontally different locations from the vertical centre of the sample, the diagonal of the square shaped 100mm*100mm speckled testing area, as depicted in the left image of Figure 4.21. Video gauging can simultaneously measure and calculate shear strain at more than one position at the same time, which aids the determination of the shear strain (angle) at any particular point on the fabric specimen. As the Zwick machine directly recorded the uniaxial force, the testing video recorded the shear strain on the surface (from the centre of the sample) using the video gauge as shown in Figure 4.21 A

The shear strain measured at the different locations in the picture frame test follows the same trend as already established during the wide strip planar tension test, generally the central positions 3 and 4 experience more shear strain than positions 1 and 6 at the ends of the diagonal, see Figure 4.21.

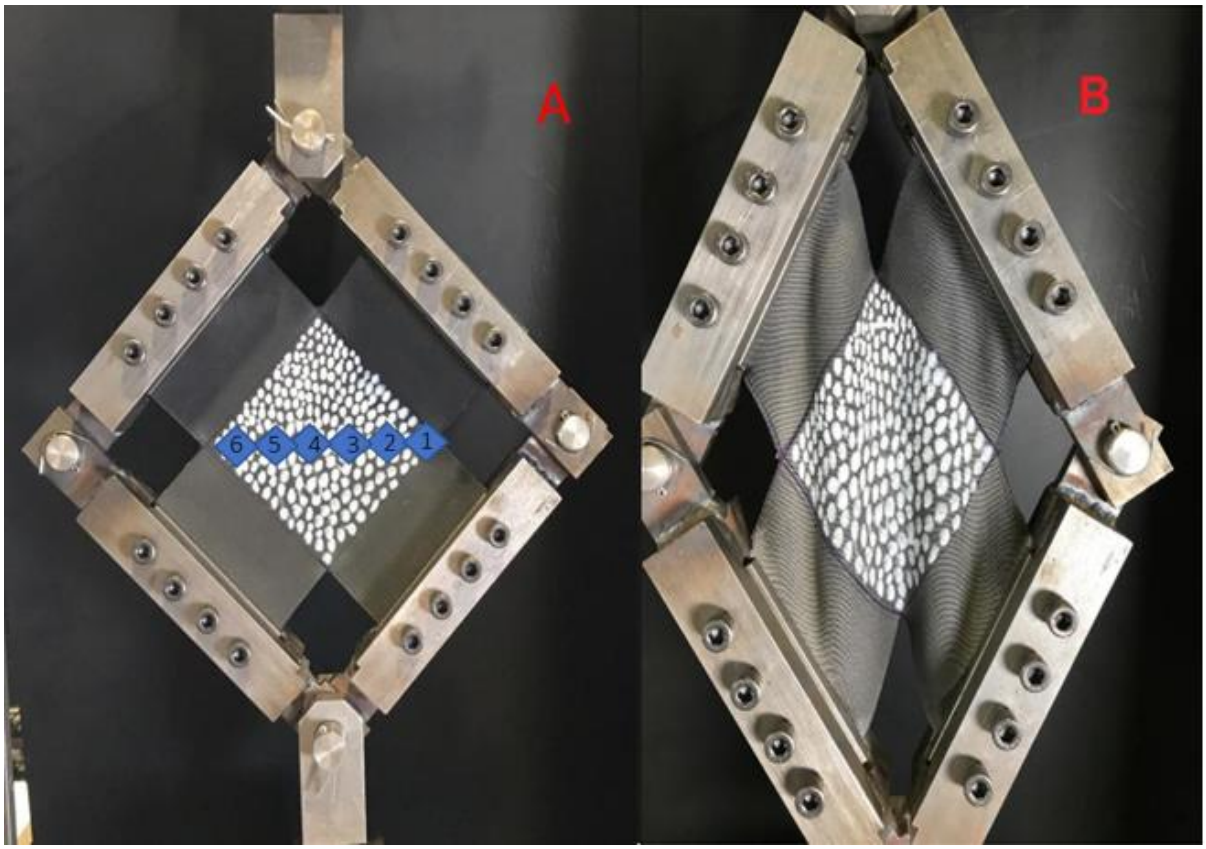

Figure 4. 14: **Picture frame test (a) at the start and (b) at the end of the test.**

Figures 4.22 to 4.24 show the shear stress-shear strain curves for samples EXA-1196, EXA-1180 and EXA-1182 respectively. All these curves were obtained by a picture frame test, with the strain obtained from the centre of the sample, position 3 or position 4 in Figure 4.21. The principal stress, which is the tensile stress in the loading direction, was calculated from the load divided by the cross-sectional area of the diagonal, taking into account the different thicknesses of the different samples. The shear stress is half of the major principal stress. The minor stress in the direction perpendicular to the loading direction is ignored due to the small compressive

stiffness of the fabric material. The results of the picture frame shear test show that the angle increases with increasing shear load and that the angle of the gradient of the shear stress-shear strain curves, as displayed in Figures 4.22 to 4.24 is an indicator for the shear stiffness.

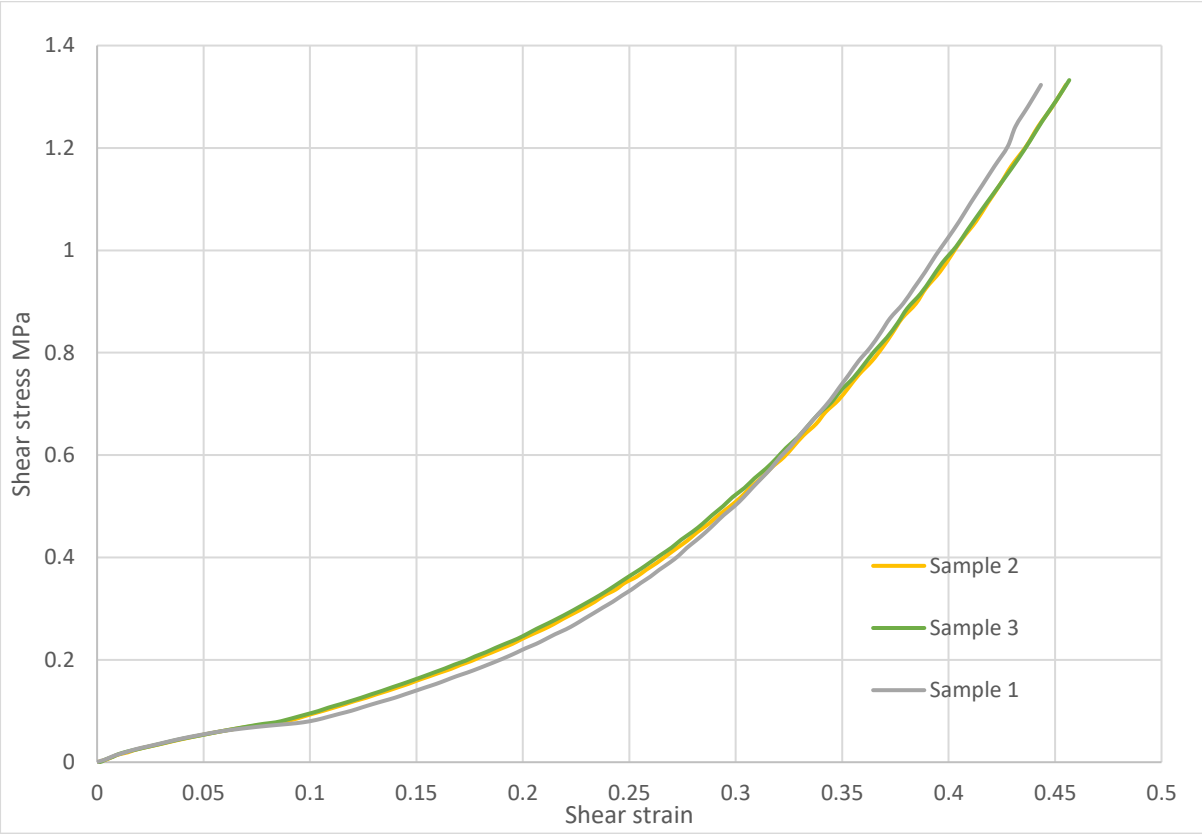

Figure 4. 15: Picture Frame shear stress vs shear strain behaviour for fibre-filled composite specimens of EXA-1196.

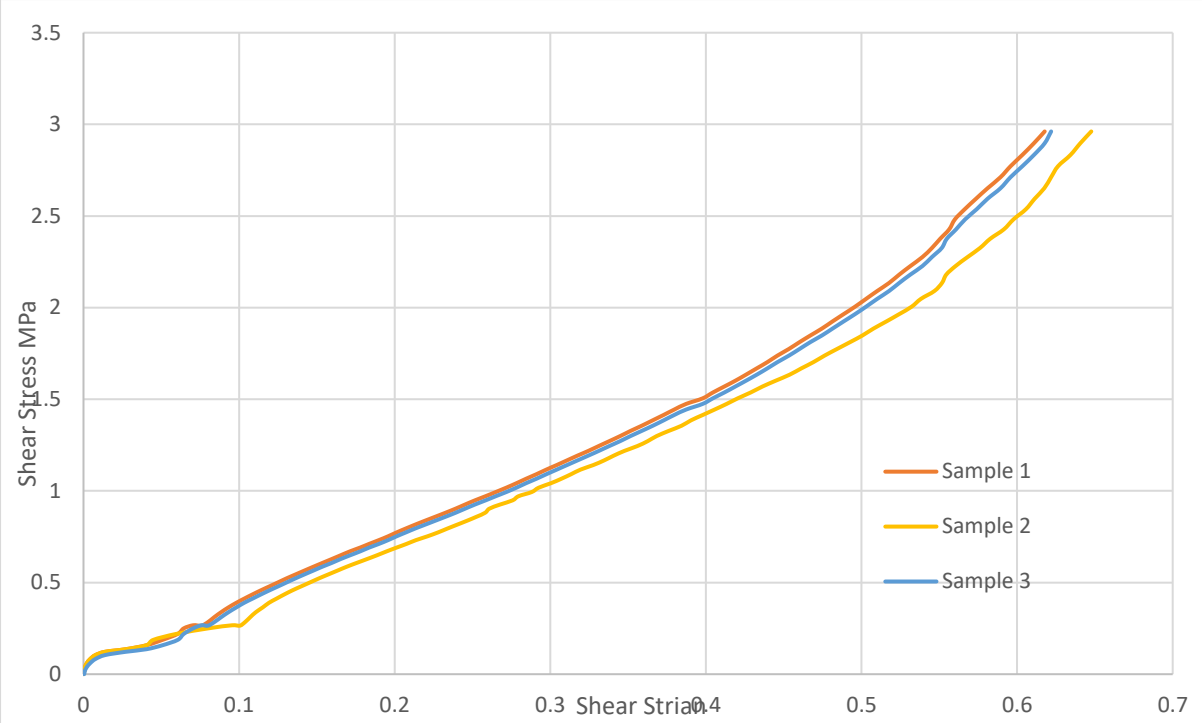

Figure 4. 16: Picture frame shear stress vs shear strain behaviour for fibre-filled composite specimens of EXA-1180.

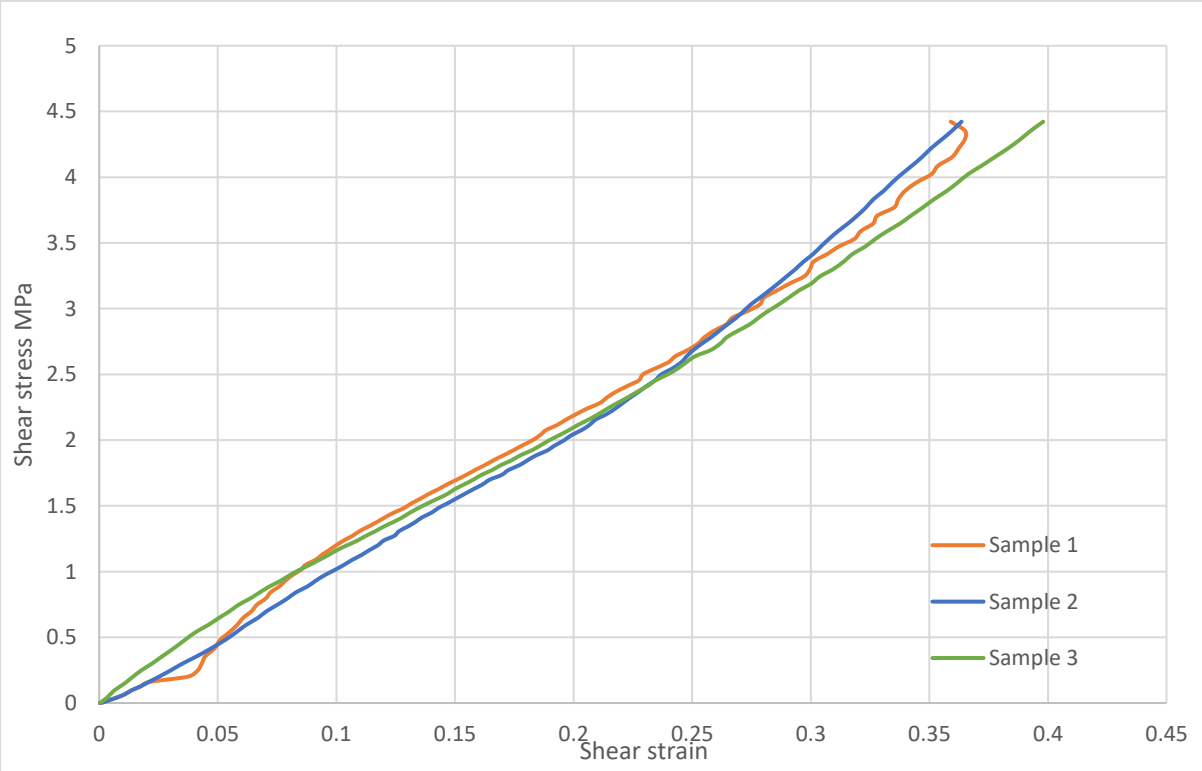

Figure 4. 17: Picture frame shear stress vs shear strain behaviour for fibre-filled composite specimens of EXA-1182.

The curves in Figures 4.22 to 4.24 show non-linear behaviour, particularly under high shear stress the shear strain seems to increase at a much slower rate, confirming increasing rigidity as a result of compression of fibrous assemblies, which under extreme is well known to cause a locking effect preventing further expansion.

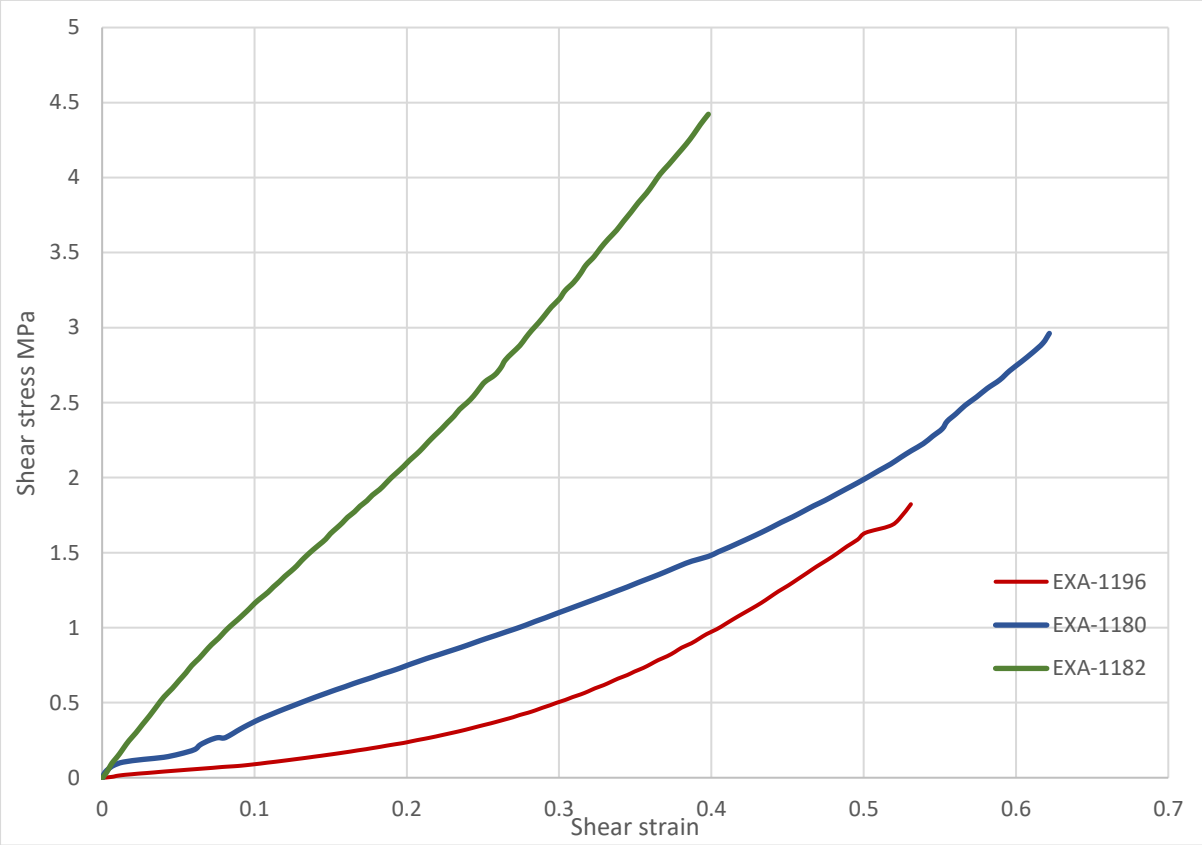

Figure 4. 18: Shear Strain versus shear stress in a picture frame test for composite specimens of all different materials

In Figure 4.25, the shear stress-shear strain curves of all three different samples are displayed for comparison. As expected, and as already established in the wide strip planar tensile test experiments, shear strain is dependent on the thickness of the sample and fibre content. The fibre gives the elastic matrix stiffness against shear, so the sample with the highest fibre content shows the stiffest behaviour, reacting with the lowest shear strain at the same value of applied shear stress.

Figure 4.25 compares the shear stress-shear strain curves for the three different samples. As expected, and as already established in the wide strip planar tensile test experiments, shear strain is dependent on the thickness of the sample and fibre content. The sample with the highest fibre content shows the stiffest behaviour.

A 5mm thick sample containing 10.5% fibres like EXA-1196 shows the largest shear strain, a 3mm thick sample with 11.5% fibre content like EXA-1180 medium shear strain and an EXA-1182 thick sample with a fibre content of 18.1% like EXA-1182 the lowest shear strain at a given shear stress value.

A thicker sample with lower fibre content, such as EXA-1196, displays greater shear strain values than a thinner sample with higher fibre content, such as EXA-1182, when subjected to the same shear stress.

4.7.2 Strain fields for Picture Frame Test

Full-field shear strain map (ε_{xy}) measurement of deformation during a picture frame test was performed using video gauging and digital image correlation. At the centre of the test area, 2D strain maps were created of the approximate height of 420 pixels and width 2100 pixels. At a working distance of 660 mm, these translated into an area of approximate height 19mm and width 95mm, as projected onto the surface of the samples as patterned with white dots. The chosen grid spacing in the tensile testing experiments was 20 pixels, which resulted in 105 horizontal and 21 vertical nodes within the strain map.

A differential ε_{xy} from the shear strain map was determined. For the contour map the smallest maximum and the most significant minimum of shear strain values were taken into consideration for calculating the shear strain contrast. Areas of lowest shear strain are colour coded violet and areas of highest shear strain are colour coded red.

Figures 4.26 to 4.28 show the DIC strain data for the complete field measured in the standard compound tissue samples, with contour diagrams of the strain fields at a load of 2500N.

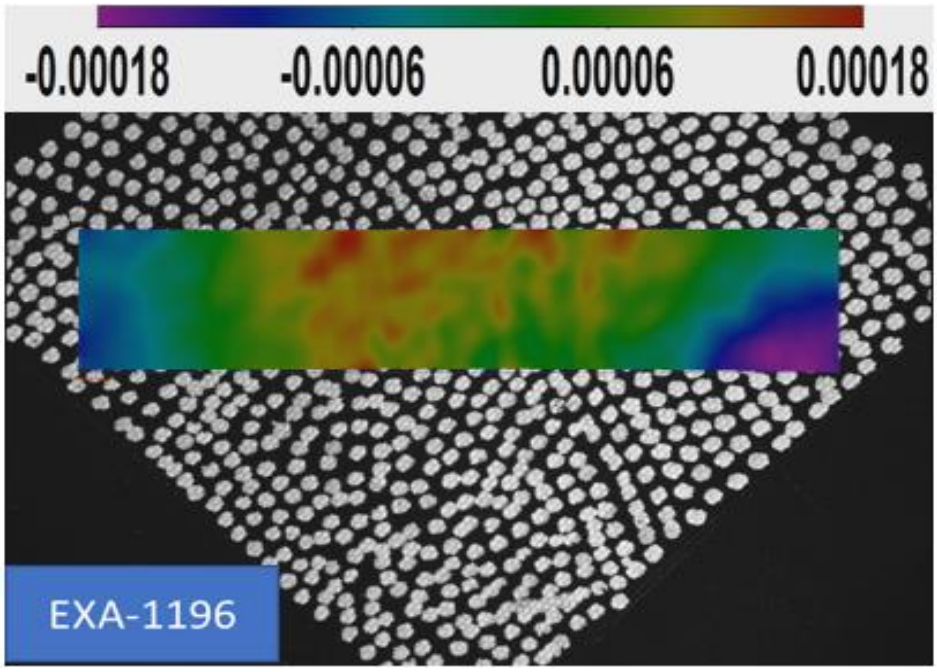

Figure 4. 19: **Strain contour map results for a picture frame of EXA-1196.**

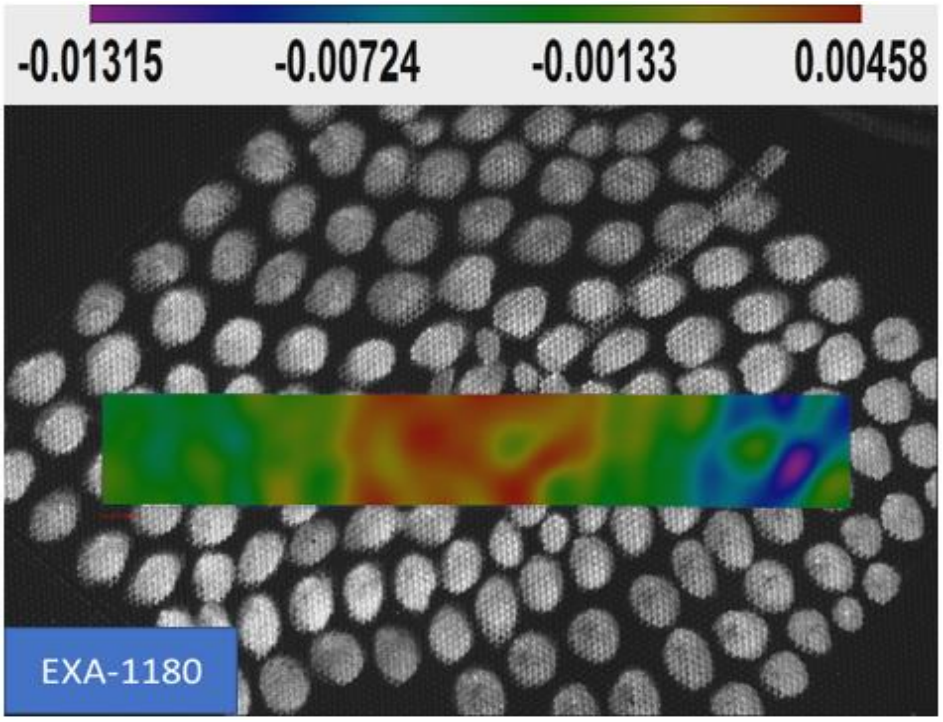

Figure 4. 20: **Strain contour map results for a picture frame of EXA-1180.**

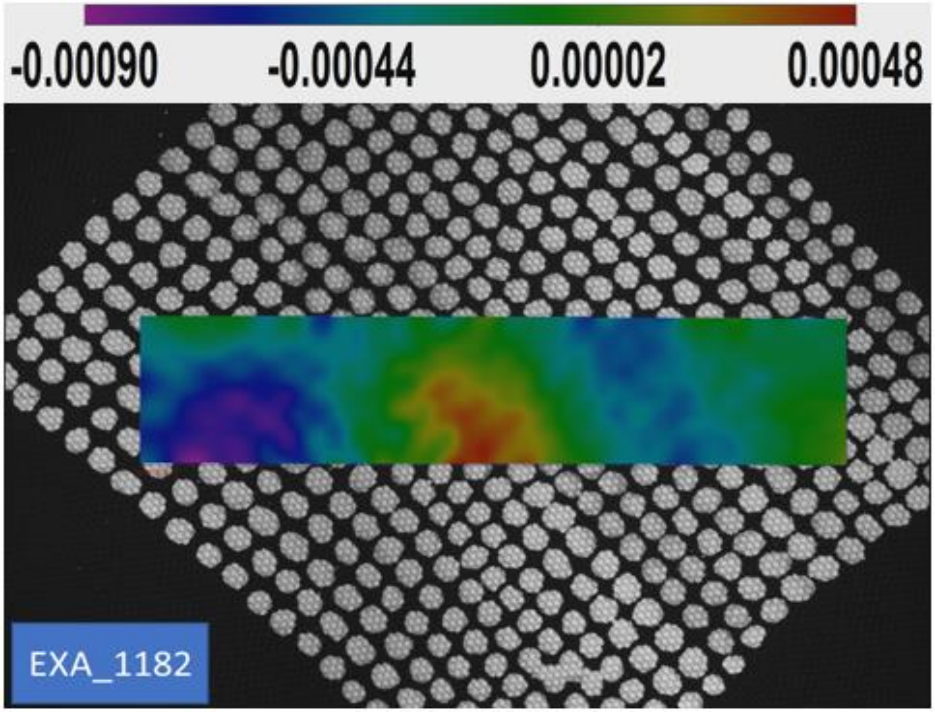

Figure 4. 21: **Strain contour map results for a picture frame of EXA-1182 thickness.**

The results of the 2D shear strain map show the strain distribution over the surface of the defined target and confirm the conclusion from previous chapters that shear strain values show a maximum at the sample centre and decrease at locations further away from the sample centre.

4.8 Conclusions

This chapter has presented suitable test methods for investigating the shearing behaviour of the three fabric types investigated throughout this thesis.

These tests were carried out at room temperature to assess the suitability of the material for structural applications. The non-contact video gauge technique used was found useful to quantify this behaviour for shear strains. With a non-contacting optical system, it is possible to take measurements at multiple positions and gather data in real-time.

Two types of shear property test methods were conducted: the planar tension and picture-frame tests. The measured shear strain for specimens loaded parallel to the warp fibre direction were generally higher than for specimens oriented in the weft direction. The composite demonstrated

anisotropic material behaviour, as confirmed by the various test results obtained for the composite loaded parallel to the weft and warp fibre directions. In addition, the nonlinear shear stress-shear strain response was observed for all the test conditions considered. The shear properties of woven fabric are determined when a shear force acts on specimens of woven fabric that are cut in various angles. Using the video gauge technique, an improved method was obtained by which measurement shear strain measurements were made in planar tension and picture frame specimens. The strain gauge rosette method showed the optical methods to be mathematically accurate.

Full-field measurements, which employ local deformations on a composite component after forming, provide a useful method by which to calculate local fibre orientations and shear angles over the component. It may also be used to examine the shear field of the cloth quantitatively and to understand better the dynamics relevant to the broad shear deformation of the in-plane and picture frame.

Chapter Five

This chapter reviews a number of aspects of mathematical and computational modelling of coated fibre-reinforced composites, giving particular emphasis to constitutive theories based on nonlinear continuum mechanics.

Using ABAQUS software, finite element analysis of load-deformation was undertaken for two simple deformations; i.e., shear and uniaxial stretch experiments, as described in chapter three and chapter four in the previous chapter for different materials.

5.1 Isotropic hyperelastic material models

A finite element analysis model, containing hyperelastic materials, requires substantial data to obtain useful results. At best, some tension or compression stress-strain test data, or simple shear test data, may exist. Processing and applying such data is critical to analyzing hyperelastic models. Curve-fitting to these data is necessary (i) to derive material constants in the strain energy function, (ii) to assess accurate findings. Such test results are typically derived from a variety of deformation modes over a broad range of stresses.

As mentioned in the previous chapter, by conducting uniaxial and pure shear testing, and recording the deformation using a non-contacting digital image correlation, the tensile and planar shear tests demonstrate the suitability of the non-contact optical technique for the capture of hyperelastic material behaviour during loading. This enables comparisons between several hyperelastic material models by using ABAQUS curve-fitting methods, with the objective of simplifying the choice of a hyperelastic model and the determination of its constants for a particular material.

The simplest form of material anisotropy is represented by transversely isotropic materials which have only a single preferred principal (fibre) direction and exhibit isotropic behaviour to arbitrary rotations about the preferred fibre direction. The strain energy density is not derived from the deformation of the materials, as with isotropic hyperelastic materials, but from a combination of both the strain energy density from the deformations and strain energy density in the principal fibre direction.

Constitutive materials models describing hyperelasticity can be formulated in terms of a strain energy function that depends upon the principal stretches, or invariants, of the strain tensor. The strain energy function (W), is directly linked to the material's stress-strain response and depends upon a series of parameters (or material constants). In order to describe a given material behaviour using a particular hyperelastic material model, the material constants must be determined through curve fitting to obtain stress-strain data experimentally. W describes the amount of energy stored in the deformed hyperelastic material as a function of strain at that point in the material (Shahzad, et al., 2015; Boyce and Arruda, 2000; Ali and Sahari, 2010; ABAQUS, 1992) and can be written as:

$$\mathrm{W} = \mathrm{f}(\mathrm{I}_{1,}\mathrm{I}_2, \mathrm{I}_3) \tag{5.1}$$

Where I_1, I_2 and I_3 are the three strain invariants of the Green deformation tensor. The strain invariants can be described in terms of the principal stretches, λ_1, λ_2 and λ_3 according to:

$$\mathrm{I}_1 = \lambda_1^2 + \lambda_2^2 + \lambda_3^2$$

$$\mathrm{I}_2 = \lambda_1^2\,\lambda_2^2 + \lambda_2^2\,\lambda_3^2 + \lambda_3^2\,\lambda_1^2 \qquad \backslash \tag{5.2}$$

$$\mathrm{I}_3 = \lambda_1^2\,\lambda_2^2\,\lambda_3^2$$

This enables the strain energy function (1) to be written as:

$$W = \sum_{i+j+k=1}^{\infty} C_{ijk}\,(I_1 - 3)^i.\ (I_2 - 3)^j\,.\,(I_3 - 1)^k \tag{5.3}$$

Where C_{ijk} is the material-specific constants. If incompressibility is assumed, $I_3 = 1$ and Eq. (5.3) can be further simplified to:

$$W = \sum_{i+j=1}^{\infty} C_{ij}\,(I_1 - 3)^i.\ (I_2 - 3)^j \tag{5.4}$$

Many specific hyperelastic materials models have been proposed (Boyce and Arruda, 2000; Seibert and Schoche, 2000) and software such as ABAQUS contains curve fitting routines for several hyperelastic strain energy functions, including those attributed to Mooney-Rivlin, Neo-Hookean, Polynomial, Ogden and Yeoh. Because these functions assume anisotropic hyperelastic material response, they are limited when applied to the modelling of anisotropic hyperelasticity, such as that demonstrated by a hyperelastic matrix (ground substance) when reinforced with a non-hyperelastic fibre phase. In such materials, as the fibre phase fraction increases, the isotropic hyperelastic contribution from the matrix to overall material behaviour diminishes, necessitating a more complex anisotropic hyperelastic material model in order to adequately describe the material (Holzapfel et al., 2000; Aboshio et al., 2014). As the fibre phase fraction increases with such materials, the isotropic hyperelastic contribution from the matrix to overall material behaviour diminishes. This necessitates a more complex anisotropic hyperelastic material model in order to adequately describe the material itself (Holzapfel et al., 2000; Aboshio et al., 2014).

Given the variation amongst hyperelastic models, in the number of material constants and their physical implications, the strain energy of each hyperelastic model is included below for reference. By integrating the observed data of uniaxial tension and pure shear deformation under particular circumstances, it is possible to reliably compute material constants.

ABAQUS commercial software has hyperelastic material modelling capability. Experimental data are input, and the relevant coefficients of selected hyperelastic material models that best fit the experimental data are identified (Julio, and Yarime, 2006). Nonlinear least-squares regression is performed to determine the hyperelastic constants, and this is then iterated to obtain the best fit to the dataset (Motulsky, and Ransnas, 1987, Hursa et al., 2009). The least-squares error is minimised, using absolute and relative errors, respectively, given by:

$$\text{Absolute error} = \sum_{\text{i}} [\text{experimental data (i)} - \text{calculated data (i)}]^2$$

$$\text{Relative error} = \sum_{\text{i}} [\, 1 - \frac{\text{experimental data (i)}}{\text{Calculated data (i)}} \,]^2$$

Using experimental data obtained from the uniaxial tension and wide strip tension (pure shear) tests, ABAQUS was applied based on the assumption of hyperelastic material model behaviour and the fact that the composite contains a high volume fraction of isotropic hyperelastic matrix material. The results of the Ogden and the Yeoh material models are illustrated in Figures 5.2, and 5.3, which show the Ogden (order N1, N2 and N3 material model parameters) and Yeoh (order N3 material model parameters), that produced best fits for samples loaded in parallel to the weft direction. For samples loaded in parallel to the warp direction (Figures 5.4 and 5.5) the Ogden (order N1 material model parameters) and Yeoh (order N2 and N3 material model parameters) gave the best fits. The results from the ABAQUS model fitting are summarised see Appendix 1.

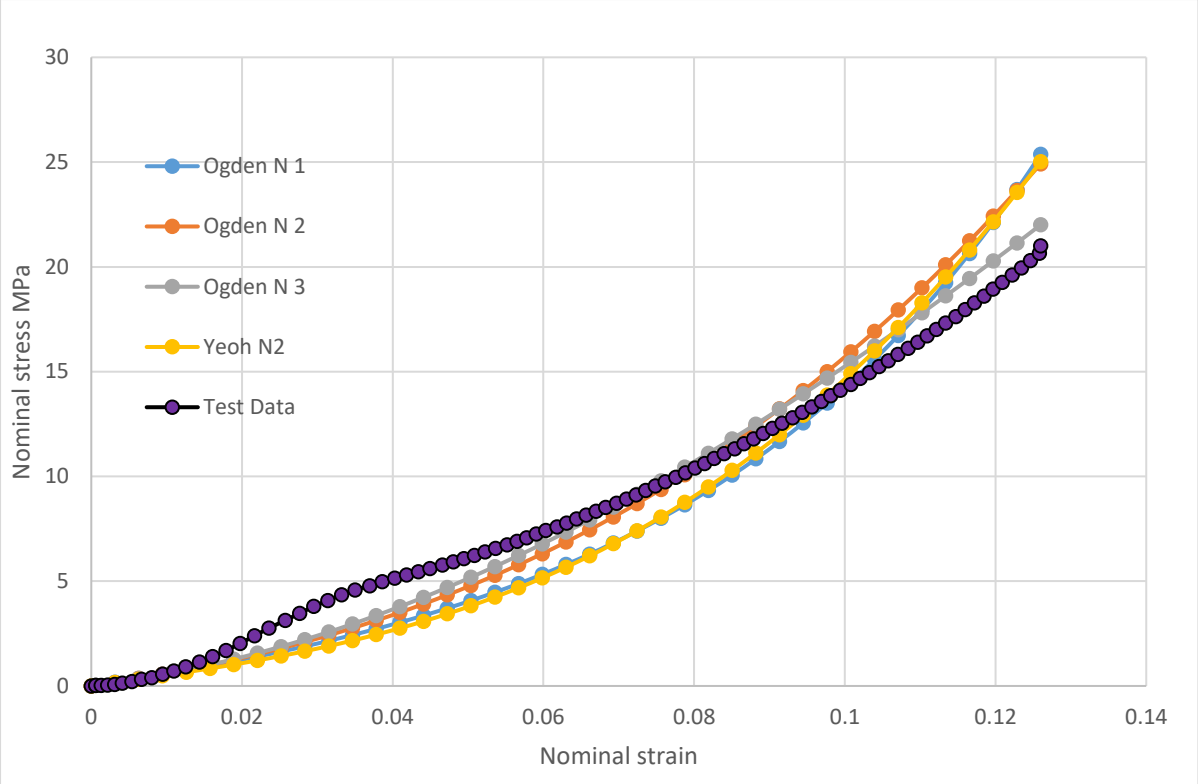

Figure 5. 1: Fitting of uniaxial data for samples loaded parallel to the weft direction using different hyperelastic models (EXA-1196).

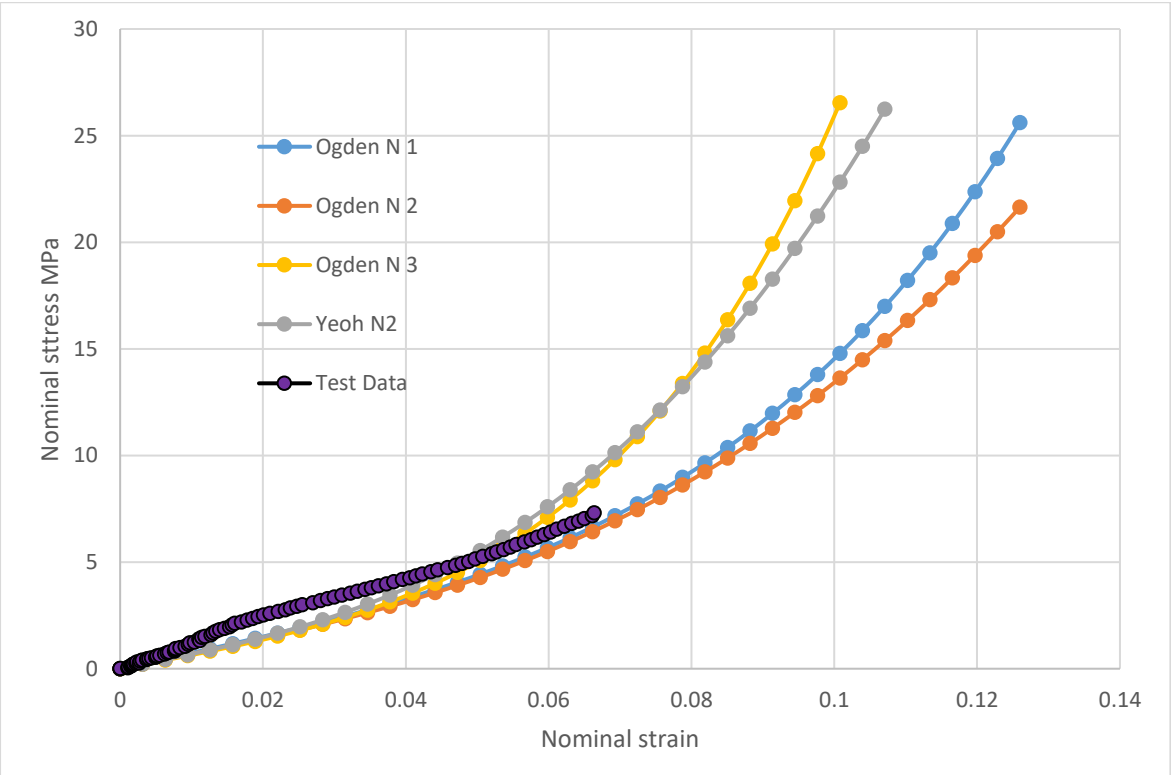

Figure 5. 2: Fitting of different hyperelastic models with planar data for samples loaded parallel to the weft direction (EXA-1196).

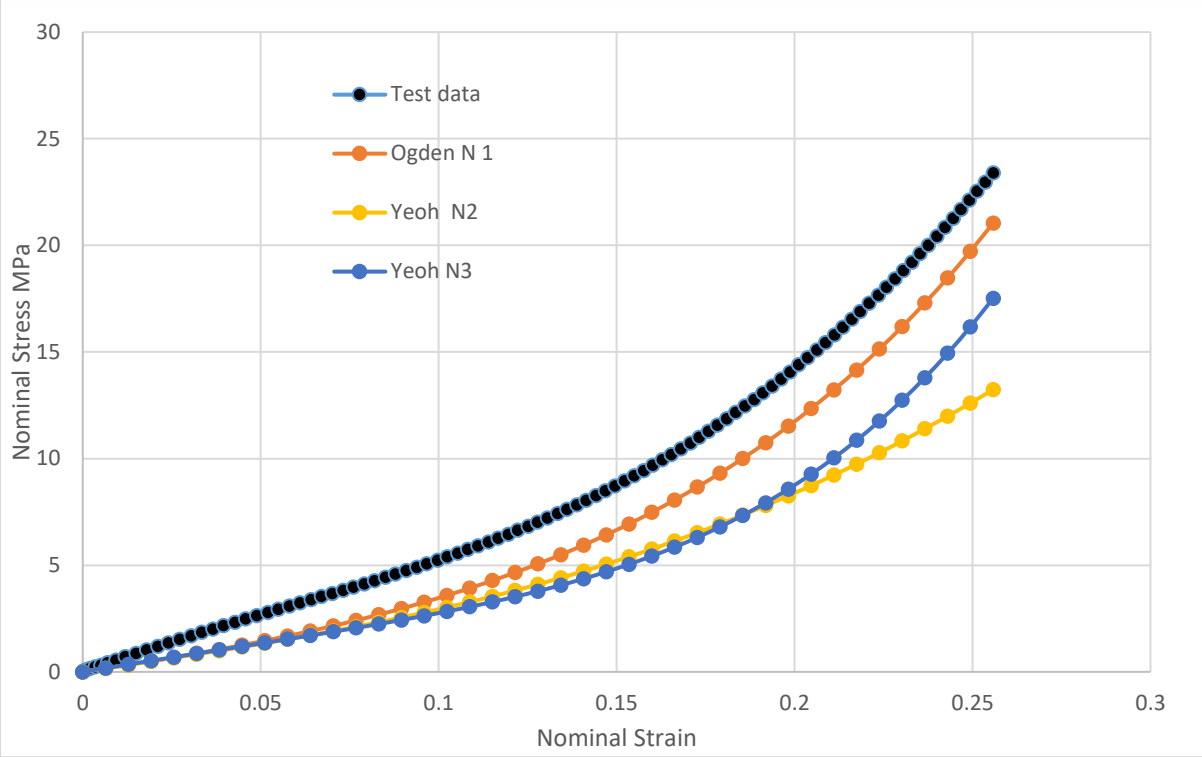

Figure 5. 3: **Fitting of different hyperelastic models with uniaxial data for samples loaded parallel to the warp direction (EXA-1196).**

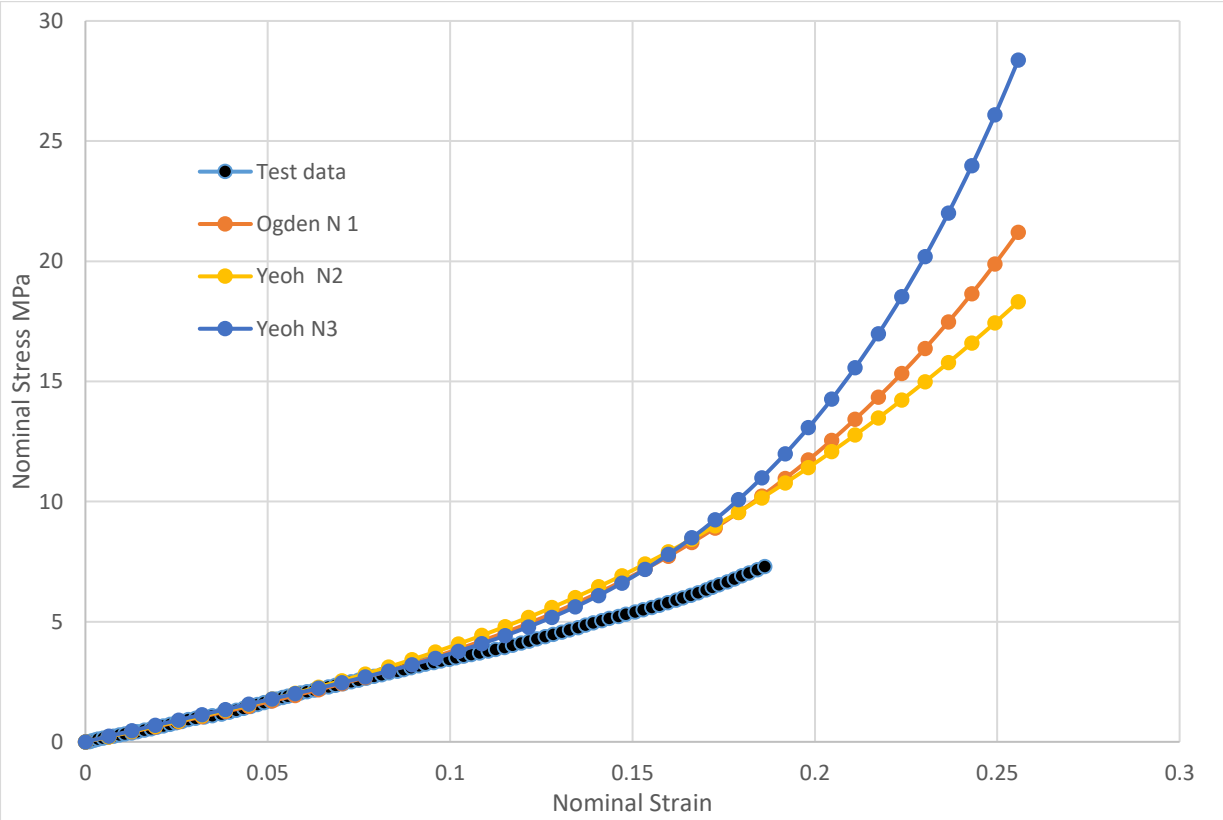

Figure 5. 4: **Fitting of different hyperelastic models with planar data for samples loaded parallel to the warp direction (EXA-1196).**

From a given set of data, curve fitting is undertaken for two models. It can intuitively comprehend the curve fitting properties of the mathematical and experimental basis of various hyperelastic models. With data obtained from stress/strain tests, curve fitting techniques have enabled tension and shear test data to be fitted to all six models from Ogden and Yeoh, as introduced above for (EXA-1196). Stable ABAQUS fitting results for data measured in the weft direction could only be achieved using Ogden N1, N2 and N3 and Yeoh N2, with the lowest least-square result of 36.74% achieved for Ogden N3. Stable ABAQUS fitting results for data measured in warp direction could only be achieved using Ogden N1 and Yeoh N2 and N3, with the lowest least-square result of 31.15% achieved for Ogden N1.

To present strain energy as a function of many independent strain invariants requires complicated mathematical analysis, especially when computing instantaneous moduli of elasticity. It is because our model uses the major stretches as an independent variable in generating the strain energy function, it is sufficiently basic for mathematical analysis to reflect the mechanical response of rubber-like materials. Among the various hyperelastic material models included within commercial FE codes, the Ogden and Yeoh relationship was best suited to model the experimental data.

5.2 Anisotropic hyperelastic material models

For a composite composed of a hyper-elastic matrix reinforced with a family of unidirectionally aligned fibres, the mechanical behaviour can be represented in the continuum mechanics system by a strain energy function W**,** which can be expressed as a scalar function of the right Cauchy-Green deformation tensor $\mathbf{C} = \mathbf{F}^T \mathbf{F}$ and the original fibre is directional unit vector $\mathbf{a}_0$ (Peng et al., 2010; Spencer, 1984; Selvadurai and Shi, 2012; Wineman, 2005)),

where $\mathbf{F} = \frac{\partial \mathrm{x}}{\partial \mathrm{X}}$ is the deformation gradient tensor: X reflects the initial (undeformed) configuration of a material point; x is the position of the point in the new (deformed) coordinate (Shahzad et al., 2015; Boyce and Arruda, 2000; Ali and Sahari, 2010; ABAQUS, 1992).

The strain energy function of the unidirectional fibre-reinforced composite is then represented as:

$$W = W\ (C\ , a_0) \tag{5.5}$$

In terms of C invariants and additional scalars, Eq. (7) can be rewritten as:

$$W\ (\boldsymbol{C}\ , \boldsymbol{a}_0) = \ W\ (\ I_1, I_2, I_3, I_4, I_5) \tag{5.6}$$

Where the invariants are rendered as,

$$I_1 = tr\boldsymbol{C}, I_2 = \frac{1}{2}[\ (trC)^2 - trC^2], I_3 = detC,$$

$$I_4 = \mathbf{a}_0\ .\ \mathbf{C}.\ \mathbf{a}_0 = \ \lambda_{\mathrm{a}}^2,$$

$$I_5 = \mathbf{a}_0\ .\ \mathbf{C}^2.\ \mathbf{a}_0$$

Where $\boldsymbol{\lambda_a}$is the stretch of fibre **a**.

If a second family of fibres with original fibre directional unit vector $\mathbf{b}_0$ reinforces the hyper-elastic body, the strain-energy function W is the isotropic invariant of **C**, $\mathbf{a_0} \otimes\ \mathbf{a}, \mathbf{b_0} \otimes\ \mathbf{b_0}$. Moreover; W can be expressed as a function of the following invariants in addition to Equation (7).

$$W\ \left(\mathbf{C}\ , \mathbf{a}_{0,}\mathbf{b_0}\right) = \mathrm{W}\ (\ I_1, I_2, I_3, I_4, I_5, I_6, I_7, I_8) \tag{5.7}$$

Where, $$I_6 = \mathbf{b}_0\ .\ \mathbf{C}.\ \mathbf{b}_0 = \ \lambda_b^2$$

$$I_7 = \mathbf{b}_0\ .\ \mathbf{C}^2.\ \mathbf{b}_0 \quad \text{And} \tag{5.8}$$

$$I_8 = \cos 2\,\theta$$

Where $\boldsymbol{\lambda_b}$ is the stretch of $\mathbf{b}$,$\mathbf{2}\,\boldsymbol{\theta} = \frac{\mathbf{a}.\boldsymbol{b}}{(\|\mathbf{a}\|.\|\mathbf{b}\|)}$, is the Cosine of the angle between two fibres in the deformed configuration also given by $(\boldsymbol{I_4}\,\boldsymbol{I_6})^{1/2}\,\mathbf{a}_0\,.\,\mathbf{C}.\,\mathbf{b}_0$.

From the above formulation, the second Piola-Kirchoff stress tensor is derived directly from the hyper-elastic function of the energy strain (Spencer, 1984; Peng et al., 2010) as

$$\mathbf{S} = \frac{2\ \partial \mathrm{w}}{\partial \mathbf{C}} \tag{5.9}$$

Then the Cauchy stress tensor is given by

$$\sigma = \mathrm{I}_3^{-1}\mathbf{FSF}^{\mathrm{T}} \tag{5.10}$$

$$\sigma = 2\ \mathrm{I}_3^{-1}\mathbf{F}\frac{\partial \mathrm{w}}{\partial \mathbf{C}}\mathbf{F}^{\mathrm{T}}$$

$$\sigma = 2I_3^{-1}\Big[(I_2W_2 + I_3W_3)I + W_1B - I_3W_2B^{-1} + I_4W_4\,a_0 \otimes a_0 + I_4W_5(a \otimes Ba + aB \otimes a) + I_6W_6b \otimes b + I_6W_7(b \otimes Bb + bB \otimes b) + \frac{1}{2}\,(I_4I_6)^{1/2}W_8(a_0 \otimes b_0 + b_0 \otimes a_0)\Big]$$

Where $\mathbf{I}$ is the second-order unit tensor, $\mathbf{B}$ is the left Cauchy-Green tensor $\mathbf{B} = \mathbf{F^T F}$, and $W_i = \frac{\partial W}{\partial I_i}$.

5.3 A particular application for fabrics of composites

Ignoring the energy dissipated by the friction between fibre yarns, and leaving aside the unloading process, the energy required to deform woven composite fabrics is approximately

equal to the strain energy calculated by the hyper-elastic hyperelastic representation discussed in the previous section.

Theoretically, the strain energy function is the combination of four terms: the strain energy functions of the matrix; the fibres in the weft direction; the fibres in the warp direction; and the shear interactions in the matrix fibre interfaces (Ogden, 2011; Holzapfel et al., 2000).

In this particular case, the strain energy expression is obtained using the following invariants:

$$\mathrm{W} = \mathrm{W}(\mathbf{C}, \mathbf{a}_0, \mathbf{b}_0) = \mathrm{W}^{\mathrm{m}} + \mathrm{W}_{\mathrm{a}}^{\mathrm{f}} + \mathrm{W}_{\mathrm{b}}^{\mathrm{f}} + \mathrm{W}^{\mathrm{fm}} \tag{5.11}$$

$$\mathrm{W}(\mathbf{C}, \mathbf{a}_0, \mathbf{b}_0) = \mathrm{W}^{\mathrm{m}}(\mathrm{I}_1) + \mathrm{W}^{\mathrm{f}}(\mathrm{I}_4, \mathrm{I}_5, \mathrm{I}_6, \mathrm{I}_7) + \mathrm{W}^{\mathrm{fm}}(\mathrm{I}_8) \tag{5.12}$$

$$\mathrm{W} = \mathrm{W}(\mathbf{C}, \mathbf{a}_0, \mathbf{b}_0) = \mathrm{W}^{\mathrm{m}}(\mathrm{I}_1) + \mathrm{W}_{\mathrm{a}}^{\mathrm{f}}(\mathrm{I}_4, \mathrm{I}_5) + \mathrm{W}_{\mathrm{B}}^{\mathrm{f}}(\mathrm{I}_6, \mathrm{I}_7) + \mathrm{W}^{\mathrm{fm}}(\mathrm{I}_8) \tag{5.13}$$

Where $\boldsymbol{W^m}$ is the contribution of the strain energy from the matrix; $\boldsymbol{W^f}$ is the strain energy of the fibres; and $\boldsymbol{W^{fm}}$ is the shearing strain energy resulting from the interaction between the matrix and the fibres in shear. Matrix and fibre volume fractions are accounted for by ν_{f} = volume fraction of fibre

ν_{m} = volume fraction of matrix

$\nu_f = \nu_a + \nu_b$ And $\nu_b = 2\,\nu_a$

Where ν_{a} and ν_{b} are the respective volume fractions of the fibres in the weft and warp directions. It is presumed that the isometric form is the familiar Neo-Hookean model with an additional term, given as

$$\mathrm{W}^{\mathrm{m}} = v_m[\, C_m(I_1 - 3) + C_{m2}(I_1 - 3)^{\alpha}] \tag{5.14}$$

The other terms are:

$$\mathrm{W}_{\mathrm{a}}^{\mathrm{f}} = v_a[\, K_1(I_4 - 1)^{\alpha_1} + K_2(I_4 - 1)^{\alpha_2}] \tag{5.15}$$

$$W_b^f = v_b[\,K_3(I_6-1)^{\alpha_3} + K_4(I_6-1)^{\alpha_4}] \tag{5.16}$$

$$W^{fm} = K_8(I_8)^{\alpha_5} \tag{5.17}$$

Adding Equations 5.7, 5.8, 5.9 and 5.10 gives the total strain energy function for the composite i.e.,

$$W = C_m(I_1-3) + C_{m2}(I_1-3)^2 + K_1(I_4-1)^3 + K_2(I_4-1)^2 + K_3(I_6-1)^3 + K_4(I_6-1)^2 + K_8(I_8) \tag{5.18}$$

Where the constant $C_m = {}^{\mu_0}/_{2}$ (with μ_0 being the shear modulus), $C_{m_2}, K_1, to\ K_{4,}\alpha$ and $\alpha_1$to α_4 can be obtained by fitting the experimental results to the model. This is shown in section 5.6. Note that, in the case of incompressible isotropic materials, the stretch ratios of the off-loading directions are related by $\lambda_2 = \lambda_3$ and $I_1 = \lambda_1^2 + \lambda_2^2 + \lambda_3^2 = \lambda_1^2 + {}^{2}/_{\lambda_1}$ and $I_3 = \lambda_1\lambda_2\lambda_3 = 1$

Therefore, the Cauchy stress tensor σ is given by:

$$\sigma = 2\begin{pmatrix} U_1\mathbf{B} + I_4U_4\,\mathbf{a}\otimes\mathbf{a} + I_6U_6\,\mathbf{b}\otimes\mathbf{b} + \\ \frac{1}{2}(I_4I_6)^{1/2}U_8(\mathbf{a}\otimes\mathbf{b} + \mathrm{b}\otimes\mathbf{a}) \end{pmatrix} \tag{5.19}$$

Where $\mathbf{a} = {}^{\mathbf{Fa}_0}/_{\sqrt{I_{4a}}}$ and $\mathbf{b} = {}^{\mathbf{Fb}_0}/_{\sqrt{I_{6b}}}$ are the fibre direction vectors for the family of fibres.

5.4 Characterisation of three fibre reinforced composite materials

5.4.1 Identification of the material parameters

The material parameters may be approximated by applying the least-squares method to the experimental data (e.g., Figures 3.26 to 3.31) obtained from the uniaxial tensile tests in the fibre yarn direction for the three materials.

Regression modelling is applied to determine mathematical function coefficients based on empirical data. The least-squares (ζ_i) approach calculates the coefficients such that the sum of the squares of the deviations of the data from the curve-fit is minimumised, as shown in the flow chart below (Figure 5.6) (Vasquez Eldredge 2011). In order to calculate the minimised squares for all test data points, the initial values of the parameters were obtained by taking the difference between the stress-strain data points obtained from the experiment and the values obtained from equations 5.16 to 5.19. The subsequently applied optimisation algorithm in Excel is designed to minimise the sum of ζi over all data points (Aboshio et al., 2014).

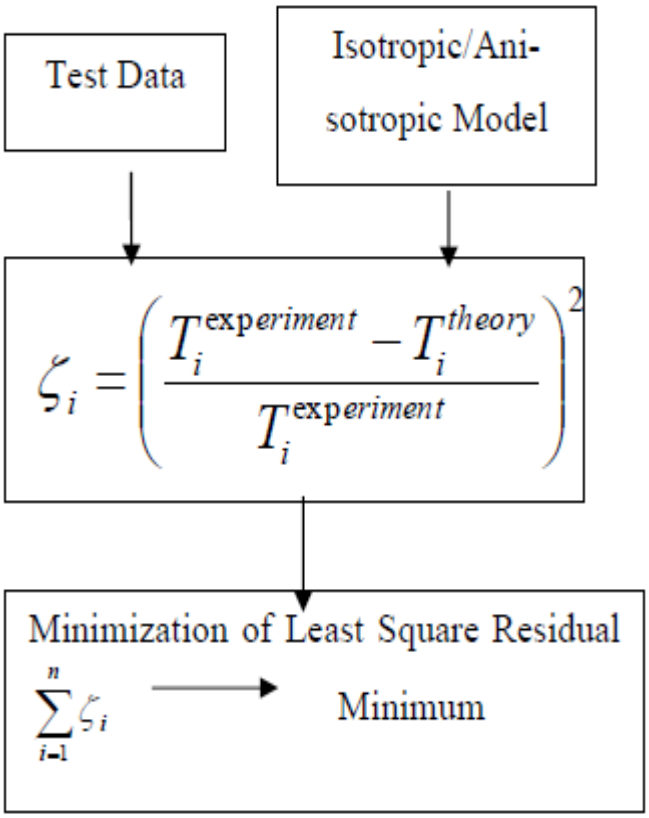

Figure 5. 5: **Schematic approach giving a description of parameters.**

Tensile strain energy density–strain curves can be obtained by integrating stress over the strain, while the tensile strain energy density$(I_1 - 3)$, $(I_4 - 1)$ and $(I_6 - 1)$ can be obtained by curve-fitting, as shown in Figures 6.7 to 6.12 for different composite materials (Peng et al., 2010). For the shear tests reported in the previous chapter, integrating the shear stress over shear strain (Figure 6.16) gives the work needed to deform the composite fabric (I_8). This is known as the total fibre-fibre contact energy (cross-over shear strain energy), as no fibre stretching occurs if the fabric is perfectly aligned in the frame. Assuming that the composite is incompressible, the density of the strain energy is calculated by averaging the strain energy over the composite volume.

The deformations found in composite experiments have been known to reduce the strain energy density in the material. That reduction of the deformation was mainly attributable to the isotropic neoprene matrix with little effect from the fibre. As discussed in Section 5.4, the

diminished strain energy densities in the weft direction were therefore obtained using Equations 5.16 and 5.17 for the different materials.

Four items of experimental data were matched to equation 5.16 to obtain the values of the coefficients. C_m and C_{m2} were respectively obtained, from the weft direction (which is the secondary fibre direction) for three different composite materials, see Appendix 2. As shown Figures 5.7 to 5.9, the typical fitting curve of Equation 5.16 to the experimental data.

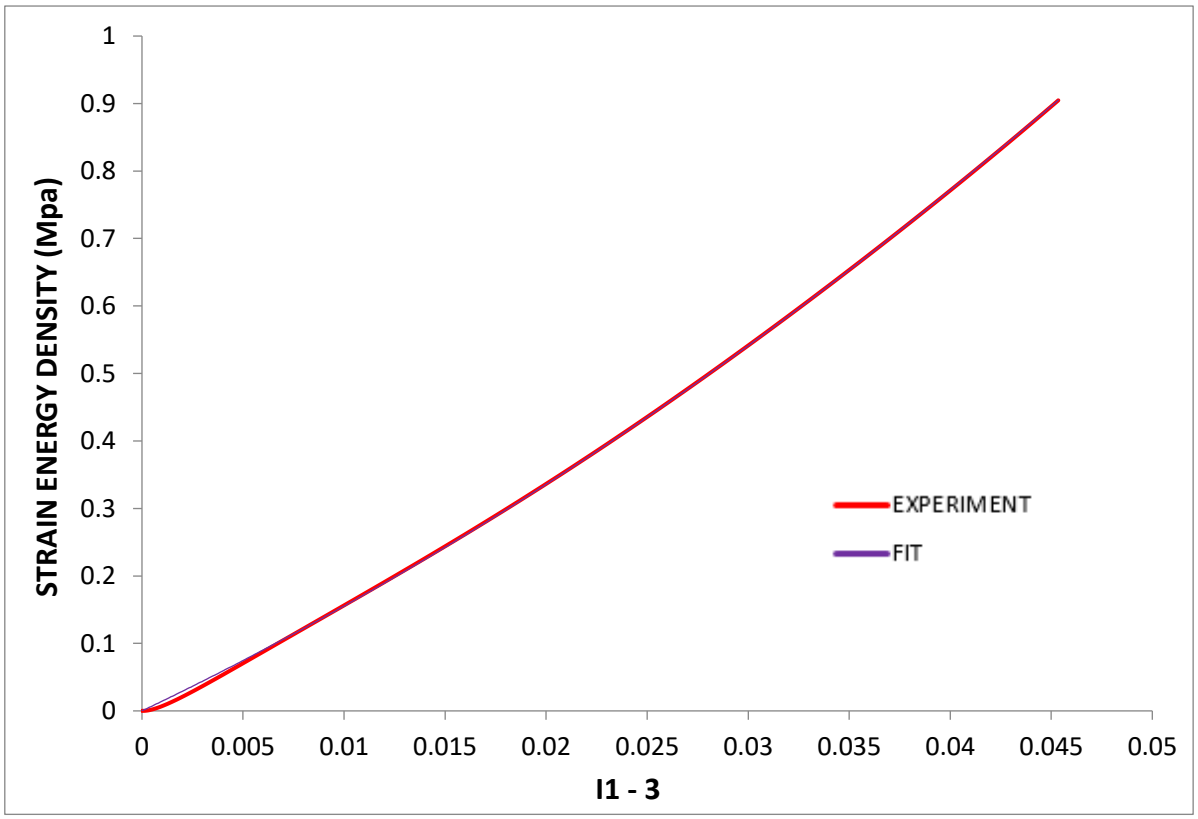

Figure 5. 6: **Strain energy density against invariant in uniaxial tensile stress-strain graph in weft direction for EXA-1196.**

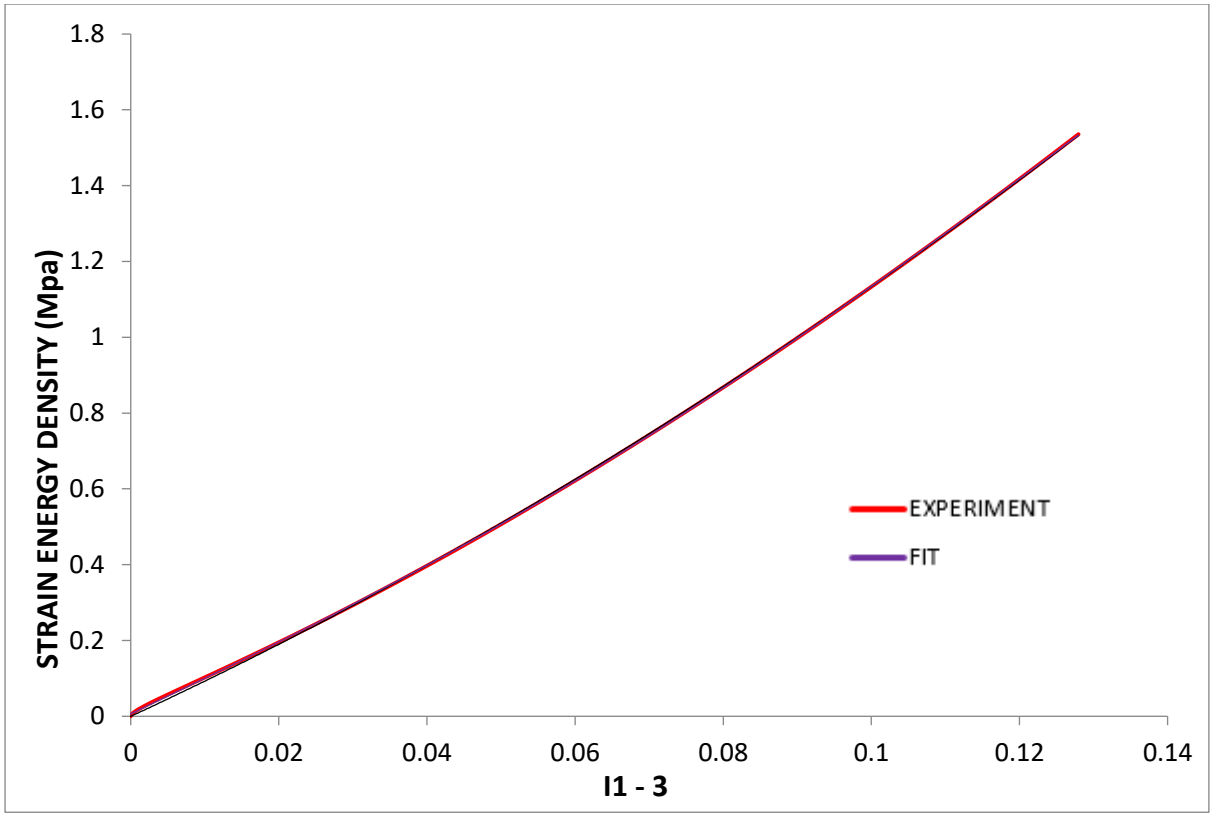

Figure 5. 7: **Strain energy density against invariant in uniaxial tensile stress-strain graph in weft direction for EXA-1180.**

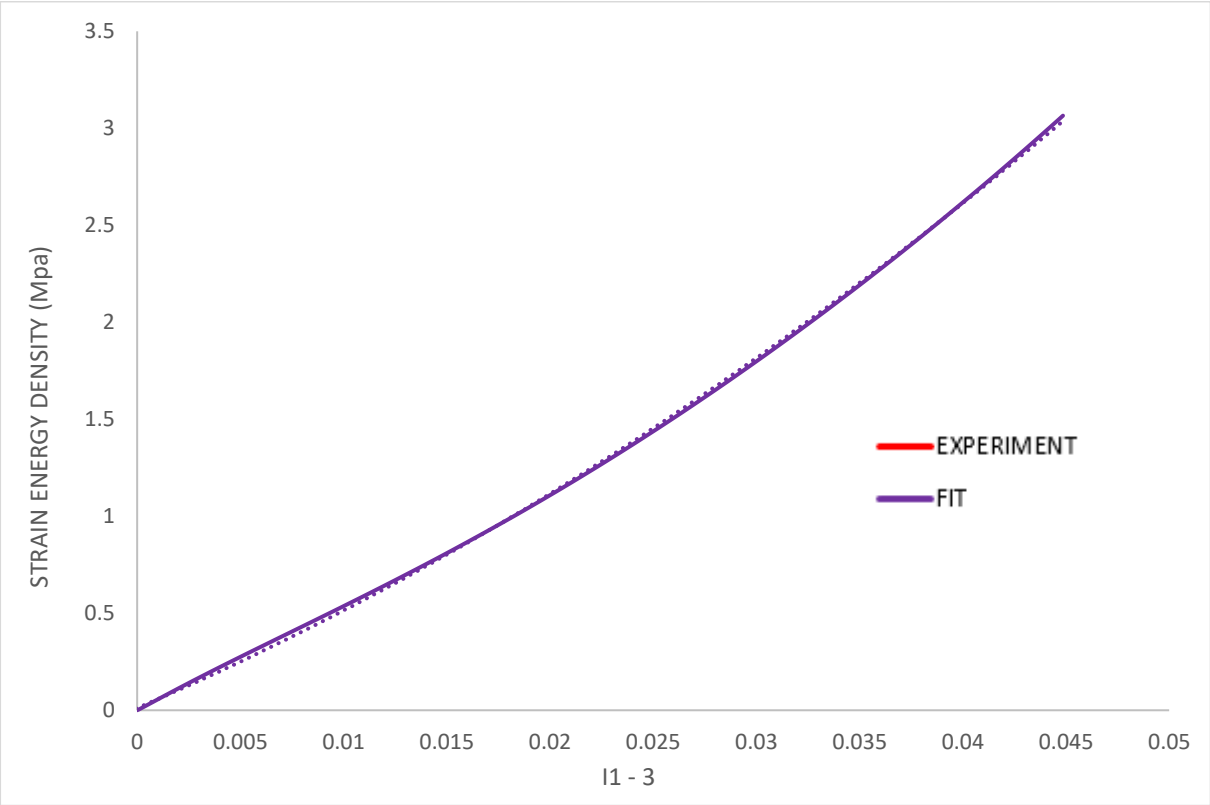

Figure 5. 8: **Strain energy density against invariant in uniaxial tensile stress-strain graph in weft direction for EXA-1196.**

As can be seen, the proposed anisotropic energy function represents the experimental results well. The coefficient values of the properties K_1 and K_2 of the material, identified for the three different materials, see Appendix 3, are plotted as a function of the fibre volume fractions, which was also matched to Equation 5.17. Figures 5.10 to 5.12 show typical fitting curve of formulae 6 to 8 to experimental data; the fitting of all relevant datasets can also be found in Table 4

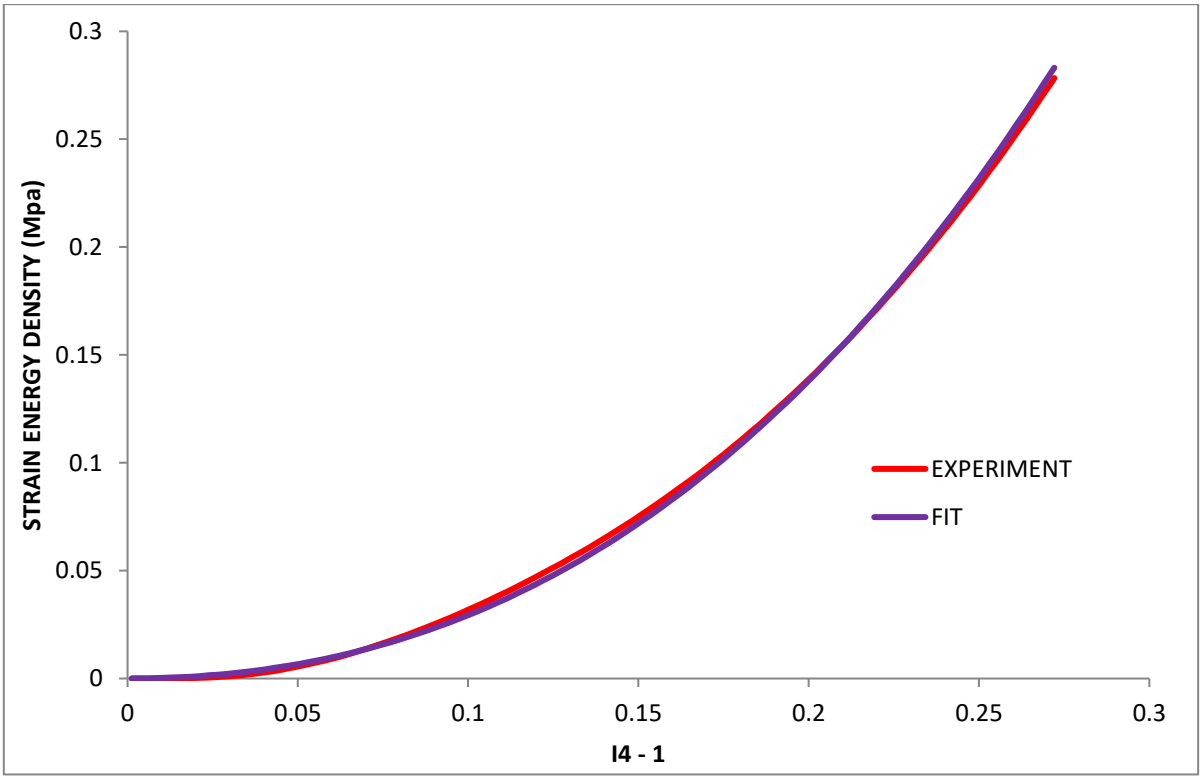

Figure 5. 9: **Strain energy density against the invariant in uniaxial tensile stress-strain graph in the weft direction for EXA-1196.**

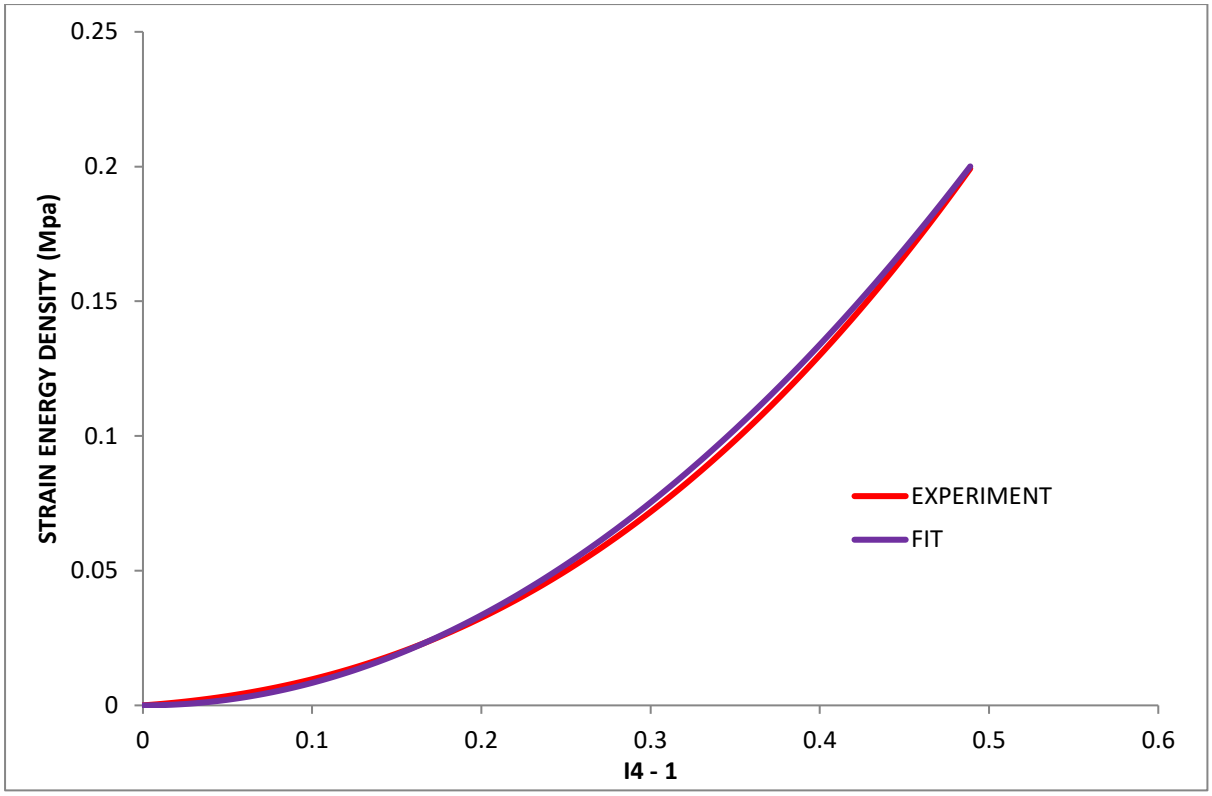

Figure 5. 10: **Strain energy density against the invariant in uniaxial tensile stress-strain graph in the weft direction for EXA-1180.**

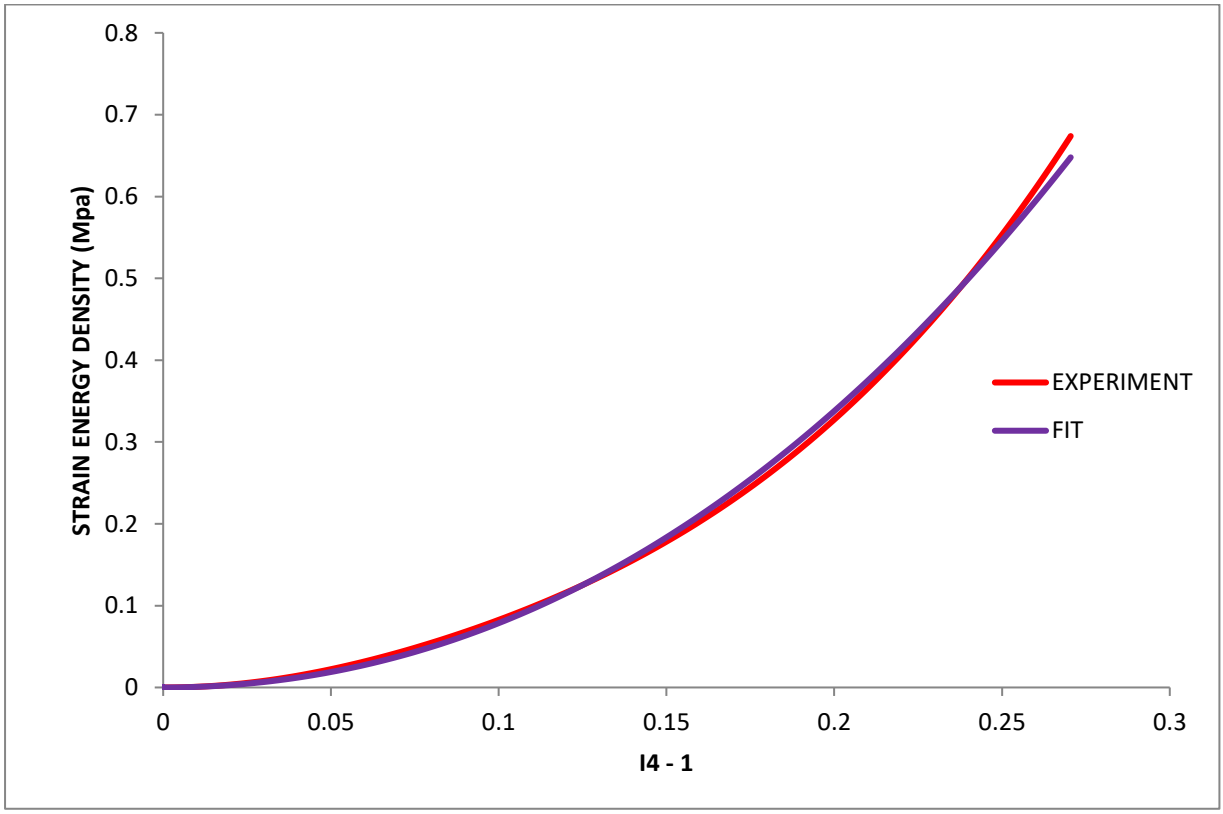

Figure 5. 11: **Strain energy density against the invariant in uniaxial tensile stress-strain graph in the weft direction for EXA-1182.**

In the direction of the warp (fibre primary), the experimental values for the composite materials were matched to equation Equation 6.18, as shown in Figure 5.13 to 5.15. The coefficient values, K_3 and K_4, were calculated, see Appendix 4.

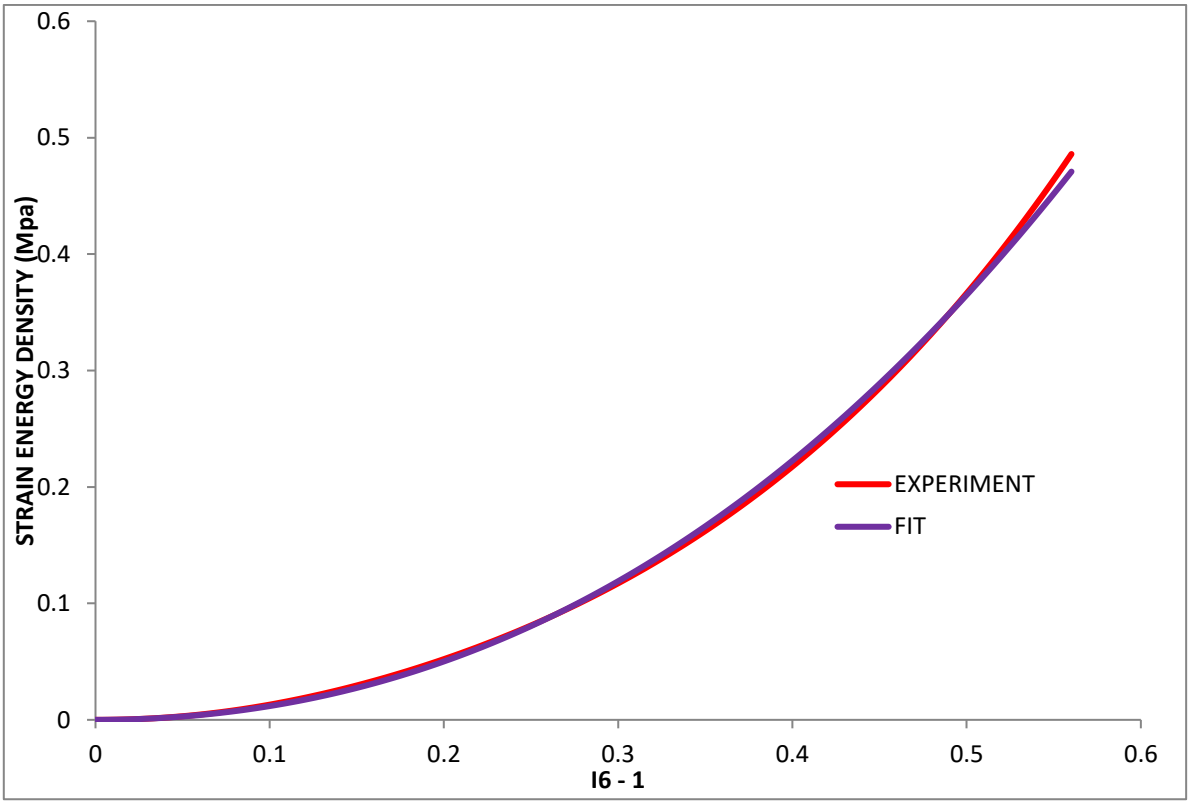

Figure 5. 12: Strain energy density against the invariant in uniaxial tensile stress-strain graph in the warp direction for EXA-1196.

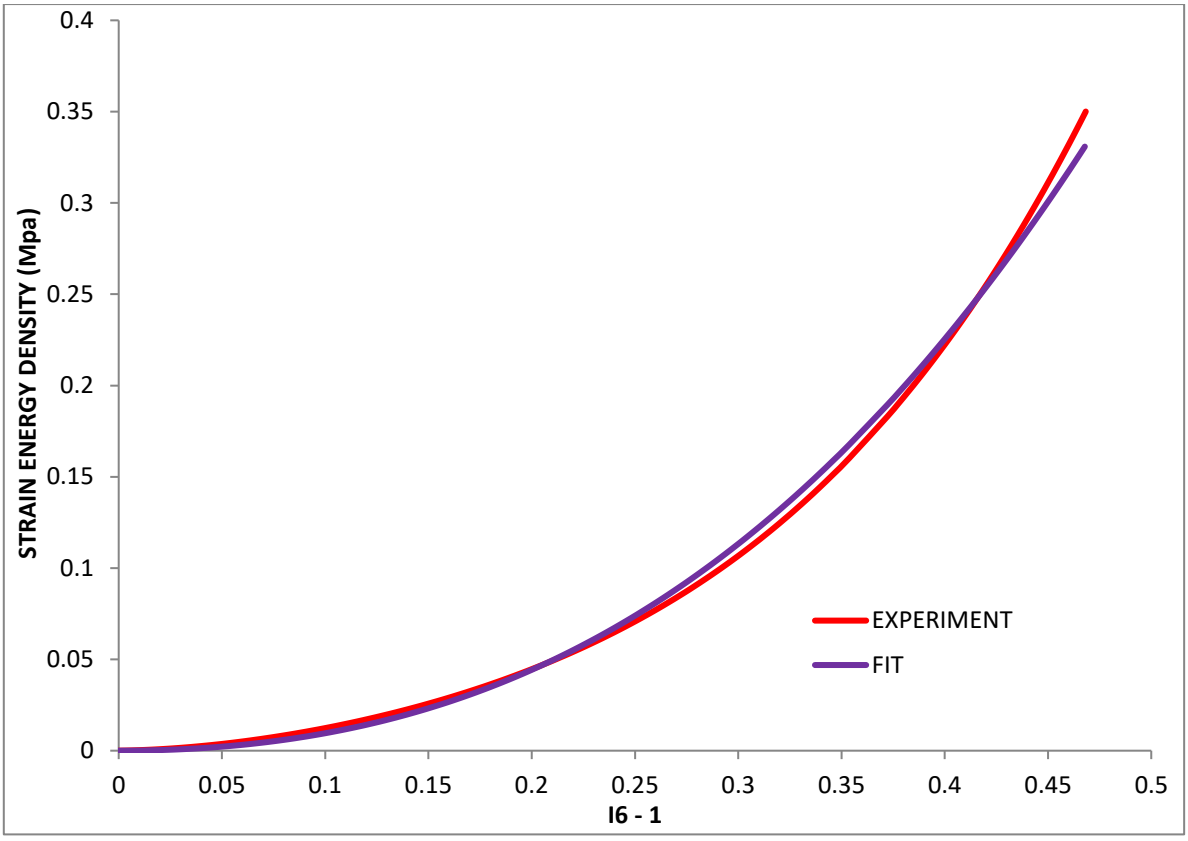

Figure 5. 13: **Strain energy density against the invariant in uniaxial tensile stress-strain graph in the warp direction for EXA-1180.**

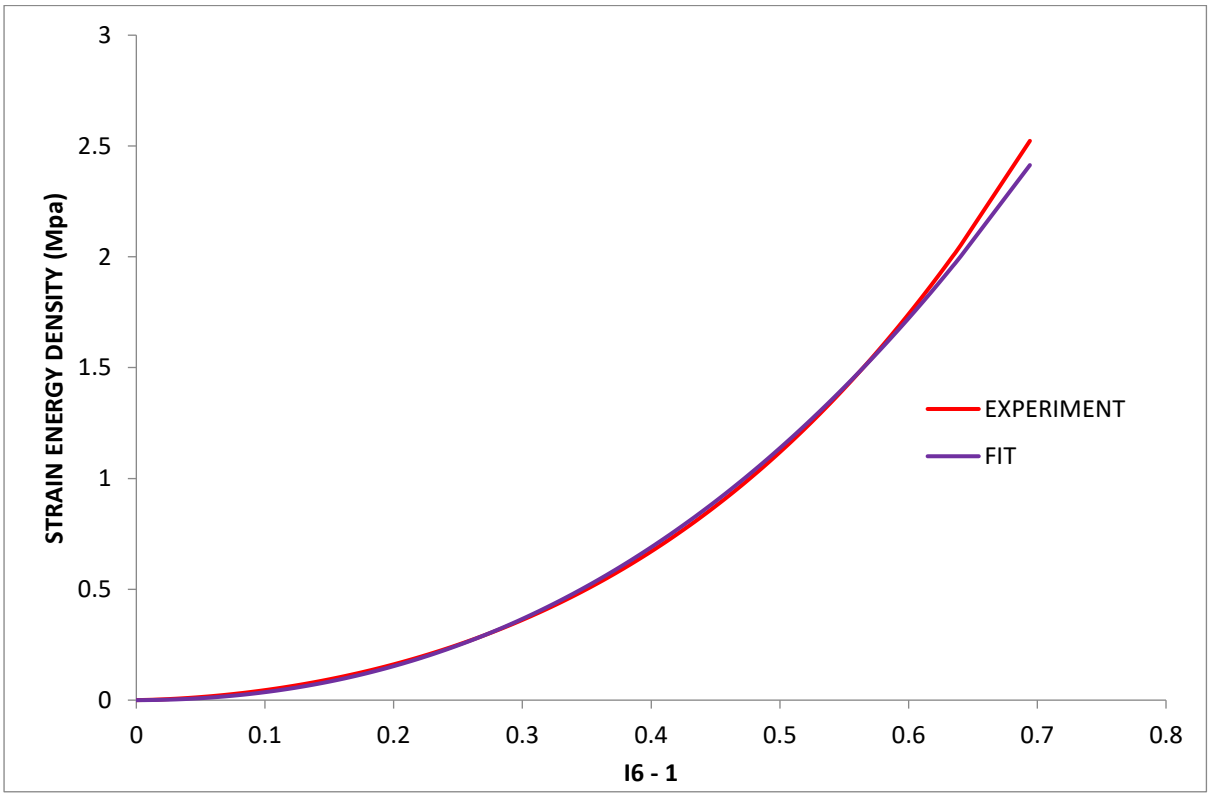

Figure 5. 14: **Strain energy density against the invariant in uniaxial tensile stress-strain graph in the warp direction for EXA-1182.**

As mentioned in Chapter Four, when the material is tested by using a picture frame along with the warp and weft directions, the shear strain energy can be expressed, as shown in Equations 5.21 to 5.23. The contribution of the strain energy function arises from the interaction of the matrix–fabric in shear. The strain energy function versus the invariant I_8 is shown in Figures 5.16 to 5.18. When matched to equation 5.19, the value obtained was as shown in Table 6 see Appendix 5. Finally, the overall strain energy function of the composite, as expressed below, can be calculated by using the average values of the coefficients (in Pascals) as calculated from the fitting method described above.

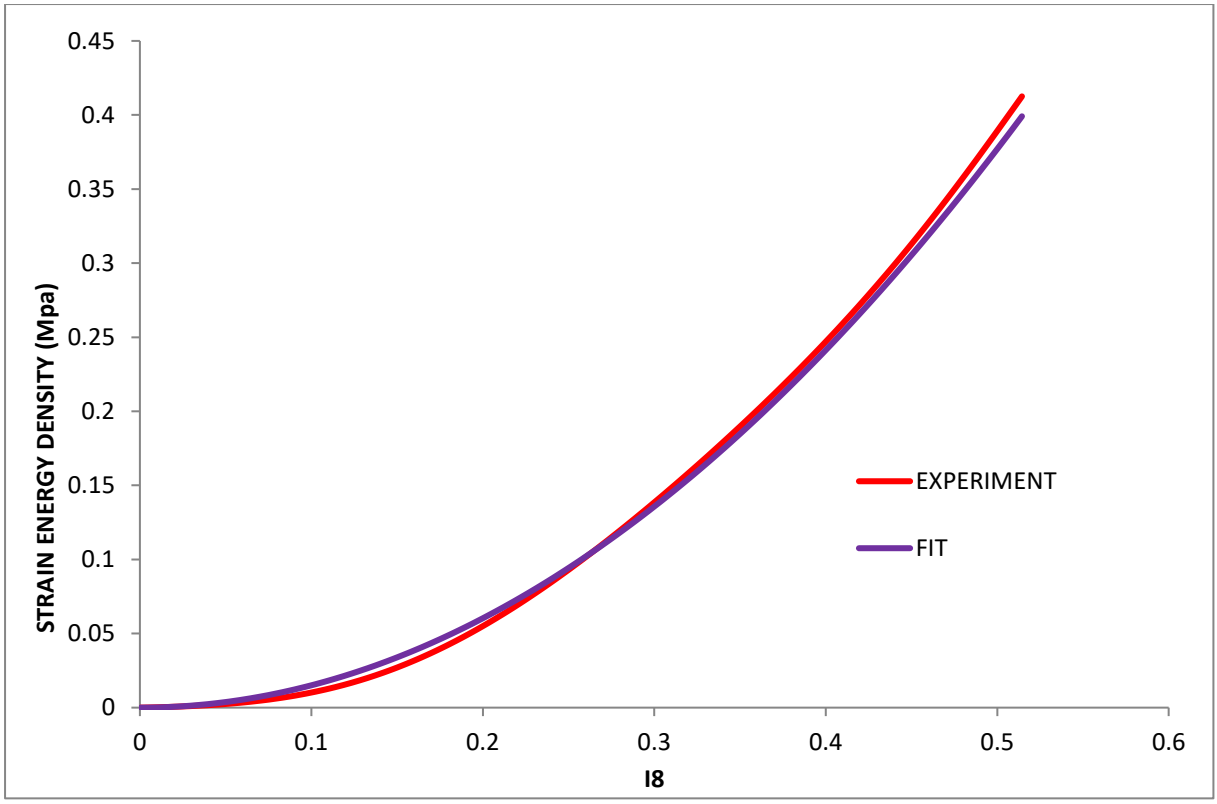

Figure 5. 15: Strain energy density against the invariant I_8 in the picture frame test for EXA-1196.

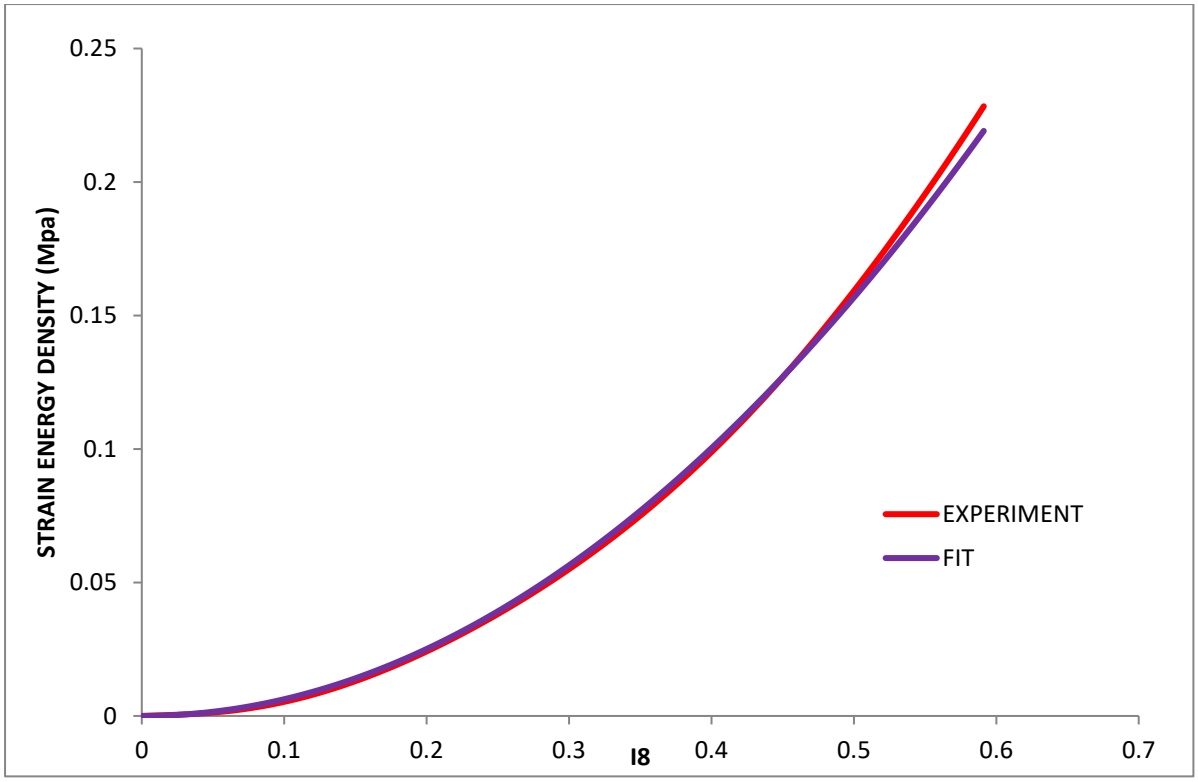

Figure 5. 16: **Strain energy density against the invariant I_8 in the picture frame test for EXA-1180.**

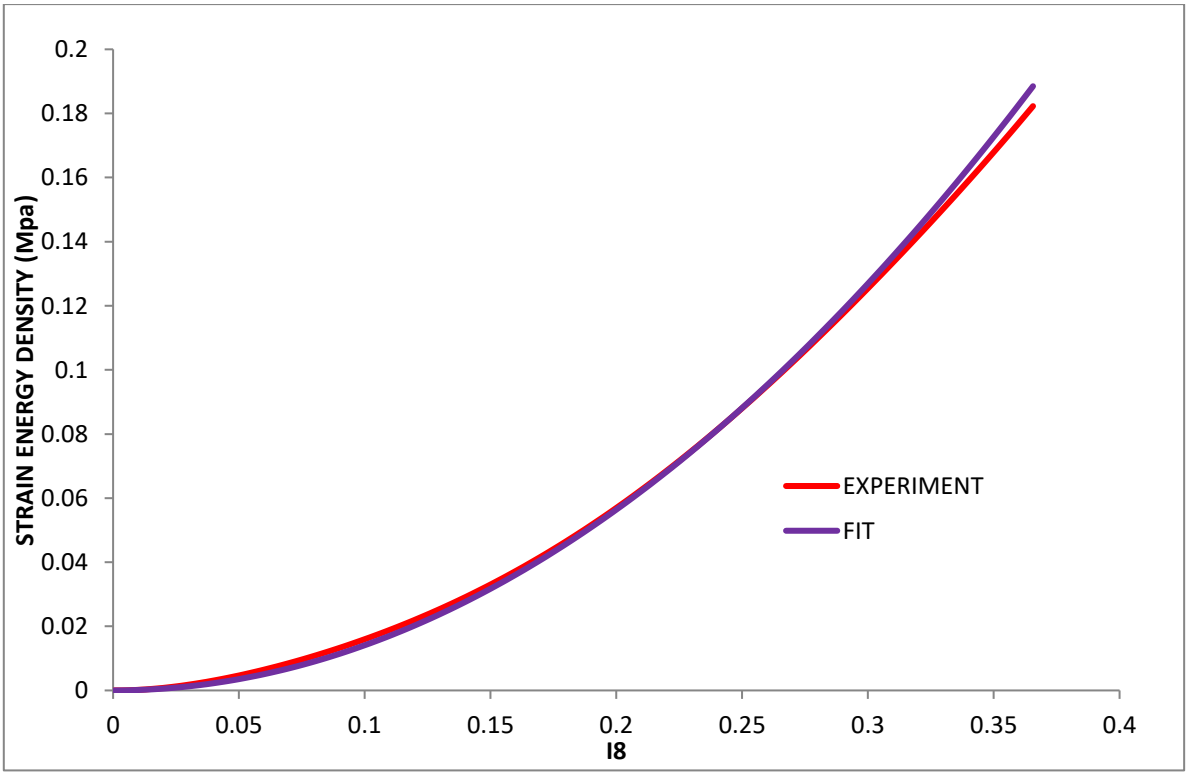

Figure 5. 17: **Strain energy density against the invariant I_8 in the picture frame test for EXA-1196.**

Finally, the overall strain energy functions Of the composite materials examined in this work (EXA 1182; EXA 1180 and EXA 1196), as expressed below, can be calculated by using the average values of the coefficients (in Pascals) as calculated from the fitting method described above.

$$W_{1182} = 19.08325 * 10^6 (I_1 - 3) + 94.622 * 10^6 (I_1 - 3)^2 + 4.424587861 * 10^6 (I_4 - 1)^3 + 2.839717581 * 10^6 (I_4 - 1)^2 + 0230801368 * 10^6 (I_6 - 1)^3 + 0.576619529 * 10^6 (I_6 - 1)^2 + 1.581610233 * 10^6 (I_8) \quad (5.20)$$

$$W_{1180} = 9.176475 * 10^6 (I_1 - 3) + 28.32975 * 10^6 (I_1 - 3)^2 + 0.060982146 * 10^6 (I_4 - 1)^3 + 0.865736274 * 10^6 (I_4 - 1)^2 + 1.636813 * 10^6 (I_6 - 1)^3 + 0.748147 * 10^6 (I_6 - 1)^2 + 0.515118094 * 10^6 (I_8) \quad (5.21)$$

$$W_{1196} = 49.47209 * 10^6 (I_1 - 3) + 258.7695 * 10^6 (I_1 - 3)^2 + 3.223707 * 10^6 (I_4 - 1)^3 + 7.012044 * 10^6 (I_4 - 1)^2 + 2.67571 * 10^6 (I_6 - 1)^3 + 3.382935 * 10^6 (I_6 - 1)^2 + 1.360031018 * 10^6 (I_8) \quad (5.22)$$

5.5 Numerical Validation of the Model

The developed hyper-elastic constitutive law was implemented in the FE software, where the ABAQUS/explicit Finite Element code was selected for its capacity to handle extremely fast dynamic loading conditions and deformations typical of the rate of loading adopted in the

laboratory for testing of the composite specimens. These use a ‘user material subroutine’, together with the results of the experimental uniaxial tensile tests in the warp and weft directions and the picture frame shearing tests.

All of the material parameters obtained in the constitutive model were used in Equations 5.20, 5.21, and 5.22 which was coded in FORTRAN and linked to ABAQUS for the composites (see Appendix 6).

The geometric model dimensions are 50 mm, 5 mm and 200 mm representing the width, thickness and length of the samples for the uniaxial tensile test. The geometric model dimensions for the picture frame test were 100 mm * 100 mm for different materials.

5.5.1 Mesh

Membrane elements (M3D4R, a quadrilateral membrane of four nodes, reduced integration, and hourglass control) were used for the simulation of 2500-elements. The main directions of the fibre were described using rectangular Cartesian coordinates.

5.5.2 Boundary Conditions and Loads

After the addition of a clamped boundary condition at one end, the model was steadily expanded at a rate close to that used in the laboratory. After deducing (from the material direction previously established for the model) the desired path of fibres, uniaxial test simulations of warp and weft were undertaken. All the degrees of freedom are fixed at the bottom, then the top has one degree of freedom in applied force direction and the side completely free.

5.5.3 Results and Discussion

From the development of a hyperelastic material model and the fact that the composite includes different volumes of the three materials of the isotropic hyperelastic matrix, the experimental data obtained from the uniaxial tension and picture frame were used to model the product behaviour.

For the different composites in the uniaxial simulation, varying loads were applied in the stretched directions of the warp and weft.

The resulting displacements and load distributions of the FE calculations are shown in Figure 5.19 (warp direction) and Figure 6.20 (weft direction). For a direct comparison of the experimental results and the simulation, respective displacements were taken from the centre of the sample.

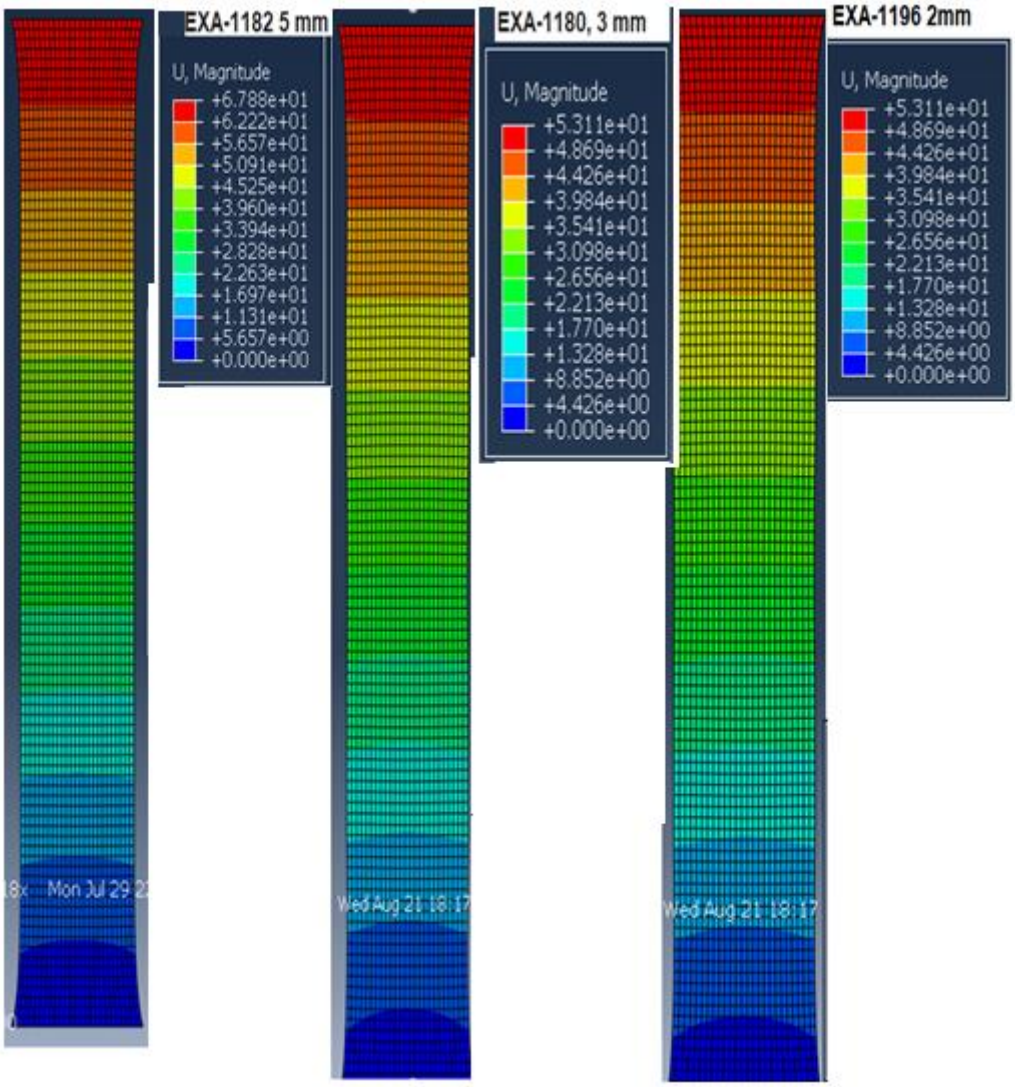

Figure 5. 18: **ABAQUS model of displacement distribution in a composite for warp direction.**

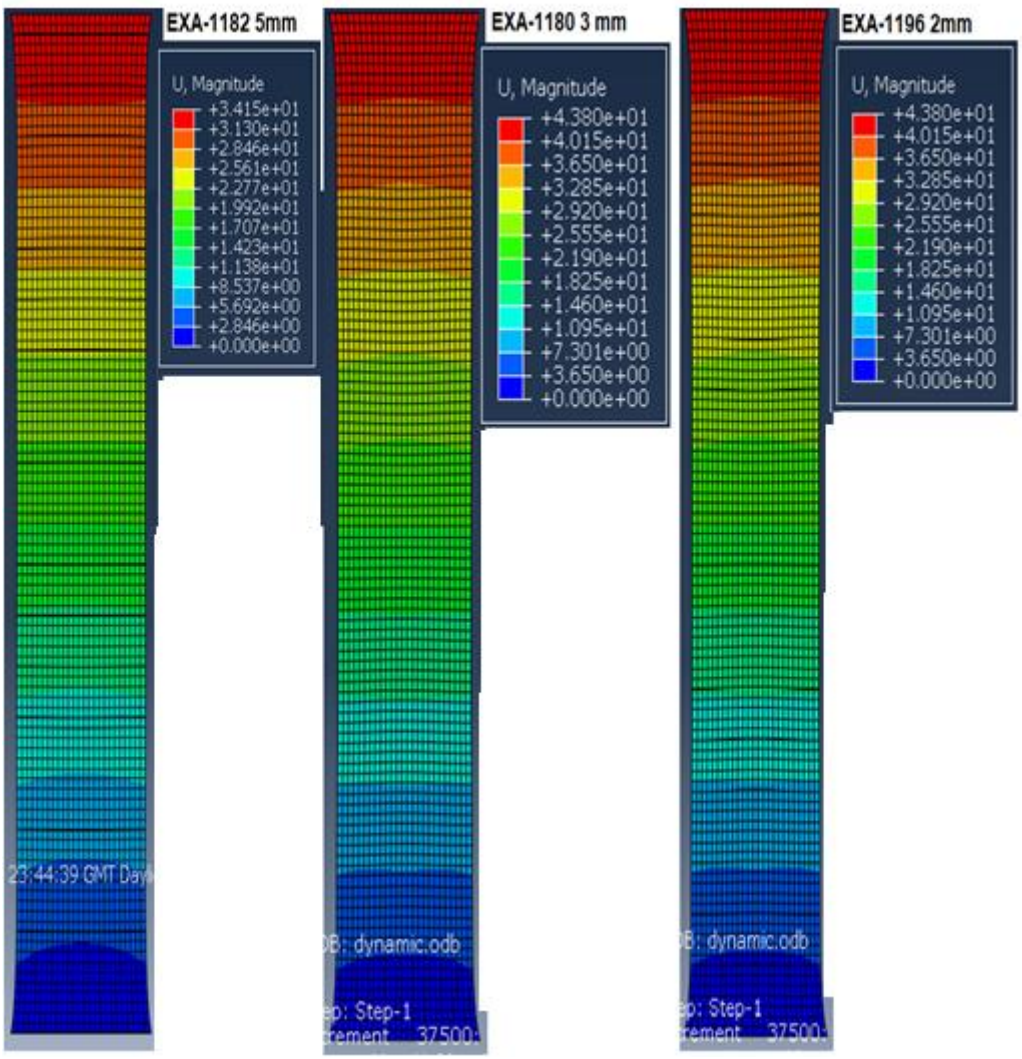

Figure 5. 19: **ABAQUS model of displacement distribution in a composite for weft direction.**

From Figures 5.21 to 5.26, the constitutive model shows close agreement with the corresponding experimental curves loaded parallel to the warp and weft directions. While the stress-strain relationships were similar, there was a closer agreement for the warp-oriented specimens. Appropriate comparisons were then possible between hypothetical loads and displacements obtained from ABAQUS modelling. These show that the new constitutive model is reliable for predicting material load-displacement behaviour. The same observation was obtained in the (Aboshio, 2014).

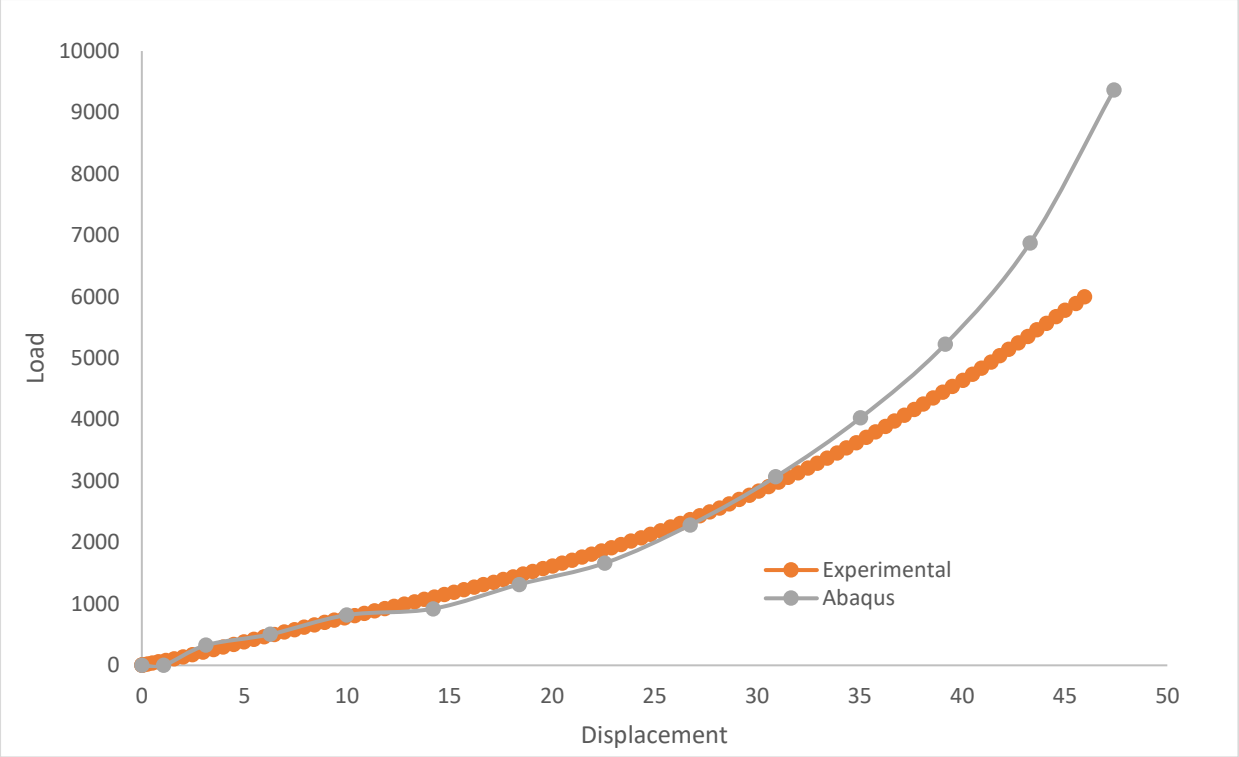

Figure 5. 20: **True load-displacement relation of the experimental and simulated model under uniaxial loading in the warp direction (EXA-1182).**

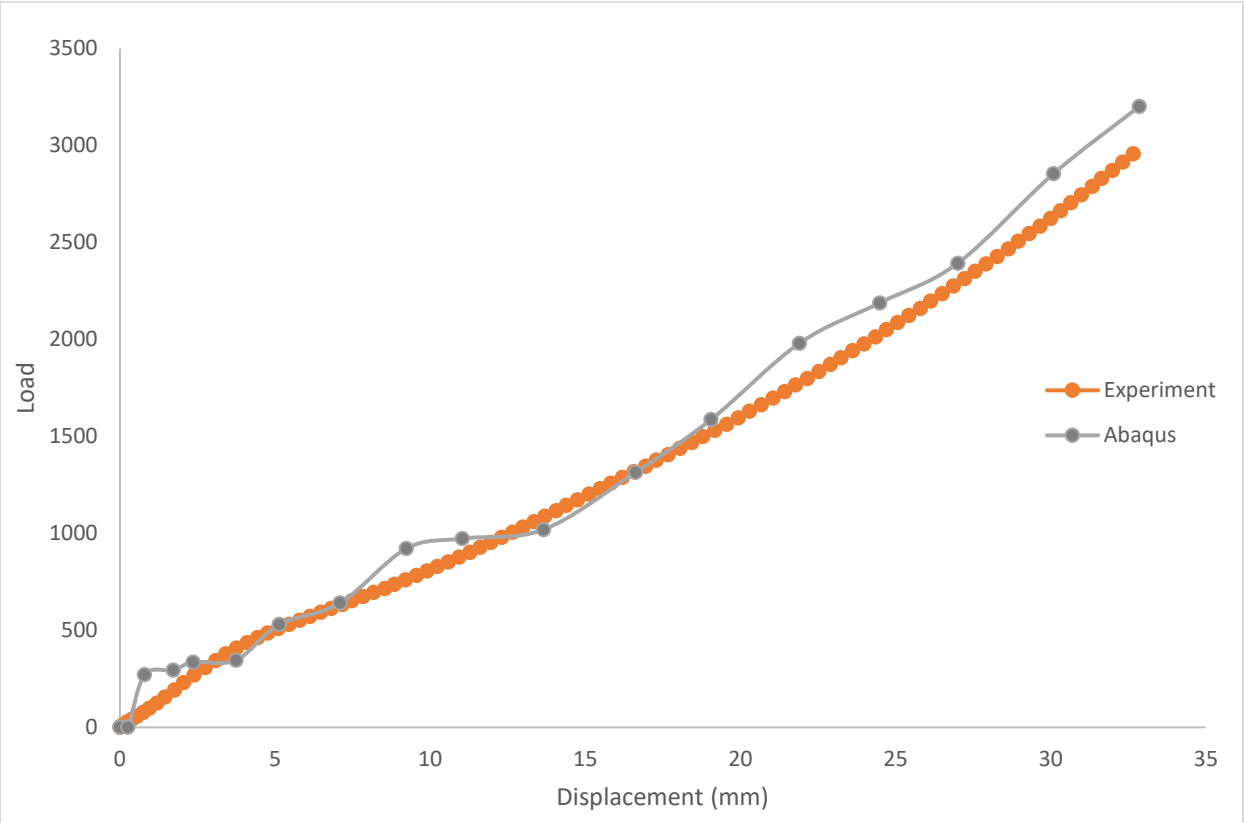

Figure 5. 21: **True load-displacement relation for the experimental and simulated model under uniaxial loading in the warp direction (EXA-1180).**

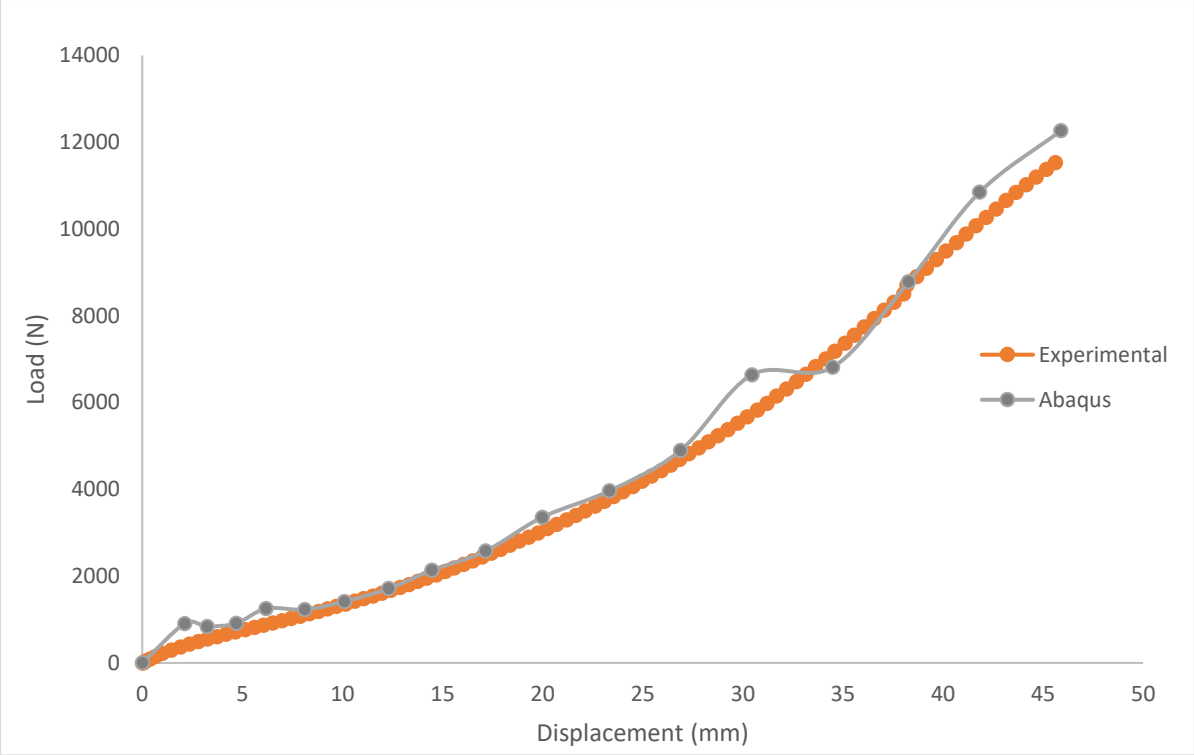

Figure 5. 22: **True load-displacement relation for the experimental and simulated model under uniaxial loading in the warp direction (EXA-1196).**

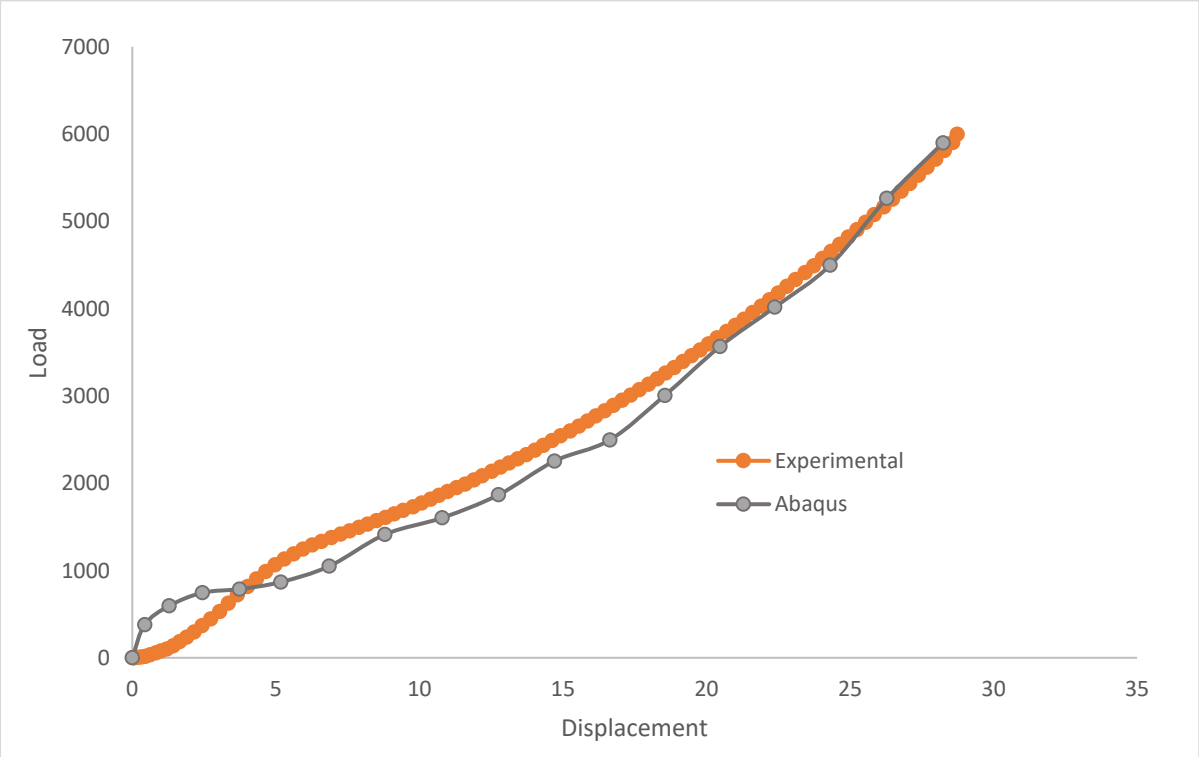

Figure 5. 23: **True load-displacement relation for the experimental and simulated model under uniaxial loading in the weft direction (EXA-1182).**

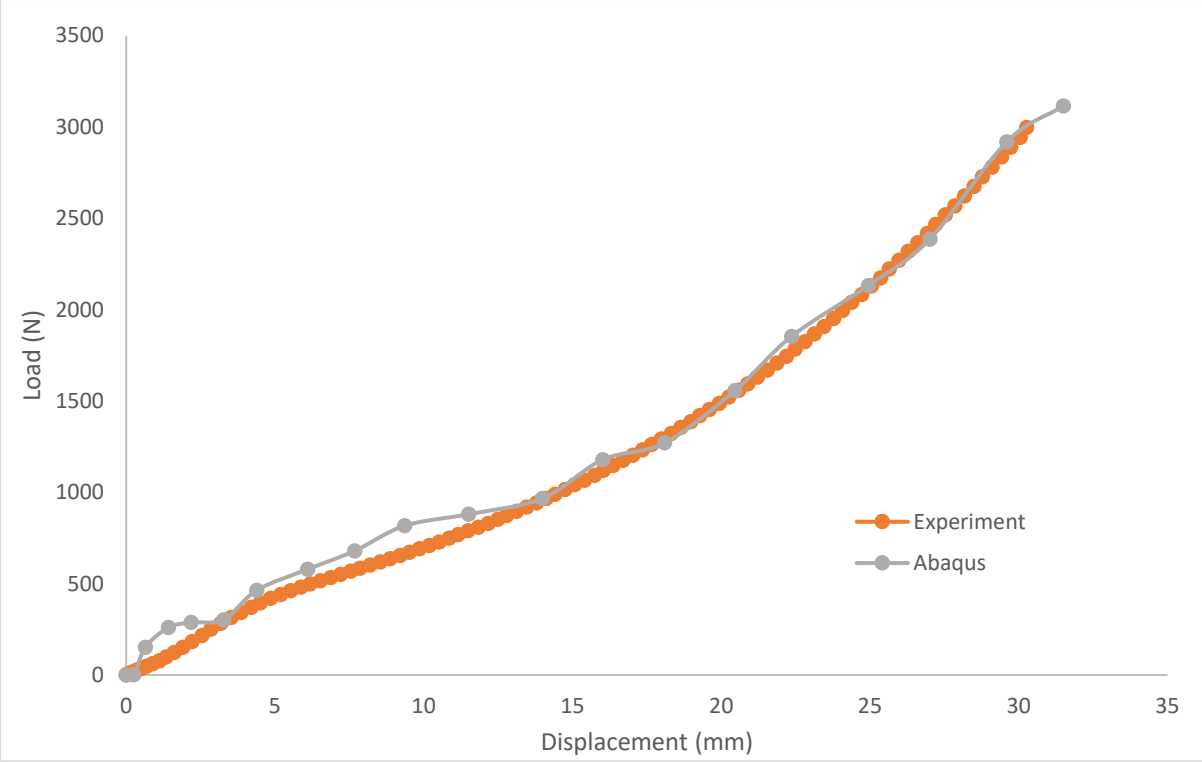

Figure 5. 24: **True load-displacement relation for the experimental and simulated model under uniaxial loading in the weft direction (EXA-1180).**

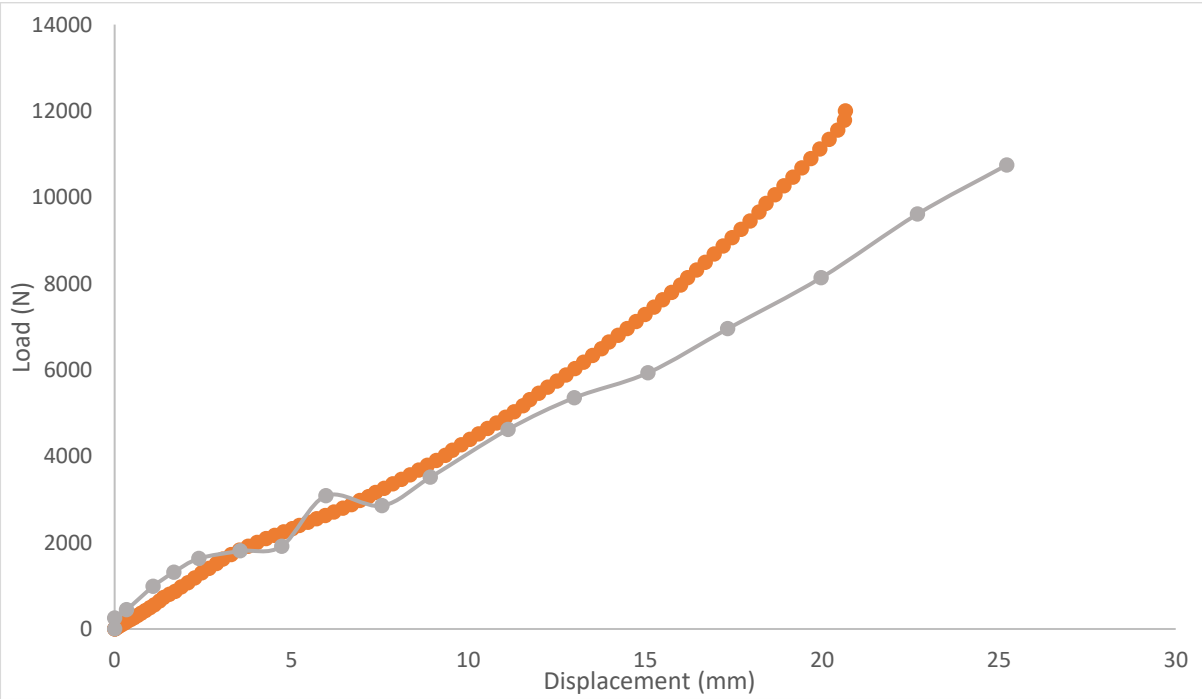

Figure 5. 25: True load-displacement relation for the experimental and simulated model under uniaxial loading in the weft direction (EXA-1196).

Close agreement between the experimental and the numerical simulations, demonstate that hypothetical models can simulate composite samples, with better agreement obtained for specimens loaded parallel to the warp direction than those loaded parallel to the weft direction. For the materials - where EXA-1196 has a thickness of 5 mm and EXA-1182 a thickness of EXA-1182 - both have the same matrix and fibre. Therefore, their only difference is the volume fraction. The effect of the thickness was apparent in both directions. EXA-1196 took almost double the load of EXA-1182, and a quarter of the load of EXA-1180. As the fibres are almost linear in the direction of the weft, they are modelled as such. All test orientations displayed nonlinear behaviour (hyperelastic).

5.6 Conclusion

In order to reflect the anisotropic nonlinear mechanical behaviour of woven composite fabrics during the deformation phase, a basic hyper-elastic fibre reinforced constitutive model was developed within the continuum mechanics system. For the proposed hyper-elastic model, to facilitate the determination of material parameters, the strain energy per unit volume was additively decomposed into tensile energy, compaction energy, and shear energy. The strain energy function that characterises a material's anisotropic behaviour can be described by four terms: interaction between fibres, the matrix, and fibre-fibre interactions in the warp and weft directions. From that basis, the processes of parameter determination were straightforward.

Ultimately, the proposed anisotropic hyper-elastic model was implemented to simulate uniaxial stress and picture-frame shear testing, with the comparison between numerical results and experimental evidence suggesting the validity and accuracy of the model

As always, many limitations apply to hypothetical models so a constitutive model that demonstrates realistic behaviour is difficult to obtain.

The comparisons and validations have demonstrated that the established constitutive model satisfactorily predicts the hyperelastic behaviour of composites described in this study.

Chapter Six

A bulge tester is a widely used test facility to apply near equibiaxial stress to a thin plate. This chapter deals with the method of bulge testing used in this project. The bulge test theory is presented after a brief overview and historical perspective of the technique. Bulge equations for samples are also presented. The general specification for the bulge test is then offered as guidance for manufacturing and mounting.

6.1 Introduction

This chapter describes a methodology for the precise mechanical experimental setup for bulge testing an amorphous hyperelastic rubber-like material (PVC-coated nylon woven fabric composites of different thicknesses). Many loading methodologies exist for applying biaxial charging. The basis of the method used in this chapter is the inflation of a thin material sheet into a bubble by pressurised oil. This requires accurate pressure calculation and determination of the strain distribution around the bubble axis.

It takes due note of the degree of precision needed or the intended function of the to-be-designed composite structure, the selection of test techniques is based on its benefits, limits, and availability. Except for specific circumstances, the uniaxial test technique may be deemed acceptable for analysing the material mechanical behaviour for modest extensions of composite materials. Yet, owing to testing equipment limitations, this test is seldom carried out to the point of failure of these materials.

6.2 Bulge Equipment Setup

- The bulge test system (Figure 6.2) consists of the following subsystems:
- The liquid pressure chamber.

- A pressure sensor with electrical signal output.
- A source of compressed oil (Hydraulic Pump).
- A control system: PC-based microcontroller system (Arduino).
- A bulge height measurement system (DIC by Imetrum system).

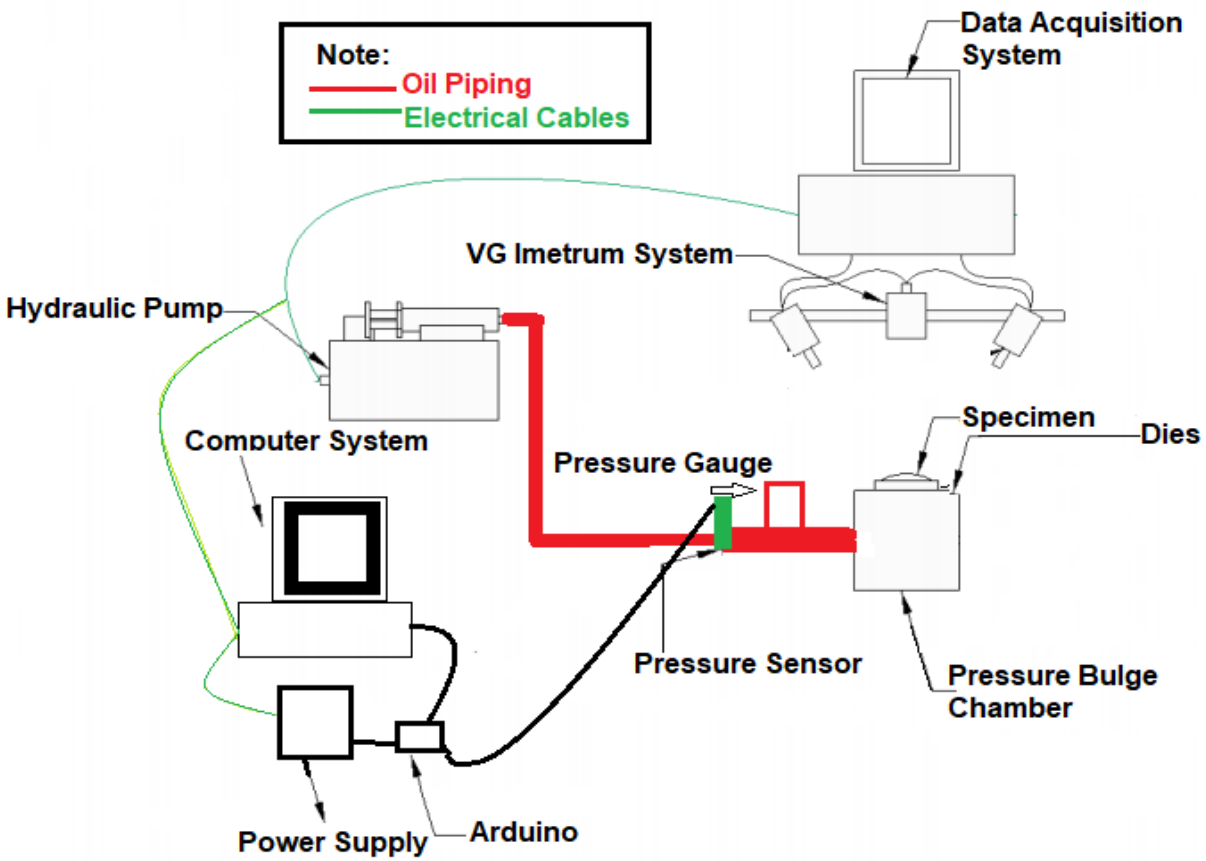

Figure 6. 1: A systematic overview of the setup of the bulge.

6.2.1. Assembly of the Bulge Chamber

The specimen was placed between the top of the pressure chamber and a ring-shaped steel plate used as a die. The diameter of the opening of the pressure chamber, as well as the inner diameter of the die, was 100 mm and the outer diameter of both the pressure chamber and the die was 180 mm. The polymer specimen was pressed between the die and the blank contour of the

pressure chamber top in the way depicted (see Appendix 7) using metal clamps. No lubrication was used at the interface between the blank and die surface. The reservoir was fitted with a hydraulic pump and pressure gauge for the inflation of the composite membrane.

6.2.2. Pressurisation System

Acting as a driving force, a high-pressure pump is required to reach 30 bar or more for composite material specimens. The Enerpac ZE3204MB electric induction pump contains a 115V/1 HP induction electric motor for durability, holds up to 1 gallon of hydraulic fluid and is suitable for powering a single-acting hydraulic cylinder or tool. Induction motors are suitable for use in harsh environments. The pump's moulded covering helps protect the motor. A steel guard protects the motor's fan. The reservoir is made of steel. A 40-micron filter helps to remove impurities, so keeping the hydraulic fluid clean. The pump has a sight gauge for monitoring the fluid level. The three-way, two-position manual valve offers advance and retract flow paths and controls the direction of the hydraulic fluid in a single-acting system. The output flow rate is 40 cubic inch per minute at a maximum operating pressure of 10,000 psi (pounds per square inch). An adjustable relief valve helps prevent overloading (see Appendix 7).

6.2.3. Pressure Sensor and Control System

Figure 6.3 (A) illustrates the pressure sensor that is widely used. It was designed to be fitted with an external pressure transducer to continually monitor and record the internal pressure of the pressure chamber of the bulge check die. The pressure sensor is used to measure the pressure of the liquid (or gas). The displayed pressure is the expression of the force needed to stop the expansion of the fluid and is usually indicated in terms of force per unit area. The pressure transducer was selected for its compatibility with the hydraulic press control system and data acquisition system. The pressure sensor generates an electrical signal relating to the

pressure applied and has a range between 0 and 25 bar. The voltage measurement sockets located on one side are shown in Figure 6.3 (B). Figure 6.3(C) shows the Arduino board connected to the power supply and the PC.

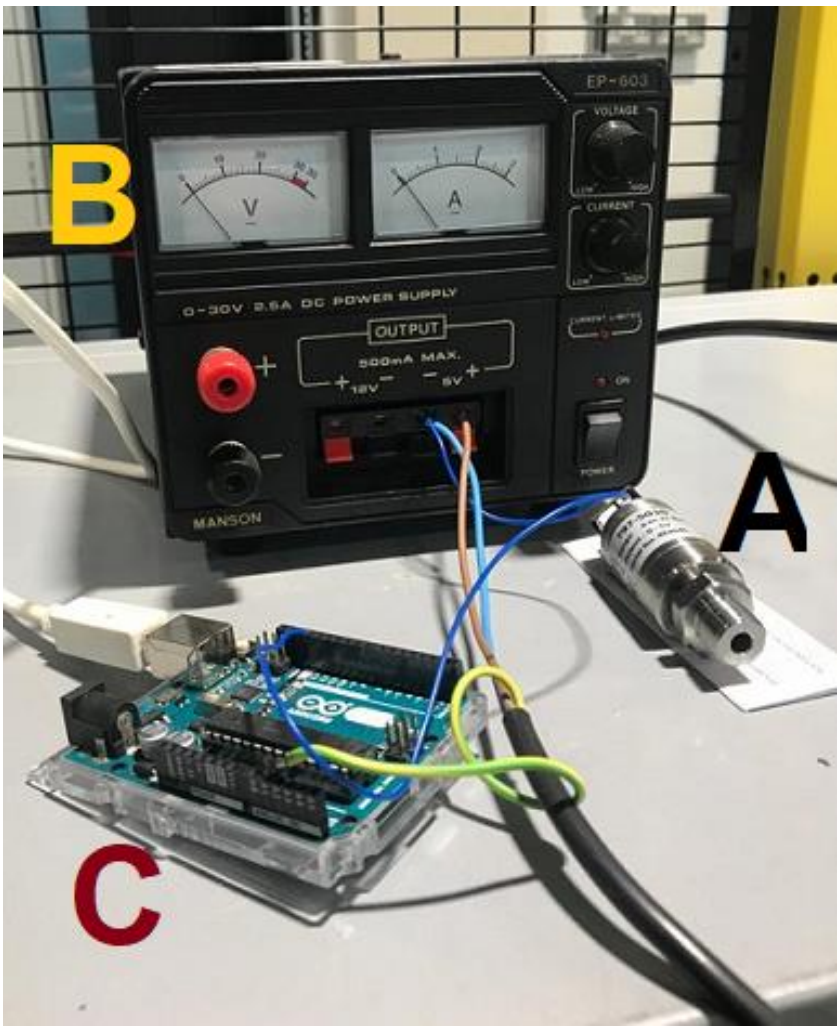

Figure 6. 2: (A) The pressure pump system. (B) Power supply. (C) Arduino.

6.3. 3D measurements

Experimental mechanical research methods such as the bulge test rely heavily on surface displacement field estimation. The DIC measurement techniques reported in chapter 3 take a full-field optical approach that uses pattern tracking and stereovision-based analysis. This technique tests the surface characteristics of a specimen undergoing a user-defined mechanical

test load (Yoneyama and Murasawa, 2009). Thus, the technique is suitable for measuring displacement and strain, where it can create a three-dimensional map of images of the surface of the whole specimen (mechanically tested). Moreover, the 3D system can be used to measure the shape of the 3D bulge and thus determine its maximum height.

6.4. Experimental Procedure

Bulge tests were performed in a custom-built hydraulic bulge testing facility. The specimen was placed between the top of the pressure chamber and a ring-shaped steel plate used as a die. The diameter of the opening of the pressure chamber, as well as the inner diameter of the die, was 100 mm and the outer diameter of both the pressure chamber and the die was 180 mm. The polymer specimen was pressed between the die and the blank contour of the pressure chamber top in the way depicted in Figure 6.4, using metal clamps. No lubrication was used at the interface between the blank and the die surface. The reservoir was fitted with a hydraulic pump and pressure gauge for the inflation of the composite membrane.

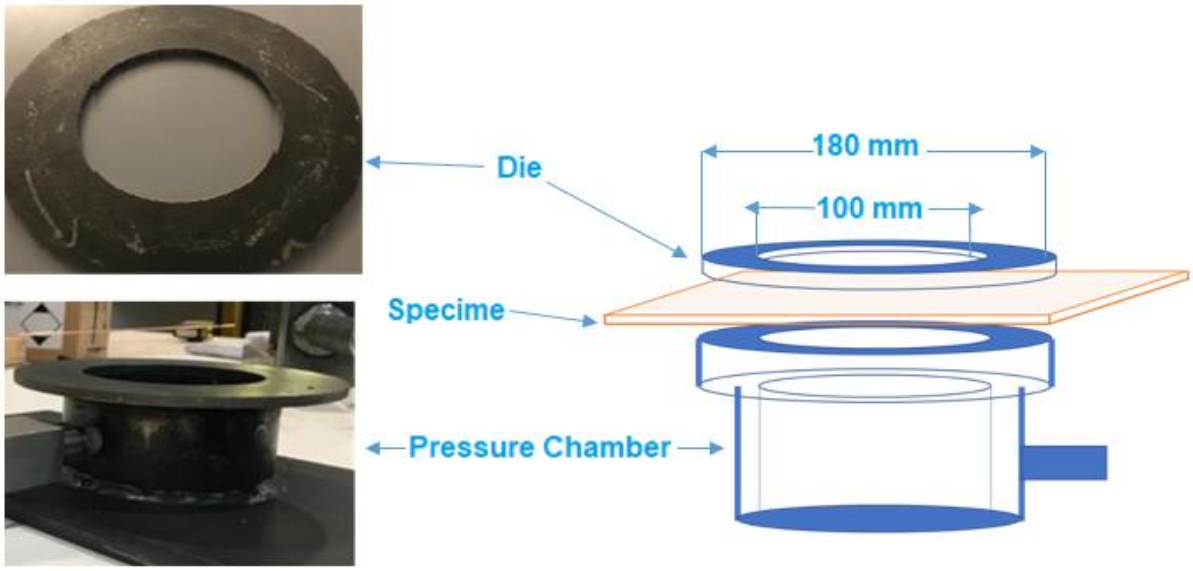

Figure 6. 3 Assembly of a pressure chamber, die and specimen for the bulge test.

Figure 6.5 shows an overview of the complete setup of the bulge test including the hydraulic pump, pressure gauge, pressure chamber, video cameras, lighting system and the appropriate computer systems controlling and measuring the oil pressure and the strain behaviour of the specimen.

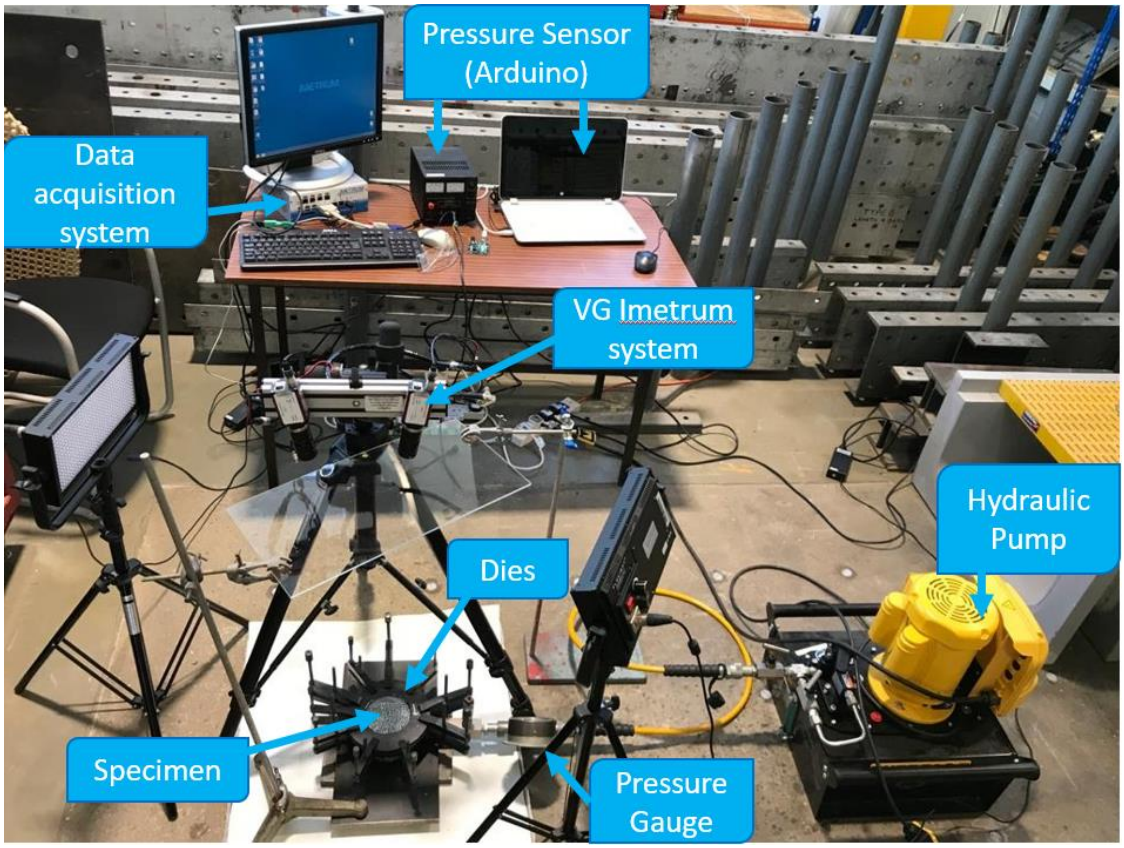

Figure 6. 4: **Schematic of the bulge testing facility, showing the bulge tester, the pressurising unit, and the video gauge system.**

The bulge deformation was monitored via video gauge after spray-painting a coarse white speckle pattern on the surface of the specimen. As the DIC recorded strain and displacement, the pressure was recorded using appropriate "Arduino" software. Pressure sensors are connected (Arduino) and interfaced with the computer. The pressure signal was transmitted every 10s through the Arduino. Using one video camera, two-dimensional video gauging allowed image pixels to be used as a native 2D coordinate system. By comparing digital images

of the test surface before and after deformation (see Figure. 6.6), measurements of full-field strains, ε_{xx} and ε_{yy}, and shear strain, ε_{xy}, were obtained.

Figure 6. 5: **Hydraulic bulge test with the video gauge system utilising two cameras.**

The utilisation of a second camera, synchronised with the first, allowed for strain and location measurements in the direction of the viewing axis of the camera system. It allocated X-, Y- and Z-co-ordinates to each of the measurement points on the bulging surface, so creating an accurate 3D coordinate frame. These 3D measurements also included the height of the dome, resulting from the viscous pressure under the material during the bulging experiment (see figure. 6.6).

6.5. Theoretical Investigation

The hydraulic bulge was used to test sheets of composite materials under a state of equibiaxial stress (tension). Based on the balance of the forces on the small circular element in the centre of the membrane, and by presuming the ratio of the thickness of the sample to the size of the bulge to be small, the average membrane stresses can be determined (Aboshio et al., 2015; Campos et al., 2014; Ranta-Eskola, Santos, et al., 2010; 1979; Gutscher et al., 2004). To determine the stress curve from the bulge test, the pressure and the dome height can be respectively determined with a pressure transducer and video gauge. When an internal gauge pressure P is applied to a specimen, it deforms into a dome of radius r and wall thickness t. As shown in Figure 6.7, the bulging specimen can be regarded as a thin-walled spherical pressure vessel in its deformed form. Since the spherical specimen is under static conditions, the stress must balance the inner pressure.

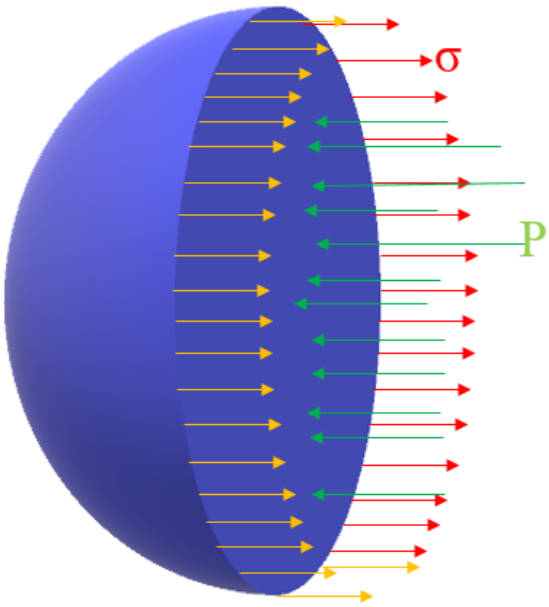

Figure 6. 6: **Depicted is the cross-section of a spherical pressure.**

Centred at the equilibrium force of a small circular feature at the centre of a membrane and assuming that the specimen's thickness to the bulge ratio is small, the average axial symmetric membrane tension is given by

$$\frac{\sigma_1}{\rho_1} + \frac{\sigma_2}{\rho_2} = \frac{P}{t} \tag{6.2}$$

Where σ_1 and σ_2 are the principal surface stresses, ρ_1 and ρ_2 are the corresponding principal radii of the curved surface, P is the hydraulic pressure, and t is the thickness of the membrane at the pole (see Figure 6.8).

Equation (6.2) relates to the general case in which $\sigma_1 \neq \sigma_2$ and $\rho_1 \neq \rho_2$. Based on the balance of forces of the small element in the centre of the membrane, and by assuming the ratio of the thickness of the sample to the size of the bulge to be small, then $\sigma_1 = \sigma_2 = \sigma$ and $\rho_1 = \rho_2 = \rho$, so resulting in the axisymmetric case (Aboshio et al., 2015; Campos et al., 2014; Ranta-Eskola, Santos et al., 2010; 1979; Gutscher et al., 2004). This allows equation (6.1) to be simplified to:

$$\sigma = \frac{P\rho}{2\,t} \tag{6.3}$$

Where σ is the biaxial stress, P is the bulging pressure, ρ is the instantaneous radius at the apex of the dome, and t is the thickness of the membrane at the pole.

Irrespective of the anisotropy of the material of the dome, given the presumed hemispherical shape of the bulging membrane, the radius of curvature can be calculated by:

$$R = \frac{a^2 + h^2}{2\,h} \tag{6.4}$$

Where R is the radius of the fillet of the cavity, a is the initial radius of the circular diaphragm specimen, and h is the dome height after deformation, assuming that the dome is spherical (Merle, 2013; Hill, 1950; Ramezani et al., 2010; Aboshio et al., 2015; Vasilescu, 2016).

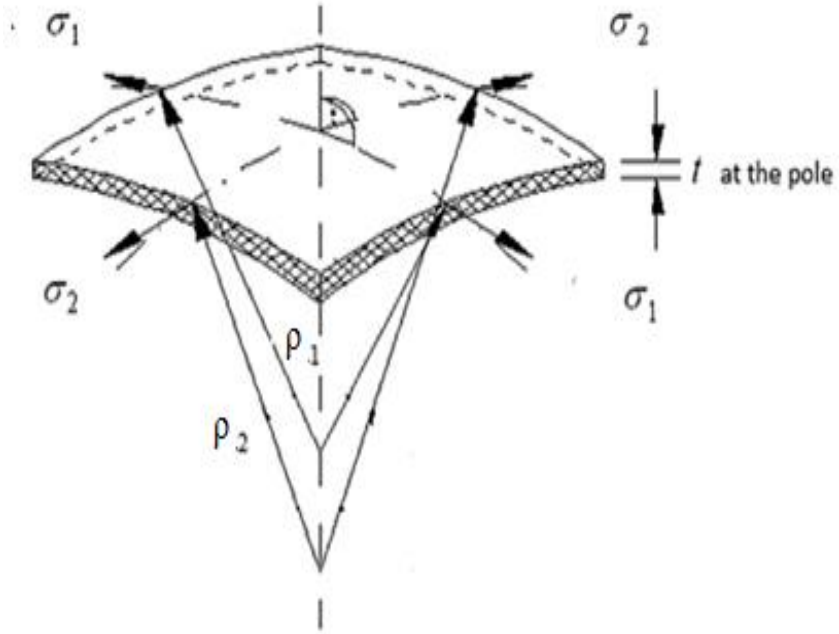

Figure 6. 7: Biaxial stress state of a membrane under the bulge test at the pole (Aboshio et al., 2015)

With the assumption that the bulge is spherical, Hill used analytical methods to describe the deformation in the hydraulic bulge test (Hill, 1950). The thickness at the top of the dome is then calculated using the following equation:

$$t = \frac{R - \sqrt{R^2 - t_0\, C_0^2}/2h}{2} \cong t_0 \left(1 + \frac{h^2}{a^2}\right)^{-2} \qquad (6.5)$$

Where C_0 is the initial gauge length measured perpendicular to the bulge axis, a is the radius of the circular specimen, and the other variables are as previously defined.

6.6. Results and Discussion

Figure 6.9 shows the height at the top of the dome (mm) against the applied fluid pressure for the different materials tested, using the methods for measurement discussed above. The polar heights are determined via a 3D coordinate video gauge using two coordinated cameras.

All the graphs display a parabolic shape. Those for the EXA-1182 and EXA-1196 samples are very similar: at a maximum pressure of 25 bar, maximum bulge heights of 19 mm and 26 mm were recorded for the EXA-1196 and EXA-1182 samples respectively. Up to a pressure of 13 bar and a dome height of 16 mm, the graph for the 3mm sample is similar to those for the other samples. Thereafter, the size of the dome and its height remained constant until the end of the experiment at 25 bar. The explanation for the difference between the 2mm and 5mm samples, and the 3mm sample, lies with the denser interlaced weaving pattern. The different characteristics of the 3mm sample might also be associated with a locking mechanism that prevents further crimping, even as the stress on the sample is raised by increasing oil pressure. In summary, the results in Figure 8 indicate that the bulge test properties of PVC woven fibre-reinforced composite are influenced by the stitching yarn form, directions and density.

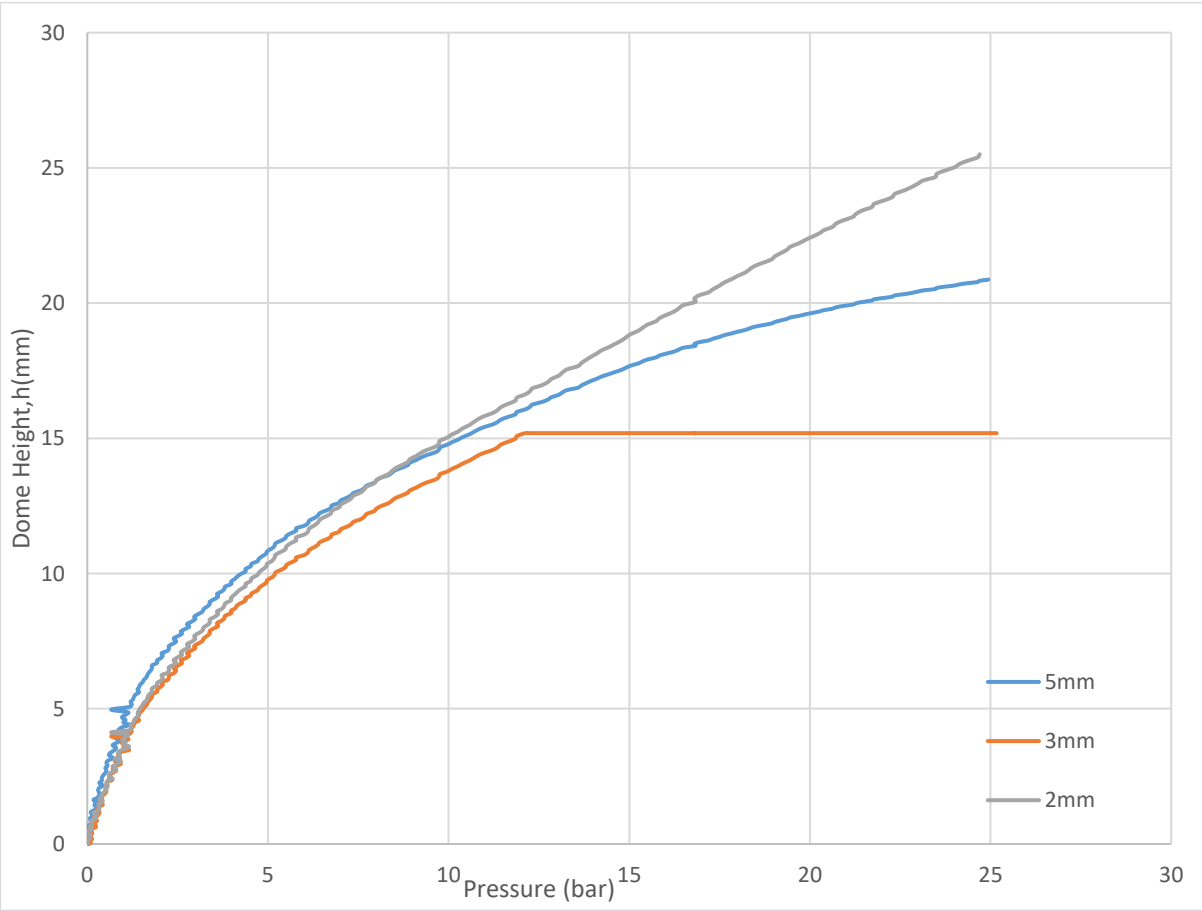

Figure 6. 8: **Pressure versus dome height.**

As calculated by equation (5.4), as the radius of the die increases, the pressure decreases as a function of the polar height (see Figure 6.10). The effect of different material thicknesses on these graphs is minimal.

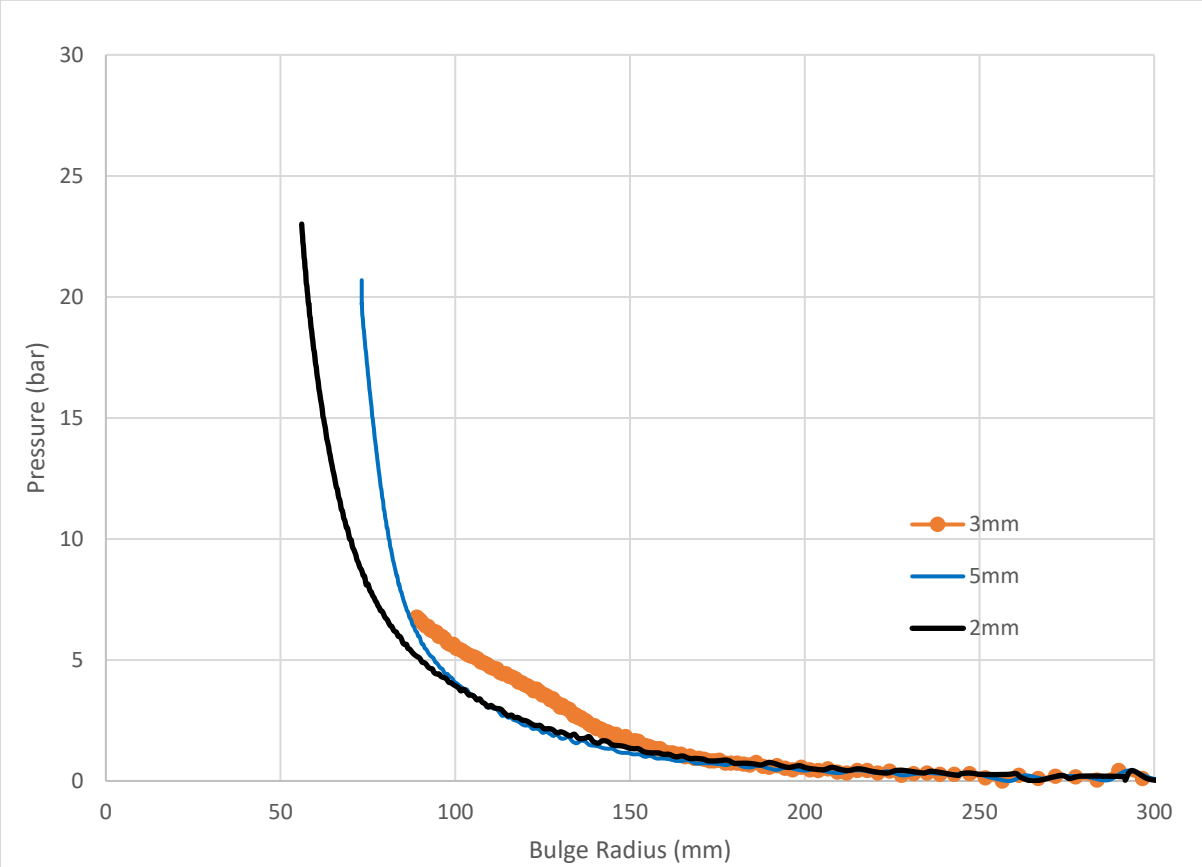

Figure 6. 9: **Dome height versus bulge radius.**

As calculated by equation (5.5), the thickness at the top of the dome is plotted against its height for various materials (see Figure 6.11). As the oil pressure increases, the bulge grows and the dome height increases. At the same time, the material is stretched and the material thickness decreases. The change in thickness of the EXA-1196 sample is greater than that of the EXA-1180 or the 2mm sample. The thickness at the pole decreases as the dome height increases, and this thinning effect increases rapidly towards the end of the procedure.

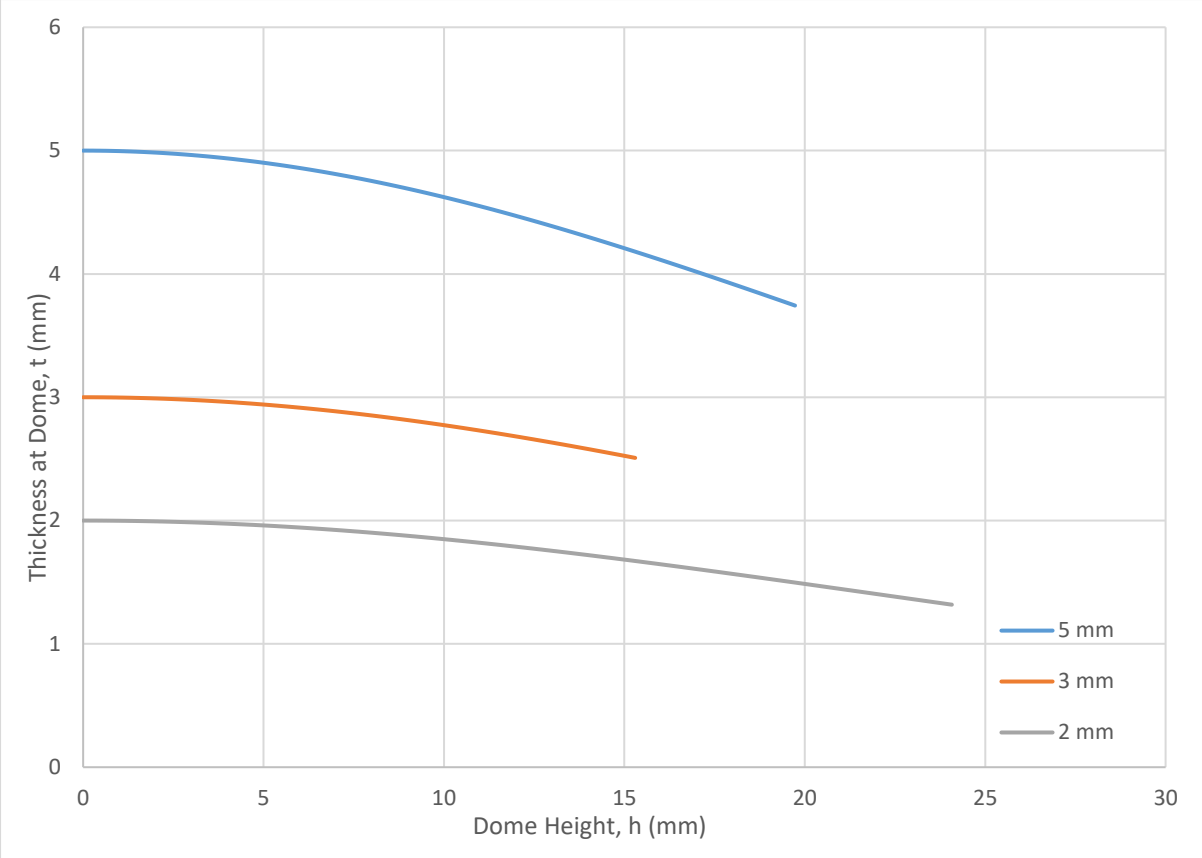

Figure 6. 10: Thickness variation versus dome height.

Figure 6.12 compares the actual strain with the theoretical strain as calculated by equation (5.3). Stress was calculated using equation (5.2) for the three types of material. There was a significant difference between the theoretical and experiential results. For minimal strains, both experimental results were well matched with theoretical expectations, but for greater stress values, the experimental strain response was below the theoretical expectations for all materials.

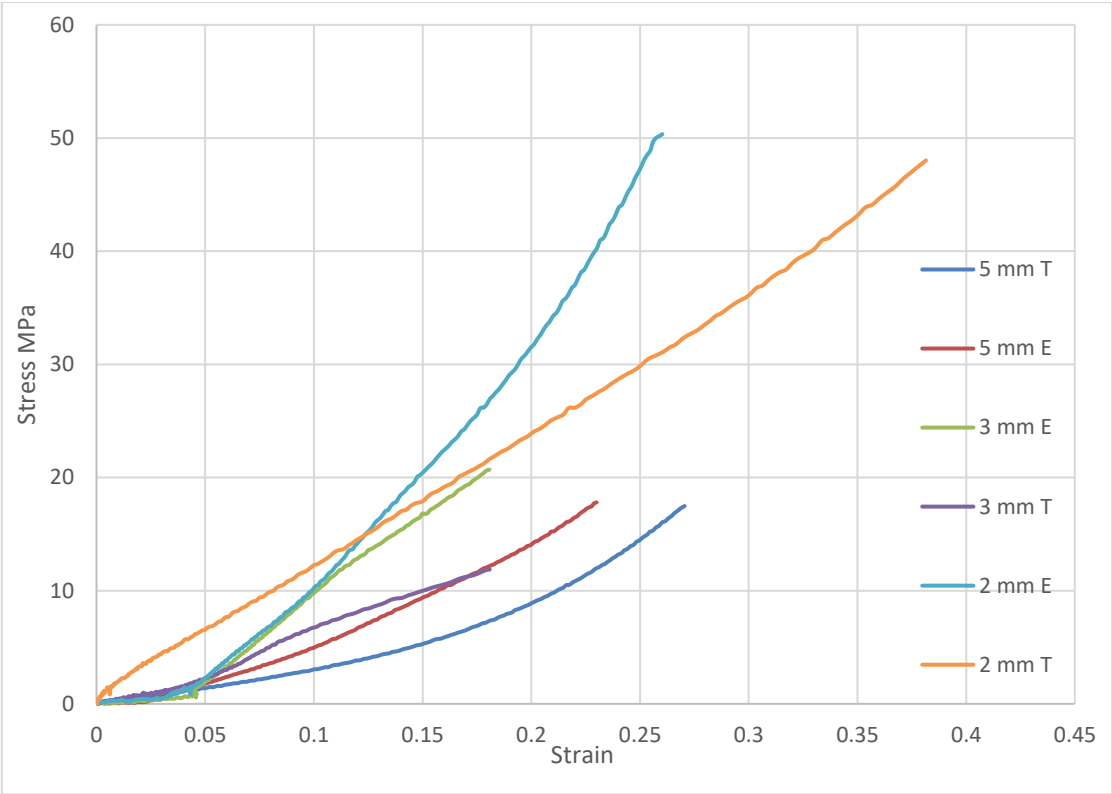

Figure 6. 11: **Stress versus strain theoretical (T) and experiential (E).**

Results of uniaxial testing and hydraulic bulge testing by video gauge have been reported for samples loaded parallel to each of the weft and warp fibre directions as shown in chapter three. The video gauge system was used to capture the strain measured from the sample surface during testing. The strains (stretches) in the weft direction were lower than those in the warp direction.

Figure 6.13 shows the stress versus strain from the bulge test, while Figure 6.14 shows the stress versus strain for the tensile test. Samples loaded parallel to the weft fibre direction attained a higher strain level compared to the same samples measured in the tensile test. In addition, for both tests, the samples loaded in the weft fibre direction attained higher strains than the samples loaded in the warp fibre direction.

Samples were loaded in parallel to the warp fibre direction had approximately the same strain levels during the hydraulic bulge test and the tensile test. The stress experienced by the material

during the tensile test was generally much larger than the stress in the hydraulic bulge test, no matter whether the samples were loaded in parallel to the weft or warp fibre directions. In the uniaxial tension, much larger strains for the EXA-1182 material were observed compared with the other two sheets with thicknesses of EXA-1196 and EXA-1180. The results obtained from the different mechanical characterisation methods show the contrast between the mechanical behaviours of the specimen under the different load conditions imposed by these two methods. The data gained from the different methods can complement each other for a better insight into the mechanical behaviour of anisotropic specimen.

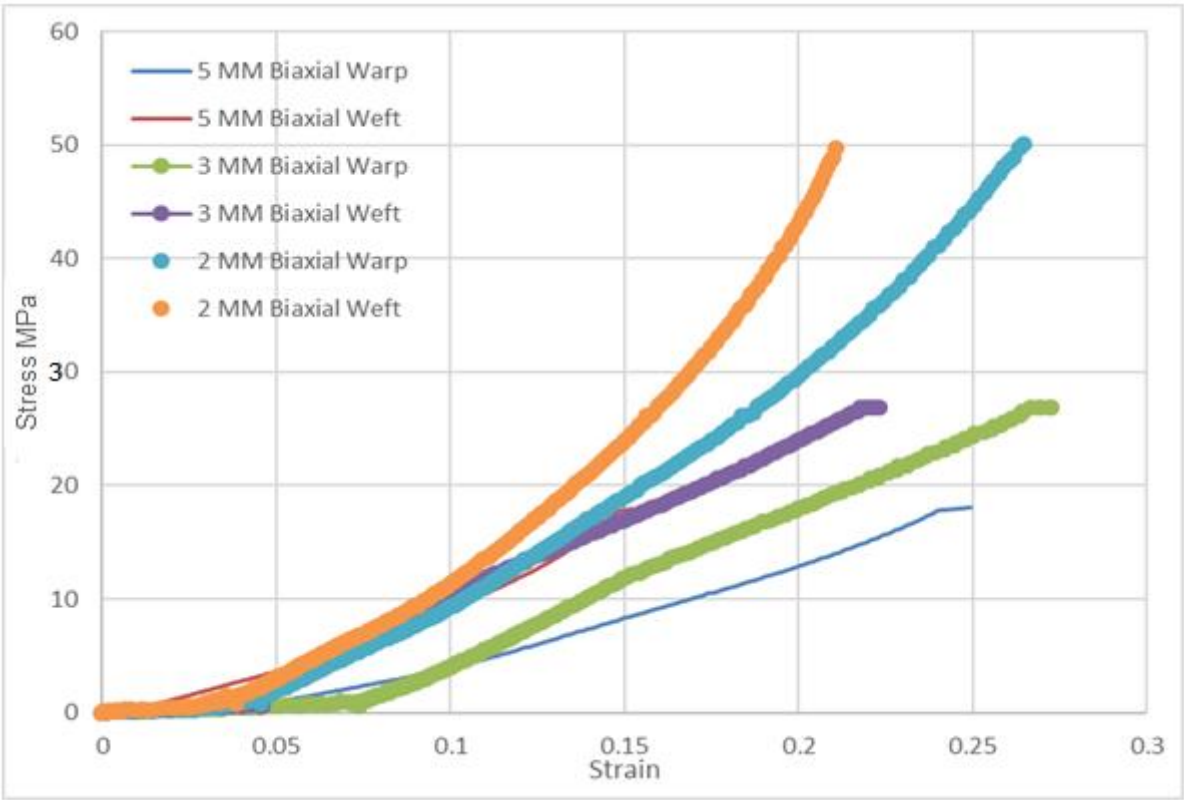

Figure 6. 12: Stress versus strain (bulge test).

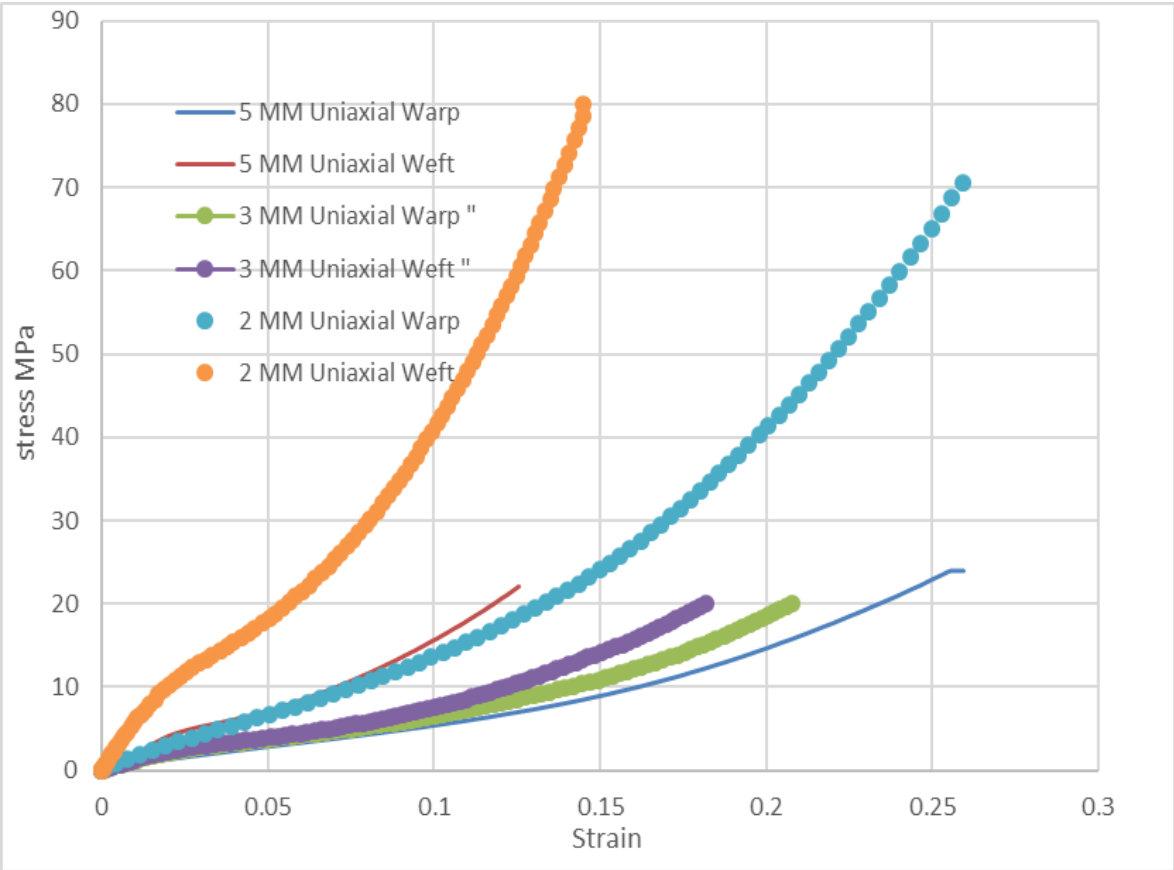

Figure 6. 13: Stress versus strain (tensile test).

Comparison of the tensile test with the bulge test is performed using the curve shape of the material observed in the bulge test. The fact that the sample is initially flat but then deflects slightly, which is caused by the biaxial stress state, reflects anisotropic mechanical behaviour caused by the way the composite sheets are produced. The bulge test offers basic knowledge of the material behaviour of these composite materials. Strain from the bulge tests shows deviations from the anisotropic behaviour observed under uniaxial tension.

The video obtained by the high-speed camera was post-processed with the video gauge software in order to measure strain at different angles under biaxial stress conditions. Video gauge allows the strain gauge to undergo free rotation in seven directions in forming an angle with the warp direction on the surface of the specimen ((warp) 0°, 15°, 30°, 45°, 60°, 75°, 90°

(weft)), as shown in figure 6.15. The deformation was recorded in the central zone of the sample.

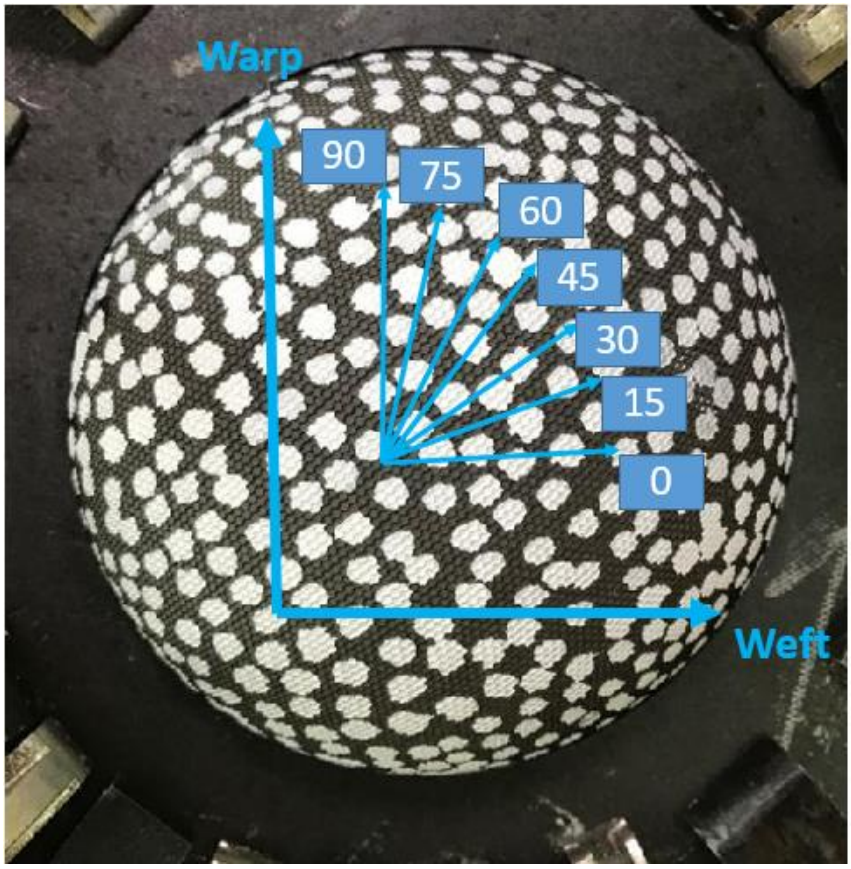

Figure 6. 14: **Schematic view of directions (angles) in the strain direction.**

As illustrated in figures 6.16, 6.17 and 6.18, for materials of different thicknesses, the observed behaviour of the stress versus strain experienced at different angles to the warp direction was nonlinear. The nonlinearity is especially visible at the start of the experiment with relatively small pressure, strain and stress. As the experiment increases pressure, the plot of the relationship between stress and strain becomes increasingly linear for all measured angles. In the initial widespread nonlinear region, the relevant parameters are the structure of the thread, the crimp, the slip between warp and weft yarns, and the initial yarn undulation. In addition, the material thickness has a substantial effect on the observed tension.

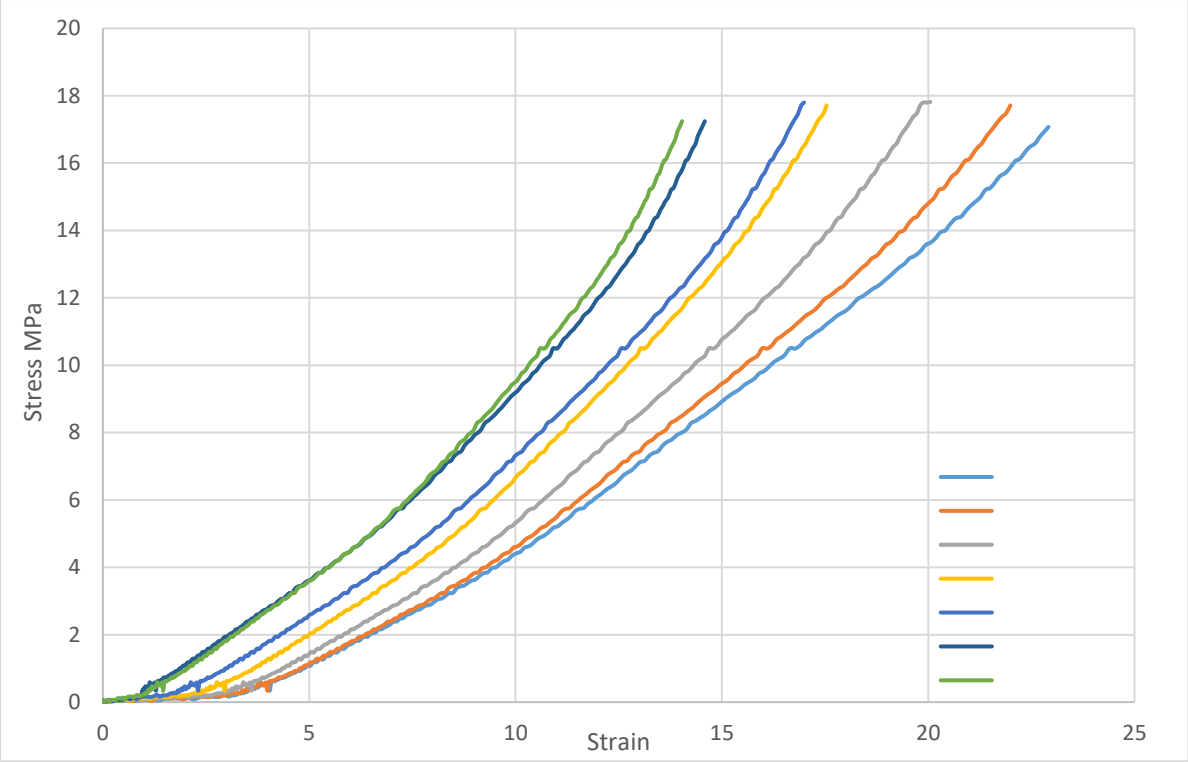

Figure 6. 15: Stress versus strain for all orientation angles θ for materials of EXA-1196.

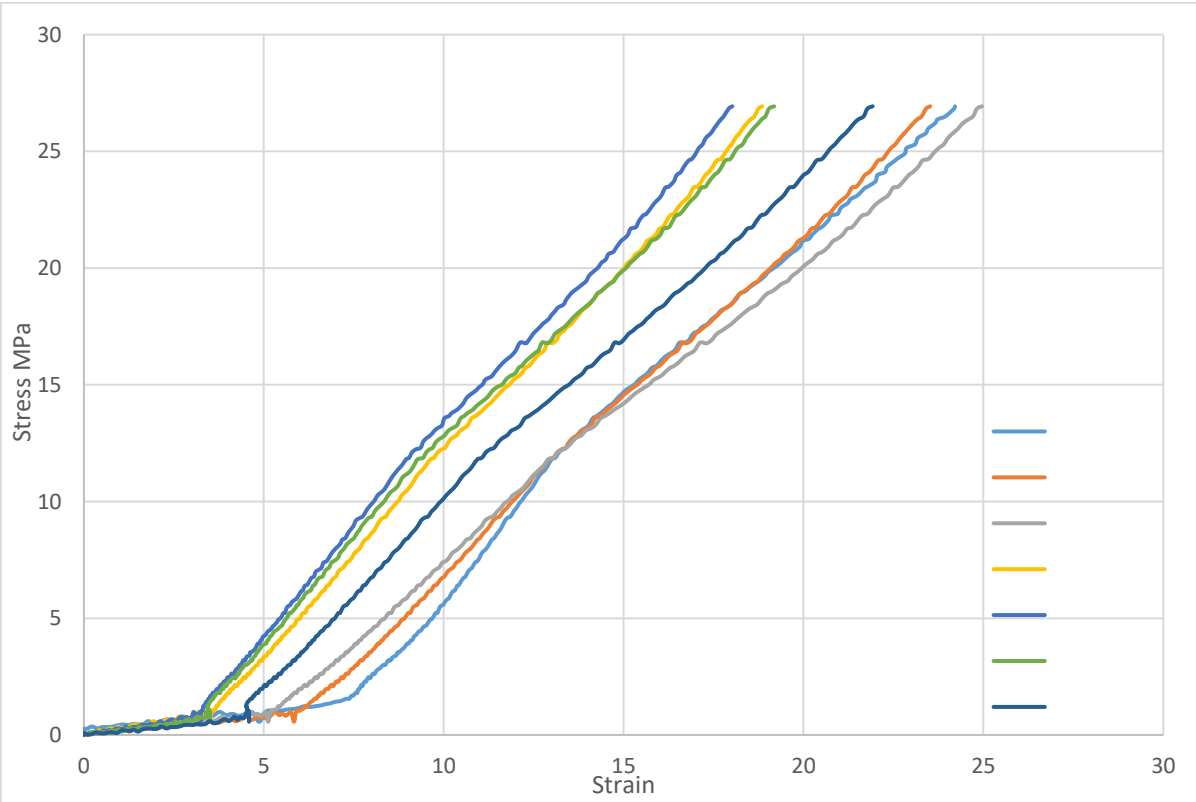

Figure 6. 16: Stress versus strain for all orientation angles θ for materials of EXA-1180.

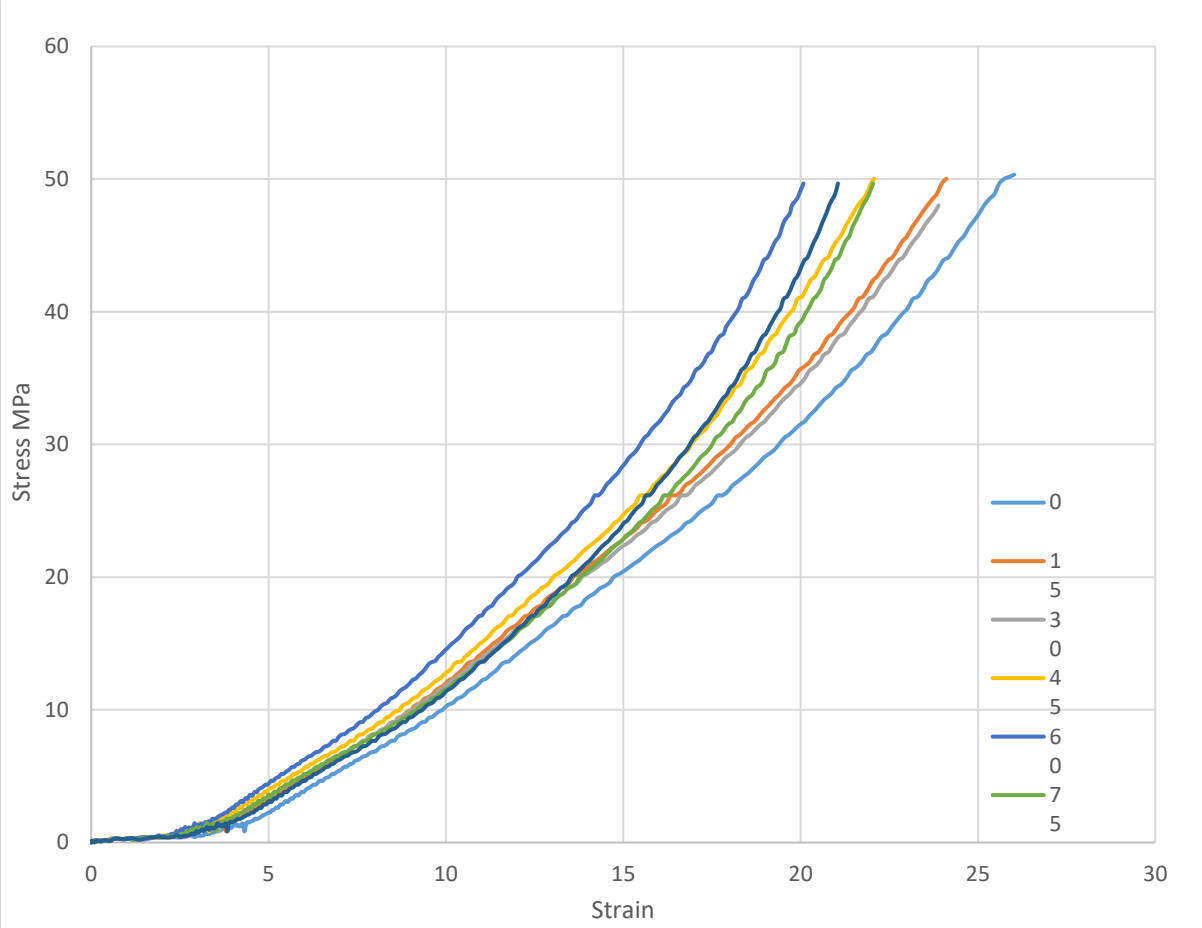

Figure 6. 17: Stress versus strain for all orientation angles θ for materials of EXA-1182 thickness.

The video gauge system was also used to measure the shear strain at six locations on the surface of each sample during loading. Shear strain measurements were taken from the in-plane distortions of the strain gauge elements oriented at + 45 and −45 ° to the biaxial tension as mentioned in chapter four. In Figure 6.19, the different positions of the measured shear stress values are depicted. Position 3 and position 4 are the most central at the top of the dome. Position 1 and position 6 at the periphery are closest to the points where the specimen is clamped between the pressure chamber and the die. The shear strain is higher when measured close to the centre than at the edges where dies restrict the material. Therefore, shear strains are calculated from the centre of the sample. In Figures 6.20 to 6.22, the different positions of the measured shear stress values are depicted.

Figure 6. 18: **Schematic shear strain with a position on the surface.**

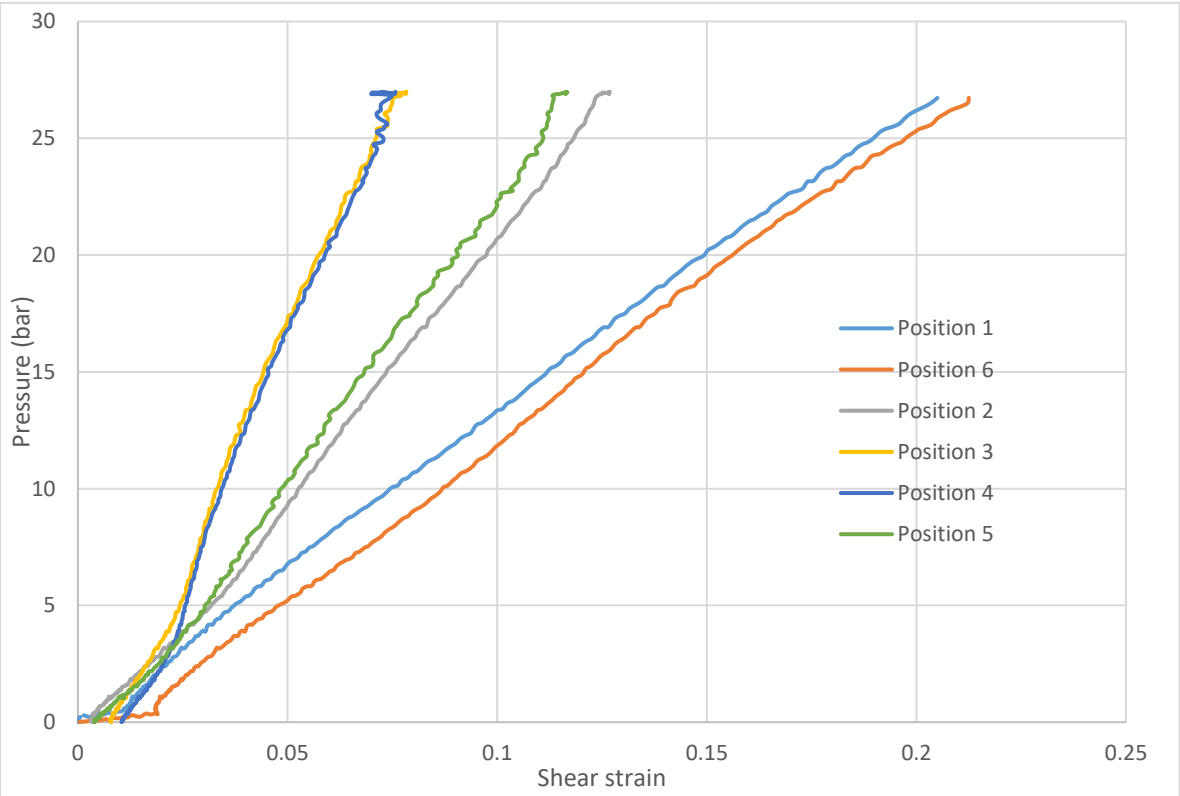

Figure 6. 19: **Pressure versus shear strain for materials of EXA-1196.**

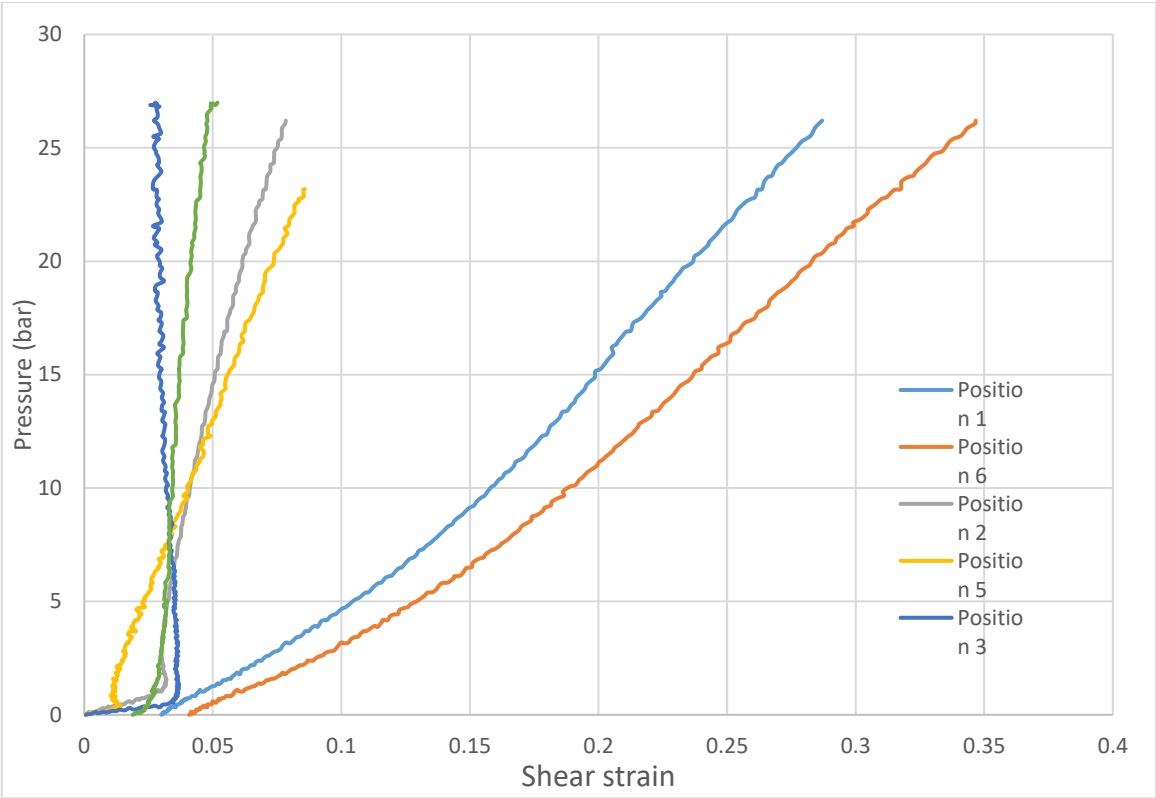

Figure 6. 20: **Pressure versus shear strain for materials of EXA-1180.**

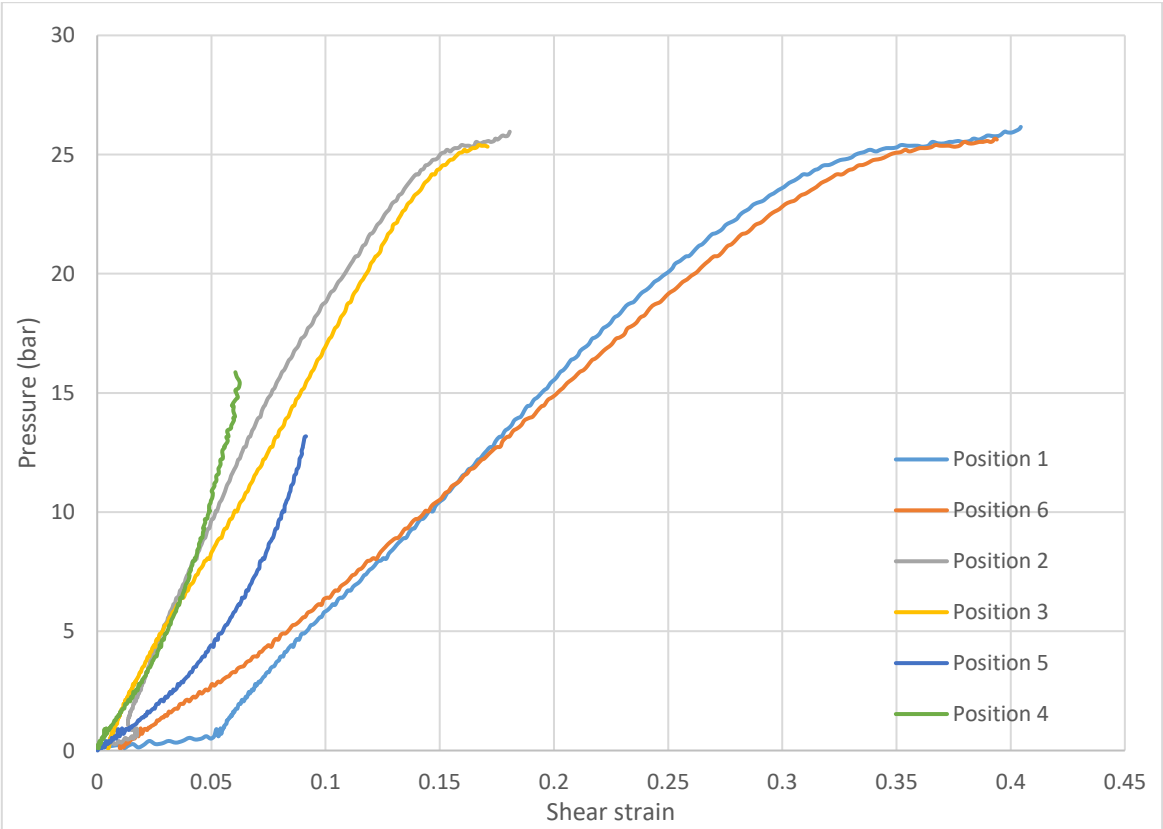

Figure 6. 21: **Pressure versus shear strain for materials of EXA-1182.**

Overall, there are similar shear strains for positions 1 and 6, for positions 2 and 5, and for positions 3 and 4, as exhibited in the diagrams above. These are consistent with the shear stress being affected only by the distance from the centre rather from absolute values of the X- and Y-directions. As compared with the polychloroprene matrix and nylon cord fabric with a EXA-1196 thickness, a larger shear strain was obtained for the composite made of the PVC/nitrile elastomeric matrix reinforced with continuous nylon weave cord fabric with a EXA-1182. As determined by the state of biaxial stress, the shear there is very small compared with the result shown in chapter four.

6.6.1 Strain Fields For Bulge Test

Increasingly featured within the experimental mechanical engineer's discipline, is the full-field (strain map) optical measurement method. A random pattern is applied to the area of interest to detect deformation. This is commonly done by spraying white paint onto the surface. The video gauge software can provide full-field strain measurement, thus giving a straightforward approach to locating concentrations of three-dimensional strain distributions or displacements, and so to determine material parameters for the surface of the specimen. The theoretical background for this method, which can be used to measure deformations of both curved and planar surfaces, is described in more detail in chapter three. The digital camera recorded images during the mechanical testing process. The software then analysed those images to calculate axial and transversal displacements as well as axial, transversal, and shear strains.

The bulge shape is extracted from the circular bulge window to determine the highest bulge height point, i.e., the middle point. The following technique is followed to find a circular bulge centre, as shown in figure 6.23.

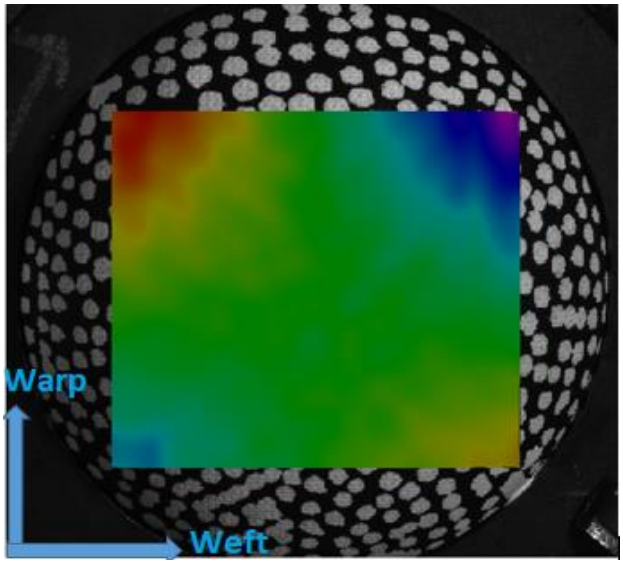

Figure 6. 22: **The specimen viewed from above during a test**

The strain maps of the specimen are shown for a late stage of the test under relatively high pressure. The maps show a range of colours, where vertical boundaries are violet and red: violet represents the lowest positive strain values (or the highest negative strain values); red represents the highest positive strain values (or the lowest negative strain values) (see Figure 6.24)

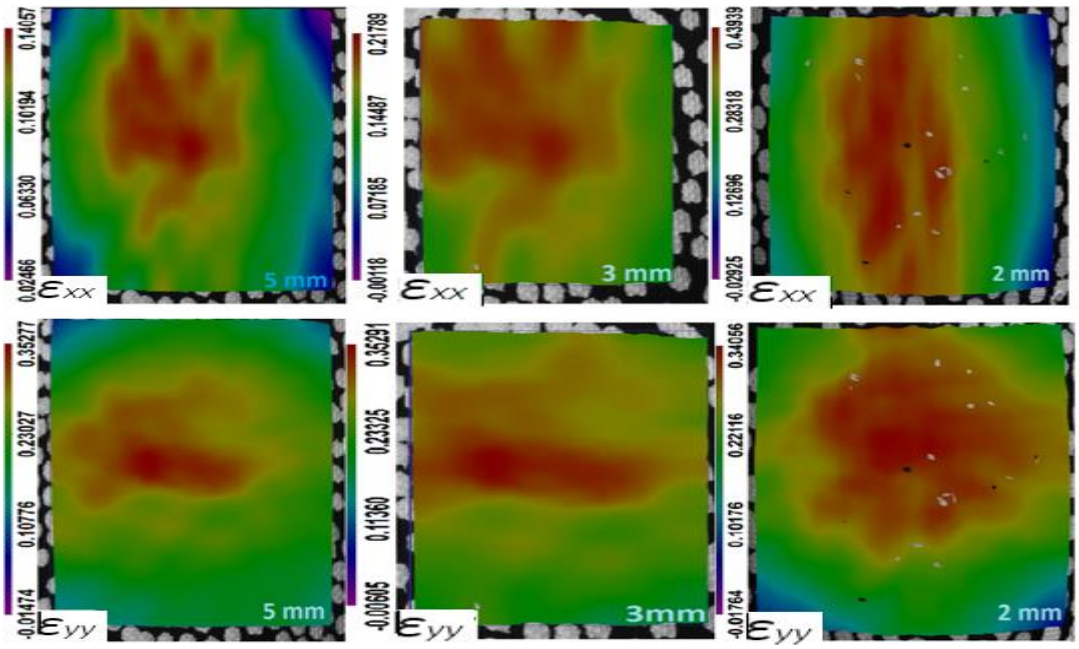

Figure 6. 23: Maps of the strain components on the undeformed configuration for ε_{xx} and ε_{yy}

Figure 6.25 shows the bulge of the specimen, with a colour plot overlay for specimens of different materials. The ε_{yy} and ε_{xx} results indicate the localised strain distribution in the highly deformed region (red colour, at the centre of the specimen). The maximum strain of ε_{xx} ('apex strain') is at 0.14057, 0.21789, and 0.43939, and the maximum strain of ε_{yy}, is at 0.35277, 0.35291 and 0.34056 for thicknesses of EXA-1196, EXA-1180 and EXA-1182, respectively. These are recorded at the centre of the specimen. The apex point is marked in the specimen, and the middle section is then used to generate a bulge profile for various specimens and pressures. The apex point, as marked in the specimen, and the centre section is used to generate the bulge profile for different specimens and at different pressures. The curvature at the free edge makes little difference to ε_{xx} and ε_{yy} and the circumferential strain field, as viewed from above the bulge.

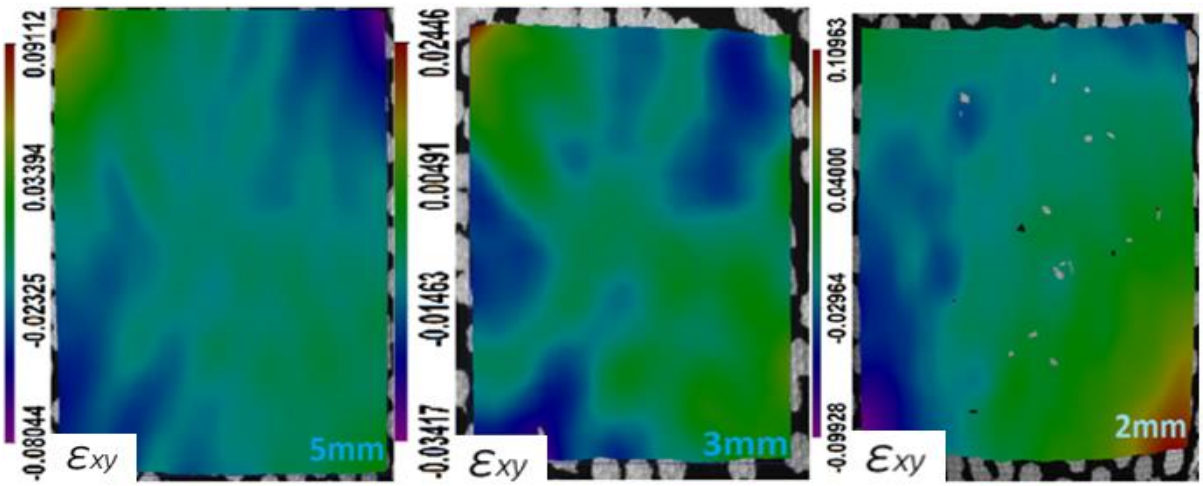

Figure 6. 24: **Maps of the shear strain components on the undeformed configuration**

The bulge of the specimen is indicated using a coloured plot overlay to show the shear strain in the specimen. At the edge of the specimen, the shear strain is approximately 0.09112, 0.02446, and 0.10963 for the EXA-1196, EXA-1180 and EXA-1182 thicknesses, respectively.

As the biaxial stress state was uniform, the observed shear strain concentration regions were very small, as shown in figure 6.28. It is also evident that the deformation at the centre section of the gauge (at 45° to the X and Y loading directions) illustrates the equibiaxial condition. This region continues to deform under equi-biaxial tension as strain deforms the centre and reaches large equivalent strains. Under equibiaxial loading, materials are randomly deformed, as might be expected of anisotropic materials.

6.7. Conclusions

A novel approach was explored to measure the equi-biaxial extension of composite materials on three different sheet thicknesses: 5 mm, 3 mm, and 2 mm. The material characterisation was achieved using optical methods to investigate movements of a specimen during a bulge test. During the inflation, the video gauge software was able to capture and process digital images of the specimen, automatically recognise the grid pattern and calculate the shape, displacements and thus strain distribution, of the balloon’s upper region in real-time. This kind of measurement constitutes a novel methodology for the characterisation of hyper-elastic materials using the bulge test. The results of the experiment presented here show the feasibility of using this setup to identify the pressure/strain, the pressure/displacement and the pressure/shear strain relationship and the mechanical characterisation of the material. A bulge test apparatus was developed that can be employed to measure the mechanical properties and observe the behaviour of hyper-elastic material.

The video gauging software captures and processes digital images of the specimen in real-time, automatically recognises the grid pattern, calculates the shape and, thereby, the strain distribution (2D) of the balloon's upper region. The grid method for measuring the strain in a bulge test is advantageous in that it gives a full-field description of the specimen's deformation state. The composite materials investigated did show different stiffnesses in the warp and the

weft directions. The bulge deformation/axial displacements observed in the experiment were generally lower than those reported for rubber materials in the literature (Sasso et al., 2006). 3D coordinate video gauging was used to measure the height of the dome, as pressure was applied from under the material during the bulging experiment.

From the bulge experiments undertaken in this research, the insights obtained - of the strain behaviour of an anisotropic sheet material consisting of a woven structure inside an elastomer matrix - provide a good starting point for the FEA modelling of these materials. The experimental results will help in adapting material parameters in the FEA model under different kinds of loadings.

Chapter Seven

7.1 Conclusions and future work

7.1.1. General

At the end of each chapter's main section, detailed conclusions have been given. The mechanical behaviour of woven fabrics was measured, and a phenomenological constitutive model developed to capture the anisotropic, nonlinear, and hysteretic behaviour observed in experiments. These offer a brief description of the study's findings.

An extensive literature review has been undertaken of the physical properties relating to the components of the composite fabric (i.e. rubber and fibres) used for these and similar structures.

In addition, the literature review was undertaken to assess the current state-of-the-art in the following areas: non-linear mechanical properties of coated woven fabrics, fabric test methods; non-linear test data representation methods; current practice in representing fabric properties for structural analysis; and predictive modelling of coated woven fabric tensile and shear behaviour.

The review concludes that vulcanised rubber materials generally have high elasticity, low stiffness and a nonlinear stress-strain relationship, and using a woven fibre structure embedded into this rubber material reduces the elasticity and increases the stiffness of the composite material retaining the nonlinear stress-strain behaviour.

In the experimental work performed in this thesis, the anisotropic nature of tensile stress-strain relationships of different samples was investigated in different ways. Both shear testing, and a new technique of incorporating test data into structural analysis, could be extremely beneficial to the business. The design of the test rig must be appropriate for the specific material

characteristics of the relevant textiles. This involves accepting enormous stresses (both positive and negative on either axis) and non-orthogonal primary axes in architectural textiles.

A thorough understanding of this anisotropic nonlinear stress-strain relationship in natural fibre reinforced composites generates essential information for technical applications, especially in structural components.

7.1.2. Conclusions

In applying optical methods to uniaxial and wide-strip tension tests, a novel investigation has been undertaken of the mechanical properties of a fibre-reinforced composite, consisting of a carbon-black filled vulcanised PVC/nitrile compound and a nylon cord fabric of two-directional warp and weft. These tests were carried out at room temperature to assess the suitability of the material for structural applications.

Non-contacting optical methods (using a video strain gauge) were found to be convenient for the measurement of large deformations where, for example, the application of other strain measurement techniques are brutal or unfeasible. With a non-contacting optical system, it is possible to take measurements at multiple points within the loaded gauge section and to gather data in real-time. In this respect, the tested composite investigated in this work has demonstrated anisotropic material behaviour, whereby loading in the weft direction invokes higher stiffness than loading in the warp direction. This result was expected and is typical of fibre-filled elastomeric materials, whereby the fibre architecture dominates the load-deformation response.

This result was used to determine normal strain, shear strain and Poisson's ratio. The composite demonstrated anisotropic material behaviour, as confirmed by the various test results obtained for the composite loaded parallel to the weft and warp fibre directions. The non-linear stress-

strain response was observed for all the test conditions considered. In order to reflect the anisotropic nonlinear mechanical behaviour of woven composite fabrics during the deformation phase, a basic hyper-elastic fibre reinforced constitutive model was developed within the continuum mechanics system. For the proposed hyper-elastic model, to facilitate the determination of material parameters, the strain energy per unit volume was additively decomposed into tensile energy, compaction energy, and shear energy. The strain energy function that characterises a material's anisotropic behaviour can be described by four terms: interaction between fibres, the matrix, and the fibre-fibre interactions in both the warp and weft directions. From that basis, the processes of parameter determination were straightforward.

Although there are many different picture frame test methods, these do not necessarily allow the measurement of the true shear strain. Using the video gauge technique, an improved method was obtained (giving prototype experimental results) whereby strain and shear strain measurements were made in uniaxial tension and picture frame specimens.

Ultimately, the proposed anisotropic hyper-elastic model was implemented to simulate uniaxial stress and picture-frame shear testing, with the comparison between numerical results and experimental evidence suggesting the validity and accuracy of the model.

Three-dimensional digital image correlation (3D-DIC) technique was shown to be a useful tool for obtaining the membrane stress and strain fields during the bulge test. The 3D video gauging, combined with DIC captures three-dimensional surface geometry and deformed surface displacements. Two-dimensional (2D) optical methods obtained strain, shear strain and full-field strain measurements on the area of interest, which was the centre of the sample.

During inflation, the VG software captures and processes digital images of the specimen, automatically recognising the grid pattern and calculating the shape, displacements and thus strain distribution of the balloon's upper region in real-time. This approach constitutes a novel

methodology for the characterisation of hyper-elastic materials using the bulge test. The results of the experiment presented here, show the feasibility of this setup to identify the pressure/strain, the pressure/displacement and the pressure/shear strain relationship and the mechanical characterisation of the material. A bulge test apparatus was developed that can be employed to observe the behaviour of hyper-elastic material and to measure the mechanical properties.

The grid method for measuring the strain in a bulge test gives a full-field description of the specimen's deformation state. Composite materials show different stiffnesses in the warp and the weft directions. The bulge deformation/axial displacements observed in the experiment were generally lower than those reported for rubber materials in the literature (Sasso et al., 2006). 3D coordinate VG was used to measure the height of the dome, as pressure was applied from under the material during the bulging experiment. This means that the material is stiffer and more durable than rubber materials and is ideal for use in structures where low deformation is required.

7.1.3. Recommendations for future work

To further develop realistic fibre-reinforced composites materials simulations, there are many opportunities for future research. This work delivers a mechanical analysis of fibre-reinforced composites for different fibre architectures. Future investigations that might involve uniaxial tensile testing at higher or lower temperatures, may provide useful information on the variability of the mechanical properties of fibre-reinforced composites.

Biaxial testing might be applied to a variety of fibre-reinforced composites. In general, bulge test methods would then obtain load/extension curves that would serve to determine the parameters for the biaxial mode of loading.–Here, the optimal fibre content of each type of

reinforcement could be calculated in a polymer matrix. In other ways, laminates could be assessed to obtain an overview of the relationship between tensile properties and test directions.

Another suggestion is to expand the model to assess the efficiency of the finite element analysis to gain a better understanding of fabric structure design, construction and more precise reliability analysis. Therefore, the Finite Element Analysis (FEA) suggested resolving the fundamental equation of more considerable deformation, of material parameters, which therefore provides a theoretical basis for future numerical simulations and storage optimisation of woven composites.

References

ABAQUS, 1992. Theory manual 6.12. Providence, RI, USA: Hibbitt, Karlsson & Sorensen Inc.

Abdul-Aziz, A. and Wroblewski, A.C., 2016. Durability analysis and experimental validation of environmental barrier coating (EBC) performance using combined digital image correlation and NDE. *Coatings*, *6*(4), p.70.

Aboshio, A., 2014. *Dynamic Study of Inflatable Offshore Barrier Structures under Impact and Environmental Loadings* (Doctoral dissertation, Lancaster University).

Aboshio, A., Green, S. and Ye, J., 2015. Experimental investigation of the mechanical properties of neoprene coated nylon woven reinforced composites. *Composite Structures*, *120*, pp.386-393.

Aboshio, A., Green, S. and Ye, J.Q., 2014. New constitutive model for anisotropic hyperelastic biased woven fibre reinforced composite. *Plastics, Rubber and Composites*, *43*(7), pp.225-234.

Adams, D.F. and Lewis, E.Q., 1995. Experimental strain analysis of the losipescu shear test specimen. *Experimental mechanics*, *35*(4), pp.352-360.

Adams, D.F., 1990. The Iosipescu shear test method as used for testing polymers and composite materials. *Polymer composites*, *11*(5), pp.286-290.

Aimène, Y., Vidal-Sallé, E., Hagège, B., Sidoroff, F. and Boisse, P., 2010. A hyperelastic approach for composite reinforcement large deformation analysis. *Journal of Composite materials*, *44*(1), pp.5-26.

Ali, A., Hosseini, M. and Sahari, B.B., 2010. A review and comparison on some rubber elasticity models. *J Scient Indust Res*, 69, 7, 2010, p 495.

Altan, T., Palaniswamy, H., Bortot, P., Heidl, W. and Bechtold, A., 2006, November. Determination of sheet material properties using biaxial bulge tests. In *Proceedings of the 2nd Int. Conference on Accuracy in Forming Technology* (Vol. 13, p. 15).

Amirbayat, J. and Hearle, J.W.S., 1986. The complex buckling of flexible sheet materials—Part I. Theoretical approach. *International journal of mechanical sciences*, *28*(6), pp.339-358.

Anuta, P.E., 1970. Spatial registration of multispectral and multitemporal digital imagery using fast Fourier transform techniques. *IEEE transactions on Geoscience Electronics*, *8*(4), pp.353-368.

Arumugam, V., Mishra, R., Militky, J. and Tunak, M., 2016. In-plane shear behavior of 3D spacer knitted fabrics. *Journal of Industrial Textiles*, *46*(3), pp.868-886.

ASTM D 5035, 2011. Standard test method for breaking force and elongation of textile fabrics (strip method). *ASTM International*.

ASTM, E., 2004. 111-04: Standard test method for Young's modulus, tangent modulus, and chord modulus. *Annual Book of ASTM Standards*, *3*.

Astrom, B.T., 1997. *Manufacturing of polymer composites*. CRC press.

Awais, H., Nawab, Y., Amjad, A., Anjang, A., Akil, H.M. and Abidin, M.S.Z., 2020. Environmental benign natural fibre reinforced thermoplastic composites: A review. Composites Part C: Open Access, p.100082.

Bai, J., Li, H., Shi, Z. and Yin, J., 2015. An eco-friendly scheme for the cross-linked polybutadiene elastomer via thiol–ene and Diels–Alder click chemistry. Macromolecules, 48(11), pp.3539-3546.

Barbero, E.J., 2017. *Introduction to composite materials design*. CRC press.

Bassett, R.J., Postle, R. and Pan, N., 1999. Experimental methods for measuring fabric mechanical properties: A review and analysis. *Textile research journal*, *69*(11), pp.866-875.

Bhatnagar, N., Bhardwaj, R., Selvakumar, P. and Brieu, M., 2007. Development of a biaxial tensile test fixture for reinforced thermoplastic composites. *Polymer Testing*, *26*(2), pp.154-161.

Bird, W.W., 1977. Role of the Fabricator - Large Fabric Structures." ASCE Spring Convention and Exhibit. Dallas, TX: American Society of Civil Engineers.

Board, M.R., 2016. Lembaga Getah Malaysia. Natural Rubber Statistics.

Boisse, P., Hamila, N., Guzman-Maldonado, E., Madeo, A., Hivet, G. and Dell'Isola, F., 2017. The bias-extension test for the analysis of in-plane shear properties of textile composite reinforcements and prepregs: a review. *International Journal of Material Forming*, *10*(4), pp.473-492.

Boubaker, B.B., Assidi, M. and Ganghoffer, J.F., 2010. Evaluation of Poisson's ratio of textiles from mesoscopic models. *International journal of material forming*, *3*(1), pp.81-84.

Boubaker, B.B., Assidi, M. and Ganghoffer, J.F., 2010. Evaluation of Poisson's ratio of textiles from mesoscopic models. *International journal of material forming*, *3*(1), pp.81-84.

Boyce, M.C. and Arruda, E.M., 2000. Constitutive models of rubber elasticity: a review. *Rubber chemistry and technology*, *73*(3), pp.504-523.

Bridgens, B.N., 2005. *Architectural fabric properties: determination, representation & prediction* (Doctoral dissertation, Newcastle University).

Brieu, M., Diani, J. and Bhatnagar, N., 2006. A New Biaxial Tension Test Fixture for Uniaxial Testing Machine--A Validation of Hyperelastic Behavior of Rubber-like Materials. *Journal of Testing and Evaluation*, *35*(4), pp.1-9.

BS 903-5, 2004 - Physical testing of rubber. Guide to the application of rubber testing to finite element analysis, 08(02) pp,20-28.

Cao, J., Akkerman, R., Boisse, P., Chen, J., Cheng, H.S., De Graaf, E.F., Gorczyca, J.L., Harrison, P., Hivet, G., Launay, J. and Lee, W., 2008. Characterization of mechanical behavior of woven fabrics: experimental methods and benchmark results. *Composites Part A: Applied Science and Manufacturing*, *39*(6), pp.1037-1053.

Chevalier, L., Calloch, S., Hild, F. and Marco, Y., 2001. Digital image correlation used to analyze the multiaxial behavior of rubber-like materials. *European Journal of Mechanics-A/Solids*, *20*(2), pp.169-187.

Chou, T.W., 1992. Microstructural design of fiber composites. NASA STI/Recon Technical Report A, 92, p.50452.

Clyne, T.W. and Withers, P.J., 1995. *An introduction to metal matrix composites*. Cambridge university press.

Cox, B.N. and Flanagan, G., 1997. Handbook of analytical methods for textile composites.

Cusick, G.E., 1961. 30—The Resistance of Fabrics to Shearing Forces: A Study of the Experimental Method due to Mörner and Eeg-Olofsson. *Journal of the Textile Institute Transactions*, *52*(9), pp.T395-T406.

Dai, X., Li, Y.I. and Zhang, X., 2003. Simulating anisotropic woven fabric deformation with a new particle model. *Textile research journal*, *73*(12), pp.1091-1099.

De Bever, A., 1992. Dynamic behaviour of rubber and rubberlike materials. *WFW-report. Netherlands: Technische Universiteit Eindhoven University of Technology*.

De Borst, R., Crisfield, M.A., Remmers, J.J. and Verhoosel, C.V., 2012. *Nonlinear finite element analysis of solids and structures*. John Wiley & Sons.

De Jong, S. and Postle, R., 1977. 39—an Energy Analysis of Woven-Fabric Mechanics by Means of Optimal-Control Theory Part I: Tensile Properties. *Journal of the Textile Institute*, *68*(11), pp.350-361.

DIN (Deutsches Institut für Normung). 2014. *Fibre-reinforced plastic composites—Shear test method using a shear frame for the determination of the in-plane shear stress/shear strain response and shear modulus.* DIN SPEC 4885. Berlin: DIN.

Divya, G.S. and Suresha, B., 2021. Impact of nano-silicon dioxide on mechanical properties of carbon fabric reinforced epoxy composites. Materials Today: Proceedings.

Dolatabadi, M.K., Kovař, R. and Linka, A., 2009. Geometry of plain weave fabric under shear deformation. Part I: measurement of exterior positions of yarns. *The Journal of The Textile Institute*, *100*(4), pp.368-380.

Duncan, B.C., Maxwell, A.S., Crocker, L.E. and Hunt, R., 1999. Verification of hyperelastic test methods.

Efunda, "Spherical Pressure Vessel," Efunda, 21 March 2015. [Online]. Available:http://www.efunda.com/formulae/solid_mechanics/mat_mechanics/pressure_vessel.cfm.

Eirich, F.R., Science and technology of rubber, 1978. *Rubber division of the American Chemical Society. Pag*, *314*, pp.315-341.

Erden, S. and Ho, K., 2017. Fiber reinforced composites. In *Fiber Technology for Fiber-Reinforced Composites* (pp. 51-79). Woodhead Publishing.

Eterovic, A.L. and Bathe, K.J., 1990. A hyperelastic-based large strain elasto-plastic constitutive formulation with combined isotropic-kinematic hardening using the logarithmic stress and strain measures. *International Journal for Numerical Methods in Engineering*, *30*(6), pp.1099-1114.

Fang, R., 2009. *The design and construction of fabric structures* (Doctoral dissertation, Massachusetts Institute of Technology).

Fetfatsidis, K.A., Soteropoulos, D., Petrov, A., Mitchell, C.J. and Sherwood, J.A., 2012. Using abaqus/explicit to link the manufacturing process to the final part quality for continuous fiber-reinforced composite fabrics. In *Simulia Customer Conference*. Rhode Island,15–17.

Fong, Y.C., Khin, A.A. and Lim, C.S., 2018. Conceptual Review and the Production, C. onsumption and Price Models of the Natural Rubber Industry in Selected ASEAN Countries and World Market. Asian Journal of Economic Modelling, 6(4), pp.403-418.

Forster, B., 1985. Engineered use of coated fabrics in long span roofs. *J. COATED FABRICS.*, *15*, pp.25-39.

Freakley, P.K. and Payne, A.R., 1978. *Theory and practice of engineering with rubber*. Applied Science Publishers.

Gatouillat, S., Bareggi, A., Vidal-Sallé, E. and Boisse, P., 2013. Meso modelling for composite preform shaping–simulation of the loss of cohesion of the woven fibre network. *Composites Part A: Applied science and manufacturing*, *54*, pp.135-144.

Gay, D., 2014. *Composite materials: design and applications*. CRC press.

Gent, A.N., 2012. *Engineering with rubber: how to design rubber components*. Carl Hanser Verlag GmbH Co KG.

Gong, Y., Song, Z., Ning, H., Hu, N., Peng, X., Wu, X., Zou, R., Liu, F., Weng, S. and Liu, Q., 2020. A comprehensive review of characterization and simulation methods for thermo-stamping of 2D woven fabric reinforced thermoplastics. Composites Part B: Engineering, p.108462.

Gough, J., 1805. A description of a property of Caoutchouc, or Indian rubber. *Memories of the Literacy and Philosophical Society of Manchester*, *1*, pp.288-295.

Gowda, T.M., Naidu, A.C.B. and Chhaya, R., 1999. Some mechanical properties of untreated jute fabric-reinforced polyester composites. *Composites Part A: applied science and manufacturing*, *30*(3), pp.277-284.

Guide, V.G.U., 2009. Imetrum Limited. *Bristol, UK*.

Gutscher, G., Wu, H.C., Ngaile, G. and Altan, T., 2000. Evaluation of formability and determination of flow stress curve of sheet metals with hydraulic bulge test. *Report no: S-ERC/NSM-00-R-15, The Ohio State University, Columbus, Ohio*.

Hanhi, K., Poikelispaa, M. and Tirila, H.M., 2007. Elastomeric materials. *Tampere University of Technology, Tampere*.

Hardiman, C.J., McKenzie, G.T. and Stiberth, L.F., PARATEC ELASTOMERS LLC, 2000. *Nitrile rubber/polyvinyl chloride blends*. U.S. Patent 6,043,318.

Harrison, P., Clifford, M.J. and Long, A.C., 2004. Shear characterisation of viscous woven textile composites: a comparison between picture frame and bias extension experiments. *Composites science and technology*, *64*(10-11), pp.1453-1465.

Härtel, F. and Harrison, P., 2014. Evaluation of normalisation methods for uniaxial bias extension tests on engineering fabrics. *Composites Part A: Applied Science and Manufacturing*, *67*, pp.61-69.

Hasan, M.R., 2013. Influence of fibre architecture on mechanical properties of Jute fibre reinforced composites.

Hearle, J.W.S. and Amirbayat, J., 1986. Analysis of drape by means of dimensionless groups. *Textile Research Journal*, *56*(12), pp.727-733.

Hecht, J., Pinto, S. and Geiger, M., 2005. Determination of mechanical properties for the hydroforming of magnesium sheets at elevated temperature. In *Advanced Materials Research* (Vol. 6, pp. 779-786). Trans Tech Publications Ltd.

Hernández Santana, M., den Brabander, M., García, S. and van der Zwaag, S., 2018. Routes to make natural rubber heal: a review. Polymer Reviews, 58(4), pp.585-609.

Hill, R., 1950. C. A theory of the plastic bulging of a metal diaphragm by lateral pressure. *The London, Edinburgh, and Dublin Philosophical Magazine and Journal of Science*, *41*(322), pp.1133-1142.

Hoa, S.V., 2009. *Principles of the manufacturing of composite materials*. DEStech Publications, Inc.

Hodgkinson, J.M. ed., 2000. *Mechanical testing of advanced fibre composites*. Woodhead publishing.

Holzapfel, G.A. and Ogden, R.W., 2010. Constitutive modelling of arteries. *Proceedings of the Royal Society A: Mathematical, Physical and Engineering Sciences*, *466*(2118), pp.1551-1597.

Holzapfel, G.A., Gasser, T.C. and Ogden, R.W., 2000. A new constitutive framework for arterial wall mechanics and a comparative study of material models. *Journal of elasticity and the physical science of solids*, *61*(1), pp.1-48.

Hu, J., 2004. *Structure and mechanics of woven fabrics*. Elsevier.

Huang, Z.M., Ramakrishna, S. and Tay, A.A.O., 2000. Modeling the stress/strain behavior of a knitted fabric-reinforced elastomer composite. Composites science and technology, 60(5), pp.671-691.

Hursa, A., Rolich, T. and Ražić, S.E., 2009. Determining pseudo Poisson's ratio of woven fabric with a digital image correlation method. *Textile research journal*, *79*(17), pp.1588-1598.

Hutchings, A., Braun, R., Masuyama, K. and Welch, J., 2009, May. Experimental determination of material properties for inflatable aeroshell structures. In *20th AIAA Aerodynamic Decelerator Systems Technology Conference and Seminar* (p. 2949).

Iosipescu, N., 1967. New accurate procedure for single shear testing of metals. *J Mater*, *2*, pp.537-566.

Jacobsen, A.J., Luo, J.J. and Daniel, I.M., 2004. Characterization of constitutive behavior of satin-weave fabric composite. *Journal of composite materials*, *38*(7), pp.555-565.

Jaia Jr, M.M.S., 2015. Learning Experience in Designing a Hydraulic Bulge Test Setup for Material Properties Characterization. 122 nd ASEE *Annual Conference & Exposition*, Paper ID #12983.

Jones, R.M., 2014. *Mechanics of composite materials*. CRC press.

Keating, T.J., Wolf, P.R. and Scarpace, F.L., 1975. An improved method of digital image correlation. *Photogrammetric Engineering and Remote Sensing*, *41*(8), pp.993-1002.

Khajehsaeid, H., Arghavani, J. and Naghdabadi, R., 2013. A hyperelastic constitutive model for rubber-like materials. European Journal of Mechanics-A/Solids, 38, pp.144-151.

Khan, M.A., 2009. *Numerical and experimental forming analyses of textile composite reiforcements based on a hypoelastic behaviour* (Doctoral dissertation, Lyon, INSA).

Kilby, W.F., 1963. 2—Planar stress–strain relationships in woven fabrics. *Journal of the Textile Institute Transactions*, *54*(1), pp.T9-T27.

Kock, N., 2015. WarpPLS 5.0 user manual. *Laredo, TX: ScriptWarp Systems*.

Kovar, R., 2003. Structure and properties of flat textiles (in Czech), TU of Liberec 2003.

Kraft, S.M., Moslehy, F.A., Bai, Y. and Gordon, A.P., 2014. Characterization of the orthotropic elastic constants of a micronic woven wire mesh via digital image correlation. *Experimental Mechanics*, *54*(4), pp.501-514.

Kular, G.S. and Hillier, M.J., 1972. Re-interpretation of some simple tension and bulge test data for anisotropic metals. *International Journal of Mechanical Sciences*, *14*(10), pp.631-634.

Launay, J., Hivet, G., Duong, A.V. and Boisse, P., 2008. Experimental analysis of the influence of tensions on in plane shear behaviour of woven composite reinforcements. *Composites science and technology*, *68*(2), pp.506-515.

Lebrun, G., Bureau, M.N. and Denault, J., 2003. Evaluation of bias-extension and picture-frame test methods for the measurement of intraply shear properties of PP/glass commingled fabrics. *Composite structures*, *61*(4), pp.341-352.

Lee, S. and Munro, M., 1986. Evaluation of in-plane shear test methods for advanced composite materials by the decision analysis technique. *Composites*, *17*(1), pp.13-22.

Li, Y. and Dai, D.X. eds., 2006. *Biomechanical engineering of textiles and clothing*. Woodhead Publishing.

Lo, W.M. and Hu, J.L., 2002. Shear properties of woven fabrics in various directions. *Textile Research Journal*, *72*(5), pp.383-390.

Lomov, S.V., Boisse, P., Deluycker, E., Morestin, F., Vanclooster, K., Vandepitte, D., Verpoest, I. and Willems, A., 2008. Full-field strain measurements in textile deformability studies. *Composites Part A: Applied Science and Manufacturing*, *39*(8), pp.1232-1244.

Malhotra, N., Sheikh, K. and Rani, S., 2012. A review on mechanical characterization of natural fiber reinforced polymer composites. *Journal of Engineering Research and Studies*, *3*(1), pp.75-80.

Mallick, P.K., 2007. *Fiber-reinforced composites: materials, manufacturing, and design*. CRC press.

Martin's Rubber Company., 2017. Nitrile Rubber Sheet | NBR Rubber | Buna-N. [online] Available at: http://www.martins-rubber.co.uk/products/sheeting/nitrile-nbr-rubber-sheet/

McCormick, N. and Lord, J., 2010. Digital image correlation. *Materials today*, *13*(12), pp.52-54.

McGuinness, G.B. and ÓBrádaigh, C.M., 1997. Development of rheological models for forming flows and picture-frame shear testing of fabric reinforced thermoplastic sheets. *Journal of Non-Newtonian Fluid Mechanics*, *73*(1-2), pp.1-28.

Merle, B., 2013. Mechanical properties of thin films studied by bulge testing. FAU University Press.

Micro-Measurements, V., 2008. Strain gage rosettes: Selection, application and data reduction. *Technical note TN*, *515*, pp.151-161.

Miller, K., 2000. Measuring material properties to build material models in FEA. *Axel Products Inc*.

Miller, K., 2000. Testing elastomers for hyperelastic material models in finite element analysis. *Axel Products Testing and Analysis Report*. Axel Products Inc. Ann Arbor, MI, USA.

Miller, K., 2002. Testing elastomers for ANSYS, Axel Products Inc. *The Focus, publication for ANSYS users*, (12).

Mooney, M., 1940. A theory of large elastic deformation. *Journal of applied physics*, *11*(9), pp.582-592.

Morton, M. ed., 2013. *Rubber technology*. Springer Science & Business Media.

Motulsky, H.J. and Ransnas, L.A., 1987. Fitting curves to data using nonlinear regression: a practical and nonmathematical review. *The FASEB journal*, *1*(5), pp.365-374.

Murman, S. and Suresh, S., 2011. Modeling Effective Stiffness Properties of IAD Fabrics. In *21st AIAA Aerodynamic Decelerator Systems Technology Conference and Seminar* (p. 25-68).

Nagdi, K., 1993. *Rubber as an engineering material: guideline for users*. Hanser Verlag.

Naik, R.A., 1996. Analysis of woven and braided fabric-reinforced composites. In *Composite materials: Testing and design: Twelfth volume*. ASTM International.

Nassiri, F., 2010. *New approach in characterizing accessory drive belts for finite element applications*. (Doctoral Dissertation University of Toronto).

Ngo, T.D., 2020. Introduction to composite materials. Composite and Nanocomposite Materials From Knowledge to Industrial Applications.

Nurazzi, N.M., Asyraf, M.R.M., Fatimah Athiyah, S., Shazleen, S.S., Rafiqah, S., Harussani, M.M., Kamarudin, S.H., Razman, M.R., Rahmah, M., Zainudin, E.S. and Ilyas, R.A., 2021. A review on mechanical performance of hybrid natural fiber polymer composites for structural applications. Polymers, 13(13), p.2170.

Odegard, G. and Kumosa, M., 2000. Determination of shear strength of unidirectional composite materials with the Iosipescu and 10 off-axis shear tests. *Composites Science and Technology*, *60*(16), pp.2917-2943.

Ogden, R., 2011. Lectures on constitutive modelling of Arteries. *delivered at Xi'an Jiaotong University, Xi'an, Chian*.

Ogden, R.W., 1972. Large deformation isotropic elasticity–on the correlation of theory and experiment for incompressible rubberlike solids. *Proceedings of the Royal Society of London. A. Mathematical and Physical Sciences*, *326*(1567), pp.565-584.

Özdemir, H. and Mert, E., 2013. The effects of fabric structural parameters on the tensile, bursting, and impact strengths of cellular woven fabrics. *Journal of the Textile Institute*, *104*(3), pp.330-338.

Palmieri, G., Chiappini, G., Sasso, M. and Papalini, S., 2009, June. Hyperelastic materials characterization by planar tension tests and full-field strain measurement. In *Proceedings of the SEM Annual Conference* (pp. 1-4). Albuquerque: Society for Experimental Mechanics.

Pan, B., Qian, K., Xie, H. and Asundi, A., 2009. Two-dimensional digital image correlation for in-plane displacement and strain measurement: a review. *Measurement science and technology*, *20*(6), p.062001.

Pan, N. and Yoon, M.Y., 1996. Structural anisotropy, failure criterion, and shear strength of woven fabrics. *Textile Research Journal*, *66*(4), pp.238-244.

Penava, Ž., Penava, D.Š. and Nakić, M., 2015. Woven fabrics behavior in pure shear. *Journal of Engineered Fibers and Fabrics*, *10*(4), p.1-15.

Penava, Ž., Šimić-Penava, D. and Knezic, Ž., 2014. Determination of the elastic constants of plain woven fabrics by a tensile test in various directions. *Fibres & Textiles in Eastern Europe*.

Peng, X.Q., Cao, J., Chen, J., Xue, P., Lussier, D.S. and Liu, L., 2004. Experimental and numerical analysis on normalization of picture frame tests for composite materials. *Composites Science and Technology*, *64*(1), pp.11-21.

Peng, X.Q., Guo, Z.Y. and Harrison, P., 2010. A simple anisotropic fiber reinforced hyperelastic constitutive model for woven composite fabrics. *International journal of material forming*, *3*(1), pp.723-726.

Postle, R., Carnaby, G.A. and De Jong, S., 1988. The mechanics of wool structures. *Ellis Horwood Limited Publishers*, Chichester. ISBN 0-7458-0322-9.

Potluri, P. and Thammandra, V.S., 2007. Influence of uniaxial and biaxial tension on meso-scale geometry and strain fields in a woven composite. *Composite Structures*, *77*(3), pp.405-418.

Potter, K.D. and Setchell, C., Imetrum Ltd, 2014. *Positional measurement of a feature within an image*. U.S. Patent 8,718,403.

Rahman, R. and Putra, S.Z.F.S., 2019. Tensile properties of natural and synthetic fiber-reinforced polymer composites. Mechanical and physical testing of biocomposites, fibre-reinforced composites and hybrid composites, pp.81-102.

Raible, T., Reese, S. and Wriggers, P., 2000. Finite element modeling of orthotropic material behaviour in pneumatic membranes. *ZAMM-Journal of Applied Mathematics and Mechanics/Zeitschrift für Angewandte Mathematik und Mechanik*, *80*(S2), pp.409-410.

Ramezani, M. and Ripin, Z.M., 2010. Combined experimental and numerical analysis of bulge test at high strain rates using split Hopkinson pressure bar apparatus. *Journal of Materials Processing Technology*, *210*(8), pp.1061-1069.

Reddy, J.N., 2010. *Principles of continuum mechanics: A study of conservation principles with applications*. Cambridge University Press.

Reese, S., Raible, T. and Wriggers, P., 2001. Finite element modelling of orthotropic material behaviour in pneumatic membranes. *International journal of solids and structures*, *38*(52), pp.9525-9544.

Reinhardt, H.W., 1976. On the biaxial testing and strength of coated fabrics. *Experimental Mechanics*, *16*(2), pp.71-74.

Rivlin, R.S. and Saunders, D.W., 1951. Large elastic deformations of isotropic materials VII. Experiments on the deformation of rubber. *Philosophical Transactions of the Royal Society of London. Series A, Mathematical and Physical Sciences*, *243*(865), pp.251-288.

Rivlin, R.S., 1948. Large elastic deformations of isotropic materials IV. Further developments of the general theory. *Philosophical Transactions of the Royal Society of London. Series A, Mathematical and Physical Sciences*, *241*(835), pp.379-397.

Ruíz, M.J.G. and González, L.Y.S., 2006. Comparison of hyperelastic material models in the analysis of fabrics. *International journal of clothing science and technology*.

Sasso, M. and Amodio, D., 2006. Development of a biaxial stretching machine for rubbers by optical methods. In *Society for Experimental Mechanics Annual Conference, St. Louis, MO, June* (pp. 4-7).

Sasso, M., Palmieri, G., Chiappini, G. and Amodio, D., 2008. Characterization of hyperelastic rubber-like materials by biaxial and uniaxial stretching tests based on optical methods. *Polymer Testing*, *27*(8), pp.995-1004.

Schwartz, P. ed., 2019. *Structure and mechanics of textile fibre assemblies*. Woodhead publishing.

Scida, D., Aboura, Z., Benzeggagh, M.L. and Bocherens, E., 1999. A micromechanics model for 3D elasticity and failure of woven-fibre composite materials. Composites Science and Technology, 59(4), pp.505-517.

Seibert, D.J. and Schoche, N., 2000. Direct comparison of some recent rubber elasticity models. *Rubber chemistry and technology*, *73*(2), pp.366-384.

Selvadurai, A.P.S. and Shi, M., 2012. Fluid pressure loading of a hyperelastic membrane. *International Journal of Non-Linear Mechanics*, *47*(2), pp.228-239.

Selvadurai, A.P.S., 2006. Deflections of a rubber membrane. *Journal of the Mechanics and Physics of Solids*, *54*(6), pp.1093-1119.

Shahabi, N.E., Saharkhiz, S. and Varkiyani, S.M.H., 2013. Effect of fabric structure and weft density on the poisson's ratio of worsted fabric. *Journal of Engineered Fibers and Fabrics*, *8*(2), p.15-58.

Shahzad, M., Kamran, A., Siddiqui, M.Z. and Farhan, M., 2015. Mechanical characterization and FE modelling of a hyperelastic material. *Materials Research*, *18*(5), pp.918-924.

Siegert, K., Jäger, S. and Vulcan, M., 2003. Pneumatic bulging of magnesium AZ 31 sheet metals at elevated temperatures. *CIRP Annals*, *52*(1), pp.241-244.

Solutions, C., 2009. Digital Image Correlation: Overview of Principles and Software 2D Image Correlation Fundamentals. *South Carolina Univ*.

Spencer, A.J.M. ed., 1984. *Continuum theory of the mechanics of fibre-reinforced composites* (Vol. 282, pp. 1-32). New York: Springer-Verlag.

Spencer, A.J.M., 2000. Theory of fabric-reinforced viscous fluids. *Composites Part A: Applied Science and Manufacturing*, *31*(12), pp.1311-1321.

Spivak, S.M. and Treloar, L.R.G., 1968. The behavior of fabrics in shear: part III: the relation between bias extension and simple shear. *Textile Research Journal*, *38*(9), pp.963-971.

Standard, A.S.T.M., 1993. D5379. Standard test method for shear properties of composite materials by the V-notched beam method. *Philadelphia: American Society for Testing and Materials*.

Sun, H., Pan, N. and Postle, R., 2005. On the Poisson's ratios of a woven fabric. *Composite Structures*, *68*(4), pp.505-510.

Taha, I., Abdin, Y. and Ebeid, S., 2013. Comparison of picture frame and Bias-Extension tests for the characterization of shear behaviour in natural fibre woven fabrics. *Fibers and Polymers*, *14*(2), pp.338-344.

Taha, I., Abdin, Y. and Ebeid, S., 2013. Comparison of picture frame and Bias-Extension tests for the characterization of shear behaviour in natural fibre woven fabrics. *Fibers and Polymers*, *14*(2), pp.338-344.

Tan, P., Tong, L. and Steven, G.P., 1997. Modelling for predicting the mechanical properties of textile composites—A review. *Composites Part A: Applied Science and Manufacturing*, *28*(11), pp.903-922.

Testa, R.B. and Yu, L.M., 1987. Stress-strain relation for coated fabrics. *Journal of engineering mechanics*, *113*(11), pp.1631-1646.

Tong, X.C., 2016. *Advanced materials and design for electromagnetic interference shielding*. CRC press.

Treloar, L.R.G., 1942. The structure and elasticity of rubber. *Reports on Progress in Physics*, *9*(1), p.113.

Treloar, L.R.G., 1944. Strains in an inflated rubber sheet, and the mechanism of bursting. *Rubber Chemistry and Technology*, *17*(4), pp.957-967.

Treloar, L.R.G., 1944. Stress-strain data for vulcanized rubber under various types of deformation. *Rubber Chemistry and Technology*, *17*(4), pp.813-825.

Treloar, L.R.G., 1973. The elasticity and related properties of rubbers. *Reports on progress in physics*, *36*(7), p.755.

Treloar, L.R.G., 1975. *The physics of rubber elasticity*. Oxford University Press, USA.

Tsakalakos, T., 1981. The bulge test: A comparison of the theory and experiment for isotropic and anisotropic films. *Thin solid films*, *75*(3), pp.293-305.

Ullah, H., 2013. *Analysis of mechanical behaviour and damage of carbon fabric-reinforced composites in bending* (Doctoral dissertation, Loughborough University).

Valanis, K.C. and Landel, R.F., 1967. The strain-energy function of a hyperelastic material in terms of the extension ratios. *Journal of Applied Physics*, *38*(7), pp.2997-3002.

Vandeurzen, P., Ivens, J. and Verpoest, I., 1996. A three-dimensional micromechanical analysis of woven-fabric composites: I. Geometric analysis. *Composites Science and Technology*, *56*(11), pp.1303-1315.

Vasilescu, M., 2016. Development of a hydraulic bulge test to determine the work hardening behaviour of sheet materials.

Venkatraman, P.D., 2015. Fabric properties and their characteristics. *Materials and technology for sportswear and performance apparel*, pp.53-86.

Wadham-Gagnon, M., Hubert, P., Semler, C., Païdoussis, M.P., Vézina, M. and Lavoie, D., 2006, April. Hyperelastic modeling of rubber in commercial finite element software (ANSYS). In *51st SAMPE International Symposium, LA*.

Walrath, D.E. and Adams, D.F., 1983. The losipescu shear test as applied to composite materials. *Experimental mechanics*, *23*(1), pp.105-110.

Wang, C., Shankar, K., Morozov, E., Ram Ramakrishnan, K. and Fien, A., 2020. Characterization of shear behavior in stainless steel wire mesh using bias-extension and picture frame tests. *Journal of Engineering Mechanics*, *146*(2), p.04019127.

Williams, R.W., 2010. *Measuring and modeling the anisotropic, nonlinear and hysteretic behavior of woven fabrics* (Doctoral dissertation, University of Iowa).

Wineman, A., 2005. Some results for generalized neo-Hookean elastic materials. *International Journal of Non-Linear Mechanics*, *40*(2-3), pp.271-279.

Xia, Y., Dong, Y., Xia, Y. and Li, W., 2005. A novel planar tension test of rubber for evaluating the prediction ability of the modified eight-chain model under moderate finite deformation. *Rubber Chemistry and technology*, *78*(5), pp.879-892.

Xu, X., Yao, X., Dong, Y., Yang, H. and Yan, H., 2021. Mechanical behaviors of non-orthogonal fabric rubber seal. Composite Structures, 259, p.113453.

Yang, H., Yao, X.F., Ke, Y.C., Ma, Y.J. and Liu, Y.H., 2016. Constitutive behaviors and mechanical characterizations of fabric reinforced rubber composites. *Composite Structures*, *152*, pp.117-123.

Yang, Y., Boom, R., Irion, B., van Heerden, D.J., Kuiper, P. and de Wit, H., 2012. Recycling of composite materials. *Chemical Engineering and Processing: Process Intensification*, *51*, pp.53-68.

Yeoh, O.H., 1993. Some forms of the strain energy function for rubber. *Rubber Chemistry and technology*, *66*(5), pp.754-771.

Yoneyama, S. and Murasawa, G., 2009. Digital image correlation. *Experimental mechanics*, *207*.

Zhang, L., 2010. *Reliability analysis of fabric structures* (Doctoral dissertation, Newcastle University).

Zhu, D., Mobasher, B., Vaidya, A. and Rajan, S.D., 2013. Mechanical behaviors of Kevlar 49 fabric subjected to uniaxial, biaxial tension and in-plane large shear deformation. *Composites Science and Technology*, *74*, pp.121-130.

Zioupos, P., Barbenel, J.C. and Fisher, J., 1992. Mechanical and optical anisotropy of bovine pericardium. Medical and Biological Engineering and Computing, 30(1), pp.76-82.

APPENDIX 1

Table 1: Results of fitting using uniaxial tension and planar data for samples loaded parallel to the weft fibre direction

Hyperelastic model	**constants**	**Least squared error**
Ogden N 1	μ_1= 18.60 α_1 = 25.00	40.21 %
Ogden N 2	μ_1= 417.55 α_1 = − 400.21 μ_2 = 8.26 α_2 = 6.13	38.67 %
Ogden N 3	μ_1 = -2672.08 α_1 = -10.35 μ_2 = 1695.67 α_2 = -6.39 μ_3 = 992.35 α_3 = -15.58	36.74 %
Yeoh N2	C10 = 8.48 C20 = 324.44	

Table 2: Results of fitting using uniaxial tension and planar data for samples loaded parallel to the warp fibre direction

Hyperelastic model	**constants**	**Least squared error**
Ogden N 1	μ_1= 8.31 α_1= 13.50	31.15 %
Yeoh N2	C10 = 4.31 C20 = 18.66	
Yeoh N3	C10 = 4.59 C20 = 3.93 C30 = 94.54	

APPENDIX 2

Table 3: Parameters for equation 5.16: characterising matrix

EXA-1182	**C_m / MPa**	**C_{m2} / MPa**	**α**
1	17.569	96.897	2
2	20.635	96.543	2
3	19.617	91.255	2
4	18.512	93.793	2
MEAN	19.08325	94.622	
EXA-1180	**C_m / MPa**	**C_{m2} / MPa**	**α**
1	9.2823	20.08	2
2	10.358	34.973	2
3	7.7598	30.214	2
4	9.3058	28.052	2
MEAN	9.176475	28.32975	
EXA-1196	**C_m / MPa**	**C_{m2} / MPa**	**α**
1	45.38837	491.9578	2
2	47.291	174.47	2
3	56.406	184.03	2
4	48.803	184.62	2
MEAN	49.47209	258.7695	

APPENDIX 3

Table 4: Parameters for equation. 5.17: characterising the fabric in the weft direction.

EXA-1182	**K_1 / MPa**	**K_2 / MPa**	**α_1**	**α_2**
1	5.157151529	2.420876057	3	2
2	7.120224626	2.333668604	3	2
3	2.671774875	3.485417411	3	2
4	2.749200415	3.118908254	3	2
MEAN	4.424587861	2.839717581		
EXA-1180	K1 / MPa	K2/MPa	α	
1	0	0.836947304	3	2
2	0.05910961	0.953176952	3	2
3	0.174317	0.812093	3	2
4	0.01050161	0.860727593	3	2
MEAN	0.060982146	0.865736274		
EXA-1196	**K_1 / MPa**	**K_2 / MPa**	**α_1**	**α_2**
1	5.816839	7.282352	3	2
2	1	7.4	3	2
3	4.55253	5.594593	3	2
4	1.52546	7.771230806	3	2
MEAN	3.223707	7.012044		

APPENDIX 4

Table 5: Parameters for equation 5.18 characterising the fabric in the primary direction

EXA-1182	**K_3 / MPa**	**K_4 / MPa**	**α_1**	**α_2**
1	0.199034122	0.621890123	3	2
2	0.333223922	0.545881917	3	2
3	0.171540018	0.557178043	3	2
4	0.219407412	0.581528034	3	2
MEAN	0.230801368	0.576619529		
EXA-1180	**K_3 / MPa**	**K_4 / MPa**	**α_1**	**α_2**
1	1.840025237	0.726897812	3	2
2	1.510798407	0.804810151	3	2
3	3.196427657	0.481202963	3	2
4	0	0.979678655	3	2
MEAN	1.636813	0.748147		
EXA-1196	**K_3 / MPa**	**K_4/MPa**	**α_1**	**α_2**
1	2.368964	3.363224	3	2
2	2.473917	3.526026	3	2
3	2.434368824	2.664834861	3	2
4	3.42559	3.977655	3	2
MEAN	2.67571	3.382935		

APPENDIX 5

Table 6: Material parameters obtained from the curve fitting process from Equation 5.19 characterising the fabric in the matrix-fabric interaction in shear.

EXA-1182	**K_8 / MPa**	**EXA-1196**	**K_8 / MPa**
1	1.508062728	**1**	1.627772495
2	1.719360032	**2**	1.410126188
3	1.604828708	**3**	1.202656123
4	1.494189463	**4**	1.199569266
MEAN	1.581610233	**MEAN**	1.360031018
EXA-1180	**K_8 / MPa**		
1	0.626952291		
2	0.472803044		
3	0.445598946		
4	0		
MEAN	0.515118094		

APPENDIX 6

Subroutine-(VUANISOHYPER) coding equation 5.17 in FORTRAN

```
C-------------------------------------------------------------
      subroutine vuanisohyper_inv (nb, nFiber, nInv, nElement, nIntPt,
     $     nLayer, nSecPt, cmname, nstatev, nfieldv, numprops,
     $     props, tempOld, tempNew, fieldOld, fieldNew, stateOld,
     $     sInvariant, zeta, uDev, duDi,d2uDiDi, stateNew)
C
      include 'vaba_param.inc'
C
      character*80 cmname
      dimension  props(numprops),
     $     tempOld(nb), fieldOld(nb,nfieldv),stateOld(nb,nstatev),
     $     tempNew(nb), fieldNew(nb,nfieldv),stateNew(nb,nstatev),
     $     sInvariant(nb,nInv), zeta(nb,nFiber*(nFiber-1)/2),
     $     uDev(nb), duDi(nb,nInv), d2uDiDi(nb,nInv*(nInv+1)/2)
C
C
C
      if (cmname(1:13) .eq. 'VUANISO_MODEL') then
         call VUANISOHYPER_INVHGO(sInvariant, uDev, zeta, nFiber, ninv,
     $     duDi, d2uDiDi, nb, numprops, props)

      else
         call xplb_abqerr(-2,'User subroutine VUANISOHYPER_INV missing!'
     *        ,intv,zero,' ')
         call xplb_exit
      end if
C
C
C
      return
      end
c-----------------------------------------------------------------
c
c     New model
c
      subroutine vuanisohyper_invhgo (ainv, ua, zeta, nfibers, ninv,
     $     ui1, ui2, nb, numprops, props)
C
      include 'vaba_param.inc'
C
      dimension ua(nb), ainv(nb,ninv), ui1(nb,ninv),
     $     ui2(nb,ninv*(ninv+1)/2), props(numprops)
C
c     ainv: invariants
c     ua  : udev
c     ui1 : dUdI
c     ui2 : d2U/dIdJ
C
      parameter ( half = 0.5d0,
     *            zero = 0.d0,
     *            one  = 1.d0,
     *            two  = 2.d0,
     *            three= 3.d0,
     *            four = 4.d0,
     *            five = 5.d0,
     *            six  = 6.d0,
c
```

```
     *            index_I1 = 1,
     *            index_J  = 3)
c
C
C     Anisotropic model
C
       a1=props(1)
       a2=props(2)
       a3=props(3)
       a4=props(4)
       a5=props(5)
       a6=props(6)
       a7=Props(7)
c
      do kb = 1,nb
        ua(kb) = zero

        do k1 = 1, nfibers
          index_i4 = indxInv4(k1,k1)
           rI1m3= (ainv(kb,index_i1) - three)
           rI4m3 =     (ainv(kb,index_i4) - one )


          ht4a    = (row*row)
          aux     = (E_alpha*E_alpha)
c energy
        ua(kb) =   a1 * rI1m3 + a2 * rI1m3*rI1m3
     *           + a3 * rI4m3*rI4m3*rI4m3 + a4 * rI4m3*rI4m3
     *           + a5 * rI4m3*rI4m3*rI4m3 + a6 * rI4m3*rI4m3
     *           + a7 * rI4m3


c ui1
        ui1(kb,index_i1) = a1 + two * a2 * rI1m3
        ui1(kb,index_i4) = three * a3 * rI4m3*rI4m3 + two * a4 * rI4m3
     *                   + three * a5 * rI4m3*rI4m3 + two * a6 * rI4m3
     *                   + a7
c
c ui2
        ui2(kb,indx(index_i1,index_i1)) = two * a2
        ui2(kb,indx(index_i4,index_i4)) = three * two * a3 * rI4m3
     *           + two * a4 + three * two * a5 * rI4m3 + two * a6

c
       end do
c

      end do
c
      return
      end
C-------------------------------------------------------------
C     Function to map index from Square to Triangular storage
C              of symmetric matrix
C
      integer function indx( i, j )
      include 'vaba_param.inc'
      ii = min(i,j)
      jj = max(i,j)
      indx = ii + jj*(jj-1)/2
      return
```

```
      end
C-------------------------------------------------------------
C
C     Function to generate enumeration of scalar
C     Pseudo-Invariants of type 4

      integer function indxInv4( i, j )
      include 'vaba_param.inc'
      ii = min(i,j)
      jj = max(i,j)
      indxInv4 = 4 + jj*(jj-1) + 2*(ii-1)
      return
      end
C-------------------------------------------------------------
C
C     Function to generate enumeration of scalar
C     Pseudo-Invariants of type 5
C
      integer function indxInv5( i, j )
      include 'vaba_param.inc'
      ii = min(i,j)
      jj = max(i,j)
      indxInv5 = 5 + jj*(jj-1) + 2*(ii-1)
      return
      end
C-------------------------------------------------------------
c
```

APPENDIX 7

Figure Appendix 7. 1 Pressure Pump System